Formation of long-ranged morphogen gradients by cell-to-cell relay

DISSERTATION

zur Erlangung des akademischen Grades

Doctor rerum naturalium

vorgelegt

dem Bereich Mathematik und Naturwissenschaften
der Technischen Universität Dresden

von
Johanna Dickmann
geboren am 1.9.1990 in Engelskirchen

Max-Planck-Institut für Physik komplexer Systeme

Max-Planck-Institut für molekulare Zellbiologie und Genetik

Dresden, September 2020

Eingereicht am 4. September 2020
Verteidigt am 7. Dezember 2020

Gutachter:
Prof. Dr. Christian Dahmann
Prof. Dr. Frank Jülicher

Abstract

Embryonic development, regeneration, and tissue renewal are spectacular tissue-patterning events. Tissue patterning requires information. This information is often provided by signalling molecules that form graded concentration profiles in space, referred to as signalling gradients or morphogen gradients. Planarian flatworms are an ideal model organism to study tissue patterning as they constantly turn over all of their tissues and are able to regenerate from arbitrary amputation fragments. At a body length of up to 2 cm, planarians are orders of magnitudes larger than tissues organised during embryonic development in other species. Yet, flatworms employ signalling gradients for tissue patterning. Like in other organisms throughout the animal kingdom, their main body axis is patterned by a Wnt signalling gradient. Experiments have suggested a positive feedback mechanism of Wnt-mediated Wnt expression to be implicated in the formation of this Wnt signalling gradient in planarians. Inspired by these observations, in this thesis we present a cell-to-cell relay mechanism based on positive feedback to explain long-ranged signalling gradient formation. To account for the cellular nature of the relay, we built a discrete model, that considers individual cells and extracellular spaces. The relay is generated by a positive feedback loop in which extracellular signalling levels positively regulate intracellular effector concentrations which in turn leads to production of more extracellular signalling molecules. We show that a cell-to-cell relay gives rise to steady-state gradients reaching length scales of the order of hundreds of cells, corresponding to millimetres. The length scale is regulated by the strength of the feedback, which allows scaling the steady-state gradient to tissue size by adapting the feedback strength. Polarised secretion of signalling molecules in response to the positive feedback leads to an effective drift of signalling molecule concentration through the system. This allows the formation of signalling gradients with a length scale of tens to hundreds of cells (millimetres) within hours to days for a physiologically relevant diffusion coefficient and degradation rate of the signalling molecules. Thus, in contrast to a diffusion/degradation-based mechanism that is widely used to explain signalling gradient formation during embryonic development, the relay mechanism requires neither extraordinarily quickly-diffusing nor very long-lived signalling molecules to explain the formation of long-ranged signalling gradients on biologically relevant time scales. The cell-to-cell relay mechanism is therefore an attractive concept to explain the long-ranged patterning effects of poorly diffusive morphogens.

Zusammenfassung

Die räumliche und zeitliche Organisation von Zellen während Embryonalentwicklung, Regeneration oder Erneuerung von Geweben ist eine faszinierende Fähigkeit lebender Organismen. Dazu benötigen die Zellen Informationen über ihre Position im Organismus. Diese Informationen werden oft in Form von Signal- oder Morphogengradienten bereitgestellt, also von Signalmolekülen, die Konzentrationsprofile im Raum bilden. Plattwürmer (Planarien) sind ein sehr geeigneter Modellorganismus, um solche Gewebeorganisationsprozesse zu erforschen, weil sie kontinuierlich alle Zellen ihres Körpers erneuern und aus kleinsten Gewebestücken regenerieren können. Bei einer Körperlänge von bis zu 2 cm muss Gewebe auf größeren Längenskalen organisiert werden, als es für die Embryonalentwicklung in anderen Spezies nötig ist. Trotzdem treten auch in Planarien Signalgradienten auf. Ihre Hauptkörperachse wird, wie bei anderen Tieren auch, von einem Wnt-Signalgradienten organisiert. Experimentelle Beobachtungen legen nahe, dass ein positiver Feedbackmechanismus, in dem ein Wnt-Signal zur Erzeugung von mehr Wnt-Molekülen führt, wesentlich zur Bildung dieses Gradienten beiträgt. Inspiriert durch diese Beobachtungen stellen wir in dieser Arbeit einen Mechanismus zur Ausbildung von Signalgradienten vor, der auf positivem Feedback basiert. Um die besondere Bedeutung der Zellen für dieses Feedback berücksichtigen zu können, ist das hier präsentierte Modell diskret und besteht aus Zellen und Extrazellularräumen. Das positive Feedback sorgt für eine Signalübertragung von Zelle zu Zelle, wobei die Konzentration der extrazellulären Signalmoleküle die Konzentration des intrazellulären Effektors positiv reguliert, was wiederum zur Bildung von mehr Signalmolekülen führt. Wir zeigen, dass dieser Signalübertragungsmechanismus langreichweitige Signalgradienten mit einer Längenskala von mehreren hundert Zellen, also in der Größenordnung von Millimetern, ausbildet. Die Längenskala wird durch die Stärke des positiven Feedbacks reguliert. Eine entsprechende Regulation der Feedbackstärke ermöglicht es, die Längenskala des Signalgradienten an die Größe des Systems anzupassen. Erfolgt die Sekretion der Signalmoleküle, die die Zellen als Antwort auf das Feedback produzieren, gerichtet, führt das zu einer gerichteten Ausbreitung der Signalmolekülkonzentration im System, also zu Drift. Auf diese Weise können bei biologisch relevanten Werten des Diffusionskoeffizienten und der Degradationsrate der Signalmoleküle Signalgradienten mit einer Längenskala von mehreren zehn bis hundert Zellen in Stunden bis Tagen gebildet werden. Im Unterschied zum Diffusions/Degradations-Mechanismus, der häufig zur Erklärung von Gradientenbildung im Kontext von Embryonalentwicklung herangezogen wird, benötigt der in dieser Arbeit präsentierte Signalübertragungsmechanismus also weder sehr schnell diffundierende noch sehr langlebige Moleküle, um

die Bildung von langreichweitigen Signalgradienten auf biologisch relevanten Zeitskalen zu erklären. Da viele Morphogene langsam diffundieren, macht das den Zell-zu-Zell-Signalübertragungsmechanismus zu einem attraktiven Konzept, um die Bildung von langreichweitigen Morphogengradienten zu erklären.

Acknowledgements

I feel very fortunate to have been inspired and supported by wonderful people over the course of my thesis work. I am very grateful to all of them.

My special thanks go to my supervisors Frank Jülicher and Jochen Rink. Thank you for giving me the opportunity to work on this interdisciplinary project. Frank, thank you for guiding me through this project, for many insightful discussions and your advice and support throughout the project. Jochen, thank you for hosting me in your lab for more than a year over the course of the project, for sharing your ideas during enthusiastic discussions and for your advice and support.

I wish to thank Christian Dahmann and Suzanne Eaton for being part of my thesis advisory committee. Thank you Christian, for always being available for TAC meetings, for helpful questions and comments on the project and for your advice on the final stretch pre-submission. Thank you Suzanne, for amazing discussions jumping from the theory to the experiential side of the project and back again, for challenging assumptions in a helpful way, and for always providing new perspectives on the project.

I am grateful to Steffen Werner, for a great introduction to the project, for welcoming me to the institute with a two-week one-on-one math lecture and for his support especially at the beginning of the project.

I wish to thank Alexander Mietke, for many discussions on science and beyond, and for his support throughout my thesis. I am deeply grateful to Jonathan Bauermann, for his support and for many interesting discussions ranging from dynamic solutions via implementing numerical solvers to politics and society. I wish to thank Charlie Duclut, for many helpful discussions, partially combined with tandem-sessions, for reading and discussing this entire thesis with me, and supporting me, especially during the final stretch. I am grateful to Daniel Aguilar-Hidalgo for helpful discussions on patterning, discrete models and beyond, as well as for his support. I wish to thank Zena Hadjivasiliou for helpful discussions on length scales and beyond. I wish to thank to Felix Meigel, for helpful discussions

on abstracts, calculations and beyond; and Christian Hanauer, for valuable plotting advice and helpful discussions on scaling. I wish to thank many present and past members of the Biological Physics department for thoughtful discussions, and good times inside and outside of the institute.

I am deeply grateful to Hanh Vu, for sharing her amazing knowledge of planarian biology, *in situ* hybridisation and many other things, as well as and for great support inside and outside of the lab. I wish to thank Mario Ivanković, for helpful discussions from western blot to neoblasts and good times inside and outside of the lab. I wish to thank James Cleland for sharing his enthusiasm about planarians, for many interesting discussions about planarian Wnt signalling, and acquainting me with planarian wet lab biology. I would like to thank Heino Andreas and Stephanie von Kannen for their support. I wish to thank Olga Frank, Markus Grohme, Andrei Rozanski, Tobias Boothe, Miquel Vila Farré, Uri Weill, Vinca Yadav, Thomas Brochier, and Radka Haneckova for good times in the lab.

I wish to thank Suat Özbek and Bérénice Ziegler for interesting discussions about Wnt proteins and Wnt signalling.

I am grateful to P. V. Sriluckshmy and Sascha Wald for being wonderful office mates. I would like to thank Felix Meigel, Hanh Vu, Omar Adame, Jonathan Bauermann, and Christian Hanauer for reading and discussing parts of this thesis with me.

I wish to thank Ulrike Burkert, Elise Voigt, and many other members of the administration for providing immediate, friendly and efficient support in many situations. I am grateful to Thomas Müller, and many other members of the IT department for their instant help with any kind of problem. I wish to thank the PhD office for their administrative support.

I wish to thank Benjamin Seebröker for countless interesting discussions on just about everything and for his constant support. I am deeply grateful Olivier Benjamin for his unconditional support, especially during the final stretch of this thesis. My special thanks go to my parents for their continuous support and encouragement throughout my life.

Contents

1. Introduction **1**

1.1. Organising tissues - a patterning challenge 1

1.2. The concept of morphogen gradients arises 4

1.3. Body axes organisation by signalling gradients 11

1.3.1. The canonical Wnt signalling pathway 12

1.3.2. Wnt signalling during embryonic development and regeneration 15

1.3.3. Wnt - a morphogen? 16

1.4. Planarian flatworms - Masters of regeneration 18

1.4.1. An introduction to planarians 18

1.4.2. The patterning system of planarians 21

1.4.3. Wnt signalling along the main body axis of planarians . . . 23

1.5. Physical models of morphogen gradient formation 32

1.6. Aim of this thesis 41

2. Signalling gradient formation using a cell-to-cell relay **43**

2.1. The challenge: Generating large-scale patterns 43

2.2. A discrete cell-to-cell relay model for signalling gradient formation 45

2.3. Boundary conditions 50

2.4. Choice of model parameters 51

2.5. Numerical solution to the model 55

2.6. Summary and discussion 56

3. The signalling gradient at steady state **58**

3.1. Large-scale pattern formation in light of positive feedback 58

3.2. Approximate analytical steady-state solution to the model 61

3.3. Linear feedback response in the limit of low effector concentration 67

3.4. The effect of positive feedback on gradient length scale 73

3.5. Gradient shape 76

3.6. Summary and discussion 82

4. Scaling of signalling gradients using the relay mechanism 85
4.1. Scaling is required for all patterning problems 85
4.2. Pattern scaling by adjusting feedback strength 85
4.3. Summary and discussion 91

5. Dynamics of gradient formation 96
5.1. How long does it take to form a steady-state signalling gradient? . 96
5.2. Dynamic solution in the limit of a linear feedback response 97
5.3. An analytical approximation to the slowest relaxation time 99
5.4. Influence of the positive feedback on the slowest relaxation time . 102
5.5. Analysing the trade-off between length scale and time scale 105
5.6. Summary and discussion 108

6. Role of tissue polarity in cell-to-cell relay 111
6.1. Impact of tissue polarity on signalling gradients formed by cell-to-cell relay 111
6.2. Effect of tissue polarity on the length scale of signalling gradients at steady state 112
6.3. Effect of tissue polarity on the trade-off between length scale and time scale 116
6.4. Summary and discussion 117

7. Discussion 120

A. Dynamic solution to the diffusion/degradation mechanism 125

B. Effect of the choice of boundary conditions 130
B.1. Model dynamics revisited 130
B.2. Outer system boundaries 136
  B.2.1. Constant width of extracellular spaces at the boundaries . 137
  B.2.2. Different widths of extracellular spaces at the boundaries . 138
B.3. Source/non-source interface 140
B.4. Discussion 141

C. Numerical solution to differential equations: Implicit-explicit Euler method 143

C.1. Explicit Euler 143

C.2. Implicit Euler 143

C.3. Implicit-explicit Euler 145

C.4. Steady-state solution 146

D. Numerical solution to the model 148

E. Analytical approximate steady-state solution to the model 150

E.1. Linearisation of the steady-state equations for signalling molecule concentration 150

E.2. Solution to the linearised steady-state equations 152

E.3. Steady-state length scale in the limit of an infinitely high feedback response 156

E.4. Steady-state length scale in the limit of feedback saturation 157

E.5. Limit of a linear feedback response 158

E.6. Shape of the signalling gradient at steady state 162

F. Definition of length scale based on the numerical steady-state solution 164

G. Dynamic solution in the limit of a linear feedback response 166

G.1. Approximate dynamic solution to the model in the limit of a linear feedback response 166

G.2. Symmetry considerations 168

G.3. Analytical approximation to slowest relaxation time in the limit of no feedback 169

List of Figures 172

Bibliography 184

1. Introduction

1.1. Organising tissues - a patterning challenge

The vast majority of cells in our body has the same genetic information [3]. They can nevertheless be very different from each other: skin cells, nerve cells, cells that give rise to our internal organs are just a few examples of the different cell types, characterised by distinct morphology, contents and function. The reason for this is that different cell types use different subsets of the genetic information they have. Thus, the question is how the distinct cell types 'know' which parts of the DNA to read out, i.e. how to regulate their gene expression. The challenge becomes even more obvious, when taking into account that virtually all cells of the body are derived from a single one: the fertilised egg. Thus, the individual cell fate choices in the forming embryo have to be coordinated both in space and in time, ensuring that the right cells are formed at the right place. At its heart, this is a patterning challenge. This intricate challenge of patterning newly-formed tissue is however not restricted to development: animals capable of regenerating missing body parts after amputation or even of whole-body regeneration from fragments are faced with this patterning challenge throughout their lives. Development and regeneration are similar in that during both new tissue is generated and organised. They are different in that development always starts from a fertilised egg and goes down a specific path that is seemingly invariant between individuals. Regeneration, on the other hand, poses the additional challenge of a variable starting point, starting from whatever is left after injury and rebuilding the missing part. Lizards, for instance, can shed their tail if threatened or as a predator defence mechanism and regenerate it [70], salamanders can rebuild an entire limb after amputation [35], zebra fish can regenerate their caudal fin, eyes, liver, pancreas, kidney, bones, sensory hair and even their heart and central nervous system [35]. Certain planarian flatworm species and the fresh water polyp hydra can even undergo whole-body regeneration, reforming their whole body from a tiny amputation fragment in the case of planarians [84], or even re-aggregating individual cells into a new organism in the case of hydra [34]. In addition to the variable initial condition, regeneration also requires the new structure to match the size and proportions of the regenerating organism. Since regeneration also happens in fully grown adult organisms, the structures to be formed are typically much larger than those formed during embryonic development. Taken together, this poses the challenge of generating large-scale, scalable patterning information.

New tissue is formed from existing tissue by division of resident cells, both during embryonic development and during regeneration. The fertilised egg is totipotent, able to give rise to all tissues of the body and all the extra embryonic tissue required for development [35]. It divides, generating pluripotent embryonic stem cells that are able to give rise to all cell types of the body. Over the course of development, these produce more specialised, multipotent stem cells that can give rise to a certain subset of tissues. Those are also still present in the adult organism as adult stem cells that replenish the respective tissues they reside in over the course of the animal's life [35]. Replenishing tissue during regeneration requires generating cells of all missing types. It thus requires either stem cells of sufficient potency or body cells to first de-differentiate and then to re-differentiate into the required cell types [35]. In particular, whole-body regeneration observed in planarians is enabled by pluripotent stem cells in the adult organism that are also present in the absence of injury. In this case, they contribute to homeostatic tissue renewal (reviewed e.g. in [84], [50]). Thus, cell division gives rise to the newly-forming embryo, in case of development, or to the newly-formed body part(s) in case of regeneration. But how is this newly-formed tissue organised? How do the cells adopt different cell fates and how is the physical shape of the organism generated?

These questions have fascinated people for centuries and because of the shared tissue-organisation challenge in both development and regeneration it may not come as a surprise that we have learned from one for the other and vice versa. Since all bilaterians, i.e. animals having a mirror-symmetric body plan, and thus the majority of animals, are characterised by three body axes, (the anteroposterior - AP or main body axis, the dorsoventral - DV, and mediolateral - ML

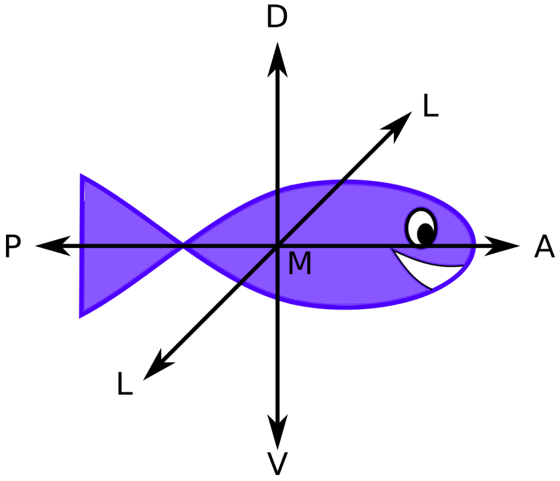

Figure 1.1.: **Bilaterians have three body axes.** Bilaterians have a mirror-symmetric body plan with the main body axis or anteroposterior (AP, head to tail) axis as the symmetry axis. Perpendicular to this axis, the dorsoventral (DV, belly to back), and mediolateral (ML, centre to left and to right) axes are defined.

axes, Fig. 1.1), a lot of work has been dedicated to deciphering tissue organisation along theses axes. Signalling, often in form of morphogen gradients, has been found to organise these body axes both during embryonic development and regeneration [15, 16, 40, 44, 45, 46, 49, 53, 58, 77, 79].

In this thesis, we introduce a relay mechanism for the formation of long-ranged morphogen gradients, in which the signal is passed on from one cell to the next by positive feedback. This idea is inspired by observations on the Wnt signalling gradient patterning the main body axis of planarian flatworms [99, 98]. In order to put this project onto context, we introduce the history of pattern formation with a special emphasis on how the concept of morphogen gradient arose and how they where identified experimentally (Section 1.2). Subsequently, we summarise how morphogen gradients are employed to pattern body axes with a special focus on canonical Wnt signalling patterning the main body axis (Section 1.3). We then introduce planarian flatworms, that are true masters of regeneration and self-renewal and thus a great model system to study patterning (Section 1.4). Finally, we present the current physical understanding of morphogen gradient formation based on diffusion and degradation (Section 1.5) and conclude by stating the specific aim of this thesis (Section 1.6).

1.2. The concept of morphogen gradients arises

In 1898, Morgan observed that the rate at which flatworms regenerated is dependent on the position of the amputation fragment along their main body axis [68]. He deduced that there were ’formative substances’ present in a graded manner along the body axis that led to this behaviour ([69] as cited in [109]). The chemical nature of signals capable of organising tissue, and their origin from a localised source inside the tissue, was shown by fascinating surgical experiments during embryonic development. A famous example is the Spemann organiser, discovered by transplanting a piece of tissue from the dorsal lip tissue of a developing newt embryo at gastrula stage into the region that gives rise to the ventral epidermis of an embryo at the same stage of a newt species with a different pigmentation (Fig. 1.2, [93]). This prompted the latter to form a second embryonic axis, eventually leading to an additional embryo joined belly-to-belly to the host. Due to the different histological properties of the two species used for tissue grafting in this experiment, it was obvious that the secondary embryo was comprised both of graft and donor tissue [93]. Mangold and Spemann concluded that formation of the secondary body axis was induced by the organiser [93].

In addition to the experimental investigation of tissue patterning, there were also purely theoretical considerations. In 1952, Alan Turing asked how a ’form producer’, that he termed ’morphogen’ obtains its spatial organisation [104]. He realised that diffusion, normally known to even out any concentration differences, can, under specific conditions, give rise to spatial patterns when combined with chemical reactions (Fig. 1.3, [104]). In the self-organised reaction/diffusion system he suggested, a slowly diffusing molecule that activates its own net production and a quickly diffusing molecule that inhibits its own net production mutually activate and repress each other’s net production. This leads to spontaneous, stable pattern formation after a local perturbation of a homogeneous steady state. When introducing the term ’morphogen’, which was ’not intended to have any very exact meaning’ [104], he probably did not foresee that we would still be using this term decades later to refer to a diffusible substance acting away from its origin of production to induce cell fate decisions in a concentration-dependent manner [35]. In his work, he also stressed the importance of mechanical forces in tissue organisation and suggested that there was an interplay between chemical patterning processes by reaction and diffusion and mechanical processes.

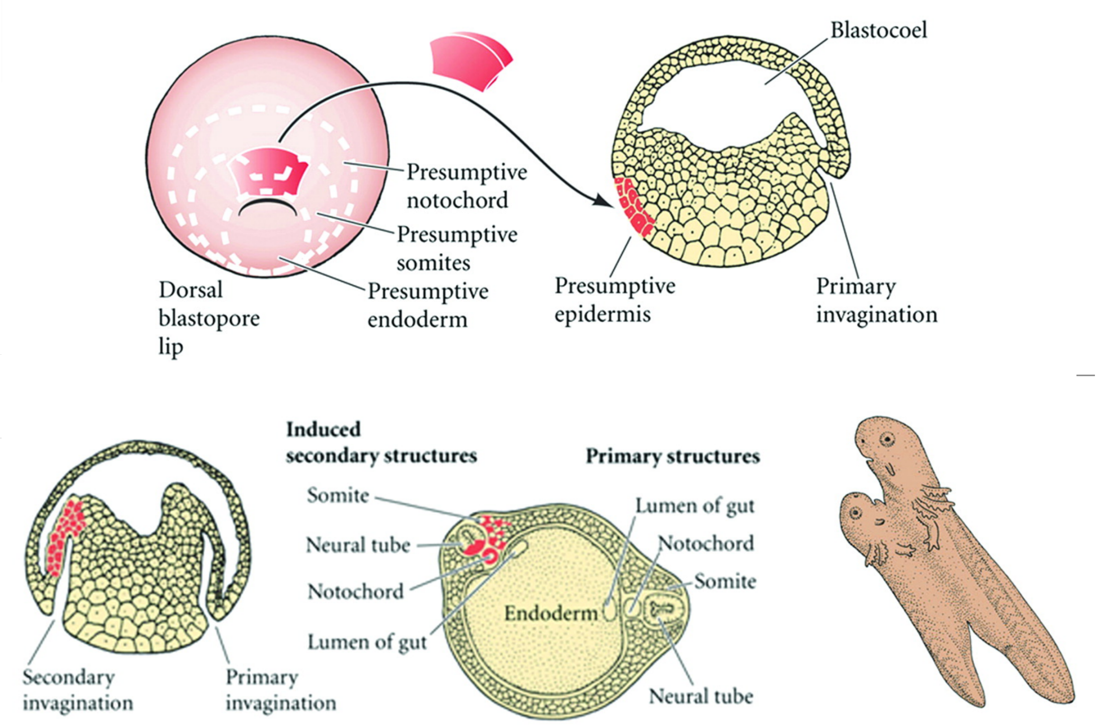
Blastocoel
Presumptive notochord
Presumptive somites
Presumptive endoderm
Dorsal blastopore lip
Presumptive epidermis
Primary invagination
Induced secondary structures
Primary structures
Somite
Neural tube
Notochord
Lumen of gut
Lumen of gut
Notochord
Somite
Endoderm
Neural tube
Secondary invagination
Primary invagination

Figure 1.2.: **The Spemann organiser.** A piece of tissue from the the dorsal blastopore lip of a pigmented donor newt embryo (rose) is transplanted into the presumptive epidermis of another un-pigmented newt embryo (host, yellow). The latter forms a secondary invagination at the site of tissue transfer, that develops into induced secondary structures. Eventually, an additional embryo is formed joined belly-to-belly to the host. Figure reproduced with permission from Ref. [88].

Focussing on the chemical signals, Lewis Wolpert introduced the concept of 'positional information' in 1969 [118]. The idea is, that a cell 'knows' where it is in space and adopts a cell fate appropriate to this position. In line with the experiments of Morgan [68], Mangold, and Spemann [93] described above, he suggested that a concentration gradient of a substance could induce cell fate in a concentration-dependent manner [118]. His illustrative example of a system generating different colors based on their positional information gave this idea the name 'French flag model'[1] (Fig. 1.4).

---

[1] Note that Wolpert originally introduced the 'French flag problem' to conceptualise the challenge of pattern formation in face of growth and regeneration: The pattern had to be scaled to tissue size and reform after amputation ([118], [117] as cited in [92]). The concept of the 'French flag model' as we use it today developed over the years based the idea of 'positional information' that he introduced as one of the possible ways to solve this problem [92].

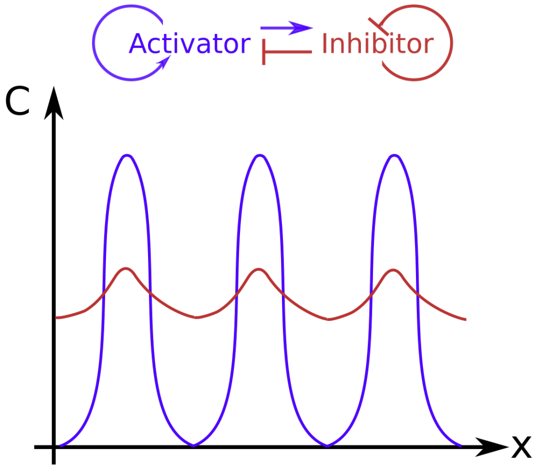

Figure 1.3.: **Turing patterns.** Two molecules species can form self-organised patterns based on reaction and diffusion. Example of a quickly diffusing inhibitor (red) and a more slowly diffusing activator (blue) that inhibit and activate their own and each-other's production, respectively, is shown.

In 1970, Francis Crick introduced a model for the formation of concentration gradients of a diffusive substance based on a local source and a local sink, giving rise to a linearly decaying steady-state profile (Fig. 1.5, [23]). Two years later, Gierer and Meinhardt suggested a refinement of Turing's idea of mutual activation and inhibition of two diffusive substances implicated in pattern formation: given a shallow source gradient, two initial distributions of a quickly diffusing inhibitor and a slowly diffusing activator self-organise into a pattern that can even roughly scale with system size if activator concentration is limited, e.g. by saturation in production [34]. It is remarkable that all of these considerations were made before a morphogen gradient had actually been shown to induce different cell fates in a concentration-dependent manner in a biological system. The first experimental proof of a morphogen gradient was accomplished years later, when Nüsslein-Volhard and co-workers discovered Bicoid[2] [32, 24, 25].

Cytoplasmic transplantation experiments using cytoplasm of *Bicoid* knock-out,

---

[2] Note that, in an attempt to unify notation conventions between different species, we will follow the convention introduced in Alberts *et al.* and refer to genes and RNAs in italics, starting with an upper case letter, e.g. *Bicoid*, whereas we will refer to proteins in roman font, starting with a capital letter, e.g. 'Bicoid', unless they traditionally have a lower case name such as e.g. 'actin' [3].

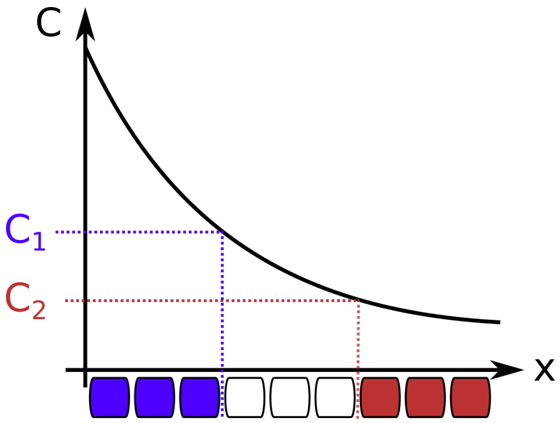

Figure 1.4.: **The French flag model.** Cells (squares) exposed to a morphogen concentration (C) above a certain threshold C_1 differentiate in a certain way (depicted as blue), those exposed to concentrations between C_1 and C_2 differentiate differently (depicted as white) and those exposed to concentration below C_2 attain yet another fate (depicted as red).

knock-in, and wild-type embryos revealed that Bicoid specifies anterior fate and represses posterior fate in a concentration-dependant manner [32]. Strikingly, its mRNA was shown to be localised at the anterior pole [31, 14]. The visualisation of the Bicoid protein gradient decaying away from the anterior pole [24] as well as the finding that Bicoid does indeed induce different fates in the anterior half of the fly embryo in a concentration-dependent manner [25] provided the first molecular evidence for, and thus confirmed the idea of, a morphogen gradient (Fig. 1.6). Moreover, the Bicoid protein gradient was shown to have an exponentially decaying profile [25].

Equivalently compelling evidence for a morphogen in vertebrate development stems from investigations of Activin (TGF-β superfamily) signalling in developing *Xenopus laevis*: different Activin concentrations led to differential gene expression in a concentration-dependent manner in unspecified *Xenopus* cells [38]. This finding was confirmed and refined *in vivo* by introducing an Activin source into the developing tissue [42]. Close to the Activin source, i.e. at high Activin concentrations, *Goosecoid* was expressed, whereas at a medium distance, i.e. at lower concentrations *Xbra* was expressed. Neither of these two genes was expressed even further away at very low Activin concentrations (Fig. 1.7, [42]). In particular, Activin was found to act by diffusion, as revealed by inserting a patch

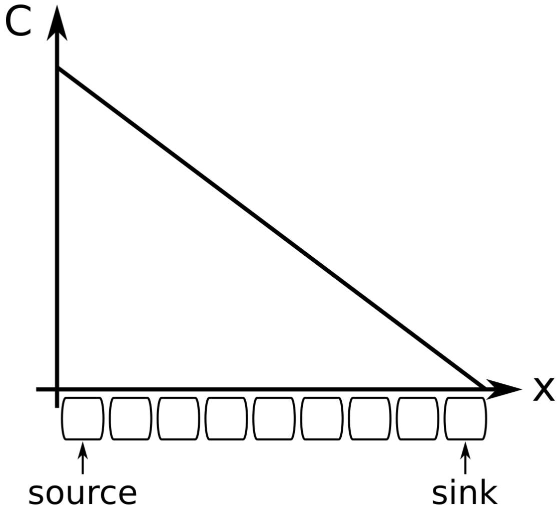

Figure 1.5.: **Crick's model for gradient formation.** A linear steady-state profile of morphogen concentration (C) is generated if the morphogen is exclusively produced by a local source cell and exclusively degraded by a local sink cell. The molecule spreads via diffusion. Figure based on [23].

of tissue blocked for protein synthesis [42]. These findings further strengthened the notion of a morphogen as a diffusible substance regulating gene expression in a concentration-dependent manner [42].

In general, morphogens are signalling molecules. Signalling molecules elicit an intracellular response by binding to a receptor on the cell surface. This binding activates an intracellular signalling cascade, called a signalling pathway [3, 35]. These signalling pathways can have a variety of effects on the cell. In particular, they can evoke changes in gene expression in the receiving cell [35]. Graded concentration profiles of signalling molecules are often referred to as 'signalling gradients' rather than 'morphogen gradients'. While the term 'morphogen gradient' stresses the diffusive and cell fate-inducing properties of the molecule, the term 'signalling gradient' stresses the concept of the cellular response induced by the binding of the molecule. Interestingly, it is not only the concept of a morphogen, but also the signalling pathways employed for patterning that are highly conserved across the tree of life.

The questions of how morphogen gradients are formed and how they are then read out in order to induce cell fates appropriate to the cell's position has con-

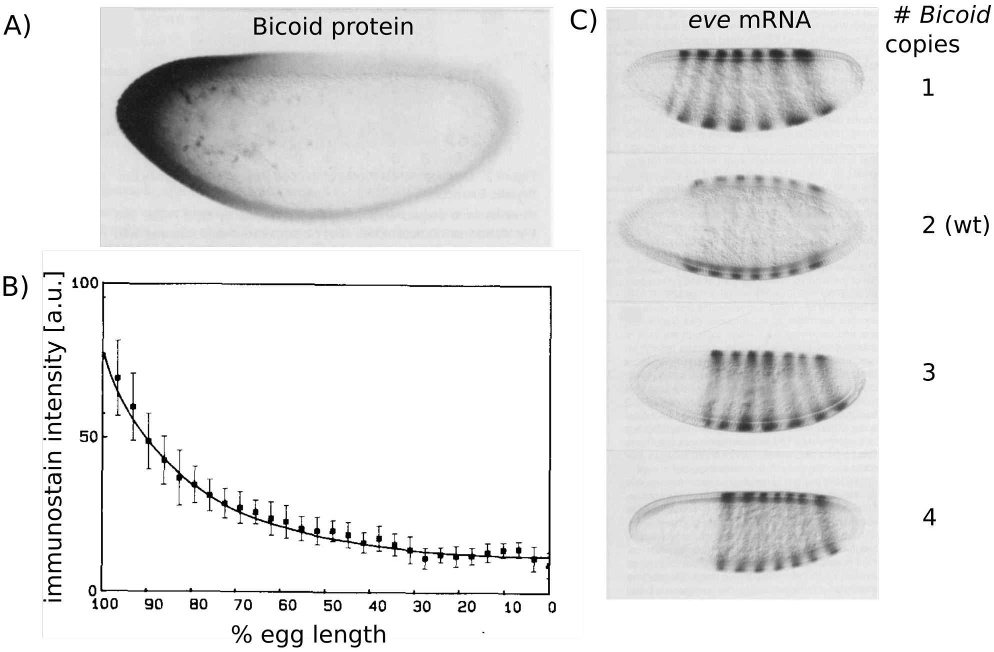

Figure 1.6.: **The first observation of a morphogen gradient. A)** The Bicoid protein gradient visualised by horse-radish peroxidase reaction in a whole mount of a wild-type *Drosophila* embryo in syncytial blastoderm stage. Modified with permission from Ref. [24]. **B)** Quantification of the Bicoid protein gradient in embryos at early nuclear cycle 14. Average immunostaining intensity along the AP axis of ten embryos ± standard deviation. Modified with permission from Ref. [24]. **C)** *eve* mRNA is expressed in response to Bicoid. The spatial onset of the expression pattern is moved posteriorly when the number of *Bicoid* gene copies in the mother is increased. Modified with permission from Ref. [25]. Anterior to the left in all panels.

tinued to fascinate researchers ever since the morphogen concept was introduced. Improving methods of molecular biology and genetics, including fluorescently tagging proteins of interest to investigate their spatial distribution and even their dynamics *in vivo* has helped this endeavour substantially. This allowed for a continued intertwined theoretical and experimental analysis of gradient formation and interpretation. The fruit fly *Drosophila* has proven an invaluable model system to this end. The first discovered morphogen gradient, the Bicoid gradient, has been studied extensively both experimentally and theoretically [39, 94]. Note that Bicoid is a transcription factor [26, 97] rather than a signalling molecule. It can still act as a morphogen since the early fly embryo is a syncytium, where all nuclei share a common cytoplasm [35]. Thus, a concentration gradient

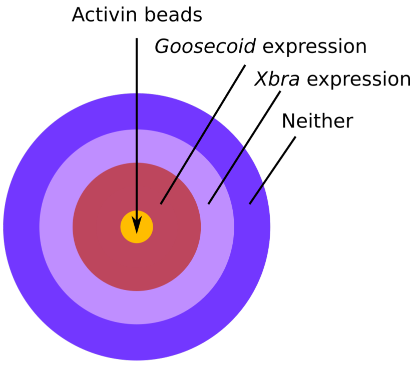

Figure 1.7.: **Experimental evidence for concentration-dependent gene expression.** Introducing an Activin source in form of beads into developing *Xenopus* embryos leads to expression of the *Goosecoid* gene in the vicinity of the beads at high Activin concentration and expression of the *Xbra* gene further away at lower Activin concretions. Neither gene is expressed far away from the beads. Based on [42], illustration inspired by [35].

in this common cytoplasm can regulate gene expression in a concentration and thus position-dependent way [26, 97]. Bicoid regulates the expression of gap genes [72, 26, 97, 22, 29, 41]. Their spatially distinct expression further patterns the AP axis in the developing fly embryo [72, 26, 97, 22, 29, 41]. Analysing the expression patterns of gap genes, the concept of positional information has been quantified [27]. Positional information provided by four gap genes is sufficient to specify the position of a cell along the anteroposterior axis with an error of approximately 1% [27]. Moreover, analysing the response of the gap gene *Hunchback* to Bicoid, the dilemma of the requirement for robustness as testified by the well-patterned organisms in nature and the stochasticity of gene expression underlying both the formation and readout of morphogen gradients has been addressed [103]. Furthermore, it has been debated whether the Bicoid protein gradient is indeed formed by diffusion or laid out by an mRNA gradient that is then translated [94]. It has also been suggested that the Bicoid gradient is read out before it has reached its steady state [13].

Another morphogen gradient that has been heavily studied in the fly embryo is the Dpp gradient (Fig. 1.8). It patterns the anteroposterior axis of the fly wing imaginal disk, the structure that will give rise to the wing in the adult fly [86, 10]. Dpp is produced locally in a stripe of cells at the boundary between the anterior and posterior compartments of the wing imaginal disk and spreads

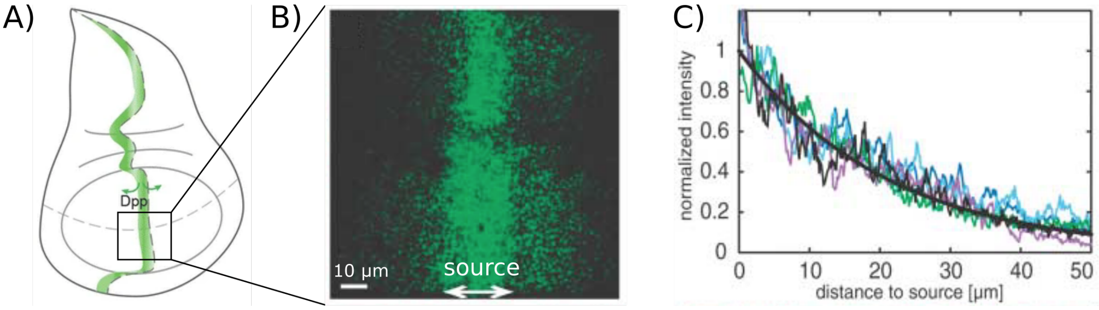

Figure 1.8.: **The Dpp gradient in the *Drosophila* wing imaginal disk. A** The fly wing imaginal disk. Anterior to the left, dorsal up. Dpp is expressed at the anterior-posterior compartment boundary (green stripe). Reproduced according to the Creative Commons CC BY licence (https://creativecommons.org/licenses/by/4.0/) from [10]. **B** Dpp-GFP (green) forms a concentration gradient around its (endogenous) source (double arrow). Modified with permission from Ref. [54]. **C)** Normalised average Dpp-GFP fluorescence intensity in the tissue outside of the source region of five wing disks. Black curve: exponential fit to black trace. Reproduced with permission from Ref. [54].

into the tissue. The formation of the gradient has been quantitatively explained by effective diffusion, with the diffusion constant, degradation rate and production rate measured by fluorescence recovery after photobleaching (FRAP) [54]. Endocytosis has been found to be essential for the formation of this gradient [54]. Therefore, transcytosis, that is molecule spreading through cells via repeated rounds of endocytosis and exocytosis, has been discussed as a mechanism of the spreading of signalling molecules in addition to their extracellular diffusion [17, 121, 2].

In the next section, we introduce the major signalling pathways patterning the body axes.

1.3. Body axes organisation by signalling gradients

Four major families of signalling molecules have been found to be implicated in organising differential gene expression and often act as morphogens, regulating gene expression in a concentration-dependent manner: The fibroblast growth factor (FGF) family, the Hedgehog family, the Wnt family and the TGF-β superfamily [35]. All of these signalling pathways consist of an extracellular signalling molecule that binds to a receptor on the cell membrane and subsequently elicits a signalling cascade inside the cell. Typically, the signalling molecules carry post-translational modifications, such as glycosylations and lipid modifications in order to be fully functional. These can be required both for correct secretion of the signalling molecule and for binding to the extracellular receptors [8, 35]. During development, these signalling pathways serve many purposes including patterning the body axes. Interestingly, which pathway is used to pattern which body axis is highly conserved throughout the animal kingdom. The anteroposterior axis is organised by canonical Wnt signalling (reviewed in [79]). The dorsoventral axis is organised by Bmp signalling (a branch of the TGF-β superfamily) (reviewed in [15]). For the ML axis, patterning strategies and mechanisms are more variant, but conservation of signalling pathways is still observed (e.g., Bmp, Slit) [62, 35].

Signalling gradients have also been found to be instrumental for tissue organisation during regeneration. In particular, the anteroposterior axis is also patterned by a Wnt signalling gradient during whole-body regeneration in hydra [46] as well as in planarians (Fig. 1.16 [44, 49, 77]). We will focus on the Wnt signalling pathway in this thesis and thus introduce both the pathway and its function in organising the main body axis in more detail in the following two sections.

1.3.1. The canonical Wnt signalling pathway

The signalling pathways, initiated upon binding of a Wnt ligand to a receptor on the cell membrane, are separated into the canonical, β-catenin-mediated Wnt signalling pathway and so called non-canonical, β-catenin-independent Wnt signalling pathways. The latter include the planar cell polarity pathway, and the Wnt/calcium pathway [35]. We will focus on the canonical Wnt signalling pathway (reviewed e.g. in [114, 36]) in this thesis because one of its many functions is to pattern the main (AP) body axis of planarians and other animals. We will refer to it as the Wnt signalling pathway for short and specify when discussing other forms of Wnt signalling.

The intracellular effector to canonical Wnt signalling (reviewed e.g. in [114] and [36]) is β-catenin. In many organisms, β-catenin has a dual role as co-transcription factor as well as in cell-cell contacts as an integral part of adherens junctions [3]. In this section, we focus on its role as co-transcription factor, regulated by Wnt signalling. In the absence of a Wnt signal, β-catenin is constantly produced and turned over by the cells (Fig. 1.9 left). β-catenin degradation is mediated by a so-called 'destruction complex', consisting of the scaffold proteins axin and APC, as well as the kinases CK1 and GSK3. The two kinases phosphorylate β-catenin in a sequential manner starting with CK1. These phosphorylations target β-catenin for ubiquitination by β-TrCP, leading to degradation by the proteasome. In the nucleus, Wnt-responsive elements (*Wre*s) on the DNA are bound by transcription factors of the Tcf/Lef1 family which in turn are bound by transcriptional repressors such as Groucho and transducin-like enhancer (TLE). Thus, the expression of Wnt-responsive genes is suppressed.

Wnt binds to a receptor complex on the cell membrane that consists of Frizzled and LRP5/6 (Fig. 1.9 right). This binding requires a lipid modification of the Wnt with a palmitic acid [36, 8]. Note that in most organisms, there are several different Wnt proteins and Fzd receptors and the respective specificity of binding is a subject of current investigation [36]. When Wnt is bound to the receptor complex, parts of the destruction complex also bind to the receptor complex via Dishevelled (Fig. 1.9 right). This leads to disruption of the degradation complex and thus accumulation of β-catenin in the cytoplasm [114]. Elevated levels of cytoplasmic β-catenin allow for β-catenin translocation to the nucleus. In the nucleus, β-catenin binds transcription factors of the Tcf/Lef1 family, replacing the transcriptional repressors. β-catenin thus acts as a transcriptional activator leading to the expression of Wnt signalling target genes [114, 36]. These expression changes can lead to cell fate specification and cell differentiation as well as to proliferation [114].

The level of Wnt signalling activity, often roughly proportional to nuclear β-catenin concentrations in the cell, are not only influenced by the amount of Wnt ligands in the extracellular environment. Wnt signalling is additionally fine-tuned extracellularly by both soluble and membrane-bound modulators (reviewed e.g. in [36, 61]). These include secreted inhibitors such as sFRPs (secreted frizzled related proteins), WIF1 (Wnt inhibitory factor), and Cerebus (Cer) that act by directly binding to Wnt proteins, blocking their ability to bind to receptors [36].

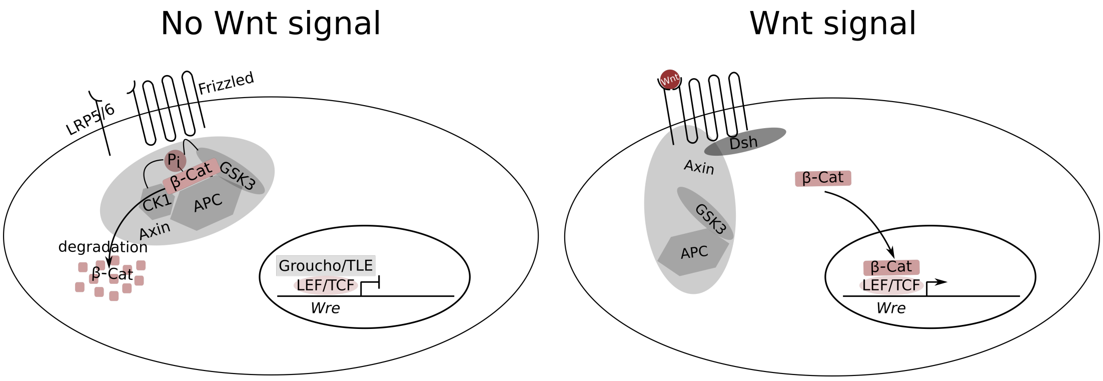

Figure 1.9.: **The canonical Wnt signalling pathway.** In the absence of a signal (left panel), β-catenin is bound by its destruction complex, marked for degradation and degraded by the proteasome. Wnt-responsive elements (*Wre*'s) on the DNA are bound by transcription factors of the Tcf/Lef1 family. These bind transcriptional repressors such as Groucho and transducin-like enhancer (TLE), repressing the expression of Wnt signalling target genes. In the presence of a Wnt signal (right panel), the degradation complex is bound to the receptor, freeing β-catenin to accumulate in the cell, to translocate to the nucleus. There, β-catenin replaces the transcriptional repressors and acts as a transcriptional activator. This leads to the expression of Wnt signalling target genes.

Moreover, Notum, Tiki1, and Tiki2 inactivate Wnt enzymatically, by cleaving of the palmitoyl group and the N-terminus of the Wnt protein, respectively [36]. The secreted Wnt signalling inhibitors Dkk (Dickkopf) and Sost bind to LRP5/6, preventing complex formation with Fzd and thus successful Wnt signalling [36]. Moreover, Wnt signalling is positively regulated by several R-spondin proteins. These secreted proteins indirectly foster a higher density of Fzd receptors on the cell membrane and thus make the cell more susceptible to Wnt signalling [36].

A common feature of signalling pathways, also found in Wnt signalling, is negative feedback. In particular, several Wnt signalling inhibitors, including *Dkk*, *sFRPs*, *Notum*, *Cer*, and *Sp5*, are direct targets of Wnt signalling [36]. Moreover, parts of the intracellular β-catenin-destruction machinery, such as *Axin2* are upregulated in response to Wnt signalling [36].

Wnt signalling is prevalent in many contexts including development, regeneration, ageing and cancer [114]. Moreover, it has important functions during tissue homeostasis, for instance in stem cell regulation [114]. In the next section, we discuss the role of Wnt signalling during embryonic development and regeneration.

1.3.2. Wnt signalling during embryonic development and regeneration

All bilaterians are faced with the challenge of patterning their main body axis during development. The vast majority of them employs Wnt signalling for this purpose [79]. Across all branches of bilaterians, the posterior end is characterised by high levels of Wnt signalling, that is, high levels of nuclear β-catenin, as well as by domains of *Wnt* gene expression [79]. In contrast, the anterior end is often characterised by the expression of Wnt inhibitors [79]. We will cite a few specific examples across the range of bilaterians here and refer to Ref. [79] for an extensive review of the subject. In early gastrulation stage of the mouse embryo, nuclear β-catenin protein as well as expression of *Wnt3* are found at the prospective primitive streak at the posterior end of the embryo, whereas the Wnt inhibitor *Dkk1* is expressed in the anterior visceral endoderm [79]. In the tailbud stage of zebrafish, *Wnt8* and *Wnt3a* are expressed posteriorly and the Wnt inhibitor *Sfrp3/frzb* is expressed anteriorly [79]. In adult planarians, *Wnt1, Wnt11-1, Wnt11-2, Wnt11-5* are expressed posteriorly [43], whereas the Wnt inhibitors *Sfrp-1* and *-2* [43], as well as *Notum* [80] are expressed anteriorly. In the larval stage of *C. elegans*, the *C. elegans* Wnt genes *Lin-44/Wnt, Egl-20/Wnt* and *Cwn-1/Wnt* are expressed posteriorly [79].

Wnt signalling organises the main body axis of animals beyond bilaterians: Cnidarians such as the fresh water polyp hydra and the sea anemone *Nematostella vectensis* are characterised by an oral-aboral axis that has been likened to the AP axis in bilaterians [79]. This axis is also characterised by high levels of nuclear β-catenin and expression of *Wnt* genes close to the oral pole and the expression of Wnt inhibitors such as *Dkk* aborally [79]. Even in poriferans there is evidence for polarised *Wnt* expression: The free swimming larvae of the demosponge *Amphimedon queenslandica* express *Wnt* at their pigmented pole pointing away from the direction of movement [79]. Thus, the role of Wnt signalling in patterning the main body axis during embryonic development is highly conserved across the animal kingdom.

The importance of Wnt signalling for patterning the main body axis is not restricted to embryonic development. It is also instrumental for AP axis pattering during regeneration [79]. As discussed above (Section 1.1), some animals are capable of varying degrees of regeneration. In zebrafish fin regeneration, Wnt signalling is the master regulator of all signalling pathways implicated in coordinating regeneration [35]. Hydra and some planarian species are capable of whole-body regeneration from tiny amputation fragments [35]. Both employ Wnt signalling to re-organise their main body axis after amputation [46, 44, 49, 77].

The widespread and profound patterning functions of Wnt, together with its spatially distinct pattern of action gave rise to the notion of Wnt acting as a morphogen. However, it has been heavily debated to what extent it can act as one. While it is certain that Wnt is able to influence cell fate decisions, it is unclear whether Wnt is a diffusible molecule. We summarise this controversy in the next section.

1.3.3. Wnt - a morphogen?

Several signalling molecules, including Wnt proteins [115], but also Hedgehog [82, 75], carry lipid modifications that are essential for their signalling function. Those lipid modifications render them hydrophobic. It is questionable whether hydrophobic molecules can spread via diffusion in an aqueous environment like the extracellular space [37, 73, 8]. Based on evidence in the imaginal fly wing disk, argosomes have been suggested to 'carry' Wnt through the extracellular space [37]. Initially described as membrane exovesicles [37], they were later found to be exogeneously derived lipoproteins [73]. Moreover, chaperones such as Swim (secreted Wnt-interacting molecule) associating with Wnt and shielding their lipid modification have been identified [36]. Additionally, Wnt proteins have been suggested to spread bound to sFRPs in *Xenopus* embryos, introducing a potential positively regulatory role for these secreted Wnt inhibitors [63].

Alternately, Wnt proteins have been shown to travel in actin-based filipodia, also called cytonemes [95]. In cytoneme-based transport, Wnt proteins are transported intracellularly to the tip of the membrane protrusion. The protrusion can extend across more than one cell diameter and contact neighbouring cells like an arm that reaches out. This way, the Wnt protein can be directly applied to the receiving cell at the cell-cell contact [95].

A piece of evidence questioning the necessity of Wnt diffusion stems from *Drosophila* development. Wingless, the main *Drosophila* Wnt protein, is able to exert its functions in the absence of diffusion: Alexandre *et al.* blocked wingless diffusion by genetically engineering it to be membrane-tethered. They observed an approximate 10 hour delay in the development of the flies and a 10-12% reduction of wing area in otherwise normally developing flies. Cells in close proximity to cells that express the membrane-tethered Wnt were found to express Wnt response genes. Hence, Wnt is able to signal to neighbouring cells when membrane-bound [4].

Evidence in favour of the idea of Wnt acting as a morphogen, has been provided in *C.elegans* [74]. A 200 µm long posterior to anterior Egl20/Wnt protein gradient has been observed *in vivo* [74]. It has been shown to be formed by free Wnt diffusion [74]. Free diffusion was shown by fast recovery after photo bleaching and a markedly reduced gradient range when tethering the Wnt to the membrane of the body wall musculature using a 'morphotrap': An anti-GFP nanobody that could bind the fluorescently tagged Wnt and was tethered to a transmembrane domain (of CD8a) which was fluorescently labelled intracellularly [74]. Physiological relevance of the resultant change in gradient shape was assayed by the migration of Q neurons. The morphotrapped Egl-20/Wnt phenocopies Wnt/Egl-20 loss of function mutants [74].

In light of this debate, it is interesting to investigate other potential means of morphogen spreading aside from diffusion. In this thesis, we present a cell-to-cell relay mechanism for signalling gradient formation. This relay is based on positive feedback that can lead to effective morphogen spreading even in the absence of diffusion. The model that we introduce in this thesis is inspired by observations of positive feedback in Wnt signalling in planarians [98]. In the next section, we introduce planarian flatworms.

1.4. Planarian flatworms - Masters of regeneration

1.4.1. An introduction to planarians

Planarians are free-living flatworms. Various planarian species can be found in fresh water, marine and terrestrial habitats. They are bilaterians, more specifically protostomes. They belong to the superphylum Lophotrochozoa, and within that to the phylum of Platyhelminthes, forming the clade Tricladida [50]. Arguably, their most fascinating feature is their amazing regeneration capability. It varies between different species, ranging all the way from robust whole-body regeneration to hardly any regenerative capacities in some marine species [106]. Many species reproduce sexually, like other organisms do, other species comprise sexual and asexual strains [106]. Asexual strains often reproduce by fissioning. That is, the animals rip off the posterior part of their body. Subsequently, both pieces regenerate into a complete animal. They thus critically depend on their regenerative capacity in order to reproduce [106].

The model presented in this thesis is inspired by observations in the planarian model species *Schmidtea mediterranea*. These fresh water planarians show very robust whole-body regeneration, regenerating from arbitrary amputation fragments [50, 106, 84]. That is, a worm cut into small pieces will regenerate an entire organism from each of the pieces. The wound is closed by muscle contraction and new tissue starts to form as early as one day post amputation with the whole worm being regenerated within two weeks (Fig. 1.10 A, [84, 50]). Planarian body size varies between 0.5 and 20 mm in length depending on their feeding status (Fig. 1.10 B, [102]). In particular, the worms grow when fed and shrink when starved [102].

The complex anatomy of planarians (Fig. 1.11) includes a set of photoreceptors that looks like eyes clearly distinguishing their wider head end from the pointier tail end. They glide across surfaces using the cilia on their ventral side [96], and feed using a muscular tube, the pharynx (see number 4 in Fig. 1.11), that they can extrude through a ventral mouth opening from the middle of their body [50]. For a large part, their inside consists of gut, forming one major branch anterior to the pharynx and two major branches around the pharynx extending

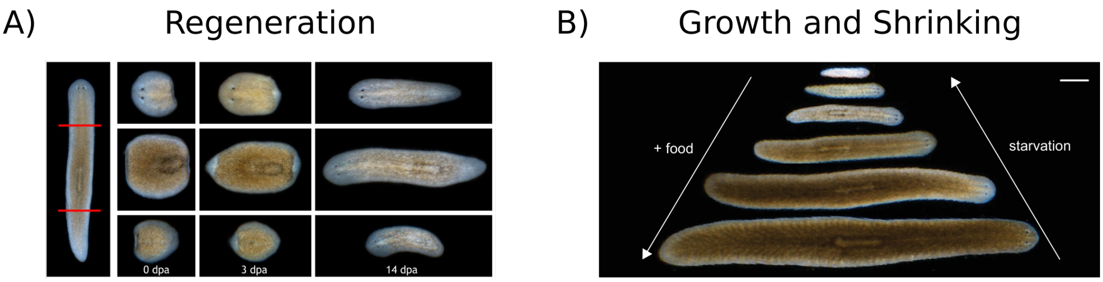

Figure 1.10.: **Regeneration and dynamic growth of the flatworm *Schmidtea mediterranea.*** **A** The flatworm fully regenerates within two weeks when cut as indicated by the red lines in the left panel. The regeneration time course of the head piece (top) trunk piece (middle) and tail piece (bottom) is shown, dpa: days post amputation. Reproduced with permission from Ref. [50]. **B)** Flatworms dynamically grow and shrink depending on the quantity of food available. Scale bar: 1 mm. Reproduced with permission from Ref. [102].

posteriorly. A complex gut network extends from these major branches (see number 2 in Fig. 1.11). The pharynx (see number 4 in Fig. 1.11) connects the gut to the outside and is used both for the uptake of food and the excretion of faeces. It can be retracted into the body. A network of protonephridia performs excretory functions similar to our kidneys (see number 3 in Fig. 1.11, [101]). Their central nervous system consists of a brain (cephalic ganglia) in the head region and two ventral nerve cords ranging from the ganglia to the posterior ends (see number 1 in Fig. 1.11, [1]). The two ventral nerve cords are bridged by transverse axons that form a peripheral nerve net [1]. The internal organs are embedded in loosely packed mesenchyme consisting of mesenchymal cells. This is where the proliferative planarian cells, the neoblasts, reside (see number 5 in Fig. 1.11, [50]). This cell population contains pluripotent stem cells [108]. They are small, round cells characterised by a large nucleus and a small amount of cytoplasm [6]. There are different classes of neoblasts including pluripotent cNeoblasts (clonogenic neoblasts, [108]) and multipotent stem cells that give rise to multiple lineages [105, 28, 67, 81, 120]. All of this is surrounded by a shell-like body wall musculature, comprised of four layers of muscle fibres: From inside to outside a layer of longitudinal fibres, a layer of diagonal fibres, a thin layer of longitudinal fibres and an outer layer of circular fibres (see number 6 in Fig. 1.11, [20]). On top of the body wall musculature, there is the basement membrane and an epidermal cell layer, which is covered by a thick layer of mucus.

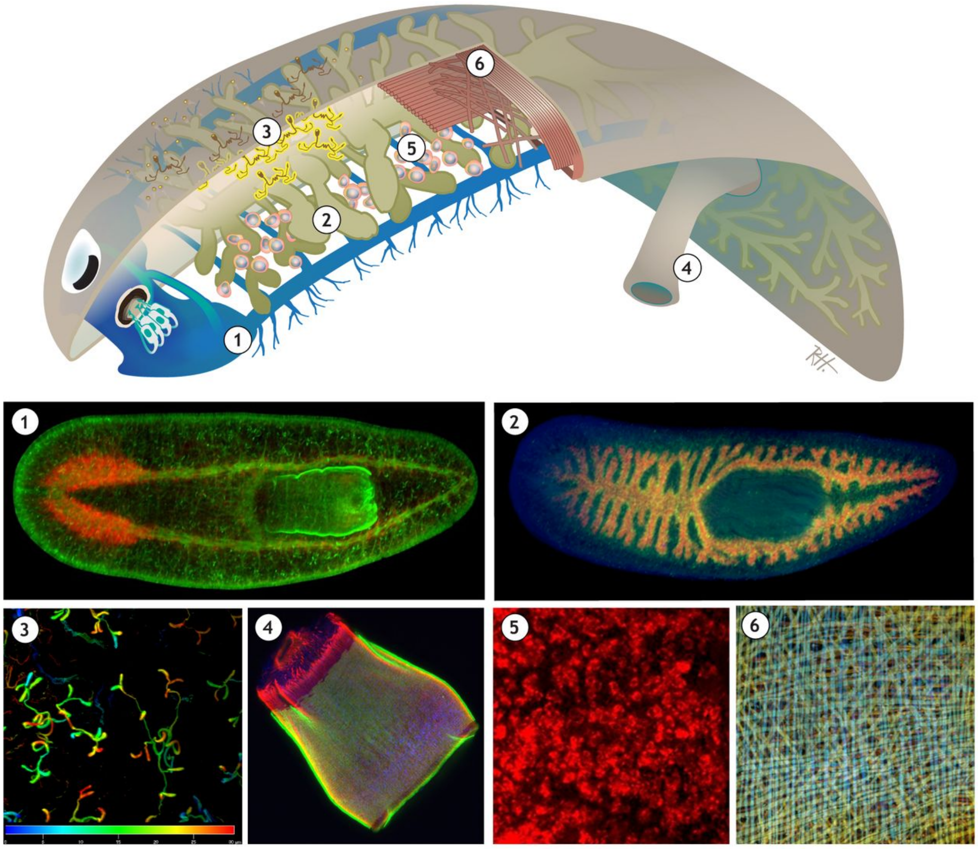

Figure 1.11.: **Planarian anatomy.** Overview (top) and microscopy (bottom) images of the main organ systems. 1) Central nervous system: two cephalic ganglia (red, *PC2 in situ* hybridisation and two ventral nerve cords (green, α-tubulin immunostaining, also labels pharynx). 2) Gut: branched network consisting of three major branches - one anterior to the pharynx and two around the pharynx (residing in the part that appears blue in the middle) in the posterior half of the worm (red, *PorcupineA in situ* hybridisation; green, *Sufu in situ* hybridisation; blue, nuclear counterstaining with DAPI). 3) Protonephridia: excretory functions similar to out kidneys. Depth-coded confocal microscopy maximum projection (acetylated-tubulin immunostaining). 4) Pharynx: muscular tube for feeding and excretion (red, phalloidin staining of muscle actin; green, acetylated-tubulin immunostaining of cilia; blue- nuclear counter staining). 5) Neoblasts: diverse population of proliferating cells, containing pluripotent stem cells (red, confocal microscopy maximum projection of *Piwi-1 in situ* hybridisation in tail area). 6) Body wall musculature: longitudinal, diagonal and circular fibres (depth-coded confocal maximum projection of 6G10 immunostaining). Reproduced with permission from Ref. [50].

The worms constantly turn over all of these complex tissues, replacing old and dying cells with new cells derived from neoblasts. Fascinating experiments showed that a single neoblast is enough to repopulate a lethally irradiated worm that would otherwise die due to a lack of neoblasts replenishing dying cells [108]. This confirms both that cell turnover is necessary to keep planarians alive and that there is a subpopulation of neoblasts, the cNeoblasts, that is pluripotent and thus capable of repopulating the entire worm (Fig. 1.12, [108]). The neoblasts also enable tissue replacement during regeneration from arbitrary amputation fragments [84]. The newly-formed cells have to differentiate into the cell type appropriate for their position in the body. The constant turn-over of cells (Fig. 1.12) along with the ability to dynamically change body size in response to the amount of food available (Fig. 1.10), and the extensive regenerative capacity of the worms (Fig. 1.10) require for patterning systems to be in place in the adult organism.

Taken together, flatworms set three major challenges to their patterning systems (Fig. 1.13): The patterning systems have to operate at adult length scales of up to 2 cm. They have to be able to dynamically scale 40-fold over 1.5 orders of magnitude with changes in body size. They have to be able to re-form in case of amputation to organise the regeneration of tissue. Thus, the patterning mechanisms have to be long-ranged, scalable and self-organised.

In the next section, we introduce the pattering systems of the worm with a special focus on the role of Wnt signalling in organising the main body axis.

1.4.2. The patterning system of planarians

In light of the extensive regenerative and scaling capabilities of flatworms, a lot of work has been dedicated to deciphering their patterning mechanisms. Well-conserved signalling pathways have been found to organise their body axes: As in other organisms [79], their anteroposterior axis is organised by Wnt signalling [44, 49, 77, 100, 99, 98]. Again, as observed in other organisms [15], their dorsoventral axis is organised by Bmp signalling [85, 66, 65, 33]. The mediolateral axis of the worms is organised by *Wnt5* and *Slit1* [19, 43].

Graft experiments between irradiated and non-irradiated worms have shown that the patterning information resides in differentiated, non-neoblast cells [89,

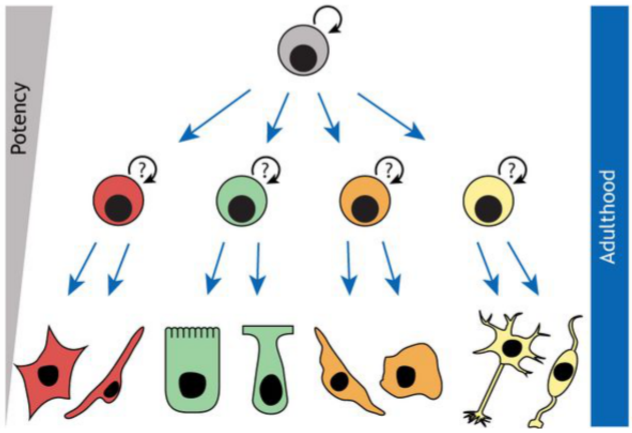

Figure 1.12.: **Cell renewal in planarians.** The population of neoblasts consists of pluripotent cNeoblasts (top) and several subpopulations of lineage-committed progenitors (middle) that can together give rise to all the cell types (bottom) in planarians throughout their lives. Reproduced with permission from Ref. [50].

52, 116]. Subsequently, the body wall musculature has been identified as the physical location of this coordinate system, where many of the genes important for patterning the worm are expressed [116, 90, 60]. Thus, the body wall musculature is thought to set up a coordinate system instructing the differentiation of stem cells in a position-dependent manner [116]. As discussed above, the body wall musculature comes in layers: two longitudinal ones, a circular one and a diagonal one (see number 6 in Fig. 1.11, [20, 60]). Interestingly, some genes involved in patterning the DV axis, such as *Admp*, or in patterning the ML axis, such as *Slit*, have been found to mainly be expressed in the longitudinal muscle fibres [60]. On the other hand, some genes involved in patterning the AP axis, such as *Wnt11-1* have been found to mainly be expressed in circular muscle fibres [60]. Thus, the patterning genes seem to mainly be expressed in the muscle fibres that run orthogonally to the axis to be patterned. Individual muscle fibres are 5-10 µm wide and 150-200 µm long [6]. With these expression patterns, there are therefore many fibres 'stacked' along the axis to be patterned, potentially allowing for a more fine-grained concentration profile of patterning gene expression along the respective axes. In the next section, we focus on patterning along the main body axis.

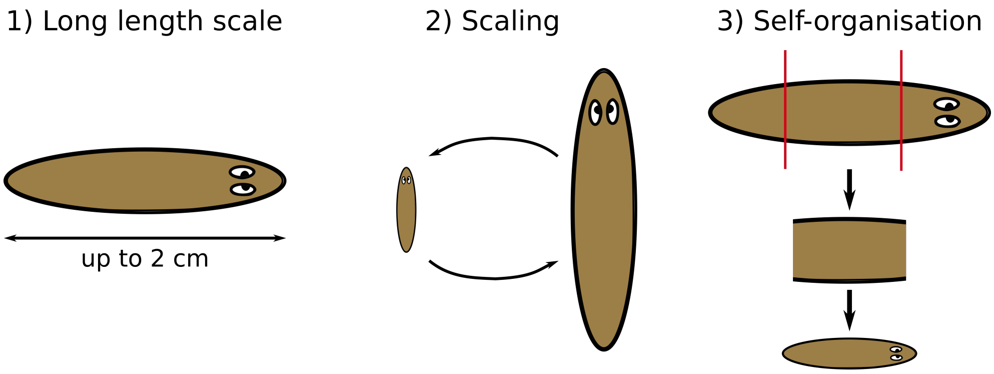

Figure 1.13.: **Patterning challenges posed by planarians.** 1) The patterning system has to work on a long length scale of up to 2 cm. 2) The patterning system has to scale with reversible changes in body size arising dynamically in response to the amount of food available. 3) The patterning system has to be self-organised in order to reform after amputation to organise the regenerating tissue.

1.4.3. Wnt signalling along the main body axis of planarians

Before describing the pivotal importance of Wnt signalling for correct AP patterning in flatworms, it is important to stress a few particularities of Wnt signalling in the worms that facilitate the interpretation of the results: In planarians, the two functions of β-catenin are divided between two different isoforms of the protein: β-catenin-1 is a co-transcription factor binding Lef1/Tcf1 transcription factors and thus the effector of Wnt signalling [21]. β-catenin-2 is a part of adherens junctions, where it interacts with α-catenin and E-cadherin [21]. We will focus on β-catenin-1 in this work and refer to it as β-catenin from here on. The Wnt signalling inhibitors Cer, and Dkk [44], as well as the Wnt signalling activator R-spondin are not present in planarians. With this in mind, we discuss the spectacular patterning phenotypes induced by disturbed Wnt signalling in both intact and regenerating planarians.

Wnt signalling during homeostasis

Consistent with the expression patterns of Wnt signalling components across the animal kingdom, the posterior end of the worm is characterised by the expression of Wnt genes, whereas the anterior end of the worm is characterised by the expression of Wnt inhibitors [79]. In particular, *Wnt1* is expressed in a stripe

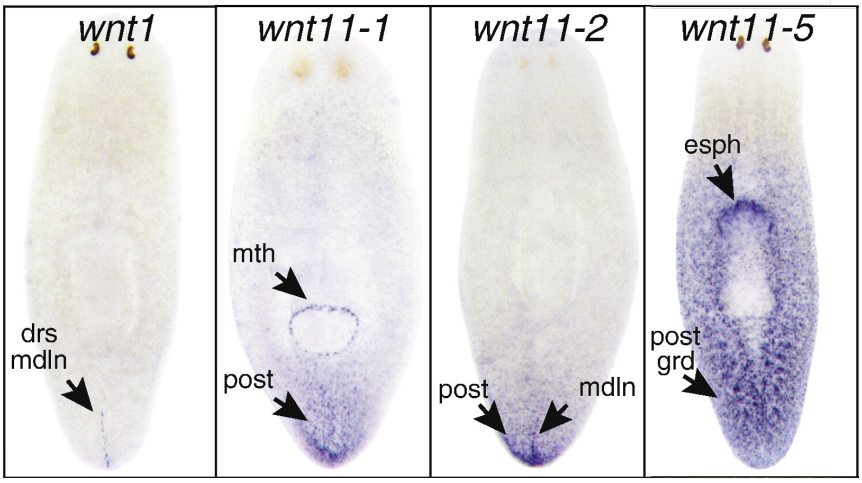

Figure 1.14.: ***Wnt* expression in planarians.** *In situ* hybridisation of indicated *Wnt* mRNAs. From left to right: *Wnt1* is expressed in the pole cells, a row of around 10 cells along the posterior dorsal midline (drs mdln). *Wnt11-1* is expressed in a posterior gradient (post) and around the mouth (mth). *Wnt11-2* is expressed in a posterior gradient (post) and along the posterior midline (mdln). *Wnt11-5* is expressed in a long posterior-to-anterior gradient (post grd) and at the esophagus (esph). Modified with permission from Ref. [43].

of around 10 cells, called pole cells, along the posterior dorsal midline ([78, 43], Fig. 1.14, left panel). Moreover, several *Wnt* genes show tail-to-head graded expression gradients ([77, 43, 87, 98, 100], Fig. 1.14). At the very anterior tip of the animal, a small population of cells expresses the Wnt inhibitor *Notum* [80]. Moreover, some Wnt inhibitors such as *Sfrps* (secreted frizzled-related proteins) show head-to-tail graded expression patterns [77, 43]. The pole cells at the tip of the tail and the head have been strongly implicated in head and tail fate specification, respectively and are thought to initiate the graded expression patterns of patterning genes observed in the head and in the tail [50].

A gradient of Wnt signalling along the AP axis of flatworms has been shown in the form of a β-catenin protein gradient [99, 98]. β-catenin concentrations decrease from the tail tip to the middle of the animal [99, 98]. In quantitative western blot analysis in *Schmidtea mediterranea*, a plateau in β-catenin levels is seen in most of the anterior half of the animal with another dip at the head (Fig. 1.15 left, [98]). Immunostaining in *Schmidtea polychroa* on the other hand revealed an increase in β-catenin concentration in the head region [99]. In this thesis, we focus on the decreasing part of the gradient spanning the posterior half of the animal, observed in both species [98, 99].

The observed β-catenin protein gradient is attributed to Wnt signalling, as *β-catenin* mRNA levels are constant along the body axis [44, 98] and knock down of *Wnt1, Wnt 11-1, Wnt 11-2, Wnt11-4, Wnt11-5* by RNAi[3] reduces the measured β-catenin gradient. Moreover, knock down of a part of the β-catenin degradation complex, *APC*(RNAi), leads to high levels of β-catenin throughout the worm, i.e. to a high but flat 'gradient'. Thus, low levels of Wnt signalling lead to low levels of β-catenin protein, whereas high levels of Wnt signalling lead to high levels of β-catenin protein, see Fig. 1.15.

The gradient of β-catenin protein has a patterning function, as changes in the global Wnt signalling level firstly change the phenotype of the intact worm (Fig. 1.15), and secondly the AP expression pattern of many genes [98].

Phenotypically, worms with ubiquitously high Wnt signalling levels (*Apc*(RNAi)) turn into a disorganised structure, expressing tail markers such as *Wnt11-5* and *Fzd4-1* in an unspecific manner across the body (Fig. 1.15 upper right panel, [98]). Worms with ubiquitously low Wnt signalling levels (*β-catenin* (RNAi)), on the other hand, form organised headlets all around their body margin, as demonstrated by the expression of head markers such as *Sfrp-1* (Fig. 1.15, lower right panel, [98]). Thus, high levels of Wnt signalling specify tail fate whereas low levels of Wnt signalling specify head fate.

---

[3] RNAi (RNA interference) is the natural response of cells to double-stranded RNA, leading to the degradation of mRNA with the same sequence [91], implicated in the defence against viruses, but also in regulating gene expression post-transcriptionally [3]. This response is used experimentally to degrade mRNA of a specified sequence, referred to as 'knock down' [76]: Introducing a double-stranded RNA of a specific sequence into the organism leads to targeted degradation of mRNA with the same sequence via RNAi [76].

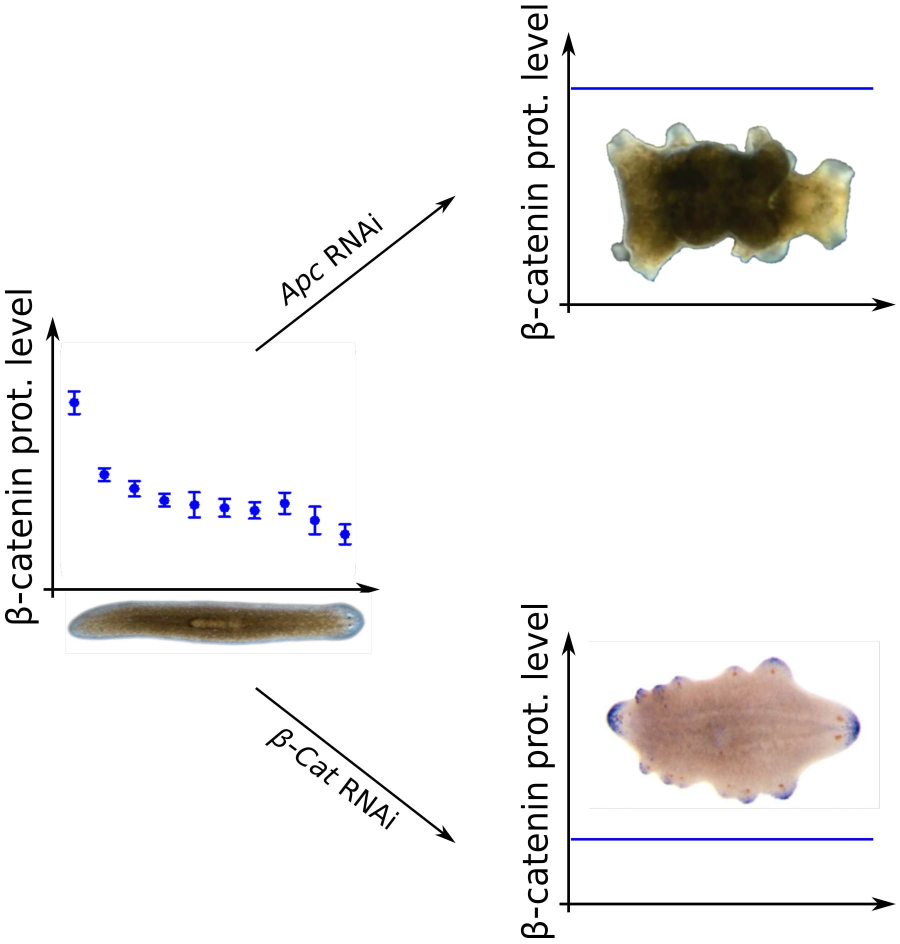

Figure 1.15.: **Wnt signalling in planarians during homeostasis.** A β-catenin protein gradient is present in the posterior half of intact animals (left panel, β-catenin protein gradient modified with permission from [98], obtained by quantitative western blotting from serial sections along the AP axis, dots: mean of ≥ 3 technical replicates, error bars: SEM, see [98] for details). Uniformly high β-catenin levels as generated by *Apc* transforms the whole worm to posterior identity (upper right panel). Uniformly low β-catenin levels as generated by *β-catenin* (RNAi) lead to the formation of small headlets all around the animal (marked by *in situ* hybridisation for *Sfrp-1*, lower right panel). Phenotype images reproduced with permission from Ref. [50].

Many genes are expressed in a manner correlated or anti-correlated with the β-catenin protein profile. Importantly, they change their expression patterns in an (anti-)correlated way when the β-catenin protein profile is changed by ubiquitously changing β-catenin levels (decrease: *β-catenin*(RNAi), increase: *Apc*(RNAi)) [98, 87, 55]. The expression of many genes encoding elements of the Wnt signalling pathway changes in a way that is highly correlated with changes in β-catenin levels [98, 87, 55]. Like in other organisms [36], this includes the negative regulators *Axin2* and *Sp5*. However, there are also several components of the Wnt pathway positively affecting signalling that change their expression in a manner highly correlated with the levels of β-catenin. These include the 'tail Wnts', *Wnt11-1, -2, -5*, as well as the Frizzled receptor *Fzd4-1* [98]. Furthermore, the expression of these and other Wnt signalling components is down-regulated when *Wnt1*, *Wnt11-1*, and *Wnt11-5* expression is knocked down by RNAi [98].

The expression of components of the Wnt-signalling pathway, in particular of the 'tail-Wnts', is largely restricted to irradiation-insensitive cells in planarians [98], consistent with the muscle-coordinate-system idea. The β-catenin protein is present in both neoblasts and differentiated cells [98, 99]. Immunostaining suggests its presence in the nuclei of the body wall musculature [99] consistent with the idea of this tissue expressing patterning genes [116, 90, 60]. However, the β-catenin gradient is sensitive to irradiation, suggesting that neoblasts account for a non-negligible portion of the measured β-catenin gradient [98]. This can be interpreted as the neoblasts reading out the Wnt signalling gradient established in the body wall musculature. Postulating that the signalling gradient has a patterning function makes it indispensable that it be interpreted by cells that are in the process of differentiation. The neoblast population in the worm consists of stem cells of varying degrees of cell-fate specification [108, 105, 28, 67, 81, 120] and is thus the population that needs to read out the patterning signals in the worm. Accordingly, we interpret the irradiation-sensitivity of the gradient [98] as the gradient being read out by the neoblasts leading to increased intracellular β-catenin levels in the neoblasts.

The anterior half of the worm has been suggested to be organised by an additional patterning system, the molecular specifics of which are not clear yet [98, 99, 50]. Importantly, the β-catenin protein gradient depends on neither the anterior pole nor the anterior pattering system to form [98]. This is shown by an unchanged β-catenin gradient shape in both *Notum*(RNAi) and *Sfrp*(RNAi) conditions [98]. Moreover, regenerated trunk pieces from *Ptc*(RNAi) animals form two tails and the β-catenin gradient forms from both ends [98].

Wnt signalling is not only important in specifying head vs. tail cell fates in the intact animal but also instrumental in patterning the worm during regeneration as we will discuss in the next section.

Wnt signalling during regeneration

Low Wnt signalling, induced by *β-catenin*(RNAi), leads to worms regenerating two heads upon amputation of head and tail (Fig. 1.16 middle column, [44, 77, 49]). The precise manifestation of the *β-catenin*(RNAi) phenotypes depends on the RNAi-dose and ranges from 'tailless' to 'radial-like hypercephalized' with no posterior identity [49]. In contrast, high Wnt signalling levels induced by *Apc*(RNAi) lead to the formation of two tails in the equivalent amputation experiment (Fig. 1.16 right column, [44]). Thus, also during regeneration, low levels of Wnt signalling lead to head formation, whereas high levels of Wnt signalling lead to tail-formation.

In *D. lacteum*, tail pieces cannot regenerate a head whereas head pieces are perfectly able to regenerate a tail [59]. The fact that head regeneration in tail pieces can be rescued by *β-catenin*(RNAi) [59], is in line with low levels of Wnt signalling corresponding to head-formation whereas high levels of Wnt signalling correspond to tail formation.

One *Wnt* gene, *Wnt1*, has been found to be part of the initial wound response [78, 43]. In this capacity, it is expressed at any wound, ranging from small wounds as induced for instance by needle poking to large wounds and tissue removal e.g. after amputation [78, 43]. In case of amputation, it is expressed along the entire wound - irrespective of the position of the wound along the body axis and of whether the wound is facing anteriorly or posteriorly (Fig. 1.16 second row, [78, 43]). This is interesting, because as discussed above, high Wnt signalling levels are associated with tail-formation. *Wnt1* expression as a generic wound response is detected between 6 and 24 hours after the amputation occurs [78].

Afterwards, its expression becomes restricted to the future posterior end, where it becomes restricted to the newly forming pole cells [78]. This is in line with high levels of Wnt signalling corresponding to posterior cell fate. Exclusively at anterior-facing wounds, *Wnt1* is counteracted by expression of the Wnt inhibitor *Notum* that starts 6 hours post amputation [80]. Thus, after an initial phase of *Wnt1* expression at all wounds [78], the new anterior and posterior poles are formed by localised expression of *Notum* [80] and *Wnt1* [78] at the anterior and posterior end, respectively. As discussed above, these are thought to initiate the head and tail specific gene-expression gradients pattering the head and the tail of the animal [50].

In contrast to the early phase of *Wnt1* expression at all wounds, the posterior-specific, later phase of *Wnt1* expression is β-catenin-dependent and irradiation-sensitive [78]. Moreover, re-establishment of the *Wnt11-5* expression pattern after amputation is β-catenin-dependent [78]. In particular, the *Wnt11-5* expression pattern is re-established from scratch. That is, in posterior-facing wounds of anterior tissue regions that do not express *Wnt11-5* at the time of amputation, it starts forming 24 hours after amputation [78]. In anterior-facing wounds of posterior tissue that express a lot of *Wnt11-5* at the time of amputation, the expression is first down-regulated and the pattern reforms starting 4 days post amputation [78]. Thus, the tail-specific expression patterns in the posterior half of the animal are re-established from the posterior pole in a β-catenin-dependent manner [78].

These observations suggest that the initial *Wnt1* expression at all wounds [78] is permissive for the initiation of a Wnt signalling gradient. This potential is then taken away from anterior-facing wounds by the anterior-specific expression of *Notum* [80]. Subsequently, the signalling gradient reforms from the posterior pole in a β-catenin–dependent manner [78, 98].

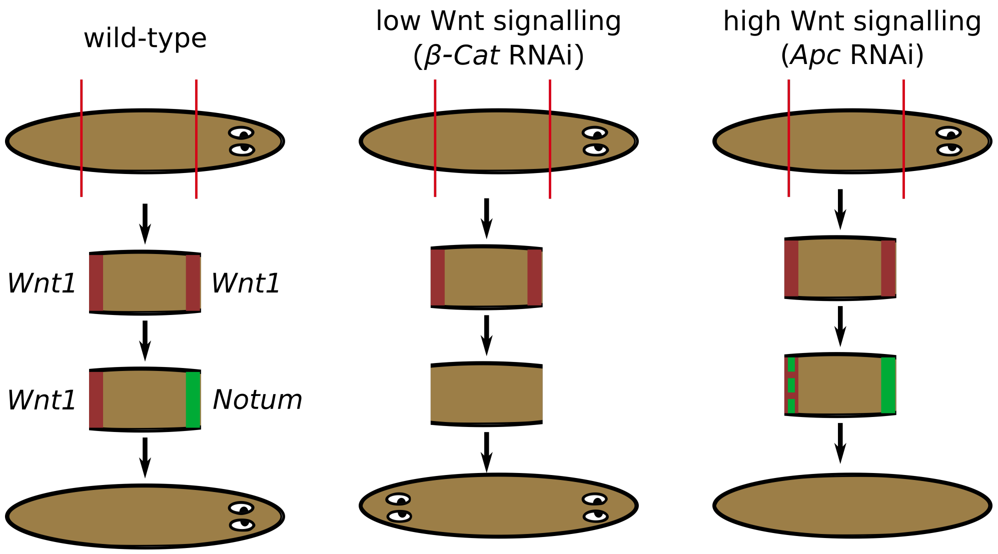

Figure 1.16.: **Wnt signalling during planarian regeneration.** Regenerative outcome of fragments cut from the central region of the animal as indicated by the red lines in different Wnt signalling backgrounds as indicated above the columns. In all cases, *Wnt1* (dark red) is expressed as a generic wound response between 6 and 24 hours after amputation. In wild-type worms (left), it is counteracted by *Notum* expression (green) at anterior-facing wounds starting 6 hours post amputation. 48 hours post amputation *Wnt1* is no longer expressed at anterior-facing wounds. Resulting high Wnt signalling at the tail end and low Wnt signalling at the head end leads to tail and head regeneration, respectively (bottom left). Both posterior-specific *Wnt1* expression and anterior-specific *Notum* expression are β-catenin-dependent and thus not observed in *β-catenin*(RNAi) animals (middle column). Two heads are regenerated in the low Wnt signalling environment generated by *β-catenin*(RNAi) (bottom middle). *APC*(RNAi) leads to increased β-catenin levels and thus *Notum* expression also at posterior-facing wounds (right column). Nevertheless, two tails are regenerated in this high Wnt-signalling environment (bottom right). Illustrations based on findings presented in [43, 78, 80].

A biological model of the Wnt signalling gradient

As discussed above, in the intact worm, the expression of several of the 'tail Wnts', goes down in response to knock down of several *Wnt* genes and up in response to *Apc*(RNAi). Moreover, several components of the Wnt pathway change their expression in a manner correlated with changes in the β-catenin protein gradient. This suggests a positive feedback via Wnt-dependent Wnt expression: Elevated Wnt signalling levels lead to elevated intracellular β-catenin levels (Fig. 1.9), while elevated β-catenin concentrations lead to the production of more Wnt signalling molecules [98].

In light of this idea, the tail-to-head graded expression of several *Wnt* genes, in particular *Wnt11-1, -2, and -5* (Fig. 1.14, [77, 43, 100, 98]) can be interpreted as a readout of the positive feedback loop: *Wnt* genes are being expressed in the presence of high β-catenin levels, i.e. their expression decreases away from the tail tip as the β-catenin levels decrease.

Interestingly, the expression of *Wnt1* is not always correlated with the levels of Wnt signalling in the intact worm, as certified by its up-regulation in response to both *Wnt 11-1*(RNAi) and *11-5*(RNAi), as well as in response to *Apc*(RNAi) [98]. Moreover, *Wnt1* is expressed at the tail tip [78] and thus at the high point of the β-catenin gradient [98, 99]. This suggests that *Wnt1* expression is independent of the other signalling pathway components and thus able to initiate the pattern, in line with the idea of the pole cells initiating pattern formation [50].

The fact that after amputation the poles reform first and posterior-specific expression patterns subsequently re-form in a β-catenin-dependent manner [78] can then be interpreted as the gradient re-forming after amputation by first establishing the symmetry-breaking input from the pole and then re-forming by the positive feedback between β-catenin and Wnt.

Motivated by these observations, we will investigate the effect that positive feedback can have on the formation of signalling gradients in this thesis. In the next section, we discuss physical models for gradient formation based on diffusion and degradation to which we will contrast the model presented in this thesis.

1.5. Physical models of morphogen gradient formation

A morphogen gradient is a concentration profile of a morphogen in space. Typically, we think of decreasing concentration profiles where the signalling molecule is produced in a local source and its concentration decays away from its origin of production. Since morphogens have been shown to spread via diffusion *in vivo* [42, 74] and to form an exponentially decaying profile [25], the local source/diffusion/degradation model has gained particular attention in explaining morphogen gradient formation. It has been used successfully to quantitatively explain the formation of the Dpp gradient in the developing fly wing imaginal disk [54].

The tissues in which morphogen gradients are observed consist of individual cells. However, in physical models of gradient formation, tissue is often coarse-grained and represented as a continuous structure in space. This representation allows using continuous models to analyse the process. If the morphogen gradient is formed along one spatial dimension, and the dimensions perpendicular to it do not contribute to the formation of the profile, that is if there are no spatial gradients along these perpendicular directions, a model with only one spatial dimension can be used to analyse it [23].

In the diffusion/degradation model, the morphogen is produced in a spatially-confined source region with rate s, spreads via diffusion with the diffusion constant D, and is degraded with rate k:

$$\partial_t C = D\,\partial_x^2 C - k\,C + s\,\theta(S - x) \tag{1.1}$$

where θ denotes the Heavyside function, i.e. $\theta(x) = 0$ for $x < 0$ and $\theta(x) = 1$ for $x \geq 0$, with S the width of the source region. The steady-state solution to this model is given by C^* (Fig. 1.17):

$$C^* = \begin{cases} C_1^{\mathrm{in}}\, e^{x/\lambda} + C_2^{\mathrm{in}}\, e^{-x/\lambda} & 0 \leq x \leq S \\ C_1^{\mathrm{out}}\, e^{x/\lambda} + C_2^{\mathrm{out}}\, e^{-x/\lambda} & S < x \leq L\ , \end{cases} \tag{1.2}$$

where the length scale λ is defined by the bulk of the system and the amplitudes

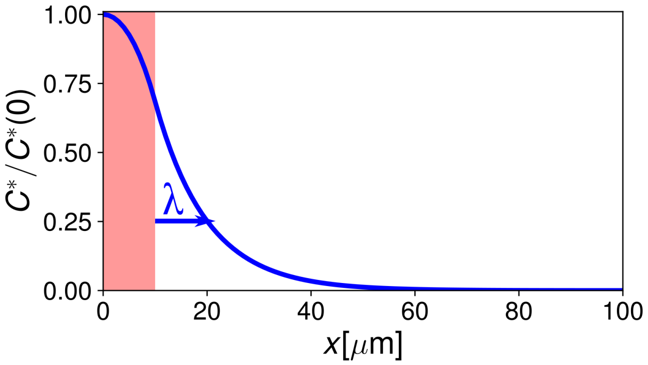

Figure 1.17.: **A steady-state concentration profile generated by diffusion and degradation.** The steady-state concentration C^* decreases in space away from the local source (shaded in red). The profile is normalised to its concentration at $x = 0$. The length scale λ is indicated by the blue arrow. The parameters are of the order of magnitude observed in the fly wing disk [54]: $D = 0.1$ µm^2/s, $k = 10^{-3}$/s, $s = 0.1$ nM/s, leading to a length scale of 10 µm.

C_1^{in}, C_2^{in}, C_1^{out}, and C_2^{out} are defined by the boundary conditions as well as the stitching conditions between the source and the non-source region. For no-flux boundary conditions, i.e. nothing leaving or entering the system at the boundaries at $x = 0$ and $x = L$:

$$\partial_x C(0) = \partial_x C(L) = 0 \ , \tag{1.3}$$

and differentiability, i.e. matching value and flux at point S, where the source and the non-source regions meet:

$$\lim_{x \nearrow S} C(x) = \lim_{x \searrow S} C(x) \ , \tag{1.4}$$

$$\lim_{x \nearrow S} \partial_x C(x) = \lim_{x \searrow S} \partial_x C(x) \ , \tag{1.5}$$

the concentration profile outside of the source region is dominated by the decreasing exponential. That is, C_1^{out} is very small and goes to zero as the system size L increases. Thus, outside of the source region the shape of the profile is governed by the decaying exponential.

The length scale of the steady-state profile, λ, is set by the diffusive properties of the morphogen and its longevity according to:

$$\lambda = \sqrt{\frac{D}{k}} . \tag{1.6}$$

We see that more diffusive and/or more long-lived molecules give rise to steady-state profiles with a longer length scale. Thus, in order to generate long-ranged gradients using a diffusion/degradation mechanism, either the diffusion constant has to be very large or the degradation rate very small. The diffusion constant is a property of the molecule and dependent on the environment in which it is diffusing. It can therefore not be arbitrarily increased by the cells. If the molecule carries post-translational modifications hampering diffusion, these can be cleaved off, increasing the diffusion constant. However, this should be thought of as a 'release of a brake' that had been put on the diffusion constant rather than an actual 'acceleration'. That is, the diffusion constant can be modulated, but not increased beyond the one given by the properties of the signalling molecule and its environment in the absence of any diffusion-hampering modifications. Therefore, the main way to change gradient length scale in a diffusion/degradation mechanism is via changing the degradation rate. Thus, in a diffusion/degradation mechanism, only long-lived molecules can give rise to long-ranged steady-state profiles.

Increasing the length scale by decreasing the degradation rate, however, comes at the price of making the dynamics of the system slower. For a linear system like this one, the slowest relaxation time, τ_{max}, is a good measure of how long it takes to relax to steady state. For the diffusion/degradation system, it is given by the inverse of the degradation rate k:

$$\tau_{\mathrm{max}} = \frac{1}{k} \tag{1.7}$$

(see Appendix A for details). Thus, increasing the length scale of the steady-state profile by decreasing the degradation rate also makes the process of pattern formation much slower. The morphogen concentration profiles that have been suggested to arise by an effective diffusion/degradation mechanism are typically of the order of tens to a few hundreds of micrometers [24, 54, 74]. Nevertheless, it has been debated whether or not a diffusion/degradation mechanism is fast enough to explain the signalling gradients across cell fields of a few hundreds of microns [23, 42, 34, 48].

The length scale of the steady-state profile can be modulated by directed transport. This introduces advective spreading of the molecules in addition to the diffusive spreading discussed above. Such directed transport can be achieved intracellularly by transport via directed molecular motors along spatially-aligned cytoskeletal filaments, or by cytoplasmic streaming, generated by motor proteins at the cell periphery [48]. On a tissue scale, it can be generated by bulk movement of extracellular fluid, for instance due to muscle contraction or ciliated cells [48]. Moreover, directed transcytosis, i.e. repeated cycles of endocytosis and exocytosis implicated in the spreading of certain morphogens [54], can lead to effective drift [17]. All of the described active, directed processes lead to drift with speed ν:

$$\partial_t C = D\,\partial_x^2 C - \nu\,\partial_x C - k\,C + s\,\theta(S - x) \ , \tag{1.8}$$

where positive values of ν indicate a transport of molecules down the concentration gradient. The steady-state solution to this equation is given by:

$$C^* = \begin{cases} C_1^{\text{in}}\,e^{x/\lambda_1} + C_2^{\text{in}}\,e^{-x/\lambda_2} & 0 \le x \le S \\ C_1^{\text{out}}\,e^{x/\lambda_1} + C_2^{\text{out}}\,e^{-x/\lambda_2} & S < x \le L \ , \end{cases} \tag{1.9}$$

where λ_1 and λ_2 are defined by the bulk and the amplitudes C_1^{in}, C_2^{in}, C_1^{out}, and C_2^{out} are defined by the boundary conditions and the stitching conditions. Equivalently to what we discussed for the diffusion/degradation mechanism above, for boundary conditions given by Eq. 1.3 and differentiability at S (Eqs. 1.4, 1.5), the profile shape outside of the source region is governed by the decreasing exponential. This is due to the fact that C_1^{out} is very small and approaches zero with increasing system size. The length scale of the steady-state profile is not only set by the diffusion constant D and the degradation rate k, but also influenced by the speed and direction of the drift ν:

$$\lambda_1 = \frac{2\,D}{\nu + \sqrt{\nu^2 + 4\,D\,k}} \ , \tag{1.10}$$

$$\lambda_2 = -\frac{2\,D}{\nu - \sqrt{\nu^2 + 4\,D\,k}} \ . \tag{1.11}$$

Since the shape of the steady-state profile is dominated by the decreasing expo-

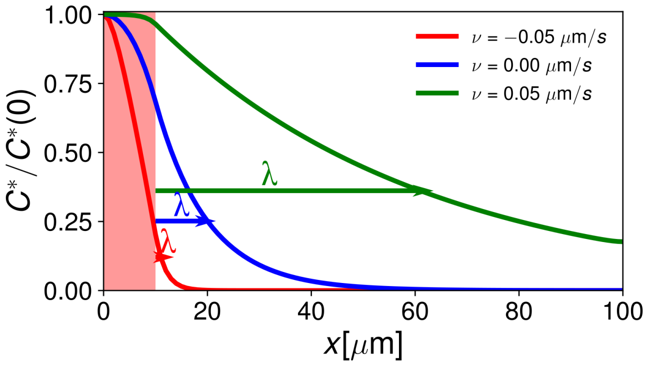

Figure 1.18.: **A steady-state concentration profile generated by diffusion, degradation and drift.** The steady-state concentration C^* decreases in space away from the local source (shaded in red). The profiles are normalised to their concentration at $x = 0$. The length scale λ is indicated by the arrow of the matching color. Note that drift down the gradient ($\nu > 0$, green line) strongly increases the length scale of the steady-state profile compared to the profile without drift ($\nu = 0$, blue line), while drift up the gradient ($\nu < 0$, red line) reduces the length scale of the steady-state concentration profile. The parameters are of the orders of magnitude observed in the fly wing disk [54]: $D = 0.1\ \mu\mathrm{m}^2/\mathrm{s}$, $k = 10^{-3}/\mathrm{s}$, $s = 0.1\ \mathrm{nM/s}$.

nential, we refer to λ_2 as the length scale of the mechanism. For transport down the gradient, i.e. $\nu > 0$, λ_2 increases with increasing drift speed ν, in particular, as $\nu^2 \gg D\,k$. This way, drift can increase the length scale of the steady-state profile beyond the length scale of the diffusion/degradation system. Figure 1.18 shows steady-state profiles for this mechanism with a positive and a negative drift. For zero drift, the system simplifies to the diffusion/degradation system discussed above. Note that drift in the direction of the concentration gradient, i.e. $\nu > 0$, markedly increases the length scale compared to a diffusion/degradation mechanism (Fig. 1.18). However, realising this kind of drift phenomenon on a tissue scale in a biological context requires inducing bulk extracellular fluid movement or transcytosis in the right direction, i.e. down the concentration gradient.

Morphogen gradients have been observed to adapt their length scale to the size of the tissue to be patterned, that changes due to growth[4] [111, 110]. When this adaptation of length scale is such that the shape of the profile remains constant relative to tissue size, the profile scales [111, 110, 112]. In this case, a profile shape $\mathcal{Z}(x/L)$ can be defined that is shared between profiles $C^*(x;L)$ in tissues of different sizes L. This constant shape is revealed as a collapse to a master curve when plotting relative concentrations C^*/C_0^* with respect to the relative spatial coordinate x/L:

---

[4] Note that strictly speaking, tissue growth also has to be accounted for in the dynamics of the morphogen concentration in form of advection and dilution. In this thesis, we assume a separation of time scales, such that the dynamics of tissue growth are much slower than

$$C^*(x;L) = C_0(L) \cdot \mathcal{Z}(x/L) \ , \tag{1.12}$$

where $C_0(L)$ denotes a - potentially size-dependent - amplitude (Fig. 1.19, [111, 110, 112]). In other words, the same relative concentration is reached at the same relative position in the system. For the diffusion/degradation mechanism, scaling is given when

$$\lambda \propto L \tag{1.13}$$

[111, 110, 112]. To see this, consider an exponentially decaying profile $C^* = C_0\ e^{-x/\lambda}$. The relative profile C^*/C_0 collapses to a size-independent master curve $e^{-(x/L)/(\lambda/L)}$ if λ/L is constant and thus $\lambda \propto L$. In the example in Fig. 1.19, scaling of the length scale is achieved by varying the degradation rate with system size. Such adjustment of degradation rate has been observed to account for scaling of the Dpp concentration profile in the developing fly wing imaginal disk [111].

In order to explain steady-state gradient scaling with system size, an expander mechanism has been suggested [7, 11, 12, 111]. The idea is that an additional molecule species, the expander, that is different from the morphogen, and homogeneously distributed in space, encodes the size of the system. It then changes the properties of the morphogen in such a way that the length scale of the steady-state profile of the morphogen scales with system size. We briefly introduce two realisations of such an expander mechanism: the expander-dilution mechanism [111] and the expansion/repression mechanism [7, 11, 12], see Fig. 1.20.

In the expander-dilution model, the system comprises a fixed amount of an expander molecule, that is very long-lived [111]. If the system grows or shrinks,

---

those of the morphogen concentration profile. In this case, the dynamics of tissue growth can be neglected for the dynamics of the morphogen concentration.

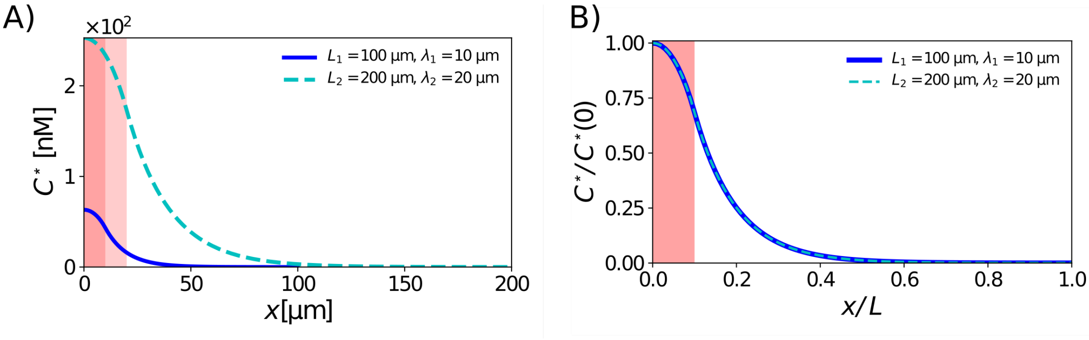

Figure 1.19.: **Scaling of morphogen gradients.** Two steady-state profiles scaling with tissue size. **A)** Concentration profiles of two differently-sized systems (L_1, L_2). **B)** Profile scaling can be appreciated as collapse to a master curve when profiles are normalised to $C^*(0)$ and plotted in relative spatial coordinates x/L. The parameters are of the order of magnitudes observed in the fly wing disk [54]: $D = 0.1$ µm^2/s, $k_1 = 10^{-3}$/s, $k_2 = 2.5 \times 10^{-4}$/s, $s = 0.1$ nM/s. Source region shaded in red.

this dilutes or concentrates the expander (Fig. 1.20, upper panel, [111]). Thus, the size of the system is encoded by the concentration of the expander. In particular, large systems have lower expander concentrations than small systems. Thus, if the length scale of the steady-state profile of the morphogen is negatively regulated by the expander concentration, the morphogen concentration profile can scale with system size. In a diffusion/degradation-based mechanism for morphogen gradient formation, such expander-based scaling can be achieved if the degradation rate of the morphogen is positively regulated by the expander concentration [111, 112] or if the diffusion constant of the morphogen is negatively regulated by the expander concentration [112]. This simple realisation of the expander mechanism is highly sensitive to loss of expander molecules [112].

Alternatively, morphogen gradient scaling can be achieved by the expansion/repression mechanism ([7, 11, 12], Fig. 1.20, lower panel). In this mechanism, the expander is not present in a fixed amount. In contrast, its production is regulated by the morphogen. In particular, expander production is negatively regulated by the morphogen such that its production is limited to regions of low morphogen concentration [7]. Thus, expander molecules are produced far away from the source region of the morphogen and the domain of expander production shrinks as the length scale of the morphogen concentration profile increases. The length scale of the steady-state morphogen concentration profile is *positively* regulated by the expander concentration in this mechanism, such that high expander concentrations expand the morphogen gradient [7]. Again, the expander has to be widely diffusible and stable, leading to spatially homogeneous steady-state concentration profiles for the expander [7, 11]. Using this feedback loop between the quickly diffusing expander and the morphogen, self-organised gradient scaling is achieved [7, 11]. Specifically, this leads to a steady-state morphogen concentration profile in which the morphogen concentration is just above the threshold concentration for expander production at the boundary at $x = L$, opposite the morphogen source region. In a diffusion/degradation mechanism for signalling gradient formation, the expander can regulate the length scale of the morphogen gradient by either negatively regulating the degradation rate or by positively regulating the diffusion constant of the signalling molecule, leading to an expansion of morphogen gradient length scale with increasing expander levels that encode increasing system size [11]. This model has successfully been used to explain self-organised scaling of the Bmp gradient organising the dorsoventral axis during *Xenopus* development [11], and the Dpp gradient organising the anteroposterior axis of the wing imaginal disk during *Drosophila* development [12].

Both the expander-dilution as well as the expansion/repression mechanism rely on a very quickly diffusing expander. Specifically, they require the length scale of the expander steady-state profile to be much larger than system size, leading to a spatially homogeneous expander concentration profile at steady state. This requirement becomes increasingly difficult to meet for increasing system size for the same reasons discussed above for the diffusion/degradation mechanism. Essentially, it requires a very quickly diffusing and/or very long-lived molecule as an expander.

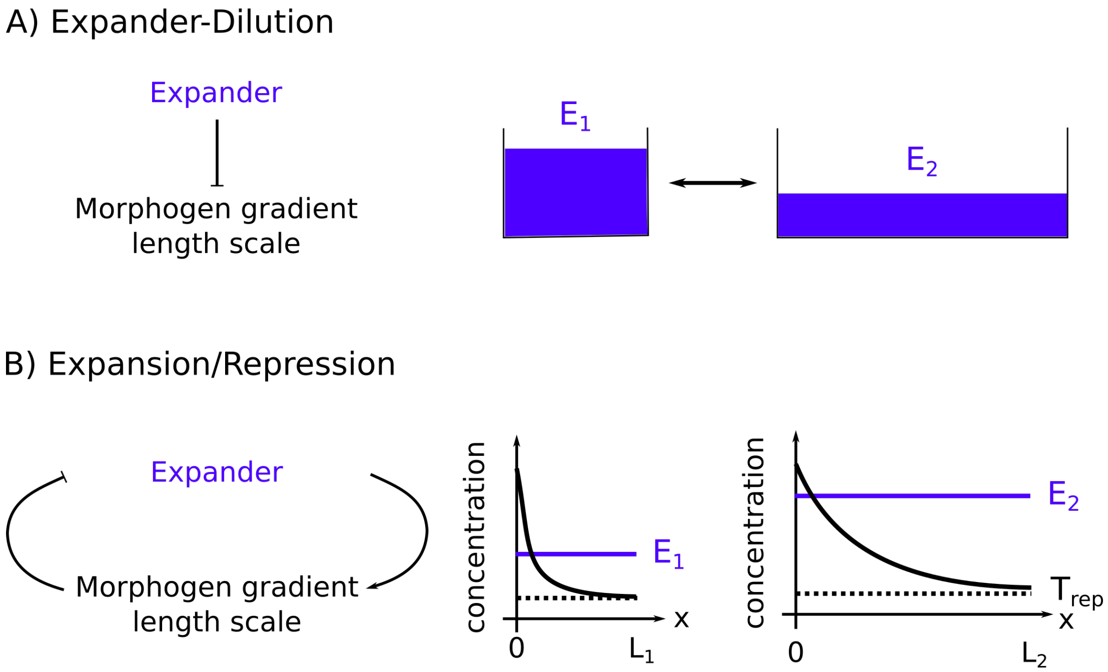
A) Expander-Dilution
Expander
Morphogen gradient length scale
E_1
E_2
B) Expansion/Repression
Expander
Morphogen gradient length scale
concentration
E_1
x
0
L_1
concentration
E_2
T_{rep}
x
0
L_2

Figure 1.20.: **An expander mechanism for gradient scaling. A)** In the expander-dilution mechanism, a constant amount of a very long-lived expander molecule (depicted in blue) encodes system size: Since the absolute amount of the expander molecule is fixed, its concentration changes as the volume of the system changes. The morphogen is regulated by the expander such that the steady-state profile length scale increases with system size, i.e. with *decreasing* expander concentrations. Illustration inspired by [112]. **B)** In the expansion/repression mechanism, the amount of expander molecule is *not* fixed. In contrast, expander production is regulated by the morphogen. In particular, only cells experiencing low morphogen concentrations below $\mathrm{T}_{\mathrm{rep}}$ produce the quickly diffusing enhancer. The morphogen is regulated by the expander to increase the length scale of the steady-state profile with increasing system size, i.e. with *increasing* expander concentration. This leads to self-organised pattern scaling with system size L, as the steady-state morphogen concentration is fixed to a value just above $\mathrm{T}_{\mathrm{rep}}$ at $x = L$. The expander concentration profile is spatially homogeneous at steady state and increases with system size. Illustration based on [11] and [110].

1.6. Aim of this thesis

Embryonic development, regeneration, and tissue renewal pose enormous patterning challenges. The required patterning information can be provided by morphogen gradients, concentration profiles of signalling molecules in space. The formation of these profiles has been extensively studied in the context of embryonic development, both experimentally and theoretically ([38, 42, 32, 24, 25, 23, 54, 39], see Sections 1.2, 1.5). In particular, a diffusion/degradation based mechanism has been used successfully to quantitatively explain the formation of the Dpp morphogen gradient in the *Drosophila* wing imaginal disk ([54], see Fig. 1.8). However, patterning is not restricted to the embryonic context. It is also required during regeneration and tissue turnover in the adult organism. Able to regenerate from tiny amputation fragments and constantly turning over all of their tissue, planarians are a great model for patterning at adult length scales. They have been found to also employ signalling gradients for tissue organisation. In particular, they rely on a Wnt signalling gradient to organise their main body axis ([99, 98], see Section 1.4.3). While signalling gradients in the developmental context are characterised by short length scales, 20 μm in case of the Dpp gradient in the fly wing disk [54], the Wnt signalling gradient in the worm shows a much longer length scale in the mm range. Thus, the first major patterning challenge the worms pose is patterning at long length scales (Fig. 1.13). The second major patterning challenge posed by the worms is their dynamic adjustment of body size in response to the quantity of food available (Fig. 1.13). Being able to dynamically adjust pattern length scale to a changing system size is also required during regeneration: Small pieces regenerate to small worms (that later on grow) and large pieces regenerate to large worms. Thus, the pattering system has to adapt to the size of the amputation fragment to correctly pattern the regenerating worm. It is thus the first pre-requisite to meet the third patterning challenge posed by the worms: self-organisation of the pattern (Fig. 1.13).

A diffusion/degradation based mechanism for gradient formation requires very long-lived molecules to form a signalling gradient on such large length scales, making the gradient formation process slow (see Section 1.5). Based on observations of positive feedback in Wnt signalling in planarians ([98], see Section 1.4.3), we propose a cell-to-cell relay mechanism for long-ranged gradient formation in this thesis. In order to conceptualise this idea, we introduce a discrete model, account-ing for an extracellular signalling molecule (Wnt) and an intracellular effector (β-catenin) that engage in a positive feedback loop, introduced in Chapter 2. We analyse the effect of this relay on steady-state gradient length scale in Chapter 3, investigating if the relay can increase the length scale of the steady-state gradient compared to a diffusion/degradation mechanism. In Chapter 4 we analyse if the length scale of the steady-state gradient can be adjusted to system size, i.e. body length, by changing the feedback strength appropriately. We analyse the dynamics and time scales of the relay mechanism in Chapter 5. In particular, we aim to understand the trade-off between achieving a long length scale and fast dynamics of gradient formation. Finally, we note that polarised secretion in response to the positive feedback can give rise to an effective drift of signalling molecule concentration through the tissue. In Chapter 6, we analyse how this influences the length scale of the steady-state gradient as well as the dynamics of gradient formation.

2. Signalling gradient formation using a cell-to-cell relay

2.1. The challenge: Generating large-scale patterns

Signalling gradients play an important role in pattern formation during embryonic development, regeneration, and tissue renewal [25, 46, 54, 98, 99]. The main body axis of planarians is patterned by a Wnt signalling gradient over the entire course of their lives ([98, 99], see Section 1.4.3). This shifts the patterning challenge to large length scales of the order of millimetres as opposed to the micrometer length scales [24, 54, 74] described in the context of embryonic patterning. As discussed in the Introduction, a diffusion/degradation-based mechanism would require extraordinarily long-lived molecules to obtain such large length scales (Section 1.5). In this thesis, we introduce a relay mechanism for the formation of long-ranged signalling gradients. This mechanism is inspired by the observation of positive feedback in the Wnt signalling gradient that patterns the main body axis of planarians [44, 49, 77, 87, 100, 99, 98]. As discussed in Section 1.4.3, Wnt ligands have been shown to be expressed in a Wnt-signalling-dependent manner in planarians [98]. Together with the changes in the β-catenin protein gradient in response to changes in Wnt expression, this suggests a positive feedback loop in which high levels of Wnt signalling lead to high intracellular levels of β-catenin protein, that in turn leads to the production of more Wnt-ligands [98]. In particular, intracellular β-catenin-degradation is decreased by a Wnt-ligand binding to a cell (Fig. 1.9). Accumulating levels of β-catenin inside the cell mediate the transcriptional response to the Wnt signal (Fig. 1.9). This can include the production of more Wnt-ligands in response to the signal. Based on this idea, we introduce a positive feedback loop that effectively leads to production of more signalling molecules in response to receiving a signal.

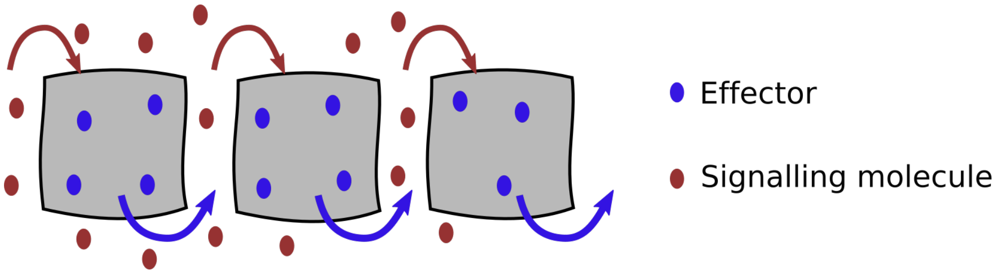

Figure 2.1.: **A cell-to-cell relay for signal propagation.** If the concentrations of signalling molecules are high enough in the extracellular space, the cell receives a signal (red arrows). As a result, the intracellular effector concentrations rise, eventually leading to secretion of signalling molecules (blue arrows). Based on this positive feedback, the signal can be propagated by a cell-to-cell relay. Cells are depicted as grey rectangles.

The signalling properties of the signalling molecule forming a gradient are commonly discussed in the context of gradient *interpretation* [25, 42, 118]. In this thesis, we include the signalling properties of the signalling molecule in the mechanism of gradient *formation*: The cellular response to receiving a signal gives rise to the positive feedback that we discuss. Abstracting from the complex specifics of Wnt signalling gradient formation in planarians, we introduce a discrete model comprising an extracellular signalling molecule (corresponding to the different Wnt-ligands impacted in AP patterning in the worms), and an intracellular effector (corresponding to β-catenin). This way, we can explicitly account for the positive feedback at the cellular level. In particular, sufficiently high concentrations of signalling molecules in the extracellular space lead to increased intracellular effector levels. Those in turn lead to production and secretion of more signalling molecules, thus closing the positive feedback loop. This way, the signal can be propagated by a cell-to-cell relay (Fig. 2.1).

In order to investigate the effect such positive feedback can have on the formation of signalling gradients, we developed a physical model that we introduce in this chapter. Additionally, we comment on our choice of boundary conditions as well as model parameters and finally introduce a numerical solution to our model.

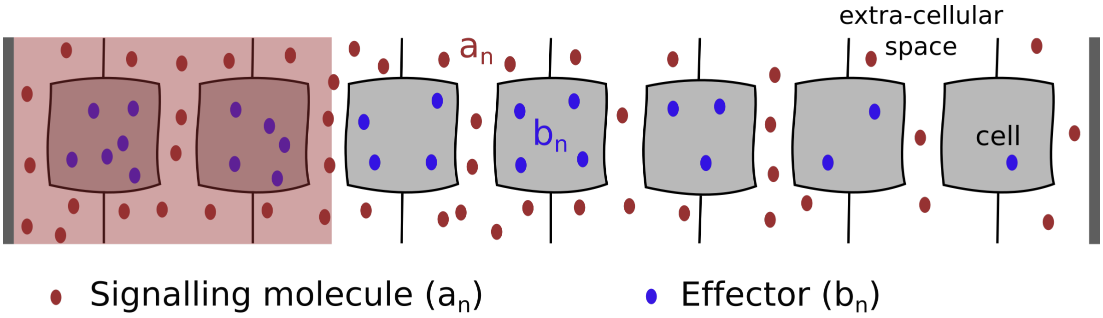

Figure 2.2.: **A discrete model of signalling gradient formation.** The model accounts for extracellular signalling molecules (red) and intracellular effectors (blue). Cells are depicted as grey rectangles. We choose to discretise the extracellular space as indicated by the thin black lines. Source region shaded in red.

2.2. A discrete cell-to-cell relay model for signalling gradient formation

In order to account for the individual cells receiving and propagating the signal, we build a discrete model, consisting of individual cells in the extracellular space. In actual tissue, the extracellular space is continuous. For ease of description, we choose to discretise it as indicated by the black lines in Fig. 2.2. We assign a single concentration of signalling molecule to each extracellular space and a single concentration of effector to each cell.

In this discrete set-up, we introduce a positive feedback to the diffusion/degradation model described in the introduction (Eq. 1.1). In contrast to the model discussed in the introduction, the model presented here is discrete in order to account for the signal relay between individual cells. The dynamics of the signalling molecule concentration in the extracellular space are given by extracellular diffusion with diffusion coefficient D (Fig. 2.3), extracellular degradation with rate k_A, constant production in a local source with rate s_A and a positive feedback dependent on the level of effector in the cells to the left and to the right of the extracellular space, denoted as $f(b_{n-1}, b_n)$ and depicted in Fig. 2.3:

$$\partial_t a_n = D\,\frac{(a_{n-1} - 2\,a_n + a_{n+1})}{\delta^2} - k_\mathrm{A} a_n + s_\mathrm{A}\,\theta(w - n) + f(b_{n-1}, b_n), \qquad (2.1)$$

where $\theta(n)$ denotes the Heaviside function, specifically, $\theta(n) = 0$ for $n < 0$,

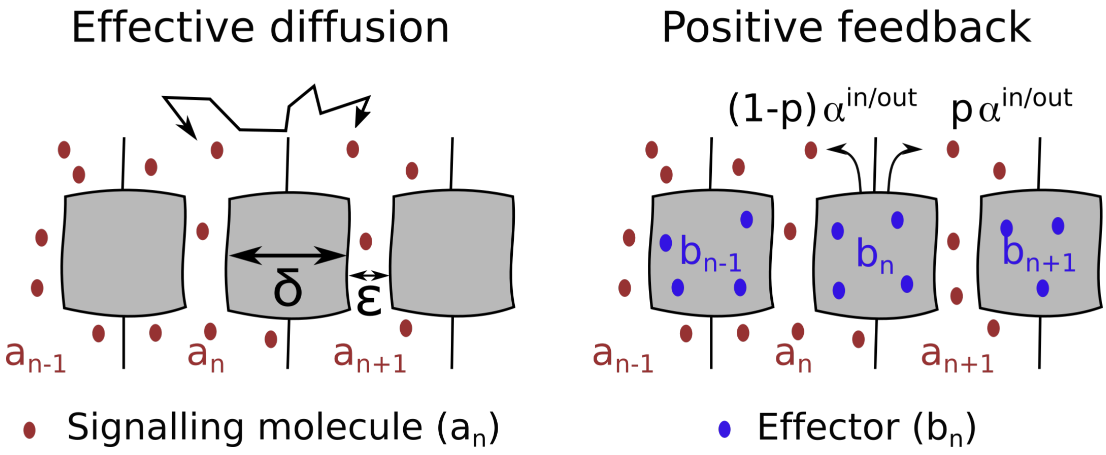

Figure 2.3.: **Model dynamics.** Left panel: Wiggly line represent effective extracellular diffusion of signalling molecules (red), i.e. exchange of signalling molecules between adjacent extracellular spaces. Cell width δ, extracellular space width ϵ. Right panel: arrows represent secretion of signalling molecules due to positive feedback with feedback strength $\alpha^{\text{in/out}}$ and polarity p.

$\theta(n) = p$ (defined below) for $n = 0$, $\theta(n) = 1$ for $n > 0$. The number of source cells is denoted by w.

The positive feedback is due to the cells secreting signalling molecules in an effector-level-dependent manner. In particular, the cells produce signalling molecules with a feedback strength α and secrete them to the extracellular spaces to their left and right with a secretion polarity p, where $p = 1/2$ corresponds to symmetric secretion and $p > 1/2$ to preferred secretion to the right, i.e. away from the local source (Fig. 2.3). The production strength is positively regulated by the effector levels in the respective cells according to $g(b_n)$:

$$f(b_{n-1}, b_n) = p\ \alpha\ g(b_{n-1}) + (1-p)\ \alpha\ g(b_n). \tag{2.2}$$

We choose a Hill activator function (Fig. 2.4 A) to capture the positive feedback from the effector levels on signalling molecule production:

$$g(b_n) = \frac{(b_n)^h}{(c_\mathrm{B})^h + (b_n)^h}, \tag{2.3}$$

where c_B is the activation threshold of the Hill function, defined as the concentration of effector b_n for which half-maximal signalling molecule production is

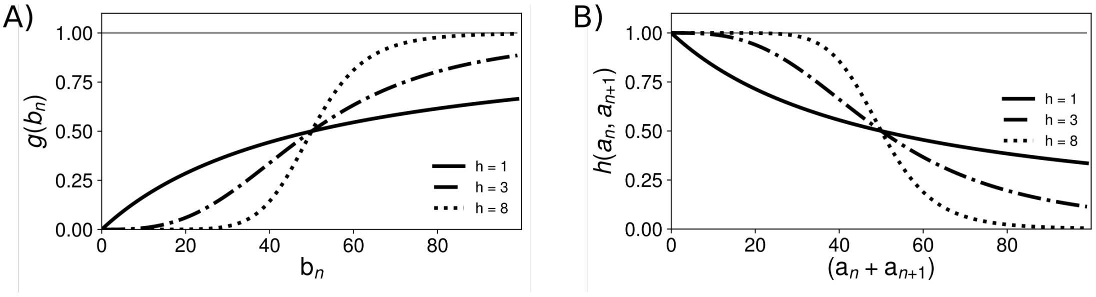

Figure 2.4.: **Hill functions. A)** Hill activator function, $g(b_n)$ (Eq. 2.3, shown for different Hill exponents h (h = 3, 5, 8, see inset). The functions saturate at 1 (horizontal grey line). For $h = 1$, the function increases and saturates. For $h > 1$, the functions become sigmoidal. For $h \to \infty$, the Hill function becomes a step function. At $b_n = c_{\mathrm{B}}$, half-maximal activation is reached. $c_{\mathrm{B}} = 50$ nM in this example. **B)** Hill inhibitor function, $h(a_n, a_{n+1})$ (Eq. 2.5), shown for different Hill exponents h (h = 3, 5, 8, see inset). The function starts at 1 (gray line) and decays to 0. For $h = 1$, the functions decreases, for $h > 1$, the functions becomes sigmoidal. For $h \to \infty$, the Hill function becomes a step function. At $(a_n + a_{n+1}) = c_{\mathrm{A}}$, half-maximal suppression is reached. $c_{\mathrm{A}} = 50$ nM in this example.

achieved. The Hill exponent h governs the shape of the response (see Fig. 2.4 A). Choosing a Hill function ensures a saturation of the response at high effector levels.

As a result of the positive feedback $f(b_{n-1}, b_n)$, every cell in the system produces signalling molecules. This is qualitatively different from diffusion/degradation models (Eq. 1.1, [54]) in which signalling molecules are exclusively produced in a spatially confined local source. We nevertheless employ the term 'source region', to refer to the region in which the signalling molecule is constantly produced with rate s_{A} (containing the cells $n \in [0, ..., (w-1)]$, shaded in red in Fig. 2.3) in addition to the production due to the positive feedback. This local, effector-level-independent source breaks the symmetry in our system. It is inspired by the Wnt signalling-independent expression of *Wnt1* at the posterior pole of the worms ([78, 98], see Section 1.4.3).

The feedback strength α can be different inside and outside of the source region. In particular, the feedback strength inside the source region is given by α^{in} and the feedback strength outside of the source region is given by α^{out}. Note that in the absence of positive feedback, i.e. $f(b_{n-1}, b_n) = 0$, the dynamics of the signalling molecule concentration simplify to a diffusion/degradation system. This occurs if the feedback strength α is zero inside and outside of the source region, i.e. $\alpha^{\text{in}} = \alpha^{\text{out}} = 0$.

The dynamics of the intracellular effector are positively regulated by the concentration of signalling molecule in the extracellular spaces to its left and to its right. In particular, the dynamics of the effector are given by a constant intracellular production with rate s_{B} and an intracellular degradation with rate k_{B}, that is modulated by the signalling molecule concentrations in the extracellular spaces adjacent to the cell according to $h(a_n, a_{n+1})$:

$$\partial_t b_n = s_{\text{B}} - k_{\text{B}}\, h(a_n, a_{n+1})\, b_n. \tag{2.4}$$

Thus, the positive feedback is executed as an inhibition of degradation. This is inspired by the Wnt signalling cascade, in which a Wnt signal saves β-catenin from degradation (Fig. 1.9). Note that activation by an inhibition of inhibition is a common phenomenon in cellular signalling [35].

We choose a Hill inhibitor function (Fig. 2.4 B) to specify this feedback according to:

$$h(a_n, a_{n+1}) = \frac{(c_{\text{A}})^h}{(c_{\text{A}})^h + (a_n + a_{n+1})^h}. \tag{2.5}$$

The Hill function is parametrised by the concentration of the signalling molecules leading to half-maximal inhibition, c_{A}, as well as the Hill exponent h, indicating how the response changes with input strength (see Fig. 2.4). Each cell senses the concentration of signalling molecules from the extracellular spaces to its left and to its right and integrates the two signals. Thus, it is the sum of the concentrations in both of these adjacent cells, $(a_n + a_{n+1})$ that influences the modulation of the degradation. Therefore, c_{A} is twice the average signalling molecule concentration in each of the adjacent extracellular spaces (n and $n+1$) at which cell n reaches half-maximal effector degradation (see Appendix B.1 for more details on this argument).

Overall, this leads to an increase in effector concentration in response to receiving a signal. Note that maximal effector degradation with rate k_B is reached in the absence of extracellular signalling molecules ($a_n = a_{n+1} = 0$) and degradation vanishes in the limit of infinitely high extracellular signalling-molecule concentrations. This closes the positive feedback loop and thus gives rise to a cell-to-cell relay in which the signal is effectively passed on from one cell to the next (Fig. 2.1).

In the remainder of the thesis, we will discuss the behaviour of this model for a Hill exponent $h = 1$. The full dynamics of the signalling molecule inside the source region, i.e. for $n \in [1, ..., (w-1)]$, thus are given by:

$$\partial_t a_n = D\,\frac{(a_{n-1} - 2\,a_n + a_{n+1})}{\delta^2} - k_\mathrm{A} a_n\, + s_\mathrm{A} + p\,\alpha^\mathrm{in}\,\frac{b_{n-1}}{c_\mathrm{B} + b_{n-1}} + (1-p)\,\alpha^\mathrm{in}\,\frac{b_n}{c_\mathrm{B} + b_n}. \tag{2.6}$$

Assuming that the constant production of signalling molecules in the source region with rate s_A follows the same secretion polarity as the production in response to positive feedback, the dynamics at the source/non-source interface are given by:

$$\partial_t a_w = D\,\frac{(a_{w-1} - 2\,a_w + a_{w+1})}{\delta^2} - k_\mathrm{A} a_w\, + p\,s_\mathrm{A} + p\,\alpha^\mathrm{in}\,\frac{b_{w-1}}{c_\mathrm{B} + b_{w-1}} + (1-p)\,\alpha^\mathrm{out}\,\frac{b_w}{c_\mathrm{B} + b_w}. \tag{2.7}$$

Outside of the source region, i.e. for $n \in [(w+1), ..., (N-1)]$, the dynamics of signalling molecule concentration obey:

$$\partial_t a_n = D\,\frac{(a_{n-1} - 2\,a_n + a_{n+1})}{\delta^2} - k_\mathrm{A} a_n\, + p\,\alpha^\mathrm{out}\,\frac{b_{n-1}}{c_\mathrm{B} + b_{n-1}} + (1-p)\,\alpha^\mathrm{out}\,\frac{b_n}{c_\mathrm{B} + b_n}. \tag{2.8}$$

The dynamics at the system boundaries, a_0 and a_N, are specified in the next section, where we discuss the boundary conditions. The dynamics of the intracellular effector are given by:

$$\partial_t b_n = s_\mathrm{B} - k_\mathrm{B}\frac{1}{1 + \frac{a_n + a_{n+1}}{c_\mathrm{A}}} b_n \tag{2.9}$$

for the whole system.

2.3. Boundary conditions

The system is comprised of a row of cells and extracellular spaces. It ends with an extracellular space of width $r_0 \times \epsilon$ on the left side, and $r_\mathrm{N} \times \epsilon$ on the right side, where $r_0, r_\mathrm{N} \in [0, \ldots, 1]$. In particular, the one extreme choice of this possible spectrum of extracellular-space widths, $r_0 = r_\mathrm{N} = 1$, corresponds to the system ending with an extracellular space of width ϵ (as in the bulk). The other extreme choice, $r_0 = r_\mathrm{N} = 0$, corresponds to the system ending with a cell on either side. We will not consider this latter case, as there will typically be at least some extracellular space at the boundary of any biological system. We therefore do not need to specify boundary conditions for the intracellular effector dynamics but rather for the dynamics of the signalling molecule concentrations in the extracellular spaces 0 and N at the system boundaries. In particular, we choose the volumes of the extracellular spaces at the system boundaries to be smaller than those in the bulk according to: $V_0 = (1-p)\,V$, $V_N = p\,V$, where V denotes the volume of an extracellular space in the bulk (Fig. 2.5). This leads to the following dynamics at the system boundaries:

$$\partial_t a_0 = \frac{D}{(1-p)} \frac{(-a_0 + a_1)}{\delta^2} - k_\mathrm{A} a_0 + s_\mathrm{A} + \alpha^\mathrm{in} \frac{b_0}{c_\mathrm{B} + b_0} \tag{2.10}$$

$$\partial_t a_N = \frac{D}{p} \frac{(a_{N-1} - a_N)}{\delta^2} - k_\mathrm{A} a_N + \alpha^\mathrm{out} \frac{b_{N-1}}{c_\mathrm{B} + b_{N-1}} \, . \tag{2.11}$$

Note that the secretion polarity in the production terms at the boundaries is balanced by this choice of boundary conditions (Fig. 2.5). To see this, consider that cells produce individual molecules. However, the other processes considered for the dynamics are concentration-dependent. Therefore, we define our model in concentrations. In order to account for the production in individual molecules, we define production rates $\widetilde{\alpha}$, $\widetilde{s}_\mathrm{A}$, and $\widetilde{s}_\mathrm{B}$ in number of molecules per second and convert them into concentration rates by dividing by the volume of the compartment the resultant molecules reside in. That is, $\alpha = \widetilde{\alpha}/V$, $s_\mathrm{A} = \widetilde{s}_\mathrm{A}/V$, and $s_\mathrm{B} = \widetilde{s}_\mathrm{B}/W$, where $V = \delta^2\,\epsilon$ denotes the volume of the extracellular space in the bulk and $W = \delta^3$ denotes the volume of the cells. With the presented choice of boundary conditions this leads to the equations presented above.

We use this choice of boundary conditions in the remainder of this thesis. We discuss the impact of this choice of boundary conditions on profile shape and

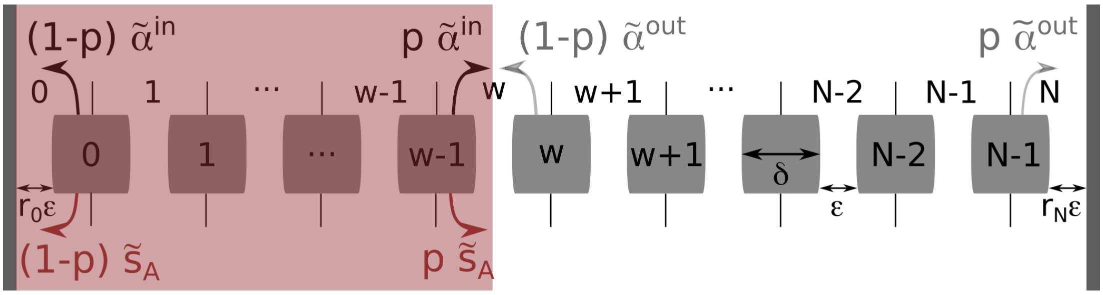

Figure 2.5.: **The cell-to-cell relay mechanism.** The system is comprised of N cells (0 - $(N-1)$) and $N+1$ extracellular spaces (0 - N). We impose reflective boundary conditions, i.e. nothing leaves or enters the system at the boundaries. Cells have width δ, extracellular spaces have width ϵ in the bulk and width $r_0 \times \epsilon$, $r_\mathrm{N} \times \epsilon$ at the boundaries, where $r_0 = (1-p)$ and $r_\mathrm{N} = p$. Source cells ($n \in [0, ..., (w-1)]$) constitutively produce and secrete signalling molecules with rate $\widetilde{s}_\mathrm{A}$ (red arrows), obeying tissue polarity p. All cells produce and secrete signalling molecules as part of the positive feedback. We distinguish between the feedback strengths inside and outside the source region ($\widetilde{\alpha}^\mathrm{in}$ - black arrows, and $\widetilde{\alpha}^\mathrm{out}$ - grey arrows, respectively). The extracellular spaces at the left system boundary, 0, and at the boundary between the source and the non-source region, w, only receive constitutively-produced signalling molecules from one side. Similarly, the extracellular spaces at the system boundaries, 0 and N, only receive signalling molecules produced by the positive feedback from one side. Source region shaded in red.

compare it to an alternative choice $V_0 = V_N = V$ in Appendix B.

2.4. Choice of model parameters

Our model comprises 8 parameters. In this section, we discuss the biological data guiding our parameter choices for the model. The width of eukaryotic cells is of the order of 10 µm [23, 48, 64]. We thus choose the cell width, δ, in our model to be 10 µm. In particular, in planarians, the smallest cells type, the neoblasts, have a cell diameter of 8 - 15 µm and the muscle fibres that express the Wnt signalling molecules are 5 -10 µm wide and 150 - 200 µm long [6]. Applying our model to the worm, the cells correspond to a 'stack' of circular muscle fibres along the AP axis. Thus, a cell width of 10 µm is a good estimate for this tissue.

The extracellular space in our model is narrow compared to the cell size. We choose ϵ to be a tenth of the cell width, i.e. 1 µm. The corresponding structure in the flatworm is the space between individual muscle fibres. Assuming that the extracellular spaces in this densely packed tissue [20, 60] are wider than those in an epithelium, 1 µm is a conceivable choice.

The diffusion coefficient of a sodium ion in water is of the order of 10^3 $\mu m^2/s$ [47]. A protein, being much bigger, has a much smaller diffusion coefficient. A spherical 100 kDa protein has a diffusion coefficient of the order of 100 $\mu m^2/s$ in water [47]. Tissues and cells are crowded environments with a viscosity much larger than water and thus in general show smaller diffusion coefficients [47, 48]. The diffusion coefficient of a protein inside a cell, for instance, is estimated to be around 5 $\mu m^2/s$ [48]. The diffusion relevant for the formation of signalling gradients happens in the extracellular space. Here, it can be hampered by the protein interacting with the extracellular matrix which may slow down the movement of the molecules beyond the effect of the viscosity of the interstitial fluid. For the signalling molecule Dpp, the diffusion coefficient in the extracellular space of the developing fruit fly wing imaginal disk has been measured to be 21 ± 3 $\mu m^2/s$ by fluorescence correlation spectroscopy (FCS) [121]. The effective diffusion coefficient in this tissue has been measured to be 0.1 $\mu m^2/s$ by fluoresce recovery after photobleaching (FRAP) [54]. This discrepancy illustrates the difference between the speed of molecular diffusion (as measured by FCS) and the effective spreading of the molecule that also takes into account interactions with the extracellular matrix as well as the cells (as measured by FRAP) [2]. In particular, Dpp depends on endocytosis for spreading in the wing disk [54, 17]. This is a slow process governed by the kinetics of receptor binding and uptake as well as secretion [2]. Thus, the dynamics of endocytosis and exocytosis are rate-limiting for molecular spreading in this case [121, 2]. They are included in the FRAP measurement of the effective diffusion coefficient of Dpp [2].

The effective diffusion coefficient of wingless, the *Drosophila* homologue of Wnt, has been measured to be 0.05 $\mu m^2/s$ in the fly wing imaginal disk by FRAP [54]. The effective diffusion coefficient of several proteins in the zebrafish blastula have been measured to be between 0.7 ± 0.2 $\mu m^2/s$ (Cyclops) and 18.9 ± 3.0 $\mu m^2/s$ (Lefty2) by FRAP [71].

In our model, diffusion is important to transmit the signal from one cell to the next. Thus, it is diffusion on rather small length scales that is important. In particular, the spreading of molecules by transcytosis does not have to be considered for this process. Therefore, the diffusion important for our model is best captured by extracellular molecular diffusion. However, as discussed in Section 1.3.3, Wnt molecules are hydrophobic molecules and thus not likely to have a fast extracellular diffusion constant. We thus choose an effective diffusion coefficient of 1 $\mu\mathrm{m}^2/\mathrm{s}$ for our model. This is the same as the diffusion coefficient used for the morphogen in Ref. [12].

The degradation rates of wingless and Dpp in the fly wing imaginal disk have been measured by FRAP to be $1.43\times10^{-3}\pm1.04\times10^{-3}$ s^{-1}, and $2.52\times10^{-4}\pm1.29\times10^{-4}$ s^{-1}, respectively [54]. Degradation rates of some proteins in the zebrafish blastula have been measured by FRAP to be between $0.53\times10^{-4}\pm0.05\times10^{-4}$ s^{-1} (Lefty1) and $1.22\times10^{-4}\pm0.13\times10^{-4}$ s^{-1} (Cyclops) [71]. We choose a degradation rate of $k_\mathrm{B} = 10^{-3}$ s^{-1} for the effector molecule and one of $k_\mathrm{A} = 10^{-3}$ s^{-1} for the signalling molecule. These choices are in agreement with the the orders of magnitude that have been measured for signalling molecules. Note that we chose a different value of $k_\mathrm{B} = 100$ s^{-1} in Chapters 5 and 6 as specified to explore the possibilities of the model.

The constant source in our model is inspired by the stripe of *Wnt1*-expressing cells, the pole cells at the posterior midline of the worm [78, 43]. This stripe has been measured to consist of around 10 cells [43]. This measurement has been performed by *in situ* hybridisation which is generally performed on small animals (1 - 2 mm long). The number of posterior pole cells has not been quantified in differently-sized worms. We choose the source region to be of the order of 10% of system size, i.e. worm length. This choice is in good agreement with the 10 cells reported in Gurley *et al.* [43].

The Hill threshold concentrations c_A and c_B denote the concentrations of half-maximal repression and activation, respectively. More precisely, c_A is twice the average signalling molecule concentration in each adjacent extracellular space (n and $n+1$) at which cell n reaches half-maximal effector degradation, as both extracellular spaces contribute to the repression (see Appendix B.1 for more details on this argument). Ben-Zvi *et al.* assumed Hill-repression coefficients of 10^{-1}µM and 1 µM. We choose $c_{\mathrm{A}} = 166.6$ nM $= 0.16$ µM which is in the reported range. We choose a threshold concentration c_{B} ensuring that $c_{\mathrm{B}} \gg b_n$. This way, the feedback response can be approximated by a linear response, as the positive feedback term $\frac{\alpha}{c_{\mathrm{B}}} \frac{b_n}{1+\frac{b_n}{c_{\mathrm{B}}}}$ simplifies to $\frac{\alpha}{c_{\mathrm{B}}} b_n$ in the limit $\frac{b_n}{c_{\mathrm{B}}} \ll 1$. To ensure $c_{\mathrm{B}} \gg b_n$, we choose $c_{\mathrm{B}} = 1.66 \times 10^5$ µM. Note that we use different choices of c_{A} and c_{B} in Chapter 4 as specified.

Signalling molecules are produced in a signalling-independent manner at rate s_{A}, and in a signalling-dependent manner with a maximal rate α^{in} inside the source region, and a maximal production rate α^{out} outside of the source region. Effector molecules are produced at rate s_{B}. These are effective rates representing the amount of signalling molecules released to the extracellular space per unit time, and the increase in intracellular effector concentration due to production, respectively. We specify these rates in number of molecules per unit time ($\widetilde{s}_{\mathrm{A}}$, $\widetilde{\alpha}^{\mathrm{in}}$, $\widetilde{\alpha}^{\mathrm{out}}$, $\widetilde{s}_{\mathrm{B}}$) and calculate the resulting change in concentration in the extracellular space by applying the volume of the extracellular space V, which is given by the width of the extracellular space and the area of the cell side as $V = \epsilon\,\delta^2$, and in the cell by applying the cellular volume $W = \delta^3$. Lee *et al.* report a β-catenin-production rate of 0.42 nM/min based on measurements in *Xenopus* egg extracts [57]. Based on FRAP data for Dpp gradient formation in the *Drosophila* wing imaginal disk, Kicheva *et al.* report a production rate of 2.69 ± 1.58 molecules per cell per second [54]. The equivalent estimate for wingless is 18.70 ± 12.92 molecules per cell per second [54]. In our model, we explicitly account for the molecule production of individual cells. We choose the constant signalling-molecule (Wnt) production rate in the source region as $\widetilde{s}_{\mathrm{A}} = 20$ molecules per cell per second according to the Wingless production rate measured in [54], and the rate of effector (β-catenin) molecule production inside the cell as $\widetilde{s}_{\mathrm{B}} = 4$ molecules per cell per second. Applying the cell volume of our model (10^3 µm^3), this leads to a production rate of 0.4 nM/min, which is in good agreement with the production rate for β-catenin measured in Lee *et al.* (0.42 nM/min [57]). Moreover, it is in good agreement with the Dpp production rate measured in Ref. [54]. We convert these production rates to units of concentration per time by applying the volume of the extracellular space and the cell, respectively: $s_{\mathrm{A}} = \widetilde{s}_{\mathrm{A}}/V$, $s_{\mathrm{B}} = \widetilde{s}_{\mathrm{B}}/W$. See Appendix B for a discussion of the effect of this conversion at the boundaries. Note that we use different choices of $\widetilde{s}_\mathrm{A}$ and $\widetilde{s}_\mathrm{B}$ in Chapter 4, and a different choice of $\widetilde{s}_\mathrm{A}$ in Chapter 5 as specified.

The feedback strengths α^in inside the source region and α^out outside of the source region are the maximal possible signalling molecule production rates, reached when the effector concentration is much larger than the threshold c_B. Thus, the actual production rate can be approximated as $\frac{\alpha}{c_\mathrm{B}}\, b_n$ as long as $c_\mathrm{B} \gg b_n$, see above. Therefore, the choice of a high value of c_B requires a large maximal production rate $\alpha^\mathrm{in/out}$ to achieve considerable production in the most common scenario that the effector concentration is lower than the threshold concentration. We analyse the effect of the feedback strength on the profile of signalling molecules and thus do not choose a fixed feedback strength but vary it. We vary it up to values of the same order of magnitude as c_B, i.e. to values of the order of $\widetilde{\alpha}^\mathrm{in/out} = 10^8$ nmol/s $= 10^5$ µmol/s. Equivalently to what we discussed before, we convert this production into a resultant change in concentration by applying the molecular volume of the extracellular space, i.e. $\alpha^\mathrm{in/out} = \widetilde{\alpha}^\mathrm{in/out}/V$. In the next section, we present a numerical solution to our model using the parameter choices discussed here.

2.5. Numerical solution to the model

We can obtain the dynamic solution to our system numerically by starting from an initial condition and computing the time evolution. We use an implicit-explicit Euler method to compute the time evolution of our system ([5], see Appendix C for details on the method). Solving the dynamics of the signalling-molecule concentration, we evaluate the linear parts (diffusion and degradation) implicitly and the non-linear parts (feedback and constant source) explicitly. For the (non-linear) dynamics of the effector concentration, we use the explicit Euler method. See Appendix D for the specific implementation of this implicit-explicit Euler method for our model. This numerical solution gives us both the dynamic evolution, as well as the steady state of the model. We show steady-state concentration profiles for the signalling molecule and the effector obtained using this method in Fig. 2.6.

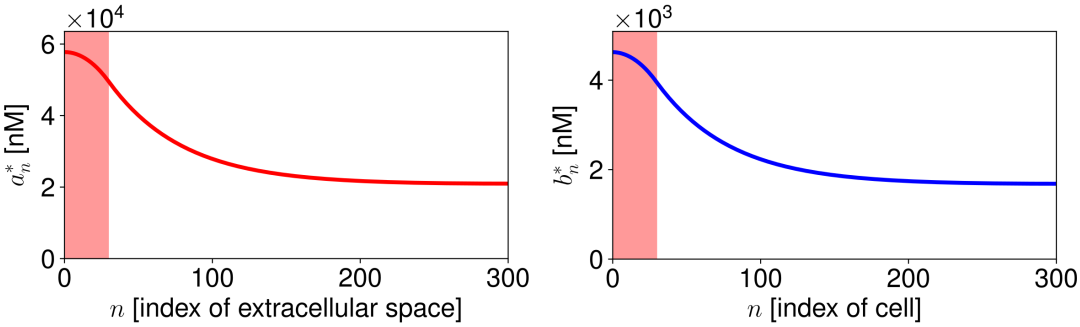

Figure 2.6.: **Numerical steady-state solution of our model.** Numerical steady-state solution for the signalling molecule profile (left, red line) and effector profile (right, blue line). Source region shaded in red. Parameters used: $\alpha^{\text{in}} = \alpha^{\text{out}} = 1.245 \times 10^8$ molecules/(s V) $= 2.075 \times 10^6$ nM, $c_{\text{A}} = 166$ nM, $c_{\text{B}} = 1.66 \times 10^8$ nM, $D = 1.0$ µm^2/s, $\delta = 10.0$ µm, $k_{\text{A}} = 10^{-3}$ s^{-1}, $k_{\text{B}} = 10^{-3}$ s^{-1}, $p = 0.5$, $s_{\text{A}} = 20$ molecules/(s V), $s_{\text{B}} = 4$ molecules/(s W), $N = 300$, $w = 30$, $V = 10^2$ µm^3, $W = 10^3$ µm^3.

2.6. Summary and discussion

In this chapter we introduced the model for the cell-to-cell relay mechanism that we will discuss in this thesis. The model is motivated by observations of positive feedback in the Wnt signalling gradient patterning the main body axis of planarians (Section 1.4.3). The model can, however, be extended to other signalling pathways that exhibit positive feedback loops.

One of the major conceptual differences between the relay mechanism suggested in this work and the diffusion/degradation mechanism discussed previously [54] is that the positive feedback introduced in the relay mechanism leads to production of signalling molecules throughout the system. The strength of production is dependent on the strength of the feedback as well as the effector levels at the position in question. On the contrary, in the diffusion/degradation mechanism there is a confined source region with a constant strength. This spatially-confined source is also present in our mechanism. Its role is to break the symmetry of the system in the relay mechanism.

Mapping the model back to planarians, the cells in our model can be likened to the circular muscle fibres of the planarian body wall musculature, the intracellular effector to β-catenin, and the signalling molecule to an effective Wnt species summarising all Wnts implicated in AP pattering in the worm. These are likely to be the so called 'tail Wnts' (Wnt1, Wnt11-1, -2, 5, see Section 1.4.2). The effector-level dependent production gives rise to a spatially varied signalling molecule production. Production is high where the effector levels are high. This can be likened to the *Wnt* expression gradients observed in planarians, that decay from the tail tip anteriorly and thus in accordance with the β-catenin protein gradient. The constant, signalling-level-independent production of signalling molecules in the source region can be likened to the constant *Wnt1* expression in the posterior pole cells in the worm.

Many signalling proteins, including Wnt proteins, rely on post-translational modifications, in particular lipid modifications, in order to signal [75, 82, 115]. The extracellular signalling molecule population in our model corresponds to those signalling molecules in the extracellular space that carry all post-translational modifications necessary to elicit a signal and thus change the effector levels inside the cell.

In the next chapter, we will analyse the steady-state concentration gradients our model gives rise to. In particular, we will investigate the effect of the proposed positive feedback on length scale of the gradient and analyse whether it can indeed explain long-ranged steady-state gradient formation.

3. The signalling gradient at steady state

3.1. Large-scale pattern formation in light of positive feedback

Signalling gradients pattern tissues during embryonic development, regeneration, and tissue turn-over ([24, 25, 38, 42, 46], see Section 1.1). The diffusion/degradation models used to explain the formation these gradients in the context of embryonic development [54] struggle to explain formation of long-ranged signalling gradients (see Section 1.5 for a discussion) such as the Wnt signalling gradient patterning the main body axis of flatworms [99, 98]. Motivated by the observation of positive feedback in Wnt signalling in flatworms ([98], see Section 1.4.3), we analyse the role of positive feedback on the formation of signalling gradients in this thesis.

In this chapter, we analyse how positive feedback impacts the length scale of the steady-state gradient. The positive feedback loop we introduced in Chapter 2 consists of the positive feedback of the signalling molecule concentration on effector levels, as well as the positive feedback of the effector levels on signalling molecule production. This positive feedback loop serves as a cell-to-cell relay mechanism, propagating the signal from one cell to the next without the need for signalling molecules to physically traverse the entire tissue. Intuitively, we can already appreciate that, when each cell produces molecules due to the positive feedback, individual molecules do not necessarily have to travel across the whole system for the pattern to have a long range. This may lead to an increased length scale compared to production of signalling molecules exclusively taking place in a local source region and molecules spreading by diffusion. Numerical solutions of our model indeed show that the length scale of the steady-state gradient increases with feedback strength (Fig. 3.1).

In order to understand and analyse the effect of positive feedback on the length scale of the steady-state gradient, we introduce an analytical approximate steady-state solution in this chapter. This reveals how the length scale depends on the parameters of the model, in particular on the feedback strength. For effector concentrations b_n that are much lower than the Hill-activator threshold c_{B}, i.e. $b_n \ll c_{\mathrm{B}}$, the feedback response is quasi-linear, as the system is far away from saturation. Analysing the system in the limit of a linear feedback response reveals an interesting relationship between the length scale and the feedback strength. Guided by the analysis in this limit, we can better understand the behaviour of the full model including saturation.

We start this chapter by introducing an analytical approximate steady-state solution to the model. We then introduce the steady-state solution to the model in the limit of low effector concentration, i.e. far away from saturation. Guided by what we learn about the relationship between the length scale and the feedback strength in this limit, we then discuss the effect of the feedback strength on the full model. Further, we discuss how the positive feedback influences gradient shape. Gradient shape is not only defined by the length scale, but also by the difference of the maximal and minimal values of the concentration profile.

Polarised secretion qualitatively changes the behaviour of the system and is discussed in Chapter 6. In this chapter, we discuss the length scale and the shape of the steady-state gradient in the absence of secretion polarity ($p = 1/2$).

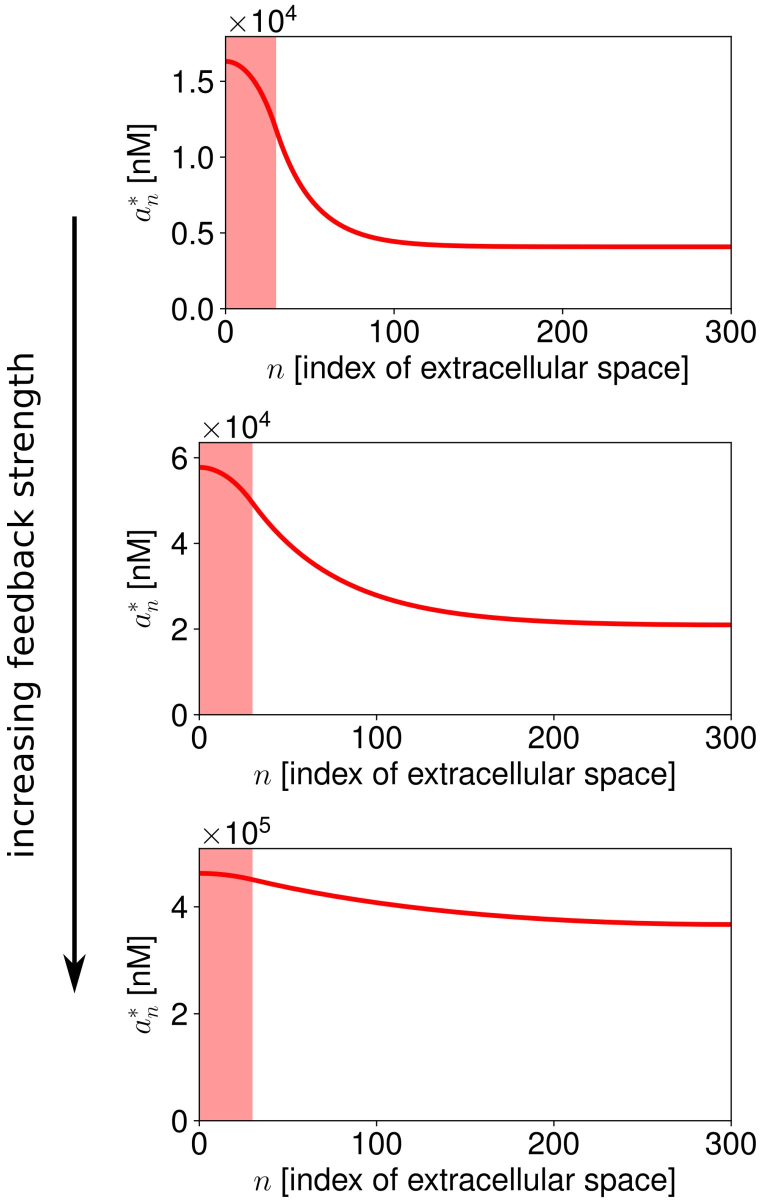

Figure 3.1.: **Steady-state solution for varying feedback strength.** Profile length scale increases with increasing feedback strength $\alpha^{\mathrm{in/out}}$. Red line: numerical steady-state solution for the signalling molecule concentration profile. Source region shaded in red. Parameters used: $\alpha^{\mathrm{in}} = \alpha^{\mathrm{out}}$ from top to bottom: $\alpha^{\mathrm{out}} = 1.225000 \times 10^8$ molecules/(s V) $= 2.042 \times 10^8$ nM/s, $\alpha^{\mathrm{out}} = 1.245000 \times 10^8$ molecules/(s V) $= 2.075 \times 10^8$ nM/s, $\alpha^{\mathrm{out}} = 1.249875 \times 10^8$ molecules/(s V) $= 2.083 \times 10^8$ nM/s, $c_{\mathrm{A}} = 166$ nM, $c_{\mathrm{B}} = 1.66 \times 10^8$ nM, $D = 1.0$ µm^2/s, $\delta = 10.0$ µm, $k_{\mathrm{A}} = 10^{-3}$ s^{-1}, $k_{\mathrm{B}} = 10^{-3}$ s^{-1}, $p = 0.5$, $s_{\mathrm{A}} = 20$ molecules/(s V), $s_{\mathrm{B}} = 4$ molecules/(s W), $N = 300$, $w = 30$, $V = 10^2$ µm^3, $W = 10^3$ µm^3.

3.2. Approximate analytical steady-state solution to the model

In order to assess the effect of the positive feedback on profile shape, we analyse the shape of the steady-state profiles. The steady-state of the system, denoted by a_n^* and b_n^*, is defined as:

$$\partial_t a_n^* = 0 \ , \tag{3.1}$$

$$\partial_t b_n^* = 0 \ . \tag{3.2}$$

Based on Eqs. 2.9 and 3.2, we find that at steady state, the concentration of the effector is a linear function of the concentration of the signalling molecule:

$$b_n^* = \frac{s_\mathrm{B}}{k_\mathrm{B}}(1 + \frac{a_n^* + a_{n+1}^*}{c_\mathrm{A}}) \ . \tag{3.3}$$

We can thus express the steady-state solution of the signalling molecule only in terms of the signalling molecule concentration by inserting Eq. 3.3 into the steady-state equations of the signalling molecule concentration (Eqs. 2.6, 2.7, 2.8, 3.1). This way, we find a piece-wise constant solution to the steady-state equation for the signalling-molecule concentration given by a constant solution inside of the source region:

$$\begin{aligned} a_\mathrm{c}^\mathrm{in} = {} & \frac{1}{2}\left(\frac{s_\mathrm{A}}{k_\mathrm{A}} + \frac{\alpha^\mathrm{in}}{k_\mathrm{A}} - \frac{c_\mathrm{A}}{2}\left(\frac{c_\mathrm{B} k_\mathrm{B}}{s_\mathrm{B}} + 1\right)\right) \\ & + \sqrt{\frac{1}{4}\left[\frac{s_\mathrm{A}}{k_\mathrm{A}} + \frac{\alpha^\mathrm{in}}{k_\mathrm{A}} - \frac{c_\mathrm{A}}{2}\left(\frac{c_\mathrm{B} k_\mathrm{B}}{s_\mathrm{B}} + 1\right)\right]^2 + \frac{c_\mathrm{A}}{2k_\mathrm{A}}\left[s_\mathrm{A}\left(\frac{c_\mathrm{B} k_\mathrm{B}}{s_\mathrm{B}} + 1\right) + \alpha^\mathrm{in}\right]} \quad , \end{aligned}$$

and a constant solution outside of the source region: (3.4)

$$\begin{aligned} a_\mathrm{c}^\mathrm{out} = {} & \frac{1}{2}\left(\frac{\alpha^\mathrm{out}}{k_\mathrm{A}} - \frac{c_\mathrm{A}}{2}\left(\frac{c_\mathrm{B} k_\mathrm{B}}{s_\mathrm{B}} + 1\right)\right) \\ & + \sqrt{\frac{1}{4}\left[\frac{\alpha^\mathrm{out}}{k_\mathrm{A}} - \frac{c_\mathrm{A}}{2}\left(\frac{c_\mathrm{B} k_\mathrm{B}}{s_\mathrm{B}} + 1\right)\right]^2 + \frac{\alpha^\mathrm{out} c_\mathrm{A}}{2k_\mathrm{A}}} \quad . \end{aligned} \tag{3.5}$$

In the absence of positive feedback, $\alpha^\mathrm{in} = \alpha^\mathrm{out} = 0$, the dynamics of the signalling molecule concentration simplify to a diffusion/degradation mechanism. Note that in this case, a_c^in simplifies to $\frac{s_\mathrm{A}}{k_\mathrm{A}}$, whereas $a_\mathrm{c}^\mathrm{out}$ vanishes as expected for a diffusion/degradation system. The numerical solution to the model confirms that the steady-state concentration profiles indeed approach these constants far away from the boundaries (Fig. 3.2).

Based on this piece-wise constant solution, we can analytically find an approximate solution to the steady-state equations of the signalling molecule. To this end, we linearise the steady-state equations for the signalling molecule a_n^* (Eqs. 2.6 - 2.8, 3.1, 3.2, 3.3) around the piece-wise constant solution given by Eqs. 3.4 and 3.5. First, we express a_n^* as a deviation from the respective constant steady-state solution in the source region (a_c^in) and outside of the source region ($a_\mathrm{c}^\mathrm{out}$), respectively:

$$a_n^* = a_\mathrm{c}^\mathrm{in} + \delta a_n^* \quad \text{for } n \in [0, \ldots, w] \ , \tag{3.6}$$

$$a_n^* = a_\mathrm{c}^\mathrm{out} + \delta a_n^* \quad \text{for } n \in [(w+1), \ldots, N] \ , \tag{3.7}$$

where δa_n represents the deviation from the respective constant solution in the extracellular space n. Then, we linearise the steady-state equations for the signalling molecule concentration (Eqs. 2.6 - 2.8, 3.1, 3.2, using Eq. 3.3) for small deviations from the respective constant solution, i.e. for small δa_n^*. See Appendix E.1 for the resultant set of linearised steady-state equations. We use an exponential ansatz to solve the system of linearised steady-state equations:

$$\delta a_n^* = C_1^\mathrm{in} e^{n/\bar{\lambda}_1^\mathrm{in}} + C_2^\mathrm{in} e^{-n/\bar{\lambda}_2^\mathrm{in}} \qquad \text{for } n \in [0, \ldots, w] \ , \tag{3.8}$$

$$\delta a_n^* = C_1^\mathrm{out} e^{n/\bar{\lambda}_1^\mathrm{out}} + C_2^\mathrm{out} e^{-n/\bar{\lambda}_2^\mathrm{out}} \qquad \text{for } n \in [(w+1), \ldots, N] \ . \tag{3.9}$$

The amplitudes of the exponentials (C_1^in, C_2^in, C_1^out, C_2^out) are given by the boundary conditions at $n = 0$ and $n = N$, as well as by the source/non-source interface stitching conditions at $n = w$ and $n = w+1$. See Appendix E.2 for how to obtain them.

As we are interested in the length scale of the system outside of the source region, we focus our analysis of the profile length scale on $\bar{\lambda}_1^\mathrm{out}$ and $\bar{\lambda}_2^\mathrm{out}$. Looking at the numerical steady-state solutions and considering that the system obtains a steady state also for large system sizes, we can deduce that the amplitude of the increasing exponential (C_1^out) is very small and goes to zero as system size increases. Therefore, the shape of the steady-state profile outside of the source region is given by the decreasing exponential. We thus define the length scale of the steady-state profile of our system, $\bar{\lambda}$, as:

$$\bar{\lambda} := \bar{\lambda}_2^{\mathrm{out}} \; . \tag{3.10}$$

It denotes the decay length of the gradient in number of cells and is given by:

$$\bar{\lambda} = \frac{\frac{2\,D}{\delta^2} + \alpha^{\mathrm{out}}\,z^{\mathrm{out}}}{(1-2\,p)\,\alpha^{\mathrm{out}}\,z^{\mathrm{out}} + \sqrt{\left[(1-2\,p)\,\alpha^{\mathrm{out}}\,z^{\mathrm{out}}\right]^2 + 2\,\left(\frac{2\,D}{\delta^2} + \alpha^{\mathrm{out}}\,z^{\mathrm{out}}\right)\left(k_{\mathrm{A}} - 2\,\alpha^{\mathrm{out}} z^{\mathrm{out}}\right)}} \; , \tag{3.11}$$

where

$$z^{\mathrm{out}} = \frac{c_{\mathrm{A}}\,c_{\mathrm{B}}\,k_{\mathrm{B}}}{s_{\mathrm{B}}\left[c_{\mathrm{A}} + \frac{c_{\mathrm{A}}\,c_{\mathrm{B}}\,k_{\mathrm{B}}}{s_{\mathrm{B}}} + 2a_{\mathrm{c}}^{\mathrm{out}}\right]^2} \; . \tag{3.12}$$

Note that $\bar{\lambda}$ defined in this way is only dependent on the feedback strength outside of the source region, α^{out}, while it is not influenced by the strength of the feedback inside of the source region, α^{in}. Note further, that in the absence of positive feedback, $\alpha^{\mathrm{out}} = 0$, we recover

$$\bar{\lambda} = \sqrt{\frac{D/\delta^2}{k_{\mathrm{A}}}} \; , \tag{3.13}$$

i.e. the length scale of a simple diffusion/degradation system as expected.

Comparing Eq. 3.11 to the length scale of the continous diffusion/degradation mechanism with drift (Eq. 1.11) introduced in Section 1.5, we can identify that the secretion polarity gives rise to an effective drift with speed ν:

$$\nu = (2\,p - 1)\,\alpha^{\mathrm{out}}\,z^{\mathrm{out}} \; . \tag{3.14}$$

We introduced ν as having positive values when the drift was directed down the gradient in Section 1.5 (Eq. 1.8). In contrast, ν as defined in Eq. 3.14 is positive for $p > 1/2$. The secretion polarity is defined such that $p > 1/2$ corresponds to preferred secretion to the right. This is consistent with positive values of ν corresponding to secretion down the gradient if the gradient decays from left to right. We defined the source region to be to the left in our model (Eq. 2.1, Fig. 2.2). Thus, a gradient decaying from left to right is one that is decaying away from the local source. This is the shape of gradient we aim to analyse. We analyse the effect of the effective drift that secretion polarity ($p \neq 1/2$) gives rise to in Chapter 6.

In the remainder of the current chapter, as well as in Chapters 4 and 5, we discuss the model for the case of symmetric secretion ($p = 1/2$). In this case, the drift vanishes and the length scale simplifies to:

$$\bar{\lambda} = \sqrt{\frac{\frac{D}{\delta^2} + \alpha^{\mathrm{out}}\,\frac{z^{\mathrm{out}}}{2}}{k_{\mathrm{A}} - 2\,\alpha^{\mathrm{out}} z^{\mathrm{out}}}}\ . \tag{3.15}$$

This analytical approximate steady-state solution is in good agreement with the numerical steady-state solution (see Fig. 3.3). In the next section, we discuss the model in the limit of a linear feedback response, valid for effector concentrations that are low compared to the Hill-activator threshold concentration c_{B}.

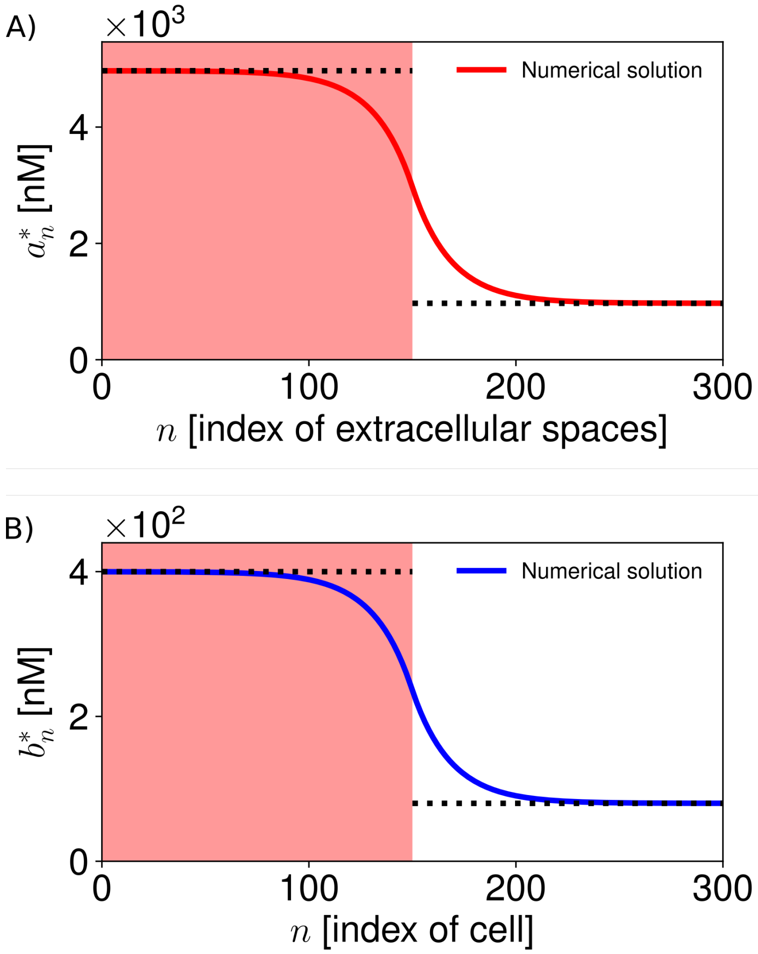

Figure 3.2.: **The piece-wise constant solution is reached far away from the boundaries. A)** a_n (signalling molecules). The piece-wise constant steady-state solution, given by a_c^{in} (Eq. 3.4) and a_c^{out} (Eq. 3.5), in the source-region and non-source region, respectively (dotted black lines). **B)** b_n (effector, β-catenin). The piece-wise constant steady-state solution is given by Eq. 3.3 based on a_c^{in} and a_c^{out} (dotted black lines). Source region shaded in red. The source region and non-source region need to be sufficiently large for a_n, b_n to reach these constant values. Parameters used: $\alpha^{\text{in}} = \alpha^{\text{out}} = 1.2125 \times 10^8$ molecules/(s V), $c_{\text{A}} = 166$ nM, $c_{\text{B}} = 1.66 \times 10^8$ nM, $D = 1.0$ µm^2/s, $\delta = 10.0$ µm, $k_{\text{A}} = 10^{-3}$ s^{-1}, $k_{\text{B}} = 10^{-3}$ s^{-1}, $p = 0.5$, $s_{\text{A}} = 20$ molecules/(s V), $s_{\text{B}} = 4$ molecules/(s W), $N = 500$, $w = 200$, $V = \epsilon\,\delta^2 = 10^2$ µm^3, $W = \delta^3 = 10^3$ µm^3.

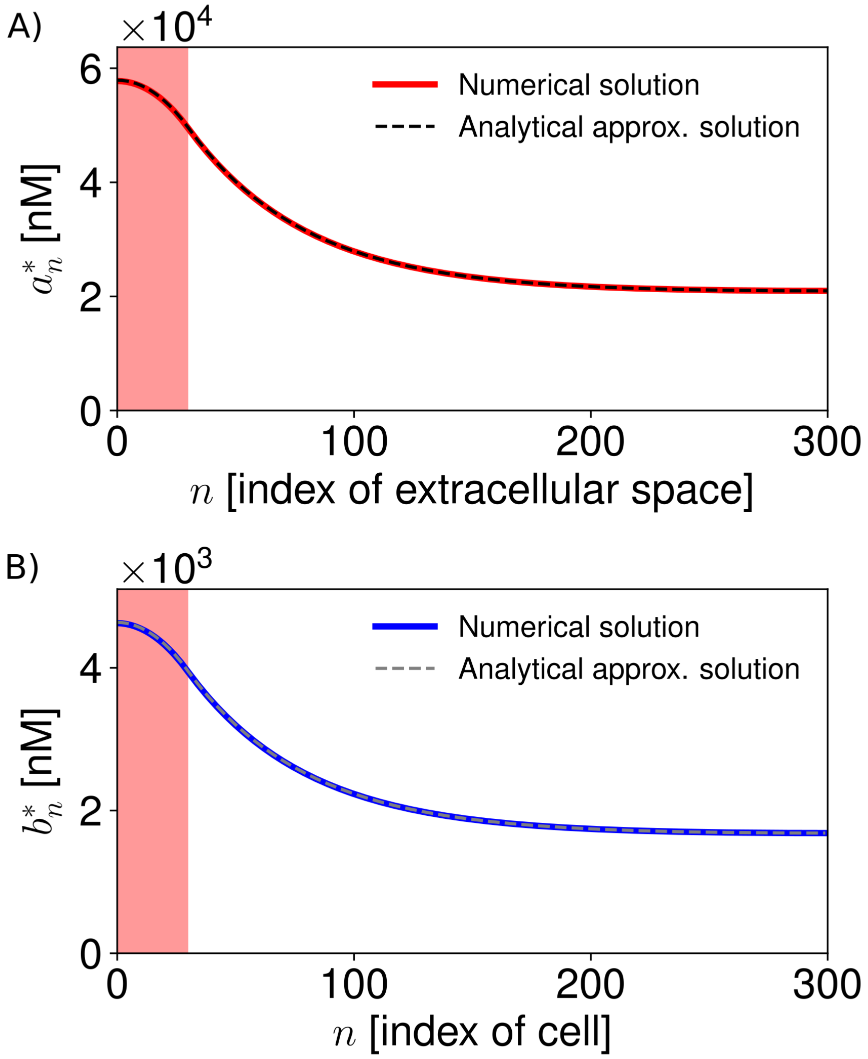

Figure 3.3.: **Analytical approximate steady-state solution.** **A)** Signalling molecule concentrations, a_n. The analytical approximate steady-state solution (dashed line, Eqs. 3.6 and 3.7) is a good representation of the numerical steady-state solution to the non-linear model (solid lines: numerical steady-state solution). **B)** Effector concentrations b_n. The analytical approximate steady-state solution (dashed line, obtained based on Eqs. 3.6 and 3.7 using Eq. 3.3) is a good representation of the numerical steady-state solution to the non-linear system. Source region shaded in red. Parameters used: $\alpha^{\mathrm{in}} = \alpha^{\mathrm{out}} = 1.245 \times 10^8$ molecules/(s V) $= 2.075 \times 10^6$ nM/s, $c_{\mathrm{A}} = 166$ nM, $c_{\mathrm{B}} = 1.66 \times 10^8$ nM, $D = 1.0\ \mu\mathrm{m}^2/\mathrm{s}$, $\delta = 10.0\ \mu\mathrm{m}$, $k_{\mathrm{A}} = 10^{-3}\ \mathrm{s}^{-1}$, $k_{\mathrm{B}} = 10^{-3}\ \mathrm{s}^{-1}$, $p = 0.5$, $s_{\mathrm{A}} = 20$ molecules/(s V), $s_{\mathrm{B}} = 4$ molecules/(s W), $N = 300$, $w = 30$, $V = \epsilon\,\delta^2 = 10^2\ \mu\mathrm{m}^3$, $W = \delta^3 = 10^3\ \mu\mathrm{m}^3$.

3.3. Linear feedback response in the limit of low effector concentration

For effector concentrations that are low compared to the Hill-activator threshold c_B, the system exhibits a linear feedback response. In this case, the feedback can be approximated by a linear response (Fig. 3.4). We can obtain this result formally in the limit $\frac{b_n}{c_\mathrm{B}} \ll 1$ in Eq. 2.3:

$$\frac{b_n/c_\mathrm{B}}{1+b_n/c_\mathrm{B}} \approx \frac{b_n}{c_\mathrm{B}} \; . \tag{3.16}$$

In this limit, the dynamic equations of the signalling molecule a_n (Eqs. 2.6 - 2.8) simplify to:

$$\partial_t a_n = D\,\frac{(a_{n-1} - 2\,a_n + a_{n+1})}{\delta^2} - k_\mathrm{A} a_n \, + s_\mathrm{A} + p\,\frac{\alpha^\mathrm{in}}{c_\mathrm{B}}\,b_{n-1} + (1-p)\,\frac{\alpha^\mathrm{in}}{c_\mathrm{B}}\,b_n \tag{3.17}$$

in the source region, i.e. for n $\in [1, \dots, (w-1)]$, and equivalently at the boundary for a_0 based on Eq. 2.10;

$$\partial_t a_w = D\,\frac{(a_{w-1} - 2\,a_w + a_{w+1})}{\delta^2} - k_\mathrm{A} a_w \, + p\,s_\mathrm{A} + p\,\frac{\alpha^\mathrm{in}}{c_\mathrm{B}}\,b_{w-1} + (1-p)\,\frac{\alpha^\mathrm{out}}{c_\mathrm{B}}\,b_w \tag{3.18}$$

at the source/non-source interface;

$$\partial_t a_n = D\,\frac{(a_{n-1} - 2\,a_n + a_{n+1})}{\delta^2} - k_\mathrm{A} a_n \, + p\,\frac{\alpha^\mathrm{out}}{c_\mathrm{B}}\,b_{n-1} + (1-p)\,\frac{\alpha^\mathrm{out}}{c_\mathrm{B}}\,b_n \tag{3.19}$$

outside of the source region, i.e. $n \in [(w+1), ..., (N-1)]$, and equivalently for the boundary condition at a_N based on Eq. 2.11.

In this limit, we can obtain an analytical steady-state solution to our model:

$$a_n^* = a^\mathrm{in}_\mathrm{c,\,lin} + C^\mathrm{in}_\mathrm{1,\,lin}\,e^{n/\bar\lambda^\mathrm{in}_\mathrm{1,\,lin}} + C^\mathrm{in}_\mathrm{2,\,lin}\,e^{-n/\bar\lambda^\mathrm{in}_\mathrm{2,\,lin}} \qquad \text{for } n \in [0, ..., w] \; , \tag{3.20}$$

$$a_n^* = a^\mathrm{out}_\mathrm{c,\,lin} + C^\mathrm{out}_\mathrm{1,\,lin}\,e^{n/\bar\lambda^\mathrm{out}_\mathrm{1,\,lin}} + C^\mathrm{out}_\mathrm{2,\,lin}\,e^{-n/\bar\lambda^\mathrm{out}_\mathrm{2,\,lin}} \qquad \text{for } n \in [(w+1), ..., N] \; , \tag{3.21}$$

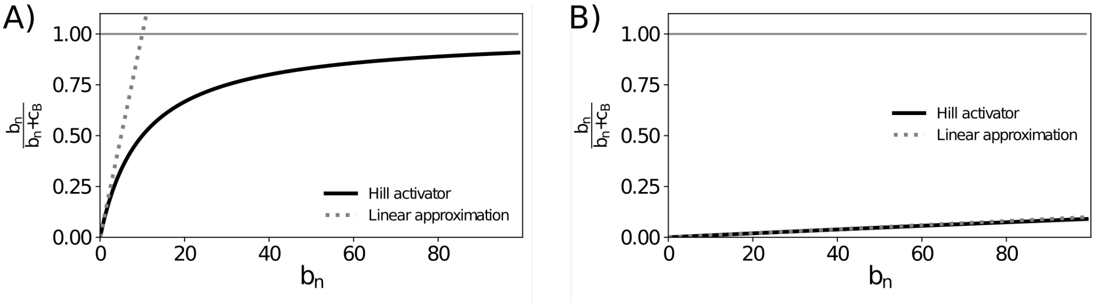

Figure 3.4.: **For $b_n \ll c_{\mathrm{B}}$, the Hill activator function can be approximated by a linear function.** Black line: Hill activator function for $h = 1$. Dashed grey line: linear approximation to it. The approximation is increasingly better as $\frac{b_n}{c_{\mathrm{B}}} \to 0$. **A)** $c_{\mathrm{B}} = 10$ nM. **B)** $c_{\mathrm{B}} = 1000$ nM.

where $a^{\mathrm{in}}_{\mathrm{c,\,lin}}$ and $a^{\mathrm{out}}_{\mathrm{c,\,lin}}$ denote the piece-wise constant solution and are given by:

$$a^{\mathrm{in}}_{\mathrm{c,\,lin}} = \frac{s_{\mathrm{A}} + \frac{\alpha^{\mathrm{in}}\, s_{\mathrm{B}}}{c_{\mathrm{B}}\, k_{\mathrm{B}}}}{k_{\mathrm{A}} - \frac{2\,\alpha^{\mathrm{in}}\, s_{\mathrm{B}}}{c_{\mathrm{A}}\, c_{\mathrm{B}}\, k_{\mathrm{B}}}} \,, \tag{3.22}$$

$$a^{\mathrm{out}}_{\mathrm{c,\,lin}} = \frac{\frac{\alpha^{\mathrm{out}}\, s_{\mathrm{B}}}{c_{\mathrm{B}}\, k_{\mathrm{B}}}}{k_{\mathrm{A}} - \frac{2\,\alpha^{\mathrm{out}}\, s_{\mathrm{B}}}{c_{\mathrm{A}}\, c_{\mathrm{B}}\, k_{\mathrm{B}}}} \,. \tag{3.23}$$

The amplitudes of the exponentials $C^{\mathrm{in}}_{1,\,\mathrm{lin}}$, $C^{\mathrm{in}}_{2,\,\mathrm{lin}}$, C^{out}_{1}, $C^{\mathrm{out}}_{2,\,\mathrm{lin}}$ are given by the boundary conditions at $n = 0$ and $n = N$, as well as by the source/non-source interface stitching conditions at $n = w$ and $n = w + 1$, and computed performing the same steps as for the non-linear model (see Appendix E.2 for details on the steps). Analogously to what we discussed for the approximate solution to the non-linear system, the length scale of model in the limit of a linear feedback response is defined as $\bar{\lambda}_{\mathrm{lin}} := \bar{\lambda}^{\mathrm{out}}_{2,\,\mathrm{lin}}$. In order to compute it, we follow the same steps as discussed for the non-linear model. Based on Eqs. 3.19, 3.1, and 3.21, we obtain:

$$\bar{\lambda}_{\mathrm{lin}} = \frac{\frac{2\,D}{\delta^2} + \frac{\alpha^{\mathrm{out}}\, s_{\mathrm{B}}}{c_{\mathrm{A}}\, c_{\mathrm{B}}\, k_{\mathrm{B}}}}{\left[(1 - 2\,p)\,\frac{\alpha^{\mathrm{out}}\, s_{\mathrm{B}}}{c_{\mathrm{A}}\, c_{\mathrm{B}}\, k_{\mathrm{B}}}\right] + \sqrt{\left[(1 - 2\,p)\,\frac{\alpha^{\mathrm{out}}\, s_{\mathrm{B}}}{c_{\mathrm{A}}\, c_{\mathrm{B}}\, k_{\mathrm{B}}}\right]^2 + 2\,\left[\frac{2\,D}{\delta^2} + \frac{\alpha^{\mathrm{out}}\, s_{\mathrm{B}}}{c_{\mathrm{A}}\, c_{\mathrm{B}}\, k_{\mathrm{B}}}\right]\,\left[k_{\mathrm{A}} - 2\,\frac{\alpha^{\mathrm{out}}\, s_{\mathrm{B}}}{c_{\mathrm{A}}\, c_{\mathrm{B}}\, k_{\mathrm{B}}}\right]}} \,. \tag{3.24}$$

For symmetric secretion, i.e. $p = 1/2$, this simplifies to:

$$\bar{\lambda}_{\mathrm{lin}} = \sqrt{\frac{\frac{D}{\delta^2} + \frac{\alpha^{\mathrm{out}}\, s_{\mathrm{B}}}{2\, c_{\mathrm{A}}\, c_{\mathrm{B}}\, k_{\mathrm{B}}}}{k_{\mathrm{A}} - \frac{2\, \alpha^{\mathrm{out}}\, s_{\mathrm{B}}}{c_{\mathrm{A}}\, c_{\mathrm{B}}\, k_{\mathrm{B}}}}} \; . \tag{3.25}$$

We term it $\bar{\lambda}_{\mathrm{lin}}$ in order to distinguish the length scale of the system in the limit of low effector concentrations from the length scale defined by the analytical approximate steady-state solution to the full system, $\bar{\lambda}$ (Eq. 3.11).

As for $\bar{\lambda}$, in the absence of positive feedback, $\alpha^{\mathrm{in}} = \alpha^{\mathrm{out}} = 0$, the length scale simplifies to $\bar{\lambda}_{\mathrm{lin}} = \sqrt{\frac{D/\delta^2}{k_{\mathrm{A}}}}$, i.e. we recover the length scale of the diffusion/degradation system. This is expected as in the absence of positive feedback, the signalling molecule part of the system simplifies to a diffusion/degradation problem. Again as for $\bar{\lambda}$, note that $\bar{\lambda}_{\mathrm{lin}}$ is only dependent on the feedback strength outside of the source region, α^{out}, while it is not influenced by the strength of the feedback inside of the source region, α^{in}.

We can show that the analytical approximate steady-state solution to the non-linear model (Eqs. 3.6, 3.7) approaches the solution obtained in this limit by formally taking the limit of $\frac{b_n}{c_{\mathrm{B}}} \to 0$ with $\alpha^{\mathrm{in/out}} = \alpha_0^{\mathrm{in/out}}\, c_{\mathrm{B}}$. Thus, in this limit the solution obtained here is the solution to the non-linear problem (see Appendix E.5 for details). Importantly, we also see that it is a good approximation to the non-linear system if the effector concentrations b_n are low compared to the threshold concentration c_{B} (Fig. 3.5).

Analysing the length scale of the system in this limit, we see that it diverges for a critical feedback strength (Fig. 3.6):

$$\alpha^{\mathrm{crit}} = \frac{k_{\mathrm{A}}\, k_{\mathrm{B}}\, c_{\mathrm{A}}\, c_{\mathrm{B}}}{2\, s_{\mathrm{B}}} \; . \tag{3.26}$$

Indeed, as we will see in Chapter 5, the system does not reach a steady state for $\alpha^{\mathrm{in/out}} \geq \alpha^{\mathrm{crit}}$ in the limit of a linear feedback response.

In order to analyse how the length scale of the relay mechanism increases with increasing feedback strength α^{out}, we rewrite the feedback strength as

$$\alpha^{\mathrm{out}} = \alpha^{\mathrm{crit}} - \delta\alpha^{\mathrm{out}} \ , \tag{3.27}$$

and analyse how the length scale behaves as a function of the *difference* from the critical feedback strength, $\delta\alpha^{\mathrm{out}}$. Note that the feedback approaches its critical value for $\delta\alpha^{\mathrm{out}} \to 0$. Re-writing the length scale as a function of $\delta\alpha^{\mathrm{out}}$, we obtain:

$$\bar{\lambda}_{\mathrm{lin}} = \sqrt{\frac{c_{\mathrm{A}}\, c_{\mathrm{B}}\, k_{\mathrm{B}}\, \left(\frac{D}{\delta^2} + \frac{1}{4} k_{\mathrm{A}}\right) - \frac{1}{2}\, s_{\mathrm{B}}\, \delta\alpha^{\mathrm{out}}}{2\, s_{\mathrm{B}}\, \delta\alpha^{\mathrm{out}}}} \ . \tag{3.28}$$

Thus, the length scale scales according to:

$$\bar{\lambda}_{\mathrm{lin}} \propto (\delta\alpha^{\mathrm{out}})^{-1/2} \tag{3.29}$$

as $\delta\alpha^{\mathrm{out}} \to \alpha^{\mathrm{crit}}$ (Fig. 3.6 B.). This divergent behaviour is not physical and is indeed not present in the full system, where the divergence is capped by the saturation of the feedback. As discussed above, the limit of a linear feedback response is only valid for effector concentrations that are low compared to the feedback threshold concentration c_{B} (Fig. 3.4). For increasing effector concentrations, the response will saturate. These increasing effector concentrations are reached for an increased feedback strength $\alpha^{\mathrm{in/out}}$, as this leads to increased signalling molecule production and thus in turn to increased effector concentrations. However, the limit of linear feedback strength discussed here uncovers an important feedback strength, α^{crit}, that also plays a special role in the full, non-linear system, as we will discuss in the next section.

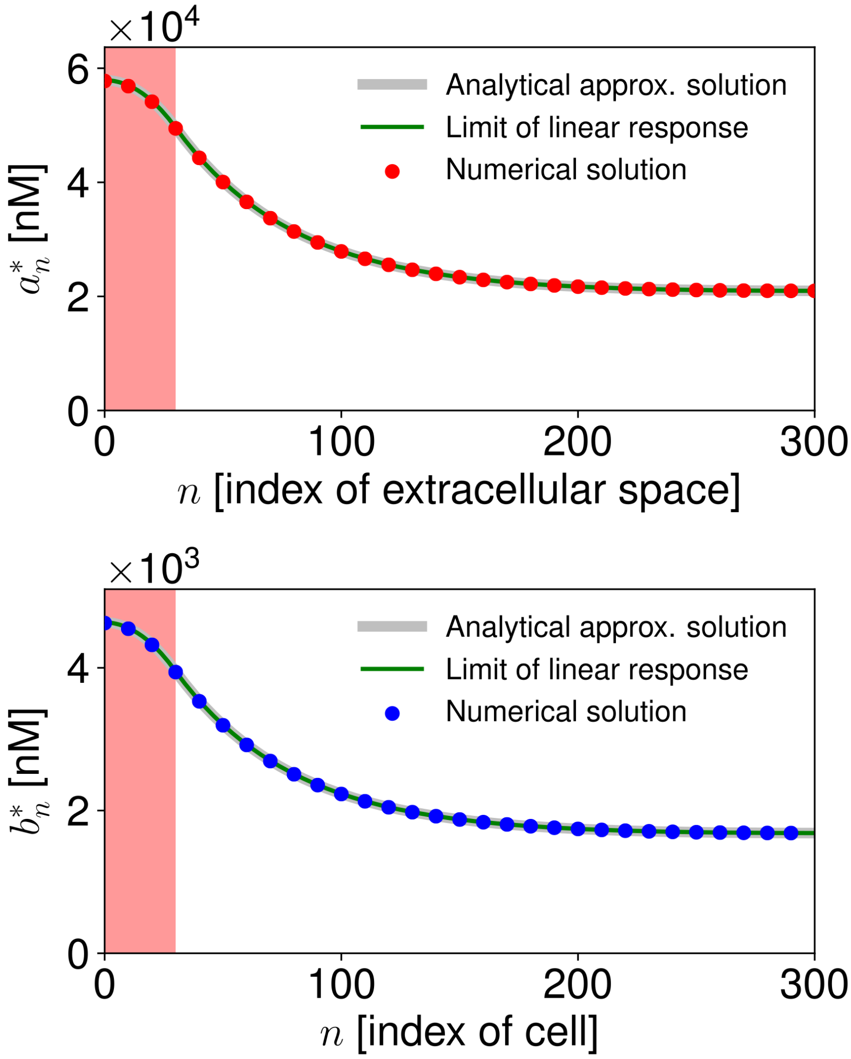

Figure 3.5.: **For large threshold concentrations c_B, the linear response limit is a good approximation.** Upper panel: signalling molecule concentration (a_n). Lower panel: effector concentration (b_n). The steady-state solution in the limit of a linear response (Eqs. 3.20, 3.21) is in good agreement with the analytical approximate steady-state solution to the full model (Eqs. 3.6, 3.7), as well as with the numerical steady-state solution (dots), if the system is in the limit of a large threshold concentration c_B, i.e. $c_\mathrm{B} \gg b_n$. Compare the maximum effector concentration b_n (lower panel) to $c_\mathrm{B} = 1.66 \times 10^8$ nM. Parameters used: $\alpha^{\mathrm{in}} = \alpha^{\mathrm{out}} = 1.245 \times 10^8$ molecules/(s V) $= 2.075 \times 10^6$ nM/s, $c_\mathrm{A} = 166$ nM, $c_\mathrm{B} = 1.66 \times 10^8$ nM, $D = 1.0\ \mu\mathrm{m}^2/\mathrm{s}$, $\delta = 10.0\ \mu\mathrm{m}$, $k_\mathrm{A} = 10^{-3}\ \mathrm{s}^{-1}$, $k_\mathrm{B} = 10^{-3}\ \mathrm{s}^{-1}$, $p = 0.5$, $s_\mathrm{A} = 20$ molecules/(s V), $s_\mathrm{B} = 4$ molecules/(s W), $N = 300$, $w = 30$, $V = \epsilon\,\delta^2 = 10^2\ \mu\mathrm{m}^3$, $W = \delta^3 = 10^3\ \mu\mathrm{m}^3$.

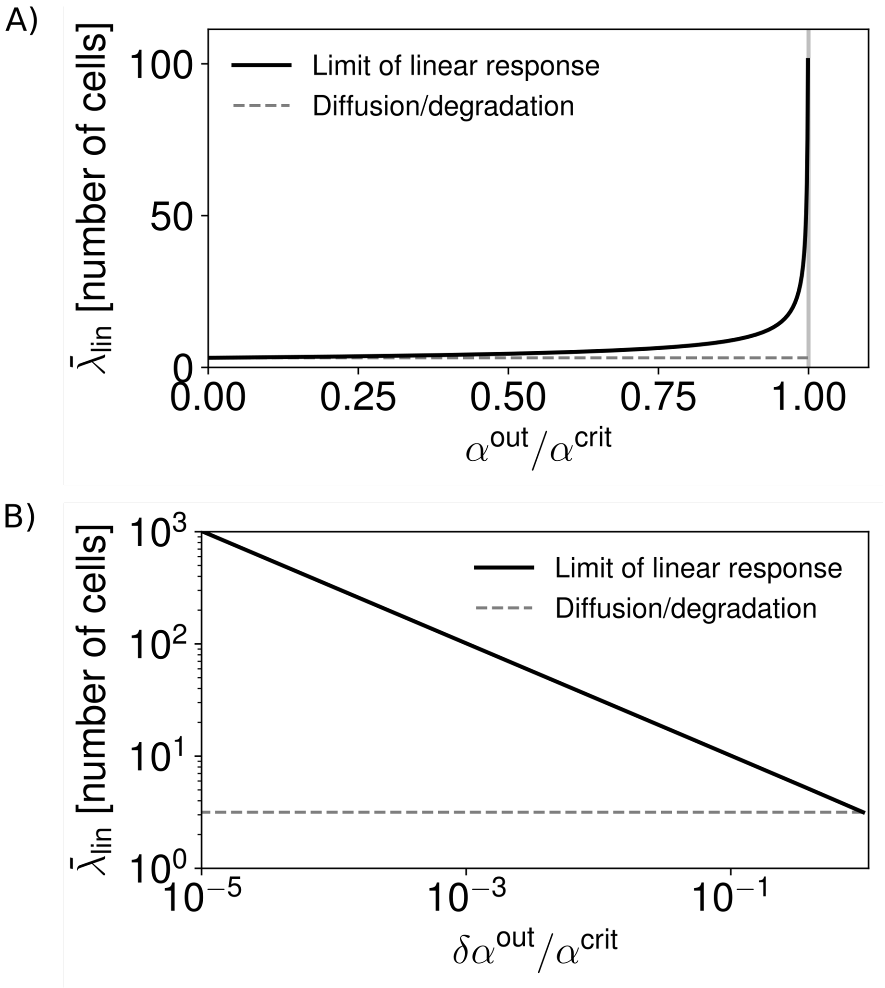

Figure 3.6.: **In the limit of a linear feedback response, the length scale diverges for a critical feedback strengths α^{crit}.** The length scale of the relay mechanisms (solid black line) is larger than that of the diffusion/degradation mechanism (dashed grey line). **A)** It diverges as $\alpha^{\text{out}} \to \alpha^{\text{crit}}$. The critical feedback strength α^{crit} is indicated by the grey vertical line. **B)** The length scale scales as $(\delta\alpha^{\text{out}})^{-1/2}$. Note that the critical feedback strength is approached for $(\delta\alpha^{\text{out}}) \to 0$, i.e. to the left of the plot. Parameters used: $c_{\text{A}} = 166$ nM, $c_{\text{B}} = 1.66 \times 10^8$ nM, $D = 1.0$ µm^2/s, $\delta = 10.0$ µm, $k_{\text{A}} = 10^{-3}$ s^{-1}, $k_{\text{B}} = 10^{-3}$ s^{-1}, $p = 0.5$, $s_{\text{A}} = 20$ molecules/(s V), $s_{\text{B}} = 4$ molecules/(s W), $N = 300$, $w = 30$, $V = \epsilon\,\delta^2 = 10^2$ µm^3, $W = \delta^3 = 10^3$ µm^3.

3.4. The effect of positive feedback on gradient length scale

In this section, we analyse the effect that positive feedback has on the length scale of the steady-state gradient in the full, non-linear system (Eqs. 2.6 - 2.8, 3.1). The positive-feedback response to effector levels is given by a Hill function (Fig. 3.4). The saturation of the feedback for effector concentrations higher than the Hill-activator threshold c_B prevents the divergence of the length scale that we found in the limit of a linear feedback response in the previous section (Fig. 3.6). Moreover, as we will discuss in Chapter 5, it also prevents the divergence of the time scale observed in the limit of a linear feedback response. Thus, steady-state solutions also exist for $\alpha^{\mathrm{in/out}} \geq \alpha^{\mathrm{crit}}$ in the full, non-linear model. However, the length scale of the full model still shows an interesting behaviour at the critical feedback strength: The length scale reaches a maximum value at the critical feedback back strength, as we observe for the length scale defined by the approximate analytical steady-state solution (Eq. 3.15), and verify using the numerical steady-state solution (Fig. 3.7). See Appendix F for how to obtain the length scale from the numerical solution.

If the feedback strength is increased beyond this critical value, the length scale of the steady-state gradient decreases. Thus, the behaviour is symmetrical around α^{crit} (Fig. 3.7). In order to analyse how the length scale changes with changes in the feedback strength, we again analyse how it scales with the *difference* from the critical feedback strength, $\delta\alpha^{\mathrm{out}}$ (Eq. 3.27). Analogous to what we found for the length scale in the limit of a linear feedback feedback response (see Eq. 3.29), we again observe:

$$\bar{\lambda} \propto (\delta\alpha^{\mathrm{out}})^{-1/2} \; . \tag{3.30}$$

However, the length scale reaches a finite maximal value at the critical feedback strength in the full, non-linear model, visible as a saturation of this scaling behaviour close to α^{crit} (Fig. 3.7 B).

Comparing the feedback mechanism to a diffusion/degradation system that our system collapses to in the absence of positive feedback, $\alpha^{\mathrm{in/out}} = 0$, we see that positive feedback increases the steady-state gradient length scale of the system

(Fig. 3.7):

$$\bar{\lambda} \geq \bar{\lambda}_{\text{Diff/Degr}} \ . \tag{3.31}$$

This increase is strongest at the critical feedback strength and decreases as the difference from the critical feedback strength, $\delta\alpha^{\text{out}}$, increases. In particular, for both, the limit of no feedback, $\alpha^{\text{out}} \to 0$, and infinitely strong feedback, $\alpha^{\text{out}} \to \infty$, the length scale approaches $\bar{\lambda}_{\text{Diff/Degr}}$. At $\alpha = 0$, there is no positive feedback, i.e. the dynamics of the signalling molecule decouple from the effector dynamics and the model collapses to a diffusion/degradation model for the signalling molecule. Therefore, in this limit, the length scale of the steady-state concentration profile of the signalling molecule is equal to that of the diffusion/degradation mechanism. Analysing how the length scale behaves in the limit of $\alpha^{\text{out}} \to \infty$, we find that it also approaches $\bar{\lambda}_{\text{Diff/Degr}}$ (see Appendix E.3 for details). This can be understood intuitively by considering that a very large feedback strength eventually leads to very high effector concentrations and thus to the feedback response saturating (see Appendix E.4 for details on the length scale in the limit of feedback saturation). In this regime, the positive feedback collapses to a constant ubiquitous source of strength α^{out}. In this case, the length scale of the steady-state profile is solely determined by the diffusion constant and the degradation rate and equal to that of the diffusion/degradation mechanism. This is because the positive feedback, reduced to a constant source, can no longer influence the length scale of the profile, just like the constant production in the source region with rate s_{A} does not influence the length scale of the profile.

Close to the critical feedback strength however ($\delta\alpha^{\text{out}} \to 0$), the length scale of the system is much larger than that of a diffusion/degradation system. This observation is based on the analytical approximate steady-state solution presented in Section 3.2 and seconded by the numerical solution to the model (Fig. 3.7).

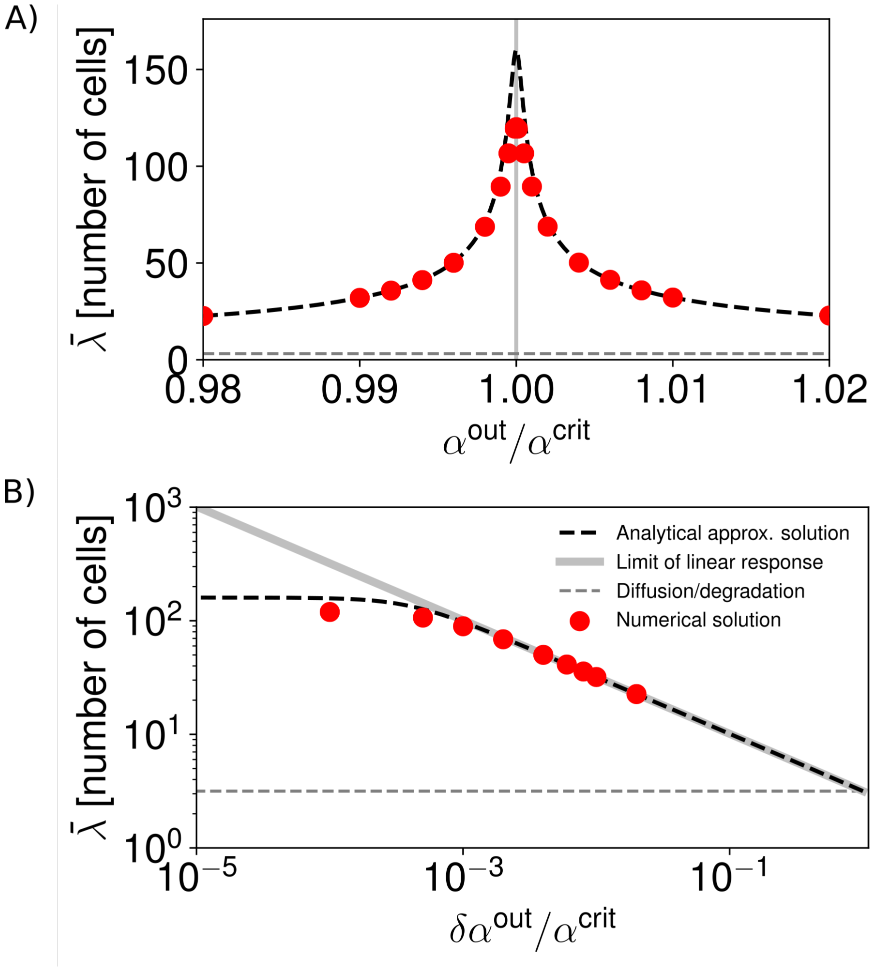

Figure 3.7.: **The length scale reaches a maximum at the critical feedback strength $\alpha^{\rm crit}$. A)** Length scale vs. feedback strength $\alpha^{\rm out}/\alpha^{\rm crit}$ based on the analytical approximate steady-state solution (dashed black line) and based on the numerical steady-state solution (red dots, see Appendix F). The critical feedback strength $\alpha^{\rm crit}$ is indicated by the vertical gray line. The length scale of the diffusion/degradation mechanism is indicated by the dashed gray line. **B)** Approaching the critical feedback strength, the length scale scales as $(\delta\alpha^{\rm out})^{-1/2}$ before it saturates very close to $\alpha^{\rm crit}$, i.e. for $(\delta\alpha^{\rm out}) \to 0$ (to the left of the plot). This saturation behaviour is not observed in the limit of a linear response (gray line). Legend in B applies to A and B. Parameters used: $c_{\rm A} = 166$ nM, $c_{\rm B} = 1.66 \times 10^8$ nM, $D = 1.0\ \mu{\rm m}^2/{\rm s}$, $\delta = 10.0\ \mu{\rm m}$, $k_{\rm A} = 10^{-3}\ {\rm s}^{-1}$, $k_{\rm B} = 10^{-3}\ {\rm s}^{-1}$, $p = 0.5$, $s_{\rm A} = 20$ molecules/(s V), $s_{\rm B} = 4$ molecules/(s W), $N = 300$, $w = 30$, $V = \epsilon\,\delta^2 = 10^2\ \mu{\rm m}^3$, $W = \delta^3 = 10^3\ \mu{\rm m}^3$.

3.5. Gradient shape

The shape of the steady-state concentration profile is not only governed by the length scale of the profile. It is also important to analyse over which concentration difference the profile decreases. This can be analysed by investigating the ratio of the constant steady-state solutions $a_\mathrm{c}^\mathrm{in}/a_\mathrm{c}^\mathrm{out}$ (Fig. 3.8). In principle, the profile can not only decrease or be flat - it can even increase. A quantity that can discriminate between these three possible profile shapes is the ratio $a_\mathrm{c}^\mathrm{in}/a_\mathrm{c}^\mathrm{out}$. It measures firstly, whether the gradient decreases or increases ($a_\mathrm{c}^\mathrm{in}/a_\mathrm{c}^\mathrm{out} >$ or < 1) and secondly, whether the profile changes over considerably different values of concentration $|a_\mathrm{c}^\mathrm{in}/a_\mathrm{c}^\mathrm{out} - 1| > 0$). We are particularly interested in decreasing long-ranged signalling gradients, i.e. $a_\mathrm{c}^\mathrm{in}/a_\mathrm{c}^\mathrm{out} > 1$. However, a long-ranged gradient can only be biologically relevant if there is an appreciable concentration difference over which the gradient decays. In other words, it is not helpful to generate a profile that has a very large length length scale but is essentially homogeneous in space, i.e. a flat line.

We use $a_\mathrm{c}^\mathrm{in}/a_\mathrm{c}^\mathrm{out} = 1$ as a discrimination between decreasing and increasing profile shape. This way, we find a threshold value $\alpha_\mathrm{T}^\mathrm{out}$ as a function of α^in (Eq. 3.32) for which profile shape changes:

$$\alpha_\mathrm{T}^\mathrm{out} = \frac{1}{2s_\mathrm{B}(c_\mathrm{A}k_\mathrm{A} + 2s_\mathrm{A})}\left[c_\mathrm{A}k_\mathrm{A}(c_\mathrm{B}k_\mathrm{B}s_\mathrm{A} + s_\mathrm{B}(2\alpha^\mathrm{in} + s_\mathrm{A})) + s_\mathrm{A}\,s_\mathrm{B}\left(2\alpha^\mathrm{in} + 2s_\mathrm{A} + k_\mathrm{A}\sqrt{\frac{c_\mathrm{A}^2(c_\mathrm{B}\,k_\mathrm{B} + s_\mathrm{B})^2}{s_\mathrm{B}^2} + \frac{4c_\mathrm{A}(c_\mathrm{B}k_\mathrm{B}(s_\mathrm{A} - \alpha^\mathrm{in}) + s_\mathrm{B}(\alpha^\mathrm{in} + s_\mathrm{A}))}{k_\mathrm{A}s_\mathrm{B}} + \frac{4(\alpha^\mathrm{in} + s_\mathrm{A})^2}{k_\mathrm{A}^2}}\right)\right]. \tag{3.32}$$

In particular, we obtain flat profiles for $\alpha^\mathrm{out} = \alpha_\mathrm{T}^\mathrm{out}$, decreasing profiles for $\alpha^\mathrm{out} < \alpha_\mathrm{T}^\mathrm{out}$, and increasing profiles for $\alpha^\mathrm{out} > \alpha_\mathrm{T}^\mathrm{out}$ (Fig. 3.9).

By analysing the limit of no signalling-independent production in the local source ($s_\mathrm{A} \to 0$), we find that for low production rates s_A in the local source, α^out must be smaller than α^in in order to obtain a decreasing profile. For large signalling-independent production rates in the local source ($s_\mathrm{A} \to \infty$), we find

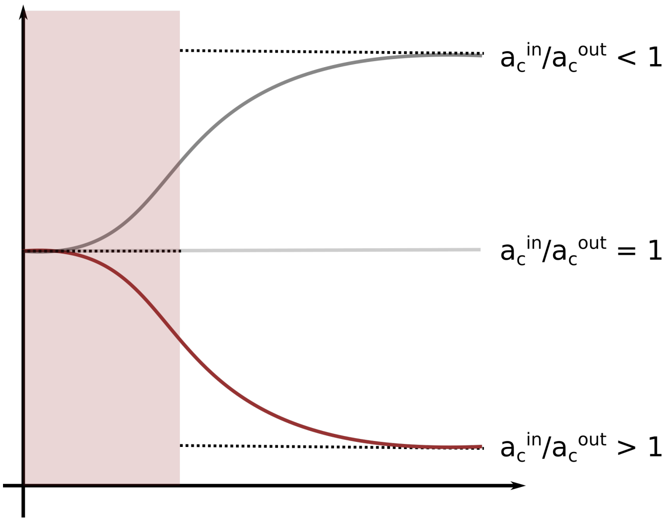

Figure 3.8.: **Possible steady-state profile shapes.** The steady-state concentration profile can have qualitatively different shapes. In particular, we distinguish a decreasing profile (red line, $a_{\mathrm{c}}^{\mathrm{in}} > a_{\mathrm{c}}^{\mathrm{out}}$), a flat profile (grey line, $a_{\mathrm{c}}^{\mathrm{in}} = a_{\mathrm{c}}^{\mathrm{out}}$), and an increasing profile (dark gray line, $a_{\mathrm{c}}^{\mathrm{in}} < a_{\mathrm{c}}^{\mathrm{out}}$). Source region shaded in red. Dotted lines mark the values of $a_{\mathrm{c}}^{\mathrm{in}}$ and $a_{\mathrm{c}}^{\mathrm{out}}$.

that the profile always decreases, i.e. the threshold for profile shape change diverges ($\alpha_{\mathrm{T}}^{\mathrm{out}} \to \infty$, see Appendix E.6 for details). Thus, the strength of the signalling-independent production in the local source with rate s_{A} has a large influence on profile shape. Fig. 3.10 shows how the position of the separatrix changes in phase space dependent on the strength of the local source. For a strong signalling-independent production in the local source ($\widetilde{s}_{\mathrm{A}} = 1000$ molecules per cell per second), the steady-state profile decreases even if $\alpha^{\mathrm{out}} > \alpha^{\mathrm{in}}$. In contrast, for a weak signalling-independent production in the local source ($\widetilde{s}_{\mathrm{A}} = 4$ molecules per cell per second), increasing profiles can be obtained in case of a strong neighbour-dependent production outside of the source region compared to inside of it ($\alpha^{\mathrm{out}} > \alpha^{\mathrm{in}}$).

We find that both $a_{\mathrm{c}}^{\mathrm{in}}$ and $a_{\mathrm{c}}^{\mathrm{out}}$ increase with increasing feedback strength (Fig. 3.11, left panels). We saw in Section 3.4, that the steady-state profile reaches its maximum length scale for $\alpha^{\mathrm{in/out}} = \alpha^{\mathrm{crit}}$. Therefore, we analyse the behaviour of the piece-wise constant steady-state solution in the vicinity of α^{crit}. Close to the critical feedback strength, we observe scaling with the inverse of the difference from the critical feedback strength (Fig. 3.11):

$$a_{\mathrm{c}}^{\mathrm{in}} \propto (\delta\alpha^{\mathrm{in}})^{-1} \; , \tag{3.33}$$

$$a_{\mathrm{c}}^{\mathrm{out}} \propto (\delta\alpha^{\mathrm{out}})^{-1} \; . \tag{3.34}$$

We can understand this scaling behaviour in the limit of a linear feedback response. To this end, we re-write the piece-wise constant steady-state solution in this limit (Eqs. 3.22, 3.23) as a function of the *difference* from the cirical feedback strength:

$$a_{\mathrm{c,\,lin}}^{\mathrm{in}} = \frac{c_{\mathrm{A}}}{2\,s_{\mathrm{B}}}\,\frac{c_{\mathrm{B}}\,k_{\mathrm{B}}\left(s_{\mathrm{A}} + \frac{1}{2}\,c_{\mathrm{A}}\,k_{\mathrm{A}}\right) - s_{\mathrm{B}}\,\delta\alpha^{\mathrm{in}}}{\delta\alpha^{\mathrm{in}}} \; , \tag{3.35}$$

$$a_{\mathrm{c,\,lin}}^{\mathrm{out}} = \frac{c_{\mathrm{A}}}{2\,s_{\mathrm{B}}}\,\frac{\frac{1}{2}\,c_{\mathrm{A}}\,c_{\mathrm{B}}\,k_{\mathrm{A}}\,k_{\mathrm{B}} - s_{\mathrm{B}}\,\delta\alpha^{\mathrm{out}}}{\delta\alpha^{\mathrm{out}}} \; . \tag{3.36}$$

Note that, as for the length scale, we observe a divergence of the piece-wise constant steady-state solution as $\delta\alpha^{\mathrm{out}} \to 0$ in the limit of a linear feedback response. This divergence is again capped by the saturation of the feedback response in the full, non-linear model (Fig. 3.11). However, the scaling relationship of the piece-wise constant steady-state solution with $\delta\alpha^{\mathrm{in}}$ and $\delta\alpha^{\mathrm{out}}$ inside the source region and outside of it, respectively is conserved in the full, non-linear model close to the critical feedback strength (Fig. 3.11).

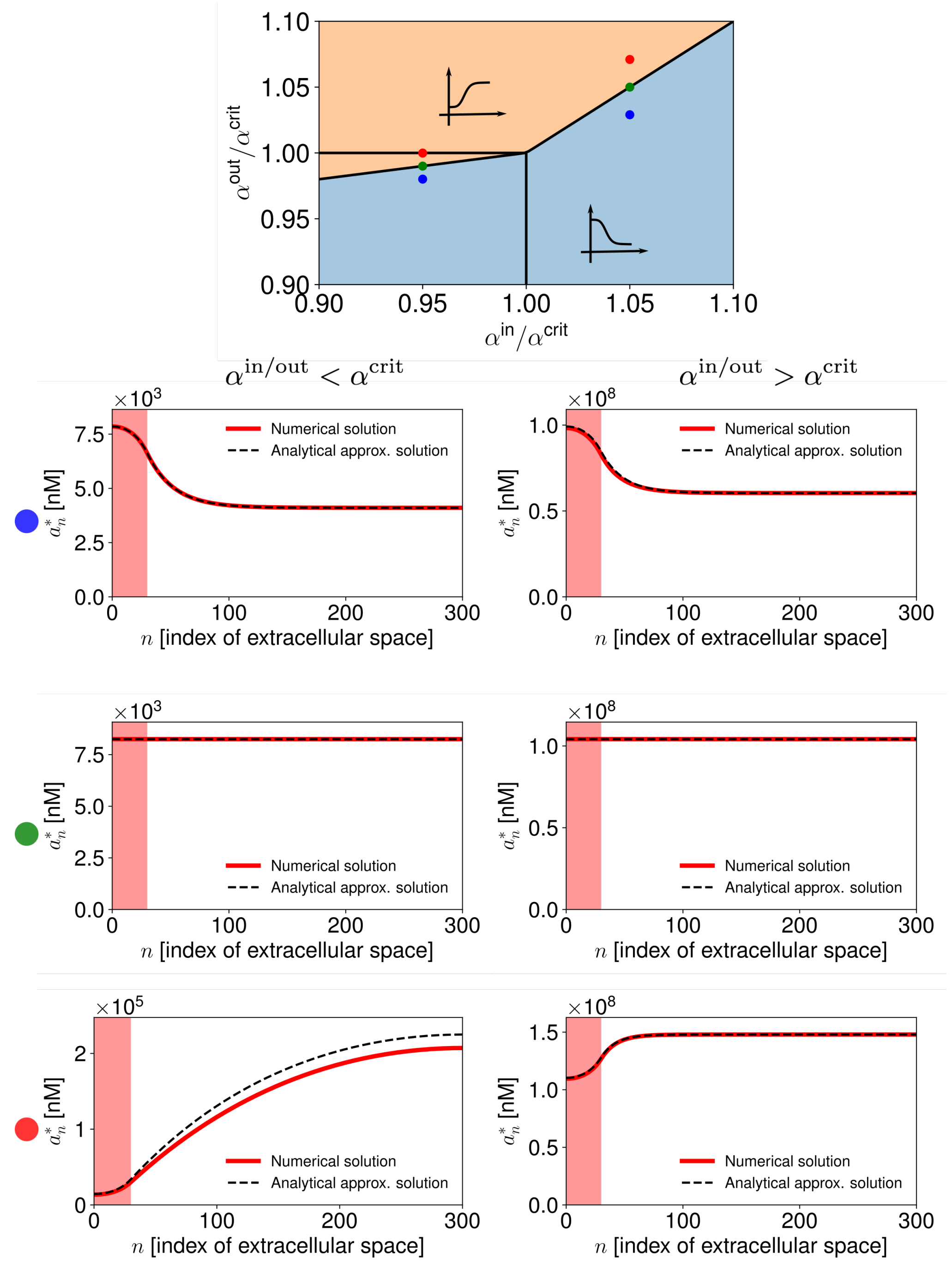

Figure 3.9.: **Gradient shape varies qualitatively dependent on the ratio $a_{\mathbf{c}}^{\mathbf{in}}/a_{\mathbf{c}}^{\mathbf{out}}$** Upper panel: Shapes of the steady-state profiles in phase space. Separatrix (black line) discriminates between decreasing and increasing profiles. Horizontal and vertical black lines indicate α^{crit}. Lower panels: Example steady-state profiles for the signalling molecule concentration (a_n^*) at indicated position in phase-space. Parameters as in Fig. 3.5.

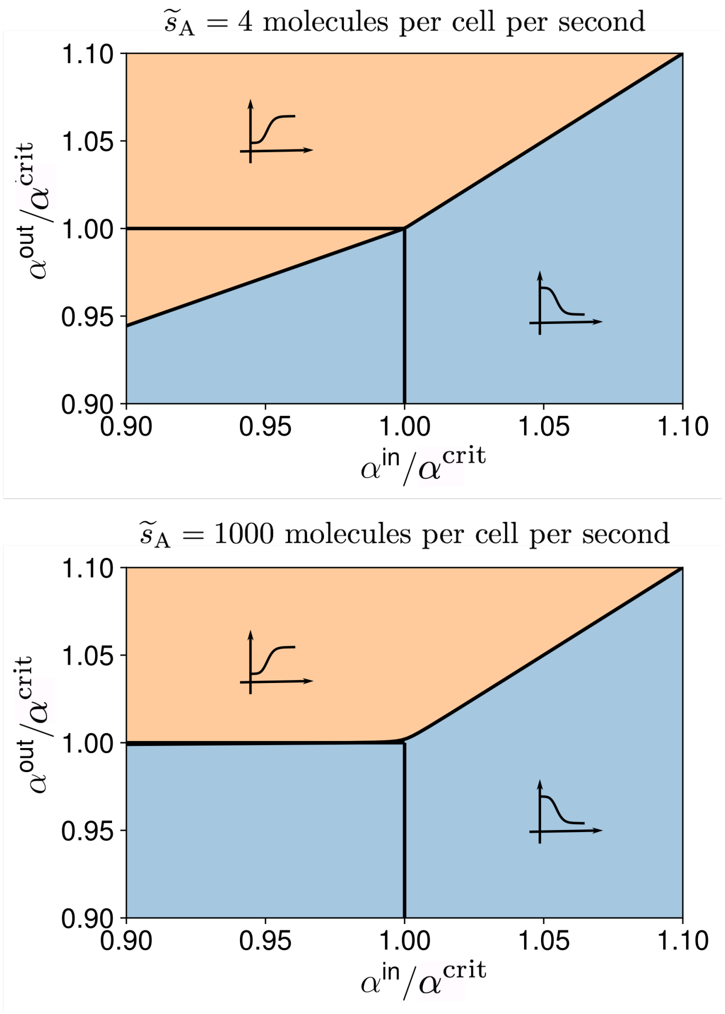

$\widetilde{s}_\mathrm{A} = 4$ molecules per cell per second

$\widetilde{s}_\mathrm{A} = 1000$ molecules per cell per second

Figure 3.10.: **The strength of the local source influences gradient shape.** The position of the separatrix at which $a_\mathrm{c}^{\mathrm{in}}/a_\mathrm{c}^{\mathrm{out}} = 1$ and the shape of the gradient changes (Eq. 3.32, black line) depends on the strength of the local source s_A. Horizontal and vertical black lines indicate α^{crit}. Parameters used: $c_\mathrm{A} = 166$ nM, $c_\mathrm{B} = 1.66 \times 10^8$ nM, $D = 1.0\ \mathrm{\mu m^2/s}$, $\delta = 10.0\ \mathrm{\mu m}$, $k_\mathrm{A} = 10^{-3}\ \mathrm{s}^{-1}$, $k_\mathrm{B} = 10^{-3}\ \mathrm{s}^{-1}$, $p = 0.5$, $s_\mathrm{A} = 20$ molecules/(s V), $s_\mathrm{B} = 4$ molecules/(s W), $N = 300$, $w = 30$, $V = \epsilon\,\delta^2 = 10^2\ \mathrm{\mu m^3}$, $W = \delta^3 = 10^3\ \mathrm{\mu m^3}$.

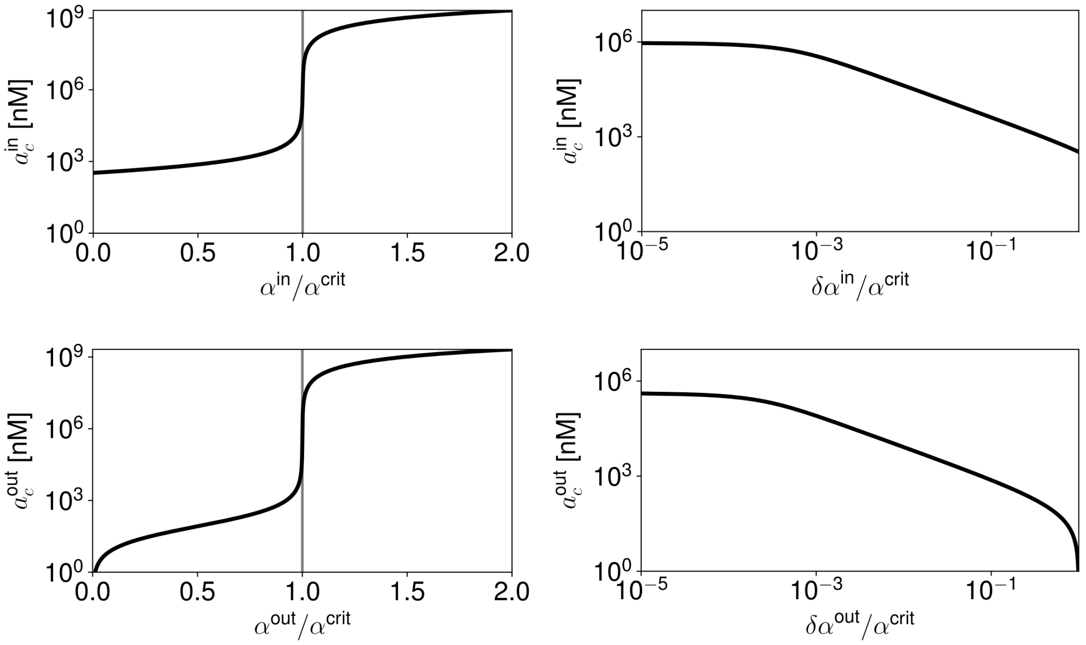

Figure 3.11.: **Piece-wise constant steady-state solution increases for increasing neighbour-dependent production rate.** The piece-wise constant steady-state solution increases as the neighbour-dependent production rate increases. The increase is more pronounced in the vicinity of α^{crit} (grey line) (left panels). Close to the critical feedback strength, $a_{\mathrm{c}}^{\mathrm{in}}$ and $a_{\mathrm{c}}^{\mathrm{out}}$ scale as $a_{\mathrm{c}}^{\mathrm{in}} \propto (\delta\alpha^{\mathrm{in}})^{-1}$ and $a_{\mathrm{c}}^{\mathrm{out}} \propto (\delta\alpha^{\mathrm{out}})^{-1}$, respectively (right panels). Parameters used: $c_{\mathrm{A}} = 166$ nM, $c_{\mathrm{B}} = 1.66 \times 10^8$ nM, $D = 1.0$ µm^2/s, $\delta = 10.0$ µm, $k_{\mathrm{A}} = 10^{-3}$ s^{-1}, $k_{\mathrm{B}} = 10^{-3}$ s^{-1}, $p = 0.5$, $s_{\mathrm{A}} = 20$ molecules/(s V), $s_{\mathrm{B}} = 4$ molecules/(s W), $N = 300$, $w = 30$, $V = \epsilon\,\delta^2 = 10^2$ µm^3, $W = \delta^3 = 10^3$ µm^3.

3.6. Summary and discussion

In this chapter, we showed that the relay mechanism increases the length scale of the steady-state gradient compared to the diffusion/degradation mechanism (Eq. 3.31, Fig. 3.7). The increase is dependent on the feedback strength outside of the source region, α^{out}. It is particularly pronounced in the vicinity of the critical feedback strength α^{crit}. This critical feedback strength is defined in the limit of a linear feedback response that is valid for effector concentrations which are low compared to the Hill-activator threshold concentration c_{B}. In this limit, the length scale diverges as the feedback strength becomes critical, $\alpha^{\text{out}} \to \alpha^{\text{crit}}$. This divergence is not present in the full, non-linear model, due to the saturation behaviour of the feedback response. However, the critical feedback strength still has an interesting effect on the full system: The system reaches a maximal length scale at the critical feedback strength (Fig. 3.7). This is a signature of the divergence of the linear response in the full system, that is capped by the saturation of the feedback response. Such saturation behaviour is characteristic of biological processes. Analysing how the length scale changes with feedback strength, we find that it scales as $\bar{\lambda} \propto (\delta\alpha^{\text{out}})^{-1/2}$ (Eq. 3.30) until it saturates close to the critical feedback strength where it reaches its maximum (Fig. 3.7).

The shape of the steady-state profile is not only governed by the length scale but also by the concentration difference over which it decays. This is captured by the ratio of the constant values the profile approaches inside and outside of the source region far away from the boundaries, i.e. $a_{\text{c}}^{\text{in}}/a_{\text{c}}^{\text{out}}$. This ratio discriminates decreasing, increasing, and flat profiles (Fig. 3.8). We find that the shape of the steady-state gradient depends on the overall production strength inside of the source region compared to outside of it. That is, the profile is highest in the region in which most molecules are produced. For a diffusion/degradation mechanism this clearly is the source region, since this is the only region in which molecules are produced. The positive feedback turns all cells of the system into producing cells. It is thus the difference between overall production in the source region, i.e. the constant production with rate s_{A} and the signalling-level-dependent production with strength α^{in}, compared to the signalling-level-dependent production outside of the source region with strength α^{out} that dictates the shape of steady-state gradients. We distinguish between three classes of profiles: decreasing profiles, in which the concentration of signalling molecules decreases with increasing distance from the local source; increasing profiles in which the concentration of signalling molecules increases with increasing distance from the local source; and flat profiles that do not show any spatial variation in signalling molecule concentration across the system. We find that if the feedback in the source region is stronger than outside of it, the profiles always decay. For a larger feedback strength outside of the source region compared to inside of it, profile shape depends on the strength of the signalling-level-independent production in the local source with rate s_A (Fig. 3.10). For large values of s_A, the shape still decreases even if the feedback is stronger outside of the source region compared to inside of it (Fig. 3.10). However, if s_A is small compared to the feedback strength, it is possible to obtain steady-state profiles increasing away from the local source, in case of stronger positive feedback outside of the source region compared to inside the source region (Fig. 3.9).

When observing a signalling gradient in a biological experiment, we intuitively assume that the source will be located where the profile is highest. In this chapter, we showed that with the relay mechanism it is possible to have profiles increasing away from the local source due to an increased positive feedback strength outside of the source region compared to inside the source region (Fig. 3.9). We are not aware of an example of such a situation in a biological context, but it is an interesting possibility to consider when observing signalling gradients.

For the system that the relay mechanism developed in this work is inspired by, planarian flatworms, we are confident that the profile we observe has its maximum inside the constant source region. The worms show a β-catenin concentration profile decaying from the tail tip anteriorly ([98, 99], Fig. 1.15). At the tail tip, a stripe of pole cells expresses *Wnt1* ([78, 43], Fig. 1.14) in a Wnt-signalling-independent manner [98]. We liken Wnt1 production in these cells to the local constant source in our model. Preliminary data suggests that *Wnt1* RNAi lowers the β-catenin levels at the tail tip compared to control (data not shown). This observation fits our hypothesis that the *Wnt1* expressing pole cells act as a local source in β-catenin gradient formation. Thus, the position of the maximum of the gradient is in the local source.

In this chapter we showed that the relay mechanism can explain the formation of long-ranged signalling gradients (Fig. 3.7) and thus meets the first challenge flatworms set for patterning mechanisms (Fig. 1.13). In the next chapter, we will analyse how the feedback strength can be used to scale the gradient to varying system sizes and thus meet the second patterning challenge set by the worms.

4. Scaling of signalling gradients using the relay mechanism

4.1. Scaling is required for all patterning problems

How to scale to the size of the structure to be organised poses a fundamental problem to every patterning mechanism. In biological contexts, patterning is most prominently required during development and regeneration. Both of these scenarios are characterised by growth, i.e. changes in size, as well as differences between individuals. Thus, in both contexts, patterning mechanisms are required to scale with system size. Indeed, signalling gradients have been observed to scale to tissue size [12, 111]. Inspired by these observations, pattern scaling has also been studied theoretically ([11, 12, 30, 113], see Section 1.5).

Planarian flatworms dynamically grow and shrink over 1.5 orders of magnitude while constantly turning over all cells in their body [102], see Section 1.4. Thus, their patterning systems have to constantly adapt to changes in body size at an adult length scale. Therefore, they combine the challenges of large-scale pattern formation and pattern scaling (Fig. 1.13). In Chapter 3, we discussed that the challenge of long-ranged pattern formation is met by the relay mechanism. In this chapter we investigate its ability to scale with system size.

4.2. Pattern scaling by adjusting feedback strength

A pattern scales if its length scale is proportional to the size of the tissue to be organised ([111, 110, 112], Eq. 1.13, see Section 1.5). In Chapter 3 we discussed

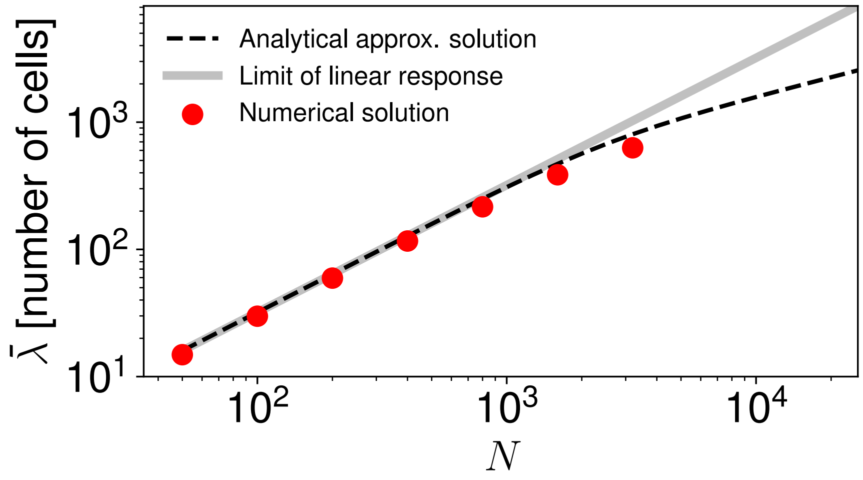

Figure 4.1.: **The length scale of the steady-state profiles scales with system size.** If $\delta\alpha^{\mathrm{out}}$ adapts to system size according to Eq. 4.1, the length scale of the steady-state profile scales with system size. Parameters used: $\alpha^{\mathrm{in}} = \alpha^{\mathrm{out}} = \alpha^{\mathrm{crit}} - \delta\alpha^{\mathrm{out}}$, $c_{\mathrm{B}} = 1.66 \times 10^6$ nM, $D = 1.0\ \mu\mathrm{m}^2/\mathrm{s}$, $\delta = 10.0\ \mu\mathrm{m}$, $k_{\mathrm{A}} = 10^{-3}\ \mathrm{s}^{-1}$, $k_{\mathrm{B}} = 10^{-3}\ \mathrm{s}^{-1}$, $p = 0.5$, $V = 10^2\ \mu\mathrm{m}^3$, $W = 10^3\ \mu\mathrm{m}^3$. Size-dependent parameters: scaling factor: $\eta = N/100$, $w = 10 \times \eta$, $\delta\alpha^{\mathrm{out}} = 0.01\alpha^{\mathrm{crit}} \times \eta^{-2}$, $s_{\mathrm{A}} = 2$ molecules/(s V) $\times\, \eta^{-2}$, $s_{\mathrm{B}} = 0.04$ molecules/(s W) $\times\, \eta^{-2}$, $c_{\mathrm{A}} = 1.66$ nM $\times \eta^{-2}$.

that in the relay mechanism, the length scale of the steady-steady-state gradient scales as $\bar{\lambda} \propto (\delta\alpha^{\mathrm{out}})^{-1/2}$ (Eq. 3.30, Fig. 3.7). Thus, if $\delta\alpha^{\mathrm{out}}$ is adjusted to system size, the scaling relationship between $\delta\alpha^{\mathrm{out}}$ and $\bar{\lambda}$ (Eq. 3.30) gives rise to scaling of the length scale with system size. In particular, if $\delta\alpha^{\mathrm{out}}$ adapts to system size according to:

$$\delta\alpha^{\mathrm{out}} \propto N^{-2} \tag{4.1}$$

this results in $\bar{\lambda} \propto N$ (Eq. 1.13, see Section 1.5) and thus profile scaling with system size. That is, profile scaling is achieved if $\delta\alpha^{\mathrm{out}}$ shrinks by a factor of 1/4 in response to a doubling in system size. This scaling behaviour of $\delta\alpha^{\mathrm{out}}$ with system size leads to scaling of the length scale of the steady-state profiles with system size across around two orders of magnitude, see Fig. 4.1.

Beyond this, the feedback mechanism starts to saturate as discussed in Chapter 3. As it saturates, the length scale no longer scales with $\delta\alpha^{\mathrm{out}}$ (see Fig. 3.7). Thus, the length scale cannot be scaled to system size by adjusting $\delta\alpha^{\mathrm{out}}$ to system size when the mechanism reaches saturation. This is due to the fact that the length scale reaches a maximal value at the critical feedback strength, i.e. for $\delta\alpha^{\mathrm{out}} = 0$, see Fig. 3.7. The fact that the scaling saturates as the feedback strength approaches its critical value is a general property of the relay mechanism, as discussed in Chapter 3. The value of the length scale at which the scaling saturates depends on the choice of model parameters. In particular, the value of the Hill-activation threshold c_{B} compared to effector concentrations b_n determines how well the full model is approximated by the limit of a linear feedback response. In this limit, the length scale scales perfectly with $\delta\alpha^{\mathrm{out}}$ (Fig. 3.6 B) and thus with system size if $\delta\alpha^{\mathrm{out}}$ adapts to system size according to Eq. 4.1, see Fig. 4.1. Thus, a high Hill-activation threshold compared to effector levels ensures close to linear behaviour of the full model and thus extended scaling of the length scale with $\delta\alpha^{\mathrm{out}}$.

As discussed in Chapter 3, not only the length scale, but also $a_{\mathrm{c}}^{\mathrm{out}}$, the concentration reached far away from the local source, is dependent on $\delta\alpha^{\mathrm{out}}$ (see Eq. 3.34). In particular, it scales as $a_{\mathrm{c}}^{\mathrm{out}} \propto (\delta\alpha^{\mathrm{out}})^{-1}$ (Eq. 3.34). Thus, if $\delta\alpha^{\mathrm{out}}$ were indeed regulated by the system such that $\delta\alpha^{\mathrm{out}} \propto N^{-2}$ (Eq. 4.1) to achieve gradient scaling, $a_{\mathrm{c}}^{\mathrm{out}}$ would scale with system size according to $a_{\mathrm{c}}^{\mathrm{out}} \propto N^2$. That is, the steady-state concentrations would increase with increasing system size.

However, this is not consistent with observations in the flatworm: Gradients in differently sized-worms have been found to decay to an approximately constant, non-zero value; yet they exhibit shape scaling when corrected for this constant offset (Hanh Vu, James Cleland, personal communication). This offset corresponds to a_N^* in our model. Motivated by the observed constant offset in the worms, we analysed how a_N^* can be kept constant while the length scale scales with system size by scaling $\delta\alpha^{\mathrm{out}}$ according to $\delta\alpha^{\mathrm{out}} \propto N^{-2}$ (Eq. 4.1).

The offset in our model, a_N^*, corresponds to $a_{\mathrm{c}}^{\mathrm{out}}$, in the sense that $a_N^* \to a_{\mathrm{c}}^{\mathrm{out}}$ for large system sizes ($N \gg \bar{\lambda}$). Thus, we postulate that the system regulates $\delta\alpha^{\mathrm{out}}$ such that $\delta\alpha^{\mathrm{out}} \propto N^{-2}$ to achieve gradient scaling, and ask which other parameters the system has to scale in response to changing system size in order to keep $a_{\mathrm{c}}^{\mathrm{out}}$ approximately constant across different system sizes. We lead this discussion guided by the expression for $a_\mathrm{c}^\mathrm{out}$ obtained in the limit of a linear feedback response (Eq. 3.23) and subsequently confront our results with the numerical solution of the full, non-linear system.

In order to achieve gradient scaling by scaling $\delta\alpha^\mathrm{out}$ as discussed above (Eq. 4.1), the system regulates how far away the feedback strength is from the critical one dependent on system size. Therefore, when scaling other parameters in addition to $\delta\alpha^\mathrm{out}$ in order to keep $a_\mathrm{c}^\mathrm{out}$ approximately constant, the system has to do that in a way that does not change α^crit (Eq. 3.26). Based on Eq. 3.36, that we repeat below for convenience, we see that if c_A and s_B go to zero the same way that $\delta\alpha^\mathrm{out}$ goes to zero, $a_\mathrm{c}^\mathrm{out}$ stays approximately constant as $\delta\alpha^\mathrm{out} \to 0$:

$$a_\mathrm{c,\,lin}^\mathrm{out} = \frac{c_\mathrm{A}}{2\,s_\mathrm{B}} \, \frac{\frac{1}{2}\,c_\mathrm{A}\,c_\mathrm{B}\,k_\mathrm{A}\,k_\mathrm{B} - s_\mathrm{B}\,\delta\alpha^\mathrm{out}}{\delta\alpha^\mathrm{out}} \; .$$

Re-scaling c_A and s_B by the same factor does not change the critical feedback strength, as $\alpha^\mathrm{crit} \propto c_\mathrm{A}/s_\mathrm{B}$ (Eq. 3.26). Therefore, when c_A and s_B scale with system size the same way as $\delta\alpha^\mathrm{out}$ does, i.e. $c_\mathrm{A} \propto N^{-2}$, $s_\mathrm{B} \propto N^{-2}$, the profiles decay to an approximately constant value, while the length scale scales with system size, see Fig. 4.2. We also assume re-scaling of s_A according to $s_\mathrm{A} \propto N^{-2}$. This way, the value the profiles start from also approximately scales with system size (taking a_c^in, Eq. 3.35, as a proxy for a_0^*).

In Fig. 4.2 A, we show that the scaling behaviour of a_N^* postulated here based on $a_\mathrm{c}^\mathrm{out}$ in the limit of a linear feedback response is approximately valid for the full, non-linear system[1]. Note, however, that neither a_N^* nor a_0^* remain exactly constant even after re-scaling additional parameters with system size. This is firstly due to the fact that even in the limit of a linear feedback response, the scaling is approximate. You can see this by looking at the equations for a_c^in and $a_\mathrm{c}^\mathrm{out}$ in the limit of linear feedback response (Eqs. 3.36, 3.35) and considering the simultaneous re-scaling of $\delta\alpha^\mathrm{out}$, c_A, s_A, and s_B as suggested. You also observe that in the linear feedback response, the scaling becomes increasingly perfect as $\delta\alpha^\mathrm{out} \to 0$. In contrast, in the non-linear model the scaling behaviour of $a_\mathrm{c}^\mathrm{out}$

---

[1] We chose a high Hill-activation threshold c_B compared to effector concentration b_n to ensure that the system behaves close to linearly for a wide range for feedback strengths. The non-linear saturation behaviour still caps the divergence, see Chapter 3.

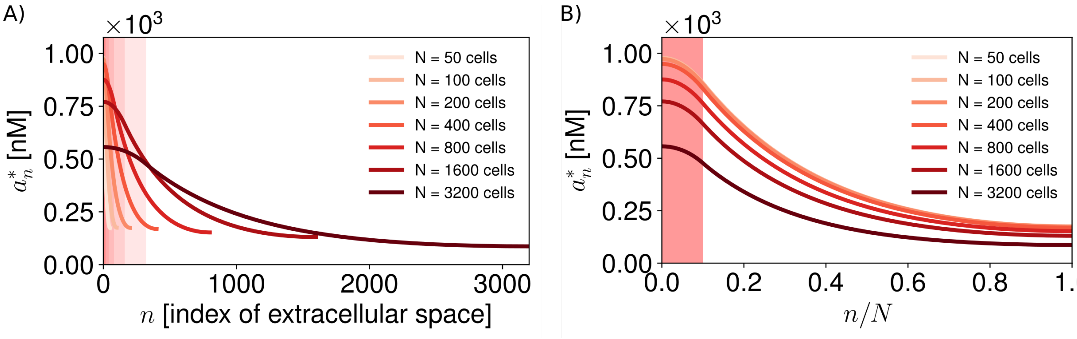

Figure 4.2.: **The steady-state profiles scale with system size. A)** Steady-state profiles for different system sizes N. **B)** Steady-state profiles shown in A) in relative spatial coordinates n/N. Profiles correspond to red dots in Fig. 4.1. Parameters used: $\alpha^{\text{in}} = \alpha^{\text{out}} = \alpha^{\text{crit}} - \delta\alpha^{\text{out}}$, $c_{\text{B}} = 1.66 \times 10^6$ nM, $D = 1.0$ µm^2/s, $\delta = 10.0$ µm, $k_{\text{A}} = 10^{-3}$ s^{-1}, $k_{\text{B}} = 10^{-3}$ s^{-1}, $p = 0.5$, $V = 10^2$ µm^3, $W = 10^3$ µm^3. Size-dependent parameters: scaling factor: $\eta = N/100$, $w = 10 \times \eta$, $\delta\alpha^{\text{out}} = 0.01\alpha^{\text{crit}} \times \eta^{-2}$, $s_{\text{A}} = 2$ molecules/(s V) $\times\, \eta^{-2}$, $s_{\text{B}} = 0.04$ molecules/(s W) $\times\, \eta^{-2}$, $c_{\text{A}} = 1.66$ nM $\times \eta^{-2}$.

with $\delta\alpha^{\text{out}}$, as well as that of a_{c}^{in} with $\delta\alpha^{\text{in}}$, saturates close to $\delta\alpha^{\text{out}} = 0$, and $\delta\alpha^{\text{in}} = 0$, respectively, i.e. close to α^{crit}, see Fig. 3.11. Thus, the re-scaling of parameters to obtain a constant $a_{\text{c}}^{\text{out}}$ and thus a_N^*, and a constant a_{c}^{in} and thus a_0^* across different system sizes is expected to become less accurate for larger system sizes where $\delta\alpha^{\text{out}}$ is smaller. This is indeed what we observe: Compare a_N^* and a_0^* between steady-state profiles of largest system sizes to those of smaller system sizes in Fig. 4.2.

The profiles are very similar when plotted with respect to relative spatial coordinates n/N, see Fig. 4.2 B. In order to analyse the shape of the profiles, we plot relative concentration profiles with respect to relative spatial coordinates, see Section 1.5. In case of scaling, this leads to collapse on a master curve, see Section 1.5. Adapted to the discrete systems we discuss in this thesis, the definition of the profile shape that is conserved between differently-sized tissues in case of scaling [112] is given as:

$$a_n(N) = A(N) \cdot \mathcal{Z}(n/N) \ , \tag{4.2}$$

where n denotes the index of the extracellular space and N denotes the total number of cells in the system. $A(N)$ is the amplitude of the system that can be dependent on the system size N and $\mathcal{Z}(n/N)$ describes the conserved shape of the profiles dependent on the relative spatial coordinate n/N ([111, 110, 112], see Section 1.5, Eq. 1.12).

As discussed above, the steady-state profiles generated by the relay mechanism decay to a constant, non-zero value. In order to analyse profile shape, we subtract this constant offset $(a_n^* - a_N^*)$ before analysing profile shape. This way we can analyse whether the shape of the profile above this constant offset scales. Indeed, we find that the shape of the profiles above the offset exhibits close-to-perfect scaling over around two orders of magnitude of system sizes, see Fig. 4.3. Note that again, the profile of the largest system size (dark red line in Fig. 4.3) shows a sightly smaller relative length scale compared to the other system sizes. This is due to the fact that $\delta\alpha^{\mathrm{out}}$, which is regulated with system size to achieve scaling (Eq. 4.1) gets closer and closer to zero with increasing system size. Since the scaling behaviour of $\bar{\lambda}$ with $\delta\alpha^{\mathrm{out}}$ saturates as $\delta\alpha^{\mathrm{out}} \to 0$ (see Fig. 3.7), the length scale of the system does not scale perfectly with system size when $\delta\alpha^{\mathrm{out}}$ adapts to system size according to Eq. 4.1, see Fig. 4.2. The larger the system gets, and thus the closer $\delta\alpha^{\mathrm{out}}$ gets to zero, the more prominent this effect becomes.

Taken together, the analysis presented in this chapter shows that the relay mechanism can not only explain gradient formation for large (millimetre to centimetre long) tissue sizes (Chapter 3) but also gradient scaling over around 2 orders of magnitude for a physiological set of parameters (see Section 2.4 for a discussion of the parameters).

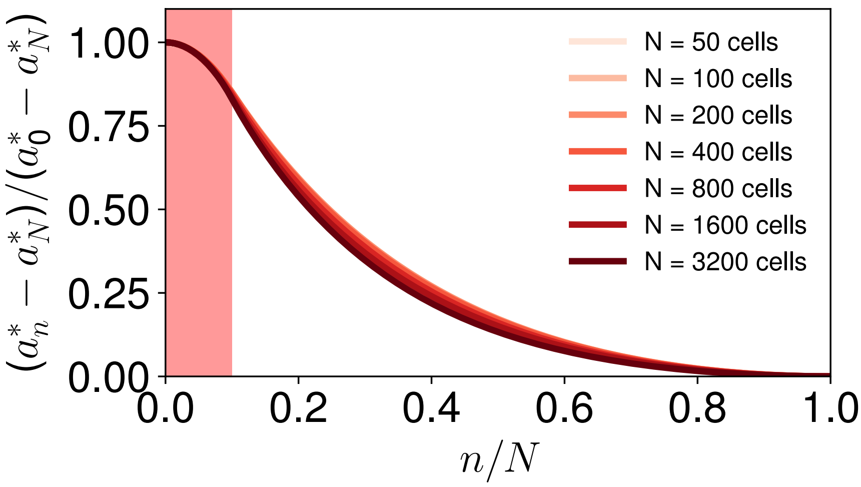

Figure 4.3.: **Offset-corrected profiles exhibit close to perfect shape scaling.** After subtracting the offset (defined as the concentration at the system boundary a_N^*), the relative concentration profiles approximately collapse to a master curve when plotted in relative spatial coordinates n/N. Parameters used: $\alpha^{\text{in}} = \alpha^{\text{out}} = \alpha^{\text{crit}} - \delta\alpha^{\text{out}}$, $c_{\text{B}} = 1.66 \times 10^6$ nM, $D = 1.0$ µm^2/s, $\delta = 10.0$ µm, $k_{\text{A}} = 10^{-3}$ s^{-1}, $k_{\text{B}} = 10^{-3}$ s^{-1}, $p = 0.5$, $V = 10^2$ µm^3, $W = 10^3$ µm^3. Size-dependent parameters: scaling factor: $\eta = N/100$, $w = 10 \times \eta$, $\delta\alpha^{\text{out}} = 0.01\alpha^{\text{crit}} \times \eta^{-2}$, $s_{\text{A}} = 2$ molecules/(s V) $\times \eta^{-2}$, $s_{\text{B}} = 0.04$ molecules/(s W) $\times \eta^{-2}$, $c_{\text{A}} = 1.66$ nM $\times\eta^{-2}$.

4.3. Summary and discussion

In this chapter we showed that, using the relay mechanism, the system can scale the length scale of the steady-state gradient to system size if the difference from the critical feedback strength is adapted to system size according to $\delta\alpha^{\text{out}} \propto N^{-2}$ (Eq. 4.1), see Fig. 4.1. Scaling of profile shape and length scale with system size is revealed by the offset-corrected relative concentration profiles ($(a_n^* - a_N^*)$ / $(a_0^* - a_N^*)$) collapsing on a master curve when plotted in relative spatial coordinates, see Fig. 4.3.

If the production rates s_{A} and s_{B}, as well as the Hill-repression threshold c_{A} are scaled with system size the same way $\delta\alpha^{\text{out}}$ is (Eq. 4.1), the values the profiles decay to are approximately constant between differently-sized systems (Fig. 4.2). This way, scaling of the length scale with system size on the one hand, and constant offsets a_N^* between different system sizes on the other hand, are achieved when $\delta\alpha^{\text{out}}$ scales according to $\delta\alpha^{\text{out}} \propto N^{-2}$ (Eq. 4.1). This is consistent with experimental observations in planarians, where the β-catenin protein gradient that organises the main body axis [44, 43, 49, 77, 100, 99, 98] decays to a value at the head end that is approximately constant between worms of different sizes, while the shape of the gradient scales with system size (Hanh Vu, James Cleland, personal communication).

We have so far discussed how the mechanism can explain shape scaling with system size, as well as an approximately size-invariant concentration at the boundary of the system a_N^*. To this end, we postulated that $\delta\alpha^{\text{out}}$, s_{A}, s_{B}, and c_{A} scale proportionally to N^{-2}. Thus, the system has to 'sense' its own size N and adapt the parameters accordingly. An expander mechanism has been proposed to explain profile scaling with system size. The idea is that an additional molecule different from the morphogen - the expander - encodes system size, see Section 1.5, Fig. 1.20). An expansion/repression mechanism has been suggested as a specific realisation of this idea to explain self-organised pattern scaling [7, 11, 12], see Fig. 1.20 B. As explained in Section 1.5, this mechanism is based on a morphogen and an expander, that regulate each other. The system reaches a steady state in which the expander concentration encodes system size. The morphogen concentration at the boundary away from its source (at N) is just above the threshold for expander production at steady state, see Fig. 1.20 B. Thus, the system self-organises to achieve an approximately constant, system size-invariant value at the boundary N, that is slightly higher than the repression threshold for expander production [11, 12]. This leads to a system size-dependent expander concentration that scales the shape of the profile according to system size [11, 12].

The relay mechanism also leads to steady-state gradients with an approximately constant, system size-invariant concentration value at N, if the parameters are scaled with system size as discussed above. Thus, an expansion/repression mechanism could be employed to 'sense' the system size. The parameters can then be regulated by the expander concentration that encodes the system size. More specifically, c_{A}, s_{A}, and s_{B} would have to be under negative regulation by the expander, i.e. decrease with system size. For the feedback strength, this is a little more intricate, as the expander would have to regulate $\delta\alpha^{\text{out}}$, the difference from the critical feedback strength, rather than the feedback strength α

directly. In order to achieve scaling with the relay mechanism using the expansion/repression mechanism, the threshold for expander production would have to be slightly lower than the approximately size-invariant value a_N^*.

The expansion/repression mechanism has been introduced in the context of a diffusion/degradation mechanism, where the diffusion constant or the degradation rate are under the control of an expander [11]. The gradient scaling achieved this way was on the order of tens to hundreds of micrometres [11, 12]. In contrast, the mechanism presented here can explain gradient scaling on millimetre to centimetre large tissues. These length scales pose a challenge to the expansion/repression mechanism as it relies on an expander profile steady-state length scale much larger than the system size, leading to spatially homogeneous expander concentrations at steady state. As the system size becomes larger, this would require an extremely long-lived molecule (see Section 1.5 for a more in-depth discussion of this point). However, in the large system presented by planarians, there is evidence for proteins, whose concentration changes with body size (Hanh Vu, personal communication). Thus, there apparently is a way to encode system size in the concentration of a protein even in large systems. One of the size-sensitive proteins could act as an expander in the system, regulating the signalling-dependent Wnt production rate α^{out}, as well as the signalling-independent Wnt and β-catenin production rates s_{A} and s_{B}, and the sensitivity to Wnt signalling c_{A}.

In diffusion/degradation mechanisms, profile scaling can mainly be achieved by decreasing the degradation rate with increasing system size, as the diffusion coefficient cannot be arbitrarily increased (see Section 1.5 for a discussion of this point). Since the length scale scales as $\lambda \propto k^{-1/2}$ in the diffusion/degradation mechanism, the degradation rate would have to scale as $k \propto N^{-2}$ in order to achieve profile scaling (Eq. 1.13). Thus, in order to scale the profile to changes in system size over two orders of magnitude, the degradation rate would have to change over four orders of magnitude. In contrast, in the relay mechanism, scaling of the length scale is achieved by scaling $\delta\alpha^{\mathrm{out}} \propto N^{-2}$. It is thus the difference from the critical feedback strength, rather than the feedback strength itself, that changes over four orders of magnitude. Thus, the actual changes to the value of the feedback strength are very small. Therefore, profile scaling across orders of magnitude of system sizes can be achieved by small changes to the feedback strength (see Fig. 4.1, Fig. 3.7). Note that this also implies that a tight regulation of the feedback strength is required, as close to the critical point, small changes in the feedback strength have a strong influence on the length scale of the steady-state profile (Fig. 3.7, Fig. 4.2). Note further that in order to keep the offset a_N^* constant across differently sized systems, s_A, s_B, and c_A have to scale with N^{-2}. Thus, keeping a_N^* constant across system sizes varying by two orders of magnitude also requires adaptation of these parameters by four orders of magnitude. However, if the system fails to adapt these parameters accordingly, only the offset a_N^* and not the shape or the length scale of the profile are affected. Thus, the relay mechanism allows adapting the length scale to system size across two orders of magnitude by small changes to the feedback strength as opposed to order of magnitude changes of the degradation rate required for profile scaling in a diffusion/degradation mechanism.

However, the scaling of the length scale with system size by adjusting $\delta\alpha^{\mathrm{out}}$ (Eq. 4.1) saturates as $\delta\alpha^{\mathrm{out}} \to 0$, see Fig. 4.1. This is due to the fact that the length scale reaches a maximal value at the critical feedback strength, where $\delta\alpha^{\mathrm{out}} = 0$ (Fig. 3.7, Fig. 4.2). Thus, the scaling relationship between $\bar{\lambda}$ and $\delta\alpha^{\mathrm{out}}$ saturates in the vicinity of α^{crit} (Fig. 3.7, Fig. 4.2). Accordingly, the scaling of $\bar{\lambda}$ with system size saturates close to α^{crit}. Therefore, the relay mechanism is characterised by a saturation of the scaling ability by tuning $\delta\alpha^{\mathrm{out}}$ very close to this critical feedback strength. Thus, there is an upper limit for system size up to which the mechanism can scale. This observation is interesting in relation to biological systems, that are typically characterised by a maximal size, introducing a natural upper limit up to where pattern scaling is required. We briefly discuss this point in the context of planarian flatworms.

Asexual flatworms usually start fissioning when they reach a body length of 6 mm and even when kept at high density, which makes them fission at larger body lengths, they rarely grow beyond 2 cm. This suggests that there is an upper limit of body size up to which the system has to be able to scale its patterning mechanisms. Interestingly, there are examples of patterning systems collapsing when a certain system size is reached. For instance, spontaneous appearance of double-headed worms has been observed in asexual *Dugesia dorotocephala* that grew very long [51]. Sexual *Schidtea mediterranea* do not reproduce by fissioning. When fed continuously, they grow to very large sizes beyond 2 cm. At these large sizes, some strains of sexual *Schidtea mediterranea* start developing patterning defects. In particular, they start making an additional set of eyes and pharynges (Hanh Vu, personal communication). These observations suggest that there is indeed a maximum system size up to which the patterning mechanism can scale, consistent with the observation of an upper limit for pattern scaling in the relay mechanism. The relay mechanism is capable of scaling systems over around 2 orders of magnitude for a physiological set of parameters, which is in good agreement with the dynamic growth and shrinking of the worms over 1.5 orders of magnitude [102].

5. Dynamics of gradient formation

5.1. How long does it take to form a steady-state signalling gradient?

In order to analyse the behaviour of the relay mechanism, we are not only interested in the shape of the steady-state profile it gives rise to, but also in its dynamics. In particular: How long does it take the system, to approach its steady state? As we saw in Chapters 3 and 4, a positive feedback loop leading to production of more signalling molecules in response to receiving a signal strongly increases the length scale of the steady-state concentration profile. Thus, the relay mechanism can explain the formation of long-ranged profiles. However, in order to exert their patterning function, these long-ranged profiles have to form. Therefore, aside from the steady-state length scale of the signalling gradient, the time it takes to reach that steady state is an important characteristic of the gradient-forming mechanism. In this chapter, we thus seek to analyse the time scale of gradient formation using the relay mechanism.

We can approximate the positive feedback by a linear response if the effector levels b_n are low compared to the Hill-activation threshold c_{B}, see Section 3.3. As discussed in Chapter 3, analysing the model in the limit of the linear feedback response reveals an interesting behaviour of the length scale of the steady-state gradient: The divergence of the length scale observed in the limit of linear feedback shows as a maximum in the length scale of the non-liner model (Fig. 3.7). Therefore, we again turn to the limit of a linear feedback response as a first step to understand the dynamics of the model.

We start this chapter by introducing an approximate analytical dynamic solution to the model in the limit of a linear feedback response. We then define the time scale of the relay mechanism in the limit of a linear feedback response based on this dynamic solution. Subsequently, we analyse the effect that positive feedback has on this time scale. Thus, we ask how the feedback loop in the signalling pathway affects the time it takes to form a gradient. Moreover, we combine this analysis with the analysis presented in Chapters 3 and 4, asking how long it takes to form a steady-state gradient of a specific length scale. That is, we analyse whether there is a trade-off between the length scale and the time scale of the signalling gradient. We also discuss what we learn about the dynamics of the non-linear system from the analysis of the system in the limit of a linear feedback response.

5.2. Dynamic solution in the limit of a linear feedback response

In this section, we introduce the approximate dynamic solution to our system in the limit of a linear feedback response. This limit is valid for low effector concentrations b_n compared to the Hill-activator threshold, c_B (see Section 3.3, Fig. 3.4).

In general, the dynamic solution to a system close to steady state can be approximated by a time-dependent infinitesimal deviation from the steady-state solution. Thus, the approximate dynamic solution to our system, $a_n(t)$, and $b_n(t)$, can be expressed as:

$$a_n(t) = a_n^* + \delta a_n(t) \ , \tag{5.1}$$

$$b_n(t) = b_n^* + \delta b_n(t) \ , \tag{5.2}$$

where a_n^* and b_n^* denote the respective steady-state solutions, and $\delta a_n(t)$ and $\delta b_n(t)$ denote the infinitesimal time-dependent deviations from it. Since the time derivative of the steady-state solution is zero by definition, the dynamics of the system is given by the dynamics of the deviation from the steady state, $\partial_t \delta a_n(t)$ and $\partial_t \delta b_n(t)$. In the following, we do not write the time dependence explicitly for brevity.

In the limit of a linear feedback response, $\partial_t \delta a_n$ is linear, see Eqs. 3.17 - 3.19, Eq. 5.1. For δb_n, we obtain:

$$\partial_t \delta b_n = \frac{c_\mathrm{A}}{c_\mathrm{A} + a_n^* + a_{n+1}^*} \left(\frac{s_\mathrm{B}}{c_\mathrm{A}} (\delta a_n + \delta a_{n+1}) - k_\mathrm{B} \delta b_n \right) . \tag{5.3}$$

based on Eqs. 2.9, 3.3, 5.1, and 5.2. The resulting system of linear equations approximating the dynamics of the system can be expressed in matrix form as:

$$\partial_t \boldsymbol{\delta x} = \boldsymbol{M} \ \cdot \ \boldsymbol{\delta x} \ , \quad \text{where } \boldsymbol{\delta x} = \begin{bmatrix} \delta a_0 \\ \delta b_0 \\ \vdots \\ \delta a_{N-1} \\ \delta b_{N-1} \\ \delta a_N \end{bmatrix} , \tag{5.4}$$

and $\boldsymbol{M}$ describes the dynamics of the system according to Eqs. 3.17 - 3.19 and Eq. 5.3. The dynamic solution to this system is given by the sum of all eigenmodes:

$$\boldsymbol{\delta x}(t) = \sum_{i=0}^{2N+1} K_i \ e^{-t/\tau_i} \ \boldsymbol{v}_{\boldsymbol{i}}^\mathrm{r} \ , \tag{5.5}$$

where $\boldsymbol{v}_{\boldsymbol{i}}^\mathrm{r}$ denotes a right eigenvector of $\boldsymbol{M}$ with eigenvalue $-\frac{1}{\tau_i}$, and the τ_i's denote the relaxation times of the system. Note that the system is comprised of both the cells and the extracellular spaces, gathered in $\boldsymbol{\delta x}$, and thus has one set of $2\,N + 1$ relaxation times and corresponding eigenvectors. The coefficients K_i are determined by the initial conditions. See Appendix G for details. Based on Eq. 5.5, we obtain the approximate dynamic solution to the system in the limit of a linear feedback response according to Eqs. 5.1 and 5.2 (Fig. 5.1).

We can define the characteristic time scale of the relay mechanism in the limit of a linear feedback response based on this dynamic solution. For a linear system like the one presented in Eq. 5.4, the dynamics of the system are governed by the slowest relaxation time τ_max for long times. In particular, this slowest relaxation time is a good estimate of how long it takes the linear system to reach its steady state. We thus define the slowest relaxation time

$$\tau_\mathrm{max} := \max\{\tau_i\} \tag{5.6}$$

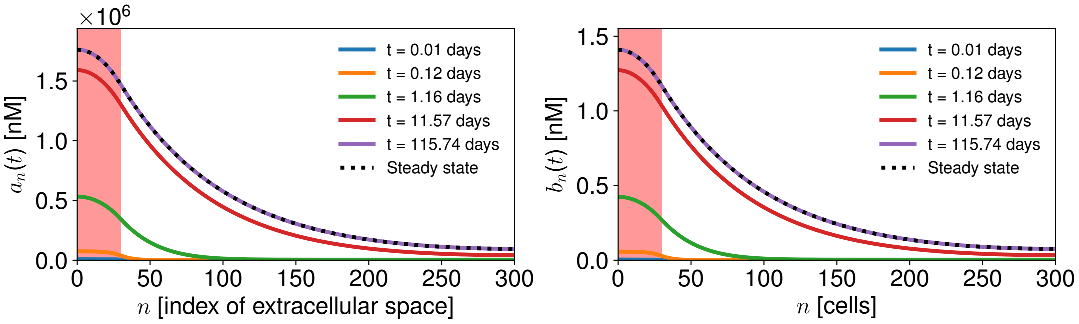

Figure 5.1.: **Dynamic solution to the linearised model.** Approximate dynamic solutions $a_n(t)$ and $b_n(t)$ according to Eqs. 5.1 and 5.2 for indicated time points. The dashed black line denotes the steady-state solution. Source region shaded in red. Parameters used: $c_\text{A} = 166$ nM, $c_\text{B} = 1.66 \times 10^8$ nM, $D = 1.0$ µm^2/s, $\delta = 10.0$ µm, $\epsilon = 1.0$ µm, $k_\text{A} = 10^{-3}$ s^{-1}, $k_\text{B} = 10^2$ s^{-1}, $p = 0.5$, $s_\text{A} = 1000$ molecules/(s V), $s_\text{B} = 4$ molecules/(s W), $N = 300$, $w = 30$, $V = 10^2$ µm^3, $W = 10^3$ µm^3.

as the time scale of the relay mechanism in the limit of a linear feedback response.

All relaxation times of the system, including the slowest one, are obtained by diagonalising $\mathbf{M}$. This is done numerically, since $\mathbf{M}$ is an $(2\,N + 1) \times (2\,N + 1)$ matrix. However, it is helpful to have an analytical estimate to the slowest relaxation time in order to understand how the different parameters of the system influence the slowest relaxation time. In particular, we are interested in how the positive feedback of the relay mechanism influences the slowest relaxation time and thus the dynamics of the system. Therefore, we derive an analytical expression approximating the slowest relaxation time of the system. We introduce this approach in the next section.

5.3. An analytical approximation to the slowest relaxation time

In this section, we introduce an approach to obtain an analytical estimate for the slowest relaxation time of the system. We first introduce how we obtain this approximation. Subsequently, we compare it to the slowest relaxation time obtained by diagonalising $\boldsymbol{M}$ (Eq. 5.4) as discussed in the previous section.

As discussed above, the dynamics of the system are given by a set of eigenmodes, each of which comes with a characteristic relaxation time (Eq. 5.5). In the diffusion/degradation system, the spatially constant eigenmode relaxes most slowly, see Appendix A. Assuming that in this aspect, the dynamics of the relay mechanism in the limit of a linear feedback response behaves qualitatively equivalently to a diffusion/degradation system, we use the relaxation time of the constant eigenmode as an estimate for the slowest relaxation time of the system.

In our system, the 'constant' eigenmode is given as $\delta a_n = \delta a^{\text{in}}$, $\delta b_n = \delta b^{\text{in}}$ inside the source region and $\delta a_n = \delta a^{\text{out}}$, $\delta b_n = \delta b^{\text{out}}$ outside of the source region. $\partial_t \delta b_n$ depends on the steady-state solution a_n^* (Eq. 5.3). In line with analysing the constant mode, we approximate the steady-state solution a_n^* by $a^{\text{in}}_{\text{c, lin}}$ and $a^{\text{out}}_{\text{c, lin}}$ inside the source region, and outside of it, respectively. Further, to approximate the slowest relaxation time, we neither consider the dynamics at the boundaries of the system, nor at the source/non-source interface. Applying these approximations, Eq. 5.4 collapses to:

$$\partial_t \begin{bmatrix} \delta a^{\text{in}} \\ \delta b^{\text{in}} \\ \delta a^{\text{out}} \\ \delta b^{\text{out}} \end{bmatrix} = \begin{bmatrix} -k_{\text{A}} & \frac{\alpha^{\text{in}}}{c_{\text{B}}} & 0 & 0 \\ \frac{2\, s_{\text{B}}}{c_{\text{A}}+2\, a^{\text{in}}_{\text{c, lin}}} & \frac{-k_{\text{B}}\, c_{\text{A}}}{c_{\text{A}}+2\, a^{\text{in}}_{\text{c, lin}}} & 0 & 0 \\ 0 & 0 & -k_{\text{A}} & \frac{\alpha^{\text{out}}}{c_{\text{B}}} \\ 0 & 0 & \frac{2\, s_{\text{B}}}{c_{\text{A}}+2\, a^{\text{out}}_{\text{c, lin}}} & \frac{-k_{\text{B}}\, c_{\text{A}}}{c_{\text{A}}+2\, a^{\text{out}}_{\text{c, lin}}} \end{bmatrix} \begin{bmatrix} \delta a^{\text{in}} \\ \delta b^{\text{in}} \\ \delta a^{\text{out}} \\ \delta b^{\text{out}} \end{bmatrix} . \tag{5.7}$$

Similarly to what we discussed in the previous section, we can obtain the relaxation times for this approximation by diagonalising the matrix defined in Eq. 5.7. We thus obtain four relaxation times:

$$\begin{aligned} \left(\tau^{\text{in}}_{1,2}\right)^{-1} = - \Bigg[& -\frac{k_{\text{A}}}{2} - \frac{k_{\text{B}}\, c_{\text{A}}}{2\,(c_{\text{A}} + 2\, a^{\text{in}}_{\text{c, lin}})} \\ & \pm \sqrt{\left(-\frac{k_{\text{A}}}{2} - \frac{k_{\text{B}}\, c_{\text{A}}}{2\,(c_{\text{A}} + 2\, a^{\text{in}}_{\text{c, lin}})} \right)^2 - \frac{k_{\text{A}}\, k_{\text{B}}\, c_{\text{A}}\, c_{\text{B}} - 2\, \alpha^{\text{in}}\, s_{\text{B}}}{c_{\text{B}}(c_{\text{A}} + 2 a^{\text{in}}_{\text{c, lin}})}} \Bigg] , \end{aligned} \tag{5.8}$$

$$\begin{aligned} \left(\tau^{\text{out}}_{1,2}\right)^{-1} = - \Bigg[& -\frac{k_{\text{A}}}{2} - \frac{k_{\text{B}}\, c_{\text{A}}}{2\,(c_{\text{A}} + 2\, a^{\text{out}}_{\text{c, lin}})} \\ & \pm \sqrt{\left(-\frac{k_{\text{A}}}{2} - \frac{k_{\text{B}}\, c_{\text{A}}}{2\,(c_{\text{A}} + 2\, a^{\text{out}}_{\text{c, lin}})} \right)^2 - \frac{k_{\text{A}}\, k_{\text{B}}\, c_{\text{A}}\, c_{\text{B}} - 2\, \alpha^{\text{out}}\, s_{\text{B}}}{c_{\text{B}}(c_{\text{A}} + 2 a^{\text{out}}_{\text{c, lin}})}} \Bigg] . \end{aligned} \tag{5.9}$$

We use the overall largest of these four relaxation times as an estimate for the dynamics of the relay mechanism in the limit of a linear feedback response. We see that $\tau_1^{\text{in/out}} > \tau_2^{\text{in/out}}$. Thus, the analytical approximation to the slowest relaxation time $\tau_{\max}^{\text{app}}$ is given as:

$$\tau_{\max}^{\text{app}} := \max\{\tau_1^{\text{in}}, \tau_1^{\text{out}}\} \ . \tag{5.10}$$

The system reaches a steady state if its slowest relaxation time is positive and finite, i.e. $0 < \tau_{\max}^{\text{app}} < \infty$. Thus, based on the approximation of the slowest relaxation time (Eq. 5.10), we see that the system reaches a steady state, if

$$\frac{k_{\text{A}}\, k_{\text{B}}\, c_{\text{A}}\, c_{\text{B}} - 2\,\alpha^{\text{in}}\, s_{\text{B}}}{c_{\text{B}}(c_{\text{A}} + 2a_{\text{c, lin}}^{\text{in}})} > 0 \ , \tag{5.11}$$

and

$$\frac{k_{\text{A}}\, k_{\text{B}}\, c_{\text{A}}\, c_{\text{B}} - 2\,\alpha^{\text{out}}\, s_{\text{B}}}{c_{\text{B}}(c_{\text{A}} + 2a_{\text{c, lin}}^{\text{out}})} > 0 \ . \tag{5.12}$$

This defines the critical feedback strength α^{crit}, that we already discussed as the feedback strength at which the steady-state length scale of the relay mechanism in the limit of a linear feedback response diverges (see Chapter 3, Eq. 3.26, repeated here for convenience):

$$\alpha^{\text{crit}} = \frac{k_{\text{A}}\, k_{\text{B}}\, c_{\text{A}}\, c_{\text{B}}}{2\, s_{\text{B}}} \ .$$

Thus, for a feedback strength greater than or equal to α^{crit}, the relay mechanism in the limit of a linear feedback response does not reach a steady state.

The system relaxes fast for $\tau_{\max} \to 0$ and increasingly slowly for $\tau_{\max} \to \infty$. In particular, this means that the system becomes slower and slower as α^{in} and/or α^{out} approach α^{crit}. At the same time, the length scale of the steady-state gradient increases as $\alpha^{\text{out}} \to \alpha^{\text{crit}}$, as discussed in Chapter 3. In the limit of a linear feedback response, discussed here, it diverges at $\alpha^{\text{out}} = \alpha^{\text{crit}}$ (Fig. 3.6).

Thus, the closer the feedback strength is to the critical one, the longer the length scale of the steady-state profile but the slower the dynamics of the system. In order to study this trade-off between length scale and relaxation time in the vicinity of the critical feedback strength, we need to understand how the relaxation time scales with $\delta\alpha^{\mathrm{in/out}}$, the difference from the critical feedback strength inside and outside of the source region. To this end, we analyse the scaling relationship between $\delta\alpha^{\mathrm{in/out}}$ and $\tau_{\mathrm{max}}^{\mathrm{app}}$ in the next section. This enables us to discuss the trade-off between length scale and relaxation time in the subsequent section.

5.4. Influence of the positive feedback on the slowest relaxation time

The slowest relaxation time τ_{max} becomes increasingly slow as the feedback strength approaches its critical value α^{crit}. In order to better understand this behaviour, we analyse how the approximation to the slowest relaxation time $\tau_{\mathrm{max}}^{\mathrm{app}}$ scales with the difference from the critical feedback strength $\delta\alpha^{\mathrm{in/out}}$. As discussed in Section 5.3, $\tau_{\mathrm{max}}^{\mathrm{app}}$ is given by the maximum of τ_1^{in} and τ_1^{out} and those depend on α^{in} and α^{out}, respectively. Thus, we first establish the scaling relationships between τ_1^{in} and $\delta\alpha^{\mathrm{in}}$, as well as between τ_1^{out} and $\delta\alpha^{\mathrm{out}}$, in the vicinity of α^{crit}.

As discussed in Section 5.3, τ_1^{in} and τ_1^{out} diverge at the critical feedback strength α^{crit}. In particular, $\alpha^{\mathrm{in/out}}$ has to be smaller than α^{crit} for the system to reach a steady state (Eqs. 5.11, 5.12). In the vicinity of α^{crit}, the scaling relationship between τ_1^{in} and $\delta\alpha^{\mathrm{in}}$, as well as that between τ_1^{out} and $\delta\alpha^{\mathrm{out}}$, are governed by the respective scaling relationships of the respective stability criteria (Eqs. 5.11, 5.12). Thus, we analyse the scaling of these stability criteria (Eqs. 5.11, 5.12) with $\delta\alpha^{\mathrm{in}}$ and $\delta\alpha^{\mathrm{out}}$, respectively, in the following. Using Eqs. 3.35 and 3.36, we can rewrite the stability criterion for τ_1^{in} (Eq. 5.11) as:

$$\frac{\left(2\, s_{\mathrm{B}}\, \delta\alpha^{\mathrm{in}}\right)^2}{c_{\mathrm{A}}\, c_{\mathrm{B}}^2\, k_{\mathrm{B}}\, \left(2\, s_{\mathrm{A}} + c_{\mathrm{A}}\, k_{\mathrm{A}}\right)} > 0 \ , \tag{5.13}$$

and the one for τ_1^{out} (5.12) as:

$$\frac{\left(2\, s_{\mathrm{B}}\, \delta\alpha^{\mathrm{out}}\right)^2}{(c_{\mathrm{A}}\, c_{\mathrm{B}})^2 k_{\mathrm{A}}\, k_{\mathrm{B}}} > 0 \ . \tag{5.14}$$

Due to the inverse in Eqs. 5.8 and 5.9, it follows that

$$\tau_1^{\mathrm{in}} \propto \left(\delta\alpha^{\mathrm{in}}\right)^{-2} \ \text{ in the vicinity of } \alpha^{\mathrm{crit}}. \tag{5.15}$$

and

$$\tau_1^{\mathrm{out}} \propto \left(\delta\alpha^{\mathrm{out}}\right)^{-2} \text{ in the vicinity of } \alpha^{\mathrm{crit}}. \tag{5.16}$$

As discussed in Chapters 3 and 4, the length scale becomes increasingly large as $\alpha^{\mathrm{out}} \to \alpha^{\mathrm{crit}}$. In particular, the length scale scales as $\bar{\lambda} \propto (\delta\alpha^{\mathrm{out}})^{-1/2}$ (Eq. 3.30). We are interested in the trade-off between an increasingly large length scale of the steady-state gradient and increasingly slow dynamics as the feedback strength approaches α^{crit}. The length scale scales with $\delta\alpha^{\mathrm{out}}$ while the time scale scales with either $\delta\alpha^{\mathrm{in}}$ or $\delta\alpha^{\mathrm{out}}$, dependent on whether $\tau_{\mathrm{max}}^{\mathrm{app}}$ is given by τ_1^{in} or τ_1^{out}. In order to compare the scaling behaviour of the length scale and the time scale, we aim to express the scaling relationship of $\tau_{\mathrm{max}}^{\mathrm{app}}$ in terms of $\delta\alpha^{\mathrm{out}}$, irrespective of whether $\tau_{\mathrm{max}}^{\mathrm{app}}$ is given by τ_1^{in} or τ_1^{out}. To this end, we assume there is a relationship between $\delta\alpha^{\mathrm{in}}$ and $\delta\alpha^{\mathrm{out}}$: $\delta\alpha^{\mathrm{in}} = f(\delta\alpha^{\mathrm{out}})$. That is, we analyse the scaling of $\tau_{\mathrm{max}}^{\mathrm{app}}$ with $\delta\alpha^{\mathrm{out}}$ for specific combinations of α^{in} and α^{out}. Note that defining these functions f is a method we use to analyse the behaviour of the system. Thus, the relationships between $\delta\alpha^{\mathrm{in}}$ and $\delta\alpha^{\mathrm{out}}$ described in f do not carry a specific meaning for the system.

We start our discussion by analysing the case in which the difference to the critical feedback strength inside of the source region is proportional to that outside of the source region:

$$\delta\alpha^{\mathrm{in}} = r\,\delta\alpha^{\mathrm{out}}\ ,\ r \in \mathbb{R}\ . \tag{5.17}$$

In this case, the estimate for the slowest relaxation time scales as

$$\tau_{\mathrm{max}}^{\mathrm{app}} \propto (\delta\alpha^{\mathrm{out}})^{-2}\ , \tag{5.18}$$

irrespective of whether τ_1^{in} or τ_1^{out} is slower since a constant factor does not change the scaling relationship. We show this scaling relationship, as well as example stead-state profiles for the case of $r = 1$, i.e. $\alpha^{\mathrm{in}} = \alpha^{\mathrm{out}}$ in Fig. 5.2. We see that both the time scale and the length scale increase as $\delta\alpha^{\mathrm{out}} \to 0$ (Fig. 5.2 B, C). Note however, that the scaling relationship obtained in Eq. 5.18 is only valid close to $\delta\alpha^{\mathrm{out}} = 0$. The change in the scaling relationship for increasing $\delta\alpha^{\mathrm{out}}$ is visible as a change in the slope of the black line ($\tau_{\mathrm{max}}^{\mathrm{app}}$) in Fig. 5.2 B. The scaling

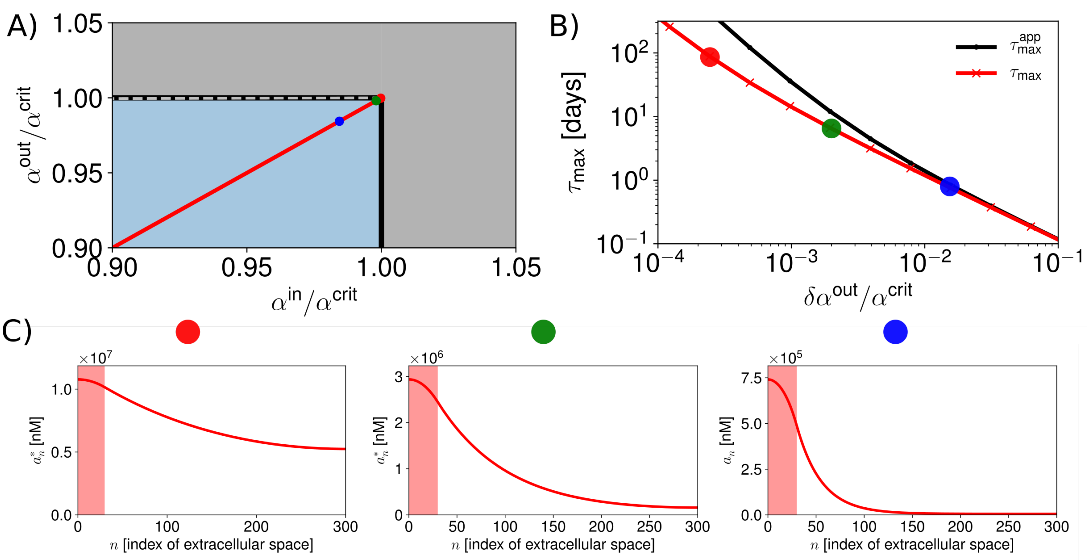

Figure 5.2.: **Scaling of the slowest relaxation time with feedback strength.** Behaviour of the slowest relaxation time for $\delta\alpha^{\text{in}} = \delta\alpha^{\text{out}}$. **A)** $\delta\alpha^{\text{in}} = \delta\alpha^{\text{out}}$ in phase space (red line). Blue region: decreasing steady-state profiles, grey dashed line: separatrix (see Fig. 3.9). Grey region: no steady state is reached in the limit of a linear feedback response discussed here. **B)** The slowest relaxation time of the system scales as $\tau_{\max} \propto (\delta\alpha^{\text{out}})^{-2}$ for $\delta\alpha^{\text{out}} \to 0$. Black dots and line: $\tau_{\max}^{\text{app}}$ (Eq. 5.10). Red line and crosses: $\tau_{\max}$ (Eq. 5.6). **C)** Example profiles with increasing time- and length scale. Dots indicate position of these profile in A) and B). Parameters used: $c_{\text{A}} = 166$ nM, $c_{\text{B}} = 1.66 \times 10^{8}$ nM, $D = 1.0$ µm^2/s, $\delta = 10.0$ µm, $k_{\text{A}} = 10^{-3}$ s^{-1}, $k_{\text{B}} = 10^{2}$ s^{-1}, $p = 0.5$, $s_{\text{A}} = 1000$ molecules/(s V), $s_{\text{B}} = 4$ molecules/(s W), $N = 300$, $w = 30$, $V = \epsilon\,\delta^2 = 10^2$ µm^3, $W = \delta^3 = 10^3$ µm^3.

exponent of -2 (Eq. 5.18) corresponds to the steep slope for small values fo $\delta\alpha^{\text{out}}$, whereas a smaller slope, corresponding to a lower absolute scaling exponent, is observed further away from the critical feedback strength (to the right of the plot). Further, the approximation to the slowest relaxation time $\tau_{\max}^{\text{app}}$ overestimates the slowest relaxation time $\tau_{\max}$ close to $\delta\alpha^{\text{out}} = 0$ (compare the red and black lines in Fig. 5.2 B).

Next, we analyse the behaviour for a power-law relationship between $\delta\alpha^{\text{in}}$ and $\delta\alpha^{\text{out}}$ according to:

$$\delta\alpha^{\text{in}} = r\,\left(\delta\alpha^{\text{out}}\right)^{\nu} \;,\; r,\; \nu\; \in \mathbb{R}\;. \tag{5.19}$$

Plugging Eq. 5.19 into the scaling relationship for τ_1^{in} (Eq. 5.15), we find that $\tau_1^{\text{in}} \propto (\delta\alpha^{\text{out}})^{-2\nu}$. The slowest relaxation time is given by the maximum τ_1^{in} and τ_1^{out} (Eq. 5.10). Thus, there is one regime in which it scales as

$$\tau_{\max}^{\text{app}} \propto (\delta\alpha^{\text{out}})^{-2} \text{ in the vicinity of } \alpha^{\text{crit}}, \tag{5.20}$$

when $\tau_{\max}^{\text{app}} = \tau_1^{\text{out}}$, and another regime in which it scales as

$$\tau_{\max}^{\text{app}} \propto (\delta\alpha^{\text{out}})^{-2\nu} \text{ in the vicinity of } \alpha^{\text{crit}}, \tag{5.21}$$

when $\tau_{\max}^{\text{app}} = \tau_1^{\text{in}}$.

Having established a way to express the scaling relationship of the estimate to the slowest relaxation time $\tau_{\max}^{\text{app}}$ to the feedback strength in terms of $\delta\alpha^{\text{out}}$, we compare the scaling relationship of the slowest relaxation time to the one of the length scale of the steady-state gradient for $\delta\alpha^{\text{out}} \to 0$ in the next section.

Note that throughout this chapter, we chose the constant production in the source region s_{A} such that we always obtain a decreasing steady-state profile, indicated by the blue area in Fig. 5.2 A.

5.5. Analysing the trade-off between length scale and time scale

For feedback strengths inside and outside of the source region that are related according to $\delta\alpha^{\text{in}} \propto \delta\alpha^{\text{out}}$ (Eq. 5.17), including constant feedback across the whole system $\alpha^{\text{in}} = \alpha^{\text{out}}$, the estimate for the slowest relaxation time scales as $\tau_{\max}^{\text{app}} \propto (\delta\alpha^{\text{out}})^{-2}$ (Eq. 5.18). Combining this with the scaling relationship of the length scale with $\delta\alpha^{\text{out}}$ (Eq. 3.30), we find that the relaxation time scales with the length scale according to:

$$\tau_{\max} \propto \bar{\lambda}^4 \text{ in the vicinity of } \alpha^{\text{crit}} \ . \tag{5.22}$$

That is, if $\delta\alpha^{\text{out}}$ changes such that the length scale doubles, the system takes $2^4 = 32$-times as long to reach a steady state. Thus, the increase in length scale

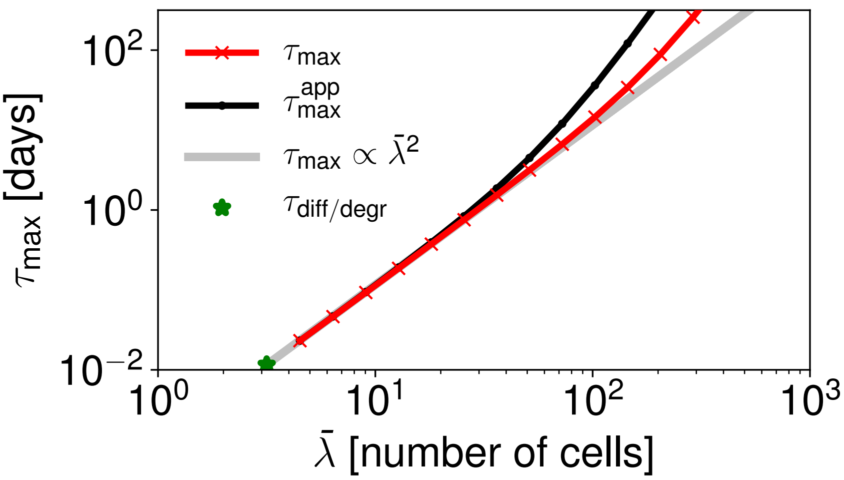

Figure 5.3.: **Trade-off between length scale and time scale.** τ_{max} scales with $\bar{\lambda}^4$ in the vicinity of α^{crit} ($\delta\alpha^{\mathrm{out}} = 0$), but with $\bar{\lambda}^2$, grey line, further away from the critical feedback strength. The green star indicates the length scale and time scale of the diffusion/degradation mechanism for the diffusion coefficient and degradation rate (k_{A}) used in this plot. Parameters used: $\alpha^{\mathrm{in}} = \alpha^{\mathrm{out}}$, $c_{\mathrm{A}} = 166$ nM, $c_{\mathrm{B}} = 1.66 \times 10^8$ nM, $D = 1.0$ µm^2/s, $\delta = 10.0$ µm, $k_{\mathrm{A}} = 10^{-3}$ s^{-1}, $k_{\mathrm{B}} = 10^2$ s^{-1}, $p = 0.5$, $s_{\mathrm{A}} = 1000$ molecules/(s V), $s_{\mathrm{B}} = 4$ molecules/(s W), $N = 300$, $w = 30$, $V = 10^2$ µm^3, $W = 10^3$ µm^3.

as the feedback strength approaches α^{crit} comes at the price of slow dynamics of the system.

We find however, that for fast turnover of effector molecules ($k_{\mathrm{B}} = 100$ s^{-1}), the scaling relationship described above does only hold very close the the critical feedback strength, that is for very large length and time scales, see Fig. 5.3. In contrast, further away from $\delta\alpha^{\mathrm{out}} = 0$, the relay mechanism in the limit of a linear feedback response follows a scaling according to $\tau_{\mathrm{max}} \propto \bar{\lambda}^2$, compare the scaling of τ_{max} and $\tau_{\mathrm{max}}^{\mathrm{app}}$ to the grey line indicating this scaling relationship in Fig. 5.3. The latter is the scaling relationship observed for a diffusion/degradation mechanism. Compare Eqs. 1.6 and 1.7 to see this.

Next, we analyse the trade-off between the length scale and the time scale for $\delta\alpha^{\mathrm{in}}$ and $\delta\alpha^{\mathrm{out}}$ related according to a power-law relationship (Eq. 5.19). We find that the scaling relationship becomes increasingly favourable for a power-law exponent $\nu < 1$, see Fig. 5.4 left panel. That is, τ_{max} scales as $\tau_{\mathrm{max}} \propto \bar{\lambda}^2$ for a large range of $\delta\alpha^{\mathrm{out}}$ (compare the red line to the grey line in Fig. 5.4), and the scaling exponent even decreases close to α^{crit} (to the right of the plot). In contrast, the trade-off between the time scale and the length scale is less favourable for a power-law exponent $\nu > 1$, see Fig. 5.4, right panel. That is, τ_{max} scales as $\tau_{\mathrm{max}} \propto \bar{\lambda}^2$ only for very large $\delta\alpha^{\mathrm{out}}$ (to the left of the plot) while the scaling exponent increases, particularly close to the critical feedback strength (to the right of the plot, compare red line and grey line).

Note in all cases discussed, $\tau_{\mathrm{max}}^{\mathrm{app}}$ overestimates τ_{max} in the vicinity of α^{crit} (compare black and red lines in Figs. 5.3, 5.4, where large values of $\bar{\lambda}$ correspond to small values of $\delta\alpha^{\mathrm{out}}$). Thus, the approximation becomes increasingly worse as $\delta\alpha^{\mathrm{out}} \to 0$. We thus note that the simple approximation $\tau_{\mathrm{max}}^{\mathrm{app}}$ we introduced is not sufficient to analyse the dynamics of the system in the vicinity of the critical feedback strength. Here, we need to analyse the slowest relaxation time τ_{max}.

Based on the slowest relaxation time τ_{max}, we see that for large values of k_{B}, the trade-off between the length scale and the time scale in the relay mechanism in the limit of a linear feedback response is given by $\tau_{\mathrm{max}} \propto \bar{\lambda}^2$ for a wide range of $\delta\alpha^{\mathrm{out}}$ and thus equivalent to that of a diffusion/degradation mechanism. For large length scales, i.e. close to the critical feedback strength, this trade-off gets better than in a diffusion/degradation mechanism if $\delta\alpha^{\mathrm{in}}$ and $\delta\alpha^{\mathrm{out}}$ are related according to a power-law relationship (Eq. 5.19) and $\nu < 1$, see Fig. 5.4, left panel.

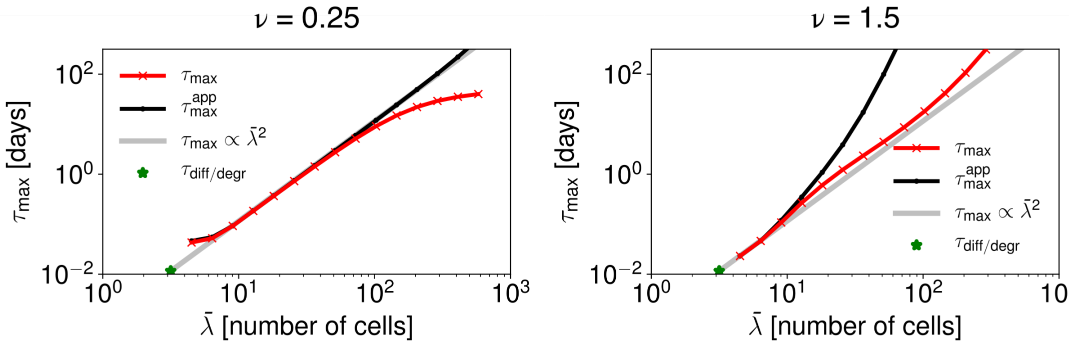

Figure 5.4.: **Scaling of the relaxation time with length scale for $\delta\alpha^{\mathrm{in}} = r\,(\delta\alpha^{\mathrm{out}})^{\nu}$.** The trade-off between length scale and time scale becomes more favourable for $\nu < 1$ (left) and less favourable for $\nu > 1$. Parameters used: $\alpha^{\mathrm{in}} = \alpha^{\mathrm{out}}$, $c_{\mathrm{A}} = 166$ nM, $c_{\mathrm{B}} = 1.66 \times 10^{8}$ nM, $D = 1.0\ \mathrm{\mu m^2/s}$, $\delta = 10.0\ \mathrm{\mu m}$, $k_{\mathrm{A}} = 10^{-3}\ \mathrm{s^{-1}}$, $k_{\mathrm{B}} = 10^{2}\ \mathrm{s^{-1}}$, $p = 0.5$, $s_{\mathrm{A}} = 1000$ molecules/(s V), $s_{\mathrm{B}} = 4$ molecules/(s W), $N = 300$, $w = 30$, $V = 10^{2}\ \mathrm{\mu m^3}$, $W = 10^{3}\ \mathrm{\mu m^3}$.

5.6. Summary and discussion

It takes increasingly longer to form steady-state gradients with a longer steady-state length scale. This is true both for the diffusion/degradation mechanism and the relay mechanism. While the length scale is increased by decreasing the degradation rate in the diffusion/degradation mechanism (see Section 1.5), it is increased by approaching the critical feedback strength in the relay mechanism. In the diffusion/degradation mechanism the length scale scales with the time scale according to $\tau_{\max} \propto \bar{\lambda}^2$. In order to compare this trade-off between length scale and time scale between the diffusion/degradation and the relay mechanism, we analysed the scaling behaviour of the time scale with the length scale in the relay mechanism in this chapter.

In order to analyse this trade-off in the relay mechanism in limit of a linear feedback response, we solved the dynamics of the model close to the steady state and defined the time scale as the slowest relaxation time of the system (Section 5.2). Further, we introduced an analytical approximation to the slowest relaxation time (Section 5.3), based on which we analysed the influence of the positive feedback on the slowest relaxation time (Section 5.4). In particular, this allowed defining a scaling relationship between the length scale and the time scale. Based on this approximation, the slowest relaxation time scales with the length scale as $\tau_{\max} \propto \bar{\lambda}^4$ if $\delta\alpha^{\mathrm{in}} \propto \delta\alpha^{\mathrm{out}}$ (Eq. 5.17). Note that this scaling relationship was derived using the stability criteria for τ_1^{in} and τ_1^{out} (Eqs. 5.11, 5.12), rather than the full expressions for τ_1^{in} and τ_1^{out} and is thus only valid close to the critical feedback strength (see Section 5.4).

Considering the full expressions for τ_1^{in} and τ_1^{out} we see that the length scale and the time scale scale according to $\tau_{\max} \propto \bar{\lambda}^2$ further away from the critical feedback strength, for large values of k_{B} (Fig. 5.3). This is the scaling relationship observed for a diffusion/degradation mechanism. We find scaling according to $\tau_{\max} \propto \bar{\lambda}^2$ in the relay mechanism for length scales on the order of 10 to 100 cells, corresponding to 0.1 mm to 1 mm (Fig. 5.3). These are length scales relevant for patterning of the worm. Moreover, if $\delta\alpha^{\mathrm{in}}$ and $\delta\alpha^{\mathrm{out}}$ are related according to a power-law relationship (Eq. 5.19) and $\nu < 1$, the scaling exponent is further decreased for large length scales, see Fig. 5.4, left panel. Thus, in this case the trade off between the length scale and the time scale is better in the relay mechanism than in the diffusion/degradation mechanism.

Note, however, that the scaling according to $\tau_{\max} \propto \bar{\lambda}^2$ as presented in this chapter does not hold in general. It was observed for a fast turnover of the effector molecule b_n, that is for a large degradation rate $k_{\mathrm{B}} = 100\ \mathrm{s}^{-1}$. In particular, the time scale of the relay mechanism is slower than discussed in this chapter for $k_{\mathrm{B}} = k_{\mathrm{A}} = 10^3\ \mathrm{s}^{-1}$, the parameters we used in Chapters 3 and 4, leading to a scaling relationship closer to $\tau_{\max} \propto \bar{\lambda}^4$. Further analysis is needed to understand how the scaling between the length scale and the time scale in the relay mechanism depends on the ratio of the two degradation rates k_{A} and k_{B}. However, in the next chapter we show that the trade-off between the length scale and the time scale of a signalling gradient formed by the relay mechanism is greatly improved by polarised secretion in response to the positive feedback. This can even boost the trade-off beyond $\tau_{\max} \propto \bar{\lambda}^2$, the one characteristic of a diffusion/degradation mechanism.

The data presented in this chapter (obtained for large values of the degradation rate k_{B}) show that the relay mechanism allows short-lived molecules to form long-ranged gradients. This opens the possibility for short-lived molecules to impact the patterning of large structures. Taking into consideration that signalling profiles are thought to already exert a patterning function as they are being formed, i.e. before they have reached steady state [30], this might open new perspectives for patterning large structures using the relay mechanism, even if its relaxation time is on the order of days. This is in stark contrast to the diffusion/degradation mechanism, in which only long-lived molecules can form a long-ranged gradient.

In this chapter, we discussed the time scale of the relay mechanism in the limit of a linear feedback response. In this limit, the time scale diverges at $\alpha^{\text{in}} = \alpha^{\text{crit}}$ or $\alpha^{\text{out}} = \alpha^{\text{crit}}$ (Eqs. 5.11, 5.12). That is, the system does not reach a steady state for feedback strengths greater than or equal to α^{crit}. In contrast, the non-linear system does reach a steady state for feedback strengths equal to or greater than α^{crit}. That is, the divergence is capped by the saturation behaviour of the positive feedback response. Numerical analysis of the non-linear system reveals that the dynamics is getting slower as the feedback strength approaches α^{crit}. This is in line with what we observed for the relaxation time of the system in the limit of a linear feedback response presented in this chapter. In contrast to what we presented in this chapter, the time scale does not diverge but reaches a maximum at the critical feedback strength in the non-linear model. Further analysis is needed to understand how the time scale of the non-linear system scales with the length scale in the vicinity of α^{crit}. Such analysis will allow comparing this scaling behaviour to the one of the diffusion/degradation system, analogously to what we did in this chapter in the limit of a linear feedback response.

In the next chapter, we discuss the influence of secretion polarity on both the length scale and the time scale of the relay mechanism. In particular, we show that polarised secretion can improve the trade-off between the length scale and the time scale of the relay mechanism even beyond $\tau_{\max} \propto \bar{\lambda}^2$, that is, beyond the one observed for the diffusion/degradation mechanism.

6. Role of tissue polarity in cell-to-cell relay

6.1. Impact of tissue polarity on signalling gradients formed by cell-to-cell relay

In Chapters 3 to 5, we discussed the properties of the relay mechanism in the absence of secretion polarity, that is for symmetric secretion of signalling molecules to the left and to the right of each cell ($p = 1/2$ in Eqs. 2.6 - 2.8). However, we introduced the model with a general secretion polarity p in Chapter 2, that is motivated by tissue polarity.

Polarity is a common phenomenon in biology. It describes the fact that two sides of a cell or a tissue are distinct, thus, there is directionality in the structure. It can be found intracellularly, manifesting in the spatially distinct organisation of the cytoskeleton and cytoplasmic components such as mRNAs and proteins, so that some components are preferentially located to a specific side of the cell [18]. This can for instance be observed during cell migration, or in asymmetric cell division [18]. Not only individual cells, but also whole tissues can be polarised. This is achieved by syncing the polarity of individual cells within a tissue. A famous example is the apical-basal polarity of epithelial tissues that form a barrier between a lumen or air and the body [18]. Aside from apical-basal polarity, epithelia also exhibit planar cell polarity, that is, a polarity in the plane of the epithelium [56, 119]. This is most noticeable in the aligned orientation of hairs, bristles, or cilia growing out of epithelial cells [56, 119]. The planar cell polarity pathway organises cell polarity within a sheet of cells by the separation of two protein complexes: one to the anterior and the other to the posterior side of each cell in the tissue [56, 119].

Thus, tissue polarity leads to distinct properties of two sides of a cell. It is therefore conceivable that it can lead to polarised secretion of signalling molecules. The polarity in our model is akin to planar cell polarity in the sense that it is a polarity in the 'plane' of the tissue, i.e. along the row of cells in our model. In Chapter 3, we identified that such polarised secretion can give rise to an effective drift of signalling molecule concentration through the system with speed $\nu = (2\,p - 1)\,\alpha^{\text{out}}\,z^{\text{out}}$ (Eq. 3.14).

In the continuous diffusion/degradation model with drift (Eq. 1.8), the length scale of the steady-state gradient is boosted by drift for positive drift speeds ν, see Fig. 1.18. Positve values of ν correspond to movement of concentration down the concentration gradient in this model. In our model, the speed of the drift is positive for the secretion polarities $p > 1/2$, see Eq. 3.14, corresponding to preferred secretion to the right. The local source is to the left of the system in our model (see Eq. 2.1, Fig. 2.2). Thus, $p > 1/2$ corresponds to drift away from the local source. This is consistent with a drift down the gradient if the profile decreases away from the local source. We thus expect a boost of the length scale of the steady-state gradient due to drift in our model for $p > 1/2$.

In this chapter, we investigate the influence that the effective drift emerging from polarised secretion has on the length scale of the steady-state signalling gradient, as well as on the trade-off between the length scale of the steady-state gradient and the time scale of gradient formation. We indeed find the expected boost of the steady-state gradient for $p > 1/2$ (Section 6.2), that also leads to a greatly imporved trade-off between the length scale and the time scale (Section 6.3), allowing to reach long-ranged steady-state gradients in biologically relevant times scales of hours to days.

6.2. Effect of tissue polarity on the length scale of signalling gradients at steady state

In accordance with what we discussed for the diffusion/degradation mechanism with drift (Section 1.5), the emerging drift changes the length scale of the steady-state gradient in the relay mechanism. In particular, preferred secretion to the right ($p > 1/2$), corresponding to secretion down the gradient (see Section 6.1),

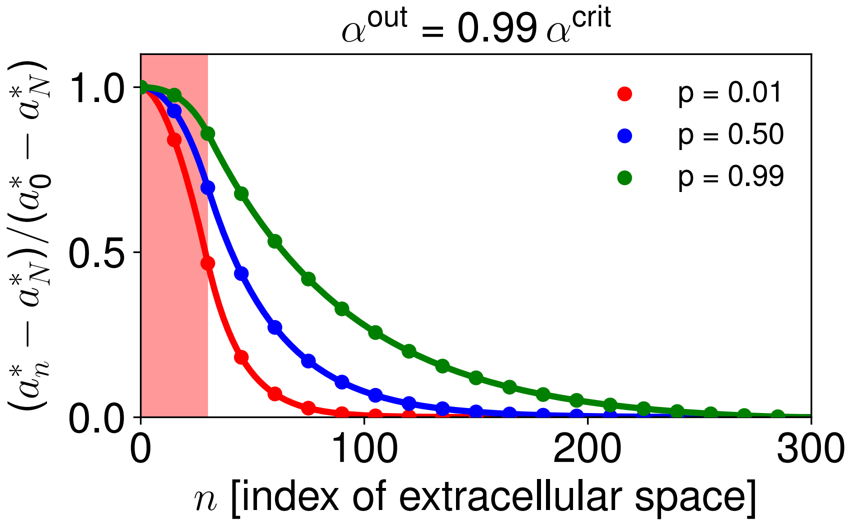

Figure 6.1.: **Secretion polarity influences profile length scale.** Baseline-corrected and maximum-normalised profiles reveal an increased steady-state length scale for preferred secretion to the right ($p > 1/2$) compared to symmetric ($p = 1/2$) secretion or secretion to the left ($p < 1/2$). Solid lines: analytical approximate steady-state solution. Dots: Numerical steady-state solution. Parameters used: $\alpha^{\text{in}} = \alpha^{\text{out}}$, $c_{\text{A}} = 166$ nM, $c_{\text{B}} = 1.66 \times 10^8$ nM, $D = 1.0$ µm^2/s, $\delta = 10.0$ µm, $k_{\text{A}} = 10^{-3}$ s^{-1}, $k_{\text{B}} = 10^{-3}$ s^{-1}, $s_{\text{A}} = 20$ molecules/(s V), $s_{\text{B}} = 4$ molecules/(s W), $N = 300$, $w = 30$, $V = 10^2$ µm^3, $W = 10^3$ µm^3.

increases the length scale of the steady-state gradient compared to symmetric secretion ($p = 1/2$), while preferred secretion to the left ($p < 1/2$) decreases it, see Fig. 6.1.

Note that secretion polarity not only changes the length scale of the steady-state concentration profile, but also the overall amount of molecules in the system: It is increased for preferred secretion to the right ($p > 1/2$) compared to symmetric secretion ($p = 1/2$) and decreased for preferred secretion to the left ($p < 1/2$), see Fig. 6.2.

In the relay mechanism, the length scale of the steady-state gradient increases as the feedback strength approaches its critical value (see Chapter 3). In particular, we find that the length scale scales as $\bar{\lambda} \propto \delta(\alpha^{\text{out}})^{-1/2}$ (Eq. 3.30) in case of symmetric secretion ($p = 1/2$). If we define a general scaling relationship $\bar{\lambda} \propto \delta(\alpha^{\text{out}})^{-\gamma}$, we find that the scaling exponent γ is dependent on p. In par-

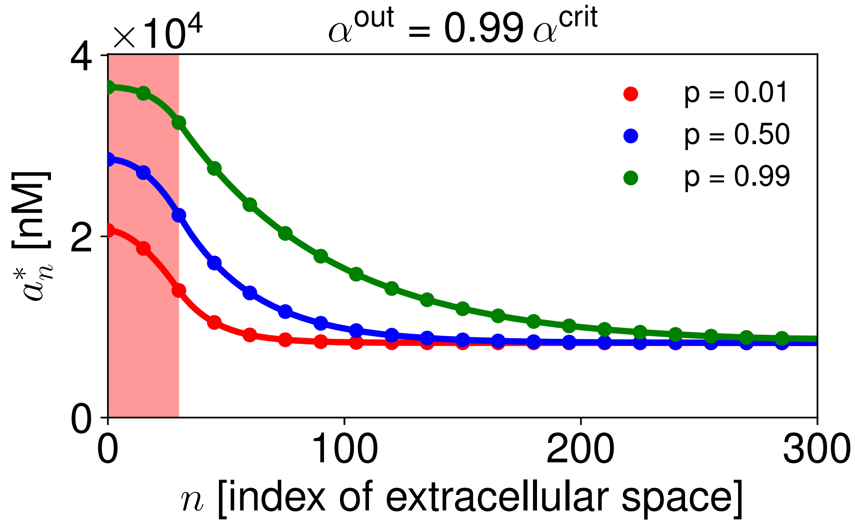

Figure 6.2.: **Secretion polarity influences steady-state concentrations.** Preferred secretion to the right ($p > 1/2$) increases the overall concentration of the steady-state profile compared to symmetric ($p = 1/2$) secretion or secretion to the left ($p < 1/2$). Solid lines: analytical approximate steady-state solution. Dots: Numerical steady-state solution. Parameters used: $\alpha^{\text{in}} = \alpha^{\text{out}}$, $c_{\text{A}} = 166$ nM, $c_{\text{B}} = 1.66 \times 10^8$ nM, $D = 1.0$ µm^2/s, $\delta = 10.0$ µm, $k_{\text{A}} = 10^{-3}$ s^{-1}, $k_{\text{B}} = 10^{-3}$ s^{-1}, $s_{\text{A}} = 20$ molecules/(s V), $s_{\text{B}} = 4$ molecules/(s W), $N = 300$, $w = 30$, $V = 10^2$ µm^3, $W = 10^3$ µm^3.

ticular, $\gamma = 1/2$ for $p = 1/2$ (Eq. 3.30), whereas $\gamma > 1/2$ for $p > 1/2$ (preferred secretion to the right) and $\gamma < 1/2$ for $p < 1/2$ (preferred secretion to the left), see Fig. 6.3. That is, for secretion to the right ($p > 1/2$) the length scale grows faster as the feedback approaches its critical strength. The opposite is true for secretion to the left ($p < 1/2$). Thus, gradients with a longer length scale are formed at the same value of $\delta\alpha^{\text{out}}$ for preferred secretion to the right, see Fig. 6.3. Note in particular that the maximal length scale the relay mechanism can achieve for a given set of parameters is increased for preferred secretion to the right (compare the values at which $\bar{\lambda}$ saturates for different values of the secretion polarity in Fig. 6.3).

The effect of secretion polarity on the length scale of the steady-state gradient is strongest close to the critical feedback strength (to the left of the plot in Fig. 6.3). We can understand this intuitively by considering that secretion polarity affects the distribution of the signalling molecules that are generated in

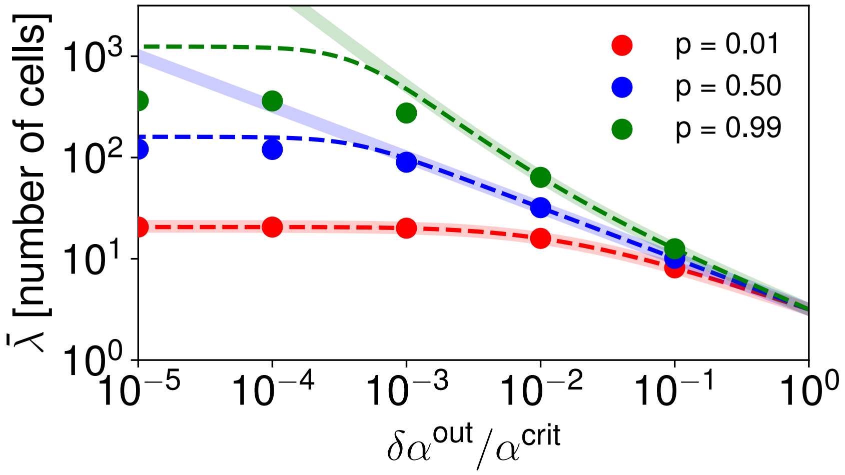

Figure 6.3.: **The effect of secretion polarity is strongest close to the critical feedback strength.** Secretion polarity leads to an effective drift with speed $\nu \propto (2p - 1)$, Eq. 3.14. Preferred secretion down the gradient ($p > 1/2$) increases the length scale of the steady-state gradient compared to symmetric secretion ($p = 1/2$). The opposite is true for preferred secretion up the concentration gradient. Length scale computed based on numerical steady-state solution (dots, see Appendix F), analytical approximate steady-state solution (dashed lines), limit of linear feedback response (transparent solid lines). Parameters used: $\alpha^{\text{in}} = \alpha^{\text{out}}$, $c_{\text{A}} = 166$ nM, $c_{\text{B}} = 1.66 \times 10^8$ nM, $D = 1.0$ μm^2/s, $\delta = 10.0$ μm, $k_{\text{A}} = 10^{-3}$ s^{-1}, $k_{\text{B}} = 10^{-3}$ s^{-1}, $s_{\text{A}} = 20$ molecules/(s V), $s_{\text{B}} = 4$ molecules/(s W), $N = 300$, $w = 30$, $V = 10^2$ μm^3, $W = 10^3$ μm^3.

response to the positive feedback. It thus exerts its effect in concert with the positive feedback. Therefore, it has the strongest effect on the length scale of the steady-state gradient when the length scale is strongly influenced by the positive feedback. The length scale is most strongly influenced by the positive feedback for close to critical feedback strengths (Fig. 3.7). Accordingly, the effect of secretion polarity is also strongest in the vicinity of the critical feedback strength (to the left of the plot in Fig. 6.3).

In the next section, we analyse how this increase in steady-state gradient length scale due to preferred secretion to the right influences the trade-off between the length scale and the time scale of the signalling gradient.

6.3. Effect of tissue polarity on the trade-off between length scale and time scale

How does polarised secretion change the trade-off between the length scale of the steady-state gradient and the time scale of its formation? In order to answer this question, we extend the analysis of the time scale of relay mechanism in the limit of a linear feedback response presented in Chapter 5 to the case $p \neq 1/2$. The analytical approximation to the slowest relaxation time obtained in Chapter 5 suggests that the slowest relaxation time is independent of secretion polarity, since $\tau_{\max}^{\text{app}}$ does not depend on p (Eq. 5.10). In the previous section, we discussed that the length scale of the steady-state profile is increased for preferred secretion to the right ($p > 1/2$), corresponding to secretion down the gradient, see Fig. 6.3. Taken together, this suggests that polarised secretion can improve the trade-off between the steady-state length scale and the time scale of gradient formation.

Indeed, we see that for preferred secretion to the right, a steady-state gradient with a longer length scale is reached in the same time compared to symmetric secretion or secretion to the left, see Fig. 6.4. Thus, secretion polarity speeds up the formation of signalling gradients. In other words, a signalling gradient of a specific length scale reaches steady state faster if the signalling molecules are preferentially secreted to the right ($p > 1/2$) compared to symmetric secretion ($p = 1/2$, compare the green lines to the blue lines in Fig. 6.4). Moreover, preferred secretion to the right greatly improves the trade-off between the length scale and the time scale beyond the one obtained by a diffusion/degradation mechanism, compare the green line in Fig. 6.4 to the grey line indicating $\tau_{\max} \propto \bar{\lambda}^2$, characteristic of a diffusion/degradation mechanism.

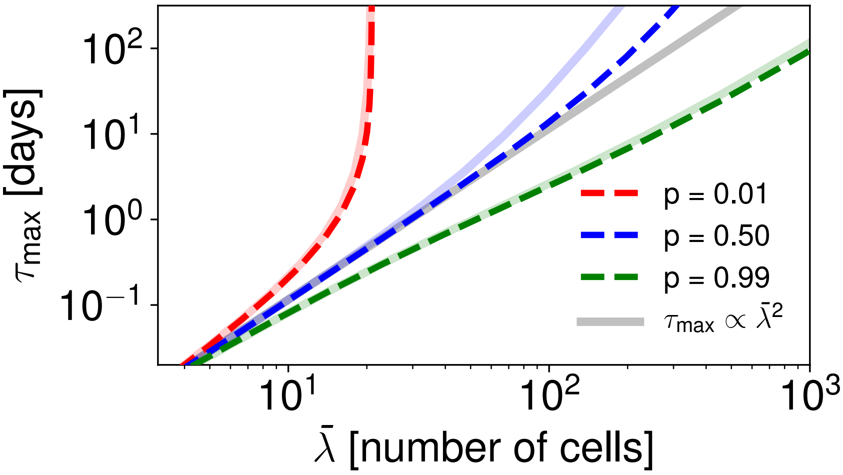

Figure 6.4.: **Effect of Secretion polarity on trade-off between length scale and time scale in the limit of a linear feedback response.** Preferential secretion to the right ($p > 1/2$, green lines) decreases the time it takes for a profile of a given length scale to form compared to symmetric secretion ($p = 1/2$, blue lines) or secretion to the left ($p < 1/2$, red lines). Dashed lines: τ_{max} according to Eq. 5.6, transparent solid lines: $\tau_{\mathrm{max}}^{\mathrm{app}}$ according to Eq. 5.10. Parameters used: $\alpha^{\mathrm{in}} = \alpha^{\mathrm{out}}$, $c_{\mathrm{A}} = 166$ nM, $c_{\mathrm{B}} = 1.66 \times 10^8$ nM, $D = 1.0$ µm^2/s, $\delta = 10.0$ µm, $k_{\mathrm{A}} = 10^{-3}$ s^{-1}, $k_{\mathrm{B}} = 10^2$ s^{-1}, $s_{\mathrm{A}} = 1000$ molecules/(s V), $s_{\mathrm{B}} = 4$ molecules/(s W), $N = 300$, $w = 30$, $V = 10^2$ µm^3, $W = 10^3$ µm^3.

6.4. Summary and discussion

In this chapter, we discussed the influence of polarised secretion of signalling molecules on the length scale of the steady-state gradient, as well as on the trade-off between the length scale and the time scale. In conclusion, the positive feedback in the relay mechanism naturally leads to the emergence of drift, if the molecules produced in response to the feedback are secreted in a polarised manner. If they are preferentially secreted to the right, corresponding to down the gradient (see Section 6.1), this leads to an increased length scale of the steady-state gradient (see Fig. 6.1, Fig. 6.3). Not only does such drift lead to steady-state profiles of an increased length scale for the same feedback strength α^{out}, but is also increases the maximal length scale the relay mechanism can reach for a given set of parameters, see Fig. 6.3.

Moreover, polarised secretion to the right improves the trade-off between the length scale and the time scale of the mechanism (see Fig. 6.4). That is, a steady-state gradient of a given length scale is reached in a shorter amount of time. This is especially important to explain the formation of long-ranged signalling gradients on biologically relevant time scales on the order of hours to days. Fig. 6.4 shows that for preferred secretion to the right, steady-state profiles with a length scale of tens to hundreds of cells, i.e. on the order of millimetres can be formed within hours to days using a physiologically relevant diffusion coefficient of 1 $\mu\mathrm{m}^2/\mathrm{s}$.

For the parameter set analysed ($k_\mathrm{B} \gg k_\mathrm{A}$, see Chapter 5), the trade-off between gradient length scale and time scale is even improved beyond the one found for a diffusion/degradation mechanism ($\tau \propto \bar{\lambda}^2$, grey line in Fig. 6.4) in case of preferred secretion down the gradient (green lines in Fig. 6.4).

The observed increase in the length scale of the steady-state gradient for positive drift speeds is consistent with what we discussed for the continuous diffusion/degradation model with drift in the Introduction (compare Fig. 6.1 to Fig. 1.18, see also Ref. [48]). However, different from the diffusion/degradation mechanisms with drift discussed in the Introduction (Section 1.5, see also Ref. [48]), the relay mechanism does not depend on cilia beating or muscle contraction giving rise to bulk movement of extracellular fluid to generate drift. In contrast, drift emerges naturally from polarised secretion in the relay mechanism. Thus, the only ingredient required to generate drift in the relay mechanism is tissue polarity.

The polarity in our model is in the plane of the tissue, i.e. along the the row of cells in our model (see Fig. 2.5). It is thus akin to planar cell polarity. The model presented in this thesis is motived by observations in planarian flatworms. These have indeed been shown to exhibit planar cell polarity [9, 107]: It is implicated in organising cilia on the ventral epithelium of planarians [9, 107] that are used for locomotion [96]. As discussed in Chapter 2, the cells in our model can be likened to the circular muscle fibres in flatworms. Muscle tissue is polarised by construction as it consists of individual muscle fibres that are aligned. The secretion polarity suggested in our model would have to be present in anteroposterior direction, i.e. perpendicular to the orientation of the individual muscle fibres.

As discussed in Section 6.1, epithelial sheets frequently show planar cell polarity perpendicular to their characteristic apical basal polarity. It is thus conceivable that such a kind of polarity could also be present in muscle cells.

In the planar cell polarity pathway, an extracellular Wnt signalling gradient has been suggested to orchestrate the segregation of the two complexes encoding the planar cell polarity to the anterior and posterior side of the cells [119]. This opens the possibility for positive feedback on a different level in our model: The tissue polarity could be organised by the Wnt signalling gradient, while the formation of the Wnt signalling gradient is aided by the polarised secretion due to the tissue polarity.

7. Discussion

During embryonic development, regeneration, and tissue turn-over, newly-formed tissue has to be patterned. The required patterning information can be provided by spatially graded concentration profiles of signalling molecules, called signalling or morphogen gradients ([25, 54, 46, 99, 98], see Section 1.2). Planarian flatworms are a great model to study tissue patterning as they constantly turn over all of their body, dynamically grow and shrink depending on the amount of food available, and are able to regenerate from arbitrary amputation fragments (reviewed e.g. in [50, 84], see Section 1.4). Thus, their patterning mechanisms have to be present at adult length scales, dynamically adjust to changes in size, and reform after amputation. Their main body axis is organised by a Wnt signalling gradient ([99, 98], see Section 1.4.3). In this thesis, we focused on the question of how signalling gradients with a length scale in the millimetre range as observed in flatworms can form and scale with tissue size. Inspired by observations of positive feedback in the Wnt signalling gradient in flatworms ([98], see Section 1.4.3), we developed a cell-to-cell relay mechanism that leads to effective spreading of the morphogen concentration based on positive feedback. In this chapter, we summarise and discuss the main results of the research presented in this thesis.

In Chapter 2, we introduced a discrete model that explicitly accounts for individual cells receiving a morphogen signal from the adjacent extracellular spaces (Fig. 2.2). This signal prevents the degradation of an intracellular effector, leading to increased intracellular effector concentrations. Those in turn positively regulate the production of signalling molecules. Thus, increased intracellular effector levels lead to increased extracellular signalling molecule concentrations, resulting in a positive feedback loop. Thus, all cells in the system produce signalling molecules. This way, the signal can be relayed from one cell to the next. Therefore, the signalling molecules do not necessarily have to diffuse across the whole tissue from a spatially-confined local source as they would have to in a diffusion/degradation mechanism for gradient formation.

We analysed the properties of the steady-state signalling gradient formed by this relay mechanism in Chapter 3. We found that the positive feedback loop indeed increases the length scale of the steady-state gradient compared to a mechanism relying exclusively on diffusion and degradation with the same diffusion constant and degradation rate (Fig. 3.7). Analysing how the length scale changes with the feedback strength α^{out}, we identified a critical feedback strength α^{crit}, at which a maximal length scale is reached. It is the difference from this critical feedback strength, $\delta\alpha^{\mathrm{out}}$, that sets the length scale of the steady-state profile. In particular, the length scale scales as $\bar{\lambda} \propto (\delta\alpha^{\mathrm{out}})^{-1/2}$. That means, that close to the critical feedback strength, the length scale is very sensitive to changes in the feedback strength.

That fact that the length scale is highly sensitive to changes in feedback strength close to α^{crit} allows for scaling the length scale of the steady-state gradient to varying tissue sizes by small adaptations of the feedback strength, as we presented in Chapter 4 (Fig. 4.1). The reason for this is that the length scale scales with the *difference* from the critical feedback strength in the relay mechanism $\delta\alpha^{\mathrm{out}}$. The proposed scaling thus requires $\delta\alpha^{\mathrm{out}}$ to scale with system size. Since the relay mechanism reaches a maximum length scale at $\alpha^{\mathrm{out}} = \alpha^{\mathrm{crit}}$, it can only scale the profile to system size up to a maximal system size, set by α^{crit}. The concentration a_N^* to which the steady-state profiles decay would also increase as the feedback strength approaches its critical value. However, it can be kept approximately constant across different system sizes when rescaling other parameters of the system with system size in addition to the feedback strength. This way, steady-state gradients with a length scale that scales with system size but that decay to an approximately constant value can be obtained (Fig. 4.2). Thus, it is conceivable that the required scaling of parameters of the system to system size could be regulated by an expansion/repression mechanism as presented in Refs. [7] and [11]. Analysing the shape of the profiles after base-line correcting, we found that the profiles exhibit close-to-perfect shape scaling across system sizes varying by more than 1.5 orders of magnitude (Fig. 4.3).

In Chapter 5, we analysed the dynamics and time scales of the relay mechanism in the limit of a linear feedback response close to steady state. We found that the dynamics of the system become increasingly slow as the feedback strength approaches its critical value α^{crit}. Since the length scale increases as the feedback approaches α^{crit}, there is a trade-off between a long length scale of the steady-state gradient and fast dynamics of gradient formation. We found that for fast turnover of effector molecules ($k_{\mathrm{B}} = 100\ \mathrm{s}^{-1}$), the time scale scales as $\tau_{\max} \propto \bar{\lambda}^2$ for length scales on the orders of ten to hundreds of cells, i.e. hundreds of micrometres to millimetres (Fig. 5.3, Fig. 5.4). This is the same scaling relationship also observed for a diffusion/degradation mechanism. For larger length scales, i.e. closer to the critical feedback strength, the scaling exponent is increased, except if the feedback strengths inside and outside of the source region are related as $\delta\alpha^{\mathrm{in}} = m(\delta\alpha^{\mathrm{out}})^{\nu}$ with $\nu < 1$. In this case, the relaxation time becomes constant as the feedback strength approaches α^{crit} (Fig. 5.4). Thus, in this case the length scale of the profile can be increased without strongly increasing the relaxation time.

If the secretion of signalling molecules in response to the positive feedback is polarised, this leads to the emergence of drift, i.e. an effective transport of signalling molecules through the tissue. The drift resulting from polarised secretion to the right, i.e. away from the local source, markedly increases the length scale of the steady-state gradient (Fig. 6.1, Fig. 6.3). Importantly, it also improves the trade-off between the length scale and the time scale. That is, gradients of a given steady-state length scale can be established in a shorter amount of time (Fig. 6.4). In particular, this means that steady-state gradients with a length scale on the order of hundreds of cells (millimetres) can be reached within one day, assuming a physiologically relevant diffusion coefficient of 1 $\mu\mathrm{m}^2/\mathrm{s}$ (Fig. 6.4). After having summarised the results of this thesis, we discuss them both in the context of planarians and from a theoretical point of view below.

Planarians can dynamically grow and shrink over 1.5 orders of magnitude [102], and thus have to scale their patterning system accordingly. Indeed, the Wnt signalling gradient, measured as a β-catenin protein gradient, has been shown to scale with animal size (Hanh Vu, James Cleland, personal communication). In order to scale a diffusion/degradation-based pattern to tissue sizes varying across two orders of magnitude, the degradation rate would have to change across four orders of magnitude. In contrast, the relay mechanism allows scaling the steady-state profile over two orders of magnitude by small changes in the feedback strength α^{out}, as the length scale scales with the *difference* from the critical feedback strength $\delta\alpha^{\text{out}}$. In order to achieve robust patterning using the relay mechanism, the feedback strength has to be tightly controlled by the system size, as discussed in Chapter 4. This poses the question of how a system senses its own size. Importantly, there is evidence for size-sensitive proteins in planarians, whose concentration changes with body size (Hanh Vu, personal communication). Future experimental work will analyse whether these proteins can act as expanders, regulating the feedback strength according to system size. In parallel, future theoretical work will have to reveal how an expansion/repression mechanism as proposed in Refs. [7] and [11] would have to be wired to regulate $\delta\alpha^{\text{out}}$, the *difference* from the critical feedback strength $\delta\alpha^{\text{out}}$, rather than α^{out} with system size. Such regulation is necessary to achieve self-organised pattern scaling using the relay mechanism.

The β-catenin gradient decays to a constant, non-zero value that is conserved between worms of different sizes (Hanh Vu, James Cleland, personal communication). This constant value can be mapped to the value the steady-state profiles decay to in our model, a_N^*. As discussed in Chapter 4, scaling of other parameters of the system in addition to the feedback strength allows keeping this value similar across different system sizes while scaling the length scale of the steady-state profile with system size (Fig. 4.2). This behaviour is thus in accordance with these experimental observations.

We observe that the relay mechanism reaches a maximum length scale for a given set of parameters at the critical feedback strength (Figs. 3.7). That is, there is a hard upper bound up to which the length scale of the steady-state profile can scale with system size. This hard upper bound for the length scale of the patterning system can be interpreted in the context of the finite size most organisms reach. In some planarian species, individuals keep growing when fed continuously. For some of those species, individuals show patterning defects when they exceed a certain size ([51], Hanh Vu, personal communication). It will be interesting to analyse the Wnt signalling gradients in such worms as they grow towards the size where their patterning mechanism breaks down, and to observe whether the scaling of the gradient with system size indeed saturates close to the size at which they start developing patterning defects.

In our model we introduce a polarity akin to planar cell polarity, that leads to the emergence of drift and thus to a strong increase in the length scale of the steady-state gradient. Importantly, this improves the trade-off between the gradient length scale and time scale (Fig. 6.4). We liken the cells in our model to the circular muscle fibres of the worms. It will be important to analyse whether the body wall muscle cells exhibit planar cell polarity and thus could employ secretion polarity in order to boost gradient length scale. Planarians have been shown to exhibit planar cell polarity in epithelial tissue organising the orientation of their cilia [9, 107].

The symmetry-breaking production of signalling molecules with rate s_A in the source region of our model, is motivated by the Wnt signalling-independent *Wnt1* expression [98] at the posterior pole of the animal [78]. We know that *Wnt1* is expressed in muscle cells [116]. It will thus be interesting to analyse whether *Wnt1* is indeed expressed in the circular muscle fibres to which we liken the cells in our model.

Many morphogens including Wnt [115] and Sonic hedgehog [75, 82] carry lipid modifications that make it unlikely for them to be highly diffusive in the aqueous extracellular environment. Thus, there is a long-standing controversy as to how such poorly diffusive molecules can give rise to signalling gradients (see Section 1.3.3). The relay mechanism developed in this thesis explains morphogen spreading not purely by diffusion, but introduces an effective spreading by positive feedback. It can thus explain the formation of morphogen gradients even in the absence of molecular diffusion of the morphogen: If a cell presents the morphogen into the extracellular space, the signal is sensed by the immediate neighbouring cell that in turn starts to also present the morphogen into the extracellular space, due to the positive feedback. This way, the information is passed on from cell to cell. Thus, the relay mechanism presents an attractive concept to rationalise the observed long-ranged patterning effects of poorly diffusive morphogens.

A. Dynamic solution to the diffusion/degradation mechanism

In this Appendix, we compute the steady-state solution and the dynamic solution to a symmetric one-dimensional continuous diffusion/degradation as specified in Fig. A.1.

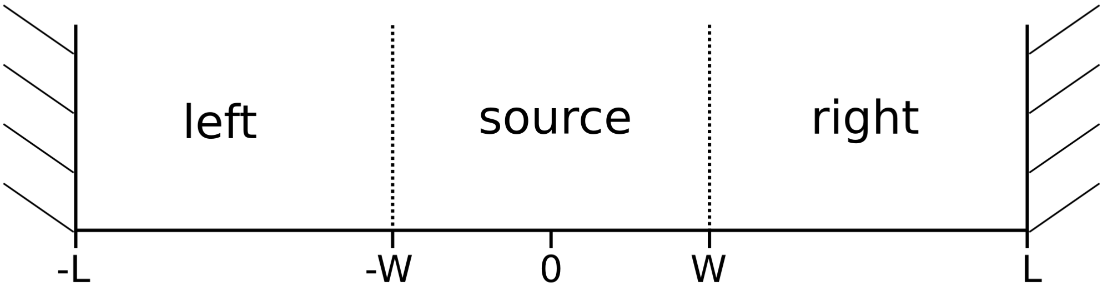

Figure A.1.: **Symmetric continuous one-dimensional diffusion/degradation system.** The system produces molecules in the central source region. Molecules spread by diffusion and are degraded. It is important to note that we are dealing with *one* system comprised of three subsystems. Thus, any dynamic equation or dynamic or steady-state solution to the system has to be defined for the whole system (potentially piece-wise).

The dynamics of the system are given as:

$$\partial_t C = s\left[\theta(x-W)-\theta(x-(-W))\right] + D\partial_x^2 C - kC\ . \tag{A.1}$$

This is an inhomogeneous differential equation

$$s\left[\theta(x-W)-\theta(x-(-W))\right] = (\partial_t - D\partial_x^2 + k)C\ . \tag{A.2}$$

with the corresponding homogeneous equation

$$\partial_t y = D\partial_x^2 y - ky \ . \tag{A.3}$$

The boundary conditions are given as no-flux boundary conditions at the system boundaries:

$$\partial_x C(-L,t) = 0 \ , \tag{A.4}$$

$$\partial_x C(L,t) = 0 \ . \tag{A.5}$$

The initial condition is given by an empty system:

$$C(x,0) = 0 \ . \tag{A.6}$$

In order to calculate the steady-state solution, denoted by C^* and defined as $\partial_t C^* = 0$, we subdivide the system into three subsystems: left, source, right, denoted by C^{l}, C^{s}, and C^{r}, respectively, and stitch them with stitching conditions demanding constant flux and constant values at the subsystem boundaries:

$$-D\ \partial_x C^{\mathrm{l}}(-W,t) = -D\ \partial_x C^{\mathrm{s}}(-W,t) \ , \tag{A.7}$$

$$C^{\mathrm{l}}(-W,t) = C^{\mathrm{s}}(-W,t) \ , \tag{A.8}$$

$$-D\ \partial_x C^{\mathrm{r}}(W,t) = -D\ \partial_x C^{\mathrm{s}}(W,t) \ , \tag{A.9}$$

$$C^{\mathrm{r}}(W,t) = C^{\mathrm{s}}(W,t) \ . \tag{A.10}$$

We then find the solution to the bulk of the three subsystems using the following Ansatz

$$C^{*,\mathrm{l}} = A^{\mathrm{l}}\ e^{x/\lambda} + B^{\mathrm{l}}\ e^{-x/\lambda} \ , \tag{A.11}$$

$$C^{*,\mathrm{s}} = \frac{s}{k} + A^{\mathrm{s}}\ e^{x/\lambda} + B^{\mathrm{s}}\ e^{-x/\lambda} \ , \tag{A.12}$$

$$C^{*,\mathrm{r}} = A^{\mathrm{r}}\ e^{x/\lambda} + B^{\mathrm{r}}\ e^{-x/\lambda} \ , \tag{A.13}$$

where $\lambda = \sqrt{\frac{D}{k}}$ and the coefficients $A^{\mathrm{l/s/r}}$ and $B^{\mathrm{l/s/r}}$ are given by the boundary conditions and the stitching conditions. They can be calculated according to:

$$\mathbf{M}\ \cdot\ \boldsymbol{\nu} = \mathbf{s}\ \Leftrightarrow \boldsymbol{\nu} = \mathbf{M}^{-1} \cdot \mathbf{s} \ , \tag{A.14}$$

where

$$\mathbf{M} = \begin{bmatrix} e^{-L/\lambda} & -e^{L/\lambda} & 0 & 0 & 0 & 0 \\ e^{-W/\lambda} & -e^{W/\lambda} & -e^{-W/\lambda} & e^{W/\lambda} & 0 & 0 \\ e^{-W/\lambda} & e^{W/\lambda} & -e^{-W/\lambda} & -e^{W/\lambda} & 0 & 0 \\ 0 & 0 & e^{W/\lambda} & -e^{-W/\lambda} & -e^{W/\lambda} & e^{-W/\lambda} \\ 0 & 0 & -e^{W/\lambda} & -e^{-W/\lambda} & e^{W/\lambda} & e^{-W/\lambda} \\ 0 & 0 & 0 & 0 & e^{L/\lambda} & -e^{-L/\lambda} \end{bmatrix} , \quad \boldsymbol{\nu} = \begin{bmatrix} A^{\mathrm{l}} \\ B^{\mathrm{l}} \\ A^{\mathrm{s}} \\ B^{\mathrm{s}} \\ A^{\mathrm{r}} \\ B^{\mathrm{r}} \end{bmatrix} , \quad \mathbf{s} = \begin{bmatrix} 0 \\ 0 \\ \frac{s}{k} \\ 0 \\ \frac{s}{k} \\ 0 \end{bmatrix} .$$

The solution to any inhomogeneous differential equation is given by the solution to the corresponding homogeneous equation plus one particular solution. We chose the steady-state solution as the particular solution. Thus,

$$C(x,t) = C^{*}(x) + y(x,t) \ , \tag{A.15}$$

where $y(x,t)$ specifies the solution to the corresponding homogeneous equation (Eq. A.3). This can also be read as the solution being given by the steady-state solution plus deviations from the steady-state solution. In this interpretation, $y(x,t)$ specifies the deviations from the steady-state solution. We will express $y(x,t)$ as a discrete Fourier series:

$$y(x,t) = \sum_{n=0}^{\infty} c_{\mathrm{n}}(t) \cos\left(\frac{n\pi x}{L}\right) + q_{\mathrm{n}}(t) \sin\left(\frac{n\pi x}{L}\right) \ , \tag{A.16}$$

where $\frac{n\pi x}{L}$ maps the x coordinate to an integer multiple of the period of the sine/cosine by scaling it to the system size $\frac{x}{2L}$ and mapping it to $2\pi n$, i.e. one period times the wave number (i.e. an integer multiple of whole period), ensuring that only whole waves are put on the system and resulting in $\frac{n\pi x}{L}$. The sines and cosines are called 'eigenmodes'. Since the steady-state solution fulfils the boundary conditions, $y(x,t)$ also has to fulfil the boundary conditions in order for $C(x,t)$ to fulfil the boundary conditions. Only the cosine part of the series fulfils the boundary conditions. Therefore, $y(x,t)$ is given as a cosine series.

In order to find the time-dependent function $c_{\mathrm{n}}(t)$, we plug the cosine series into the homogeneous differential equation (Eq. A.3):

$$0 = \sum_{n=0}^{\infty} \left[\partial_t c_{\mathrm{n}} + \left(\frac{Dn^2\pi^2}{L^2} + k\right) c_{\mathrm{n}}\right] \cos\left(\frac{n\pi x}{L}\right) \ . \tag{A.17}$$

Since cosines for different arguments are linearly independent, it follows:

$$\Rightarrow 0 = \partial_t c_{\mathrm{n}} + \left(\frac{Dn^2\pi^2}{L^2} + k \right) c_{\mathrm{n}} \ , \tag{A.18}$$

and thus

$$c_{\mathrm{n}}(t) = K_n \ e^{-\left(\frac{Dn^2\pi^2}{L^2}+k\right) \ t} \ . \tag{A.19}$$

Each eigenmode comes with a characteristic decay time τ_n.

$$\tau_n = \frac{1}{\left(\frac{Dn^2\pi^2}{L^2} + k\right)} \ . \tag{A.20}$$

We see that modes with a long wave length (small values of n) have a higher relaxation time τ_n. Thus, they decay more slowly. In particular, the constant mode with $n = 0$ has the slowest relaxation time given by

$$\tau_{\max} = \frac{1}{k} \ . \tag{A.21}$$

The K_n are given by the initial condition according to:

$$c_{\mathrm{n}}(0) = K_n \ e^{0/\tau_n} = K_n \ . \tag{A.22}$$

That is, $y(x, t)$ describes how, over time, the initial condition exponentially relaxes to the steady state. Thus,

$$c_{\mathrm{n}}(t) = c_{\mathrm{n}}(0) \ e^{-t/\tau_n} \ . \tag{A.23}$$

Based on the initial condition (Eq. A.6) we find:

$$y(x, 0) = -C^* = \sum_{n=0}^{\infty} K_n e^{-0/\tau_n} \cos\left(\frac{n\pi x}{L}\right) \ .$$

From here we determine

$$K_n = \begin{cases} \frac{1}{2L} \int_{-L}^{L} -C^* \ dx & n = 0 \\ \frac{1}{L} \int_{-L}^{L} -C^* \cos\left(\frac{n\pi x}{L}\right) & n \neq 0 \ . \end{cases} \tag{A.24}$$

Thus, the full dynamic solution to Eq. A.1 is given by

$$C(x,t) = C^* + \sum_{n=0}^{\infty} K_n e^{-t/\tau_n} \cos\left(\frac{n\pi x}{L}\right) \ , \tag{A.25}$$

with τ_n and K_n as specified above. Since the steady state is defined piece-wise, the integral to calculate K_n is evaluated piece-wise:

$$\begin{aligned} K_n &= \frac{1}{L}\left\{\int_{-L}^{-W} -C^{*,\mathrm{l}} \cos\left(\frac{n\pi x}{L}\right) dx\right\} \\ &+ \frac{1}{L}\left\{\int_{-W}^{W} -C^{*,\mathrm{s}} \cos\left(\frac{n\pi x}{L}\right) dx\right\} \\ &+ \frac{1}{L}\left\{\int_{W}^{L} -C^{*,\mathrm{r}} \cos\left(\frac{n\pi x}{L}\right) dx\}\right\} \ , \end{aligned} \tag{A.26}$$

and equivalently for K_0.

B. Effect of the choice of boundary conditions

B.1. Model dynamics revisited

In order to discuss what happens at the boundaries of the system it is helpful to revisit the dynamic equations of the model, analysing if the individual terms of the model are governed by changes in molecule numbers or concentrations. Of course, these two quantities can be converted into one another using the volume of the respective compartment. However, as we start changing the volume of the compartments at the boundaries compared to those in the bulk, we introduce spatially distinct conversion factors between molecule numbers and concentrations. Therefore, it is helpful to clearly distinguish between concentrations and molecule numbers. To this end, please note the following choice of notation: lower case letters (a_n, b_n, c_A, c_B) denote concentrations; upper case letters (A_n, B_n, C_A, C_B) denote molecule numbers. V_N specifies the volume of extracellular space n and W_n stands for the volume of cell n. Thus, $a_n = A_n/V_N$, $b_n = B_n/W_n$, $c_\mathrm{A} = C_\mathrm{A}/V$, $c_\mathrm{B} = C_\mathrm{B}/W$. Note further that we chose a constant cell volume $W_n = W \, \forall \, n$ and thus drop the index. We chose $V_N = V \, \forall \, n \in [1, ..., (N-1)]$, i.e. in the bulk and discuss the choice of V_0 and V_N, i.e. the volume of the extracellular spaces at the boundaries as well as the impact of this choice below.

Let us first consider the production and secretion of signalling molecules. The source cells constantly produce and secrete signalling molecules with rate $\widetilde{s}_\mathrm{A}$ and in an effector concentration-dependent way with rate $\widetilde{\alpha}^\mathrm{in}$. The non-source cells produce and secrete signalling molecules in an effector concentration-dependent manner with rate α^out. The produced molecules are secreted on both sides of the cell. That is, the molecules ending up in extracellular space n stem from the cells $n-1$ and n. In Eqs. 2.6 and 2.6 we have already divided by the volume of the extracellular space in the bulk (V) and in case of s_{A} added the contributions from both cells. This is helpful to discuss what happens in the bulk of the system using simplified equations. In order to discuss what happens at the boundaries, it is helpful to consider the contributions of individual cells. We assume the cells follow the same secretion polarity for the constant production as they do for the effector-dependent production. For the change in molecule number due to production and secretion we then get:

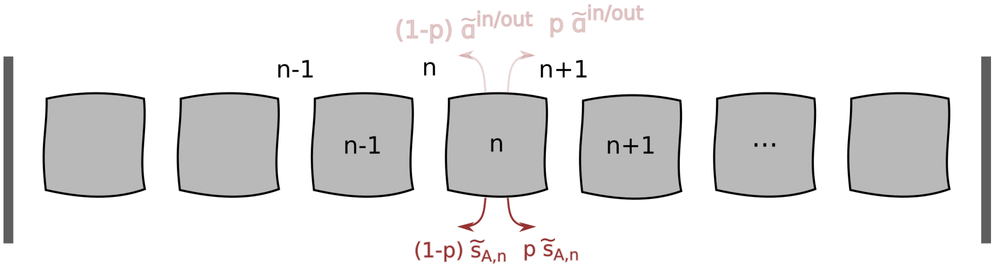

Figure B.1.: **Polarised secretion.** Source cells ($n \in [0, ..., (w-1)]$) constitutively produce signalling molecule (Wnt) with rate $\tilde{s}_{\text{A}}$ (red arrows) that they distribute to their adjacent extracellular spaces obeying tissue polarity p. All cells produce signalling molecule (Wnt) as part of the positive feedback and secrete it obeying tissue polarity p.

$$p\,\tilde{s}_{\text{A, n-1}} + (1-p)\,\tilde{s}_{\text{A, n}} + p\ \tilde{\alpha}^{\text{in/out}}\ \frac{B_{n-1}}{C_{\text{B}}+B_{n-1}} + (1-p)\ \tilde{\alpha}^{\text{in/out}}\ \frac{B_n}{C_{\text{B}}+B_n}\ .$$

In order to describe the change in concentration due to production and secretion, we need to account for the volume of the extracellular space the molecules are secreted into:

$$p\,\frac{\tilde{s}_{\text{A, n-1}}}{V_N} + (1-p)\,\frac{\tilde{s}_{\text{A, n}}}{V_N} + p\ \frac{\tilde{\alpha}^{\text{in/out}}}{V_N}\ \frac{b_{n-1}}{c_{\text{B}}+b_{n-1}} + (1-p)\ \frac{\tilde{\alpha}^{\text{in/out}}}{V_N}\ \frac{b_n}{c_{\text{B}}+b_n}$$

for $V_N = V$:

$$= p\,s_{\text{A, n-1}} + (1-p)\,s_{\text{A, n}} + p\ \alpha^{\text{in/out}}\ \frac{b_{n-1}}{c_{\text{B}}+b_{n-1}} + (1-p)\ \alpha^{\text{in/out}}\ \frac{b_n}{c_{\text{B}}+b_n}\ .$$

Next, we revisit the Hill-type interaction terms between a_n and b_n (Eqs. 2.3, 2.5). Cells produce signalling molecules (a, Wnt) in response to increased effector levels (b, β-catenin) according to Eq. 2.3. The motivation for this term is the idea that cells experiencing increased signalling levels produce more signalling molecules. The mental model behind this is that a Wnt signal leads to increased β-catenin concentrations in the cell that in turn leads to translocation of more β-catenin to the nucleus. In the nucleus, β-catenin alters transcription - in this case, according to the mental model, in such a way that more Wnt is transcribed that will then also be translated and secreted. This is motivated by the observation in planarians, that *Wnt* expression is increased in response to elevated β-catenin levels (see Section 1.4.3). Following these lines of argument, the corresponding term in the model is influenced by concentrations rather than molecule numbers as the processes described here are governed by mass-action (Eq. 2.3). Multiplying numerator and denominator in Eq. 2.3 with W, we get an equivalent term in molecule numbers:

$$\frac{B_n}{C_\mathrm{B} + B_n} \ . \tag{B.1}$$

Thus, even though we know the process is driven by changes in concentrations, we can also describe it by changes in molecule numbers as the process happens inside one compartment of a given size and thus the two representations can be easily converted into each other. Since all cells have the same volume W, the conversion factor does not have any spatial dependence and is thus the same across the whole system. What's more, since this is a dimensionless fraction, even the numerical value of the term is not affected by the choice of either concentration or molecule number to represent it since both numerator and denominator are affected equally by the conversion.

With regard to the inhibitory term in the dynamic equation for b_n (Eq. 2.5), the idea is that, the higher the Wnt concentration in the extracellular spaces to the left and to the right of the cell, the more Wnt molecules will bind to a Wnt receptor at the cell surface and the more β-catenin will be saved from degradation. This is motivated by the mode of action of the well-conserved Wnt-signalling pathway (Fig. 1.9). Again, the receptor binding is assumed to follow mass action and is thus dependent on the concentration of signalling molecules in the respective extracellular spaces. In particular, we can think of the term as comparing the average of the concentrations in the two adjacent extracellular spaces (n and $n+1$) to a threshold concentration c'_{A}:

$$\frac{1}{1+\frac{(a_n+a_{n+1})/2}{c'_{\mathrm{A}}}} \ . \tag{B.2}$$

With $c'_{\mathrm{A}} = 1/2\ c_{\mathrm{A}}$ we recover Eq. 2.5. We can express this term in terms of molecule numbers as

$$\frac{1}{1+\frac{(A_n/V_n+A_{n+1}/V_{n+1})\,V}{C_{\mathrm{A}}}} \ .$$

In the bulk, i.e. $n \in [1, ..., (N-1)]$, where $V_N = V$, this is equal to Eq. 2.5. However, at the boundaries, where V_0 and V_N may differ from V, we need to take these differences into account and explicitly compute

$$\frac{1}{1+\frac{(A_0/V_0+A_1/V)\,V}{C_{\mathrm{A}}}} \ ,$$

and

$$\frac{1}{1+\frac{(A_{N-1}/V+A_N/V_N)\,V}{C_{\mathrm{A}}}} \ .$$

Finally, let us consider the diffusion term. As far as the diffusion is concerned, the number of molecules is conserved. Thus,

$$\partial_t A_n = -(J^{\mathrm{A}}_{\mathrm{n}} - J^{\mathrm{A}}_{\mathrm{n\text{-}1}}) \ , \tag{B.3}$$

where $J^{\mathrm{A}}_{\mathrm{n}}$ is the diffusive molecule flux [#/t] across cell n, i.e from extracellular space n to extracellular space $n+1$ (Fig. B.2).

We define $J^{\mathrm{A}}_{\mathrm{n}}$ as

$$\begin{aligned} J^{\mathrm{A}}_{\mathrm{n}} &= -\sigma D_{\mathrm{p}} \frac{a_{n+1}-a_n}{\delta} \\ &= -\sigma D_{\mathrm{p}} \frac{A_{n+1}/V_{n+1}-A_n/V_N}{\delta} \ . \end{aligned} \tag{B.4}$$

The reason for choosing this definition of the diffusive molecule flux is as follows: A diffusive flux is caused by differences in concentration in space (*not* in molecule number). Hence, we consider the difference in concentration in two adjacent extracellular spaces $(n+1)$ and n. In our one-dimensional model, the

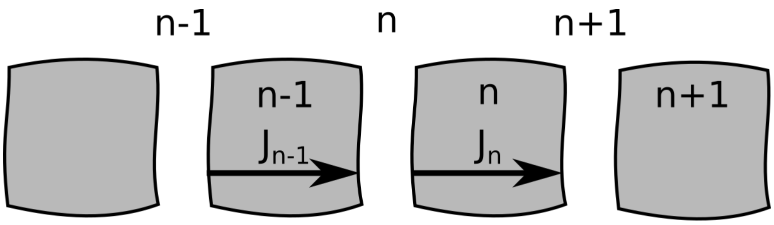

Figure B.2.: **Definition of the diffusive molecule flux.** The diffusive molecule flux $J_{\mathrm{n}}^{\mathrm{A}}$ [#/t] across cell n gives the number of molecules flowing from extracellular space n to extracellular space $n+1$ due to differences in concentrations in the respective extracellular spaces. Cells depicted in grey.

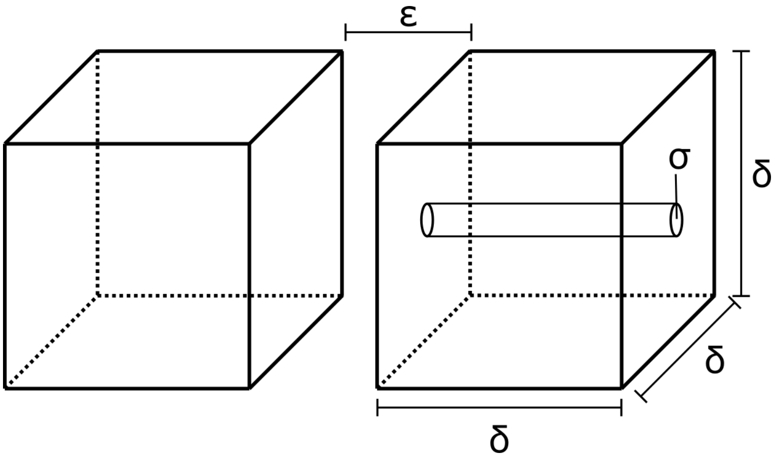

Figure B.3.: **Illustration of the diffusive flux.** To conceptualise molecules flowing around a cell, picture them flowing 'through' the cell via a pipe connecting the two extracellular spaces. δ: cell width = pipe length, ϵ: extracellular space width, σ: cross-sectional area of pipe.

diffusion around the cells in the three-dimensional reality is captured by molecules 'jumping' between extracellular spaces. We can conceptualise this as molecules diffusing 'through' the cell via a small pipe (Fig. B.3). In this analogy, the molecular diffusion happens inside the pipe with a diffusions coefficient D_{p} across the width of the cell δ. The molecules flowing through the pipe enter and leave it through its ends with a cross-sectional area of σ.

Following from Eqs. B.3 and B.4, the temporal change in molecule numbers due to diffusion is given by:

$$
\begin{aligned}
\partial_t A_n &= \sigma D_\mathrm{p} \delta \, \frac{(A_{n-1}/V_{n-1} - 2\, A_n/V_N + A_{n+1}/V_{n+1})}{\delta^2} \\
&\quad \text{for } n \in [2, ..., (N-2)] : \\
\partial_t A_n &= \frac{\sigma D_\mathrm{p} \delta}{V} \, \frac{(A_{n-1} - 2\, A_n + A_{n+1})}{\delta^2} \\
&\quad \text{with } V = \delta^2 \epsilon \\
&= \frac{\sigma D_\mathrm{p}}{\delta \epsilon} \, \frac{(A_{n-1} - 2\, A_n + A_{n+1})}{\delta^2} \quad .
\end{aligned}
$$

In order to define the corresponding diffusion term in concentrations, we need to define the diffusive concentration flux J_n [# /(t l^2)]:

$$
J_\mathrm{n} = -\frac{\sigma}{\delta^2} D_\mathrm{p} \frac{a_n - a_{n-1}}{\delta} \quad .
$$

The rationale for this definition is that in order to account for molecules only diffusing though the 'pipe' in our pipe picture (cross-sectional area σ, Fig. B.3) we define the average area across which molecules can diffuse as $\frac{\sigma}{\delta^2}$. The rest of the definition is the same as for J_n^A.

The dynamic equation for the concentration is given by

$$
\partial_t a_n = -\frac{J_\mathrm{n+1} - J_\mathrm{n}}{x} \quad ,
$$

where x is a length. In the geometry of our model it is not *a priori* obvious, whether $x = \delta$ or $x = \epsilon$. Using the conservation law (Eq. B.3), we find $x = \epsilon$ and recover the diffusion term we used in Eqs. 2.6 - 2.8.

Taking these considerations together, we get the following equations for our model in concentrations:

$$
\begin{aligned}
\partial_t a_n = & \frac{\sigma \, D_\mathrm{p} \, \delta}{V_N} \, \frac{(a_{n-1} - 2\, a_n + a_{n+1})}{\delta^2} - k_\mathrm{A} a_n + p \, \frac{\widetilde{s}_\mathrm{A,\ n\text{-}1}}{V_N} + (1-p) \, \frac{\widetilde{s}_\mathrm{A,\ n}}{V_N} \\
& + p \, \frac{\widetilde{\alpha}^\mathrm{in/out}}{V_N} \, \frac{b_{n-1}}{c_\mathrm{B} + b_{n-1}} + (1-p) \, \frac{\widetilde{\alpha}^\mathrm{in/out}}{V_N} \, \frac{b_n}{c_\mathrm{B} + b_n} \qquad \text{(B.5)}
\end{aligned}
$$

$$\partial_t b_n = \frac{\widetilde{s}_\mathrm{B}}{W} - k_\mathrm{B} \frac{1}{1 + \frac{a_n + a_{n+1}}{c_\mathrm{A}}} b_n \tag{B.6}$$

and in molecule numbers:

$$\begin{aligned}\partial_t A_n &= \sigma D_\mathrm{p} \delta \, \frac{(A_{n-1}/V_{n-1} - 2\, A_n/V_N + A_{n+1}/V_{n+1})}{\delta^2} - k_\mathrm{A} A_n + p\, \widetilde{s}_{\mathrm{A,\ n\text{-}1}} \\ &\quad + (1-p)\, \widetilde{s}_{\mathrm{A,\ n}} + p\ \widetilde{\alpha}^{\mathrm{in/out}}\ \frac{B_{n-1}}{C_\mathrm{B} + B_{n-1}} + (1-p)\ \widetilde{\alpha}^{\mathrm{in/out}}\ \frac{B_n}{C_\mathrm{B} + B_n} \qquad \text{(B.7)} \\ \partial_t B_n &= \widetilde{s}_\mathrm{B} - k_\mathrm{B} \frac{1}{1 + \frac{A_n/V_N + A_{n+1}/V_{n+1}}{C_\mathrm{A}/V}} B_n\ . \qquad \text{(B.8)}\end{aligned}$$

B.2. Outer system boundaries

At the outside boundaries of the system, we impose reflective boundary conditions, i.e. nothing leaves or enters the system from the outside. That is, the concentration in the hypothetical extracellular spaces $a_{-1} = a_{N+1} = 0$, and the concentration in the hypothetical cells $b_{-1} = b_N = 0$. All cells in the source region ($n \in [0, ..., (w-1)]$) constitutively produce signalling molecule with rate $\widetilde{s}_\mathrm{A}$ and in an effector-dependent manner with rate $\widetilde{\alpha}^\mathrm{in}$. Cells in the non-source system ($n \in [w, ..., (N-1)]$) produce signalling molecule in an effector-dependent manner with rate $\widetilde{\alpha}^\mathrm{out}$. Thus, the dynamic equations at the system boundaries read:

$$\partial_t a_0 = \frac{\sigma\, D_\mathrm{p}\, \delta}{V_0}\, \frac{(-\, a_0 + a_1)}{\delta^2} - k_\mathrm{A} a_0\ + (1-p)\, \frac{\widetilde{s}_\mathrm{A}}{V_0} + (1-p)\, \frac{\widetilde{\alpha}^\mathrm{in}}{V_0}\, \frac{b_0}{c_\mathrm{B} + b_0} \tag{B.9}$$

$$\partial_t a_N = \frac{\sigma\, D_\mathrm{p}\, \delta}{V_N}\, \frac{(a_{N-1} - a_N)}{\delta^2} - k_\mathrm{A} a_N\ + p\, \frac{\widetilde{\alpha}^\mathrm{out}}{V_N}\, \frac{b_{N-1}}{c_\mathrm{B} + b_{N-1}} \tag{B.10}$$

or

$$\partial_t A_0 = \sigma D_\mathrm{p} \delta \, \frac{(-\, A_0/V_0 + A_1/V_1)}{\delta^2} - k_\mathrm{A} A_0 + (1-p)\, \widetilde{s}_\mathrm{A} + (1-p)\ \widetilde{\alpha}^\mathrm{in}\ \frac{B_0}{C_\mathrm{B} + B_0} \tag{B.11}$$

$$\partial_t A_N = \sigma D_\mathrm{p} \delta \, \frac{(A_{N-1}/V_{n-1} -\ A_N/V_N)}{\delta^2} - k_\mathrm{A} A_\mathrm{N} + p\, \widetilde{\alpha}^\mathrm{out}\ \frac{B_\mathrm{N\text{-}1}}{C_\mathrm{B} + B_\mathrm{N\text{-}1}}\ . \tag{B.12}$$

The dynamic equations for b_n or B_n at the system boundaries read:

$$\partial_t b_0 = s_{\mathrm{B}} - k_{\mathrm{B}} \frac{1}{1 + \frac{a_0 + a_1}{c_{\mathrm{A}}}} b_0 \tag{B.13}$$

$$\partial_t b_{N-1} = s_{\mathrm{B}} - k_{\mathrm{B}} \frac{1}{1 + \frac{a_{N-1} + a_N}{c_{\mathrm{A}}}} b_{N-1} \tag{B.14}$$

or

$$\partial_t B_0 = \widetilde{s}_{\mathrm{B}} - k_{\mathrm{B}} \frac{1}{1 + \frac{A_0/V_0 + A_1/V}{C_{\mathrm{A}}/V}} B_n \tag{B.15}$$

$$\partial_t B_{\text{N-1}} = \widetilde{s}_{\mathrm{B}} - k_{\mathrm{B}} \frac{1}{1 + \frac{A_{N-1}/V + A_N/V_N}{C_{\mathrm{A}}/V}} B_n \ . \tag{B.16}$$

We consider two variants of these boundary conditions: First, we consider all extracellular spaces to have the same volume $V = \delta^2\,\epsilon$. Secondly, we consider the extracellular spaces at the system boundaries to have a different volume $V_0 \neq V$ and $V_N \neq V$ (Fig. B.4).

B.2.1. Constant width of extracellular spaces at the boundaries

If all extracellular spaces have the same volume $V = \delta^2\,\epsilon$, the boundary conditions specified in Eqs. B.9 - B.12 simplify to

$$\partial_t a_0 = D\,\frac{(-\,a_0 + a_1)}{\delta^2} - k_{\mathrm{A}} a_0 \, + (1-p)\, s_{\mathrm{A}} + (1-p)\,\alpha^{\mathrm{in}}\,\frac{b_0}{c_{\mathrm{B}} + b_0} \tag{B.17}$$

$$\partial_t a_N = D\,\frac{(a_{N-1} - a_N)}{\delta^2} - k_{\mathrm{A}} a_N \, + p\,\alpha^{\mathrm{out}}\,\frac{b_{N-1}}{c_{\mathrm{B}} + b_{N-1}} \tag{B.18}$$

or

$$\partial_t A_0 = D\,\frac{(-\,A_0 + A_1)}{\delta^2} - k_{\mathrm{A}} A_0 + (1-p)\,\widetilde{s}_{\mathrm{A}} + (1-p)\;\widetilde{\alpha}^{\mathrm{in}}\;\frac{B_0}{C_{\mathrm{B}} + B_0} \tag{B.19}$$

$$\partial_t A_N = D\,\frac{(A_{N-1} -\, A_N)}{\delta^2} - k_{\mathrm{A}} A_{\mathrm{N}} + p\,\widetilde{\alpha}^{\mathrm{out}}\;\frac{B_{\text{N-1}}}{C_{\mathrm{B}} + B_{\text{N-1}}} \ . \tag{B.20}$$

Based on Eqs. B.13 and B.16, the dynamic equations for B_n at the system boundaries read:

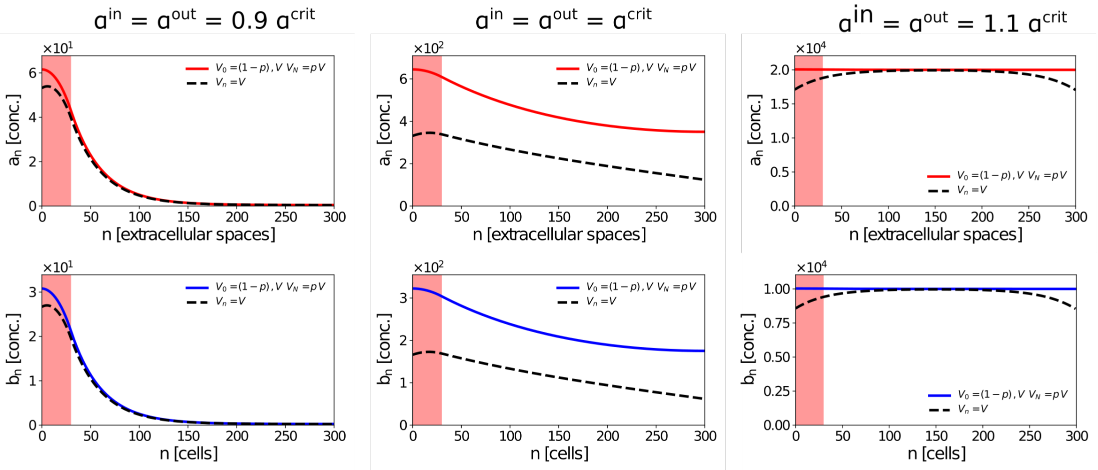

Figure B.4.: **Boundary effects.** The choice of the width of the extracellular space at the system boundaries affects the shape of the steady-state profile. Numerically obtained steady-state profiles for $V_0 = V_N = V = \delta^2\epsilon$ (dashed lines) and for $V_0 = (1-p)\,V$ and $V_N = p\,V$ (solid lines). Upper panels show steady-state profiles for a (signalling molecule, Wnt concentrations); lower panels those for b (effector, β-catenin concentrations). Left panel: $\alpha^{\text{in}} = \alpha^{\text{out}} = 0.9\,\alpha^{\text{crit}} = 1800$ nM/s, middle panel: $\alpha^{\text{in}} = \alpha^{\text{out}} = \alpha^{\text{crit}} = 2000$ nM/s, right panel: $\alpha^{\text{in}} = \alpha^{\text{out}} = 1.1\,\alpha^{\text{crit}} = 2200$ nM/s. Parameters used: $c_{\text{A}} = 0.1$ nM, $c_{\text{B}} = 10^5$ nM, $D = 1.0$ µm^2/s, $\delta = 10$ µm, $k_{\text{A}} = 0.0001$ 1/s, $k_{\text{B}} = 0.0001$ 1/s, $N = 300$, $p = 0.5$, $s_{\text{A}} = 0.1$ nmol/V, $s_{\text{B}} = 0.0025$ nmol/W, $V = \epsilon\,\delta^2 = 10^2$ µm^3, $W = \delta^3 = 10^3$ µm^3, $w = 30$. Source region shaded in red.

$$\partial_t B_0 = \widetilde{s}_{\text{B}} - k_{\text{B}} \frac{1}{1 + \frac{A_0 + A_1}{C_{\text{A}}}} B_n \tag{B.21}$$

$$\partial_t B_{\text{N-1}} = \widetilde{s}_{\text{B}} - k_{\text{B}} \frac{1}{1 + \frac{A_{N-1} + A_N}{C_{\text{A}}}} B_n \tag{B.22}$$

and Eqs. B.13 and B.14 remain unchanged as they are independent of V_0 and V_N.

B.2.2. Different widths of extracellular spaces at the boundaries

In general, the extracellular spaces at the system boundaries may have different volumes from those in the bulk. Specifically, we chose their volumes to be $V_0 =$

$(1-p)\,V$ and $V_N = p\,V$ ($r_0 = (1-p)$, $r_{\mathrm{N}} = p$ in Fig. 2.5). In particular, for $p = 1/2$, i.e. symmetric secretion, this corresponds to the extracellular spaces at the system boundaries having only half the volume of those in the bulk ($r_0 = r_{\mathrm{N}} = 1/2$ in Fig. 2.5). This choice results in a system without a slope in the concentration profile at the boundaries (Fig. B.4). This is equivalent to what one finds in continuous systems when choosing refectory boundary conditions. These choices result in:

$$\partial_t a_0 = \frac{D}{(1-p)}\frac{(-a_0 + a_1)}{\delta^2} - k_{\mathrm{A}} a_0 + s_{\mathrm{A}} + \alpha^{\mathrm{in}}\,\frac{b_0}{c_{\mathrm{B}} + b_0} \tag{B.23}$$

$$\tag{B.24}$$

$$\partial_t a_N = \frac{D}{p}\,\frac{(a_{N-1} - a_N)}{\delta^2} - k_{\mathrm{A}} a_N + \alpha^{\mathrm{out}}\,\frac{b_{N-1}}{c_{\mathrm{B}} + b_{N-1}} \tag{B.25}$$

$$\tag{B.26}$$

for concentrations and

$$\partial_t A_0 = D\,\frac{-\frac{1}{(1-p)}\,A_0 + A_1}{\delta^2} - k_{\mathrm{A}} A_0 + (1-p)\,\widetilde{s}_{\mathrm{A}} + (1-p)\,\widetilde{\alpha}^{\mathrm{in}}\,\frac{B_0}{C_{\mathrm{B}} + B_0} \tag{B.27}$$

$$\begin{aligned}\partial_t A_1 = {} & D\,\frac{\frac{1}{(1-p)}\,A_0 - 2\,A_1 + A_2}{\delta^2} - k_{\mathrm{A}} A_1 + \widetilde{s}_{\mathrm{A}} \\ & + p\;\widetilde{\alpha}^{\mathrm{in}}\,\frac{B_0}{C_{\mathrm{B}} + B_0} + (1-p)\;\widetilde{\alpha}^{\mathrm{in}}\,\frac{B_1}{C_{\mathrm{B}} + B_1}\end{aligned} \tag{B.28}$$

$$\begin{aligned}\partial_t A_{N-1} = {} & D\,\frac{(A_{N-2} - 2\,A_{N-1} + \frac{1}{p}\,A_N)}{\delta^2} - k_{\mathrm{A}} A_{N-1} + p\;\widetilde{\alpha}^{\mathrm{out}}\,\frac{B_{\text{N-2}}}{C_{\mathrm{B}} + B_{\text{N-2}}} \\ & + (1-p)\;\widetilde{\alpha}^{\mathrm{out}}\,\frac{B_{\text{N-1}}}{C_{\mathrm{B}} + B_{\text{N-1}}}\end{aligned} \tag{B.29}$$

$$\partial_t A_N = D\frac{(A_{N-1} - \frac{1}{p}\,A_N)}{\delta^2} - k_{\mathrm{A}} A_{\mathrm{N}} + p\,\widetilde{\alpha}^{\mathrm{out}}\,\frac{B_{\text{N-1}}}{C_{\mathrm{B}} + B_{\text{N-1}}} \tag{B.30}$$

for molecule numbers. Note that we need to also specify the dynamic equitations for A_1 and A_{N-1} (Eqs. B.28 and B.29, respectively), as they are also dependent on V_0 and V_N, respectively.

The dynamic equations for the outermost cells of the system (Eqs. B.15, B.16), simplify to:

$$\begin{aligned}
\partial_t B_0 &= \widetilde{s}_{\mathrm{B}} - k_{\mathrm{B}} \frac{1}{1 + \frac{\frac{1}{1-p} A_0 + A_1}{C_{\mathrm{A}}}} B_0 \\
\partial_t B_{\text{N-1}} &= \widetilde{s}_{\mathrm{B}} - k_{\mathrm{B}} \frac{1}{1 + \frac{A_{N-1} + \frac{1}{p} A_N}{C_{\mathrm{A}}}} B_{\text{N-1}} \ .
\end{aligned}$$

Those in concentration (Eq. B.13 and B.14) are neither dependent on V_0 nor on V_N and thus do not change, i.e. they are the same as in the bulk.

Note that the equation for b_n or B_n is the same in the source and the non-source system as the source of B_n or b_n is constant in space.

The two notations can be converted into each other following

$$\begin{aligned}
\partial_t a_n &= \frac{\partial_t A_n}{V_N} \\
\partial_t b_n &= \frac{\partial_t B_n}{W} \ .
\end{aligned}$$

B.3. Source/non-source interface

We further need to specify the stitching condition where the source system and the non-source system meet. Specifically, cells $n \in [0, ..., (w-1)]$ produce a with constant rate $\widetilde{s}_{\mathrm{A}}$, cells $n \in [w, ..., (N-1)]$ do not and the effector-dependent signalling-molecule production rates are $\widetilde{\alpha}^{\mathrm{in}}$ and $\widetilde{\alpha}^{\mathrm{out}}$ for the two subsystems, respectively. Thus, the equation for the extracellular space w at the interface of the two systems reads:

$$\begin{aligned}
\partial_t a_w = D \, &\frac{(a_{w-1} - 2\, a_w + a_{w+1})}{\delta^2} - k_{\mathrm{A}} a_w \ + p \, s_{\mathrm{A}} \\
&+ p \, \alpha^{\mathrm{in}} \, \frac{b_{w-1}}{c_{\mathrm{B}} + b_{w-1}} + (1-p) \, \alpha^{\mathrm{out}} \, \frac{b_w}{c_{\mathrm{B}} + b_w} \qquad \text{(B.31)}
\end{aligned}$$

or

$$\begin{aligned}
\partial_t A_w = D \, &\frac{A_{w-1} - 2\, A_w + A_{w+1}}{\delta^2} - k_{\mathrm{A}} A_w + p \, \widetilde{s}_{\mathrm{A}} \\
&+ p \ \widetilde{\alpha}^{\mathrm{in}} \ \frac{B_{\text{w-1}}}{C_{\mathrm{B}} + B_{\text{w-1}}} + (1-p) \ \widetilde{\alpha}^{\mathrm{out}} \ \frac{B_w}{C_{\mathrm{B}} + B_w} \ . \qquad \text{(B.32)}
\end{aligned}$$

The subsystem boundary does not affect the dynamic equation for b_n or B_n. Thus, the latter are described by the respective equations for the bulk.

We will discuss the model in concentrations using $V_0 = (1-p)\,V$ and $V_N = p\,V$ in the main text of this thesis. We end this appendix by discussing the effect of the choice of boundary conditions on profile shape.

B.4. Discussion

If we choose the outer system boundary conditions as $V_0 = V_N = V$, we observe a non-zero slope of the profile at the boundaries (Fig. B.4). This impression of the system boundaries acting like effective sinks stems from the fact that in the bulk, each extracellular space receives material from the cells on both of its sides. At the boundary, a cell is only present at one side of the extracellular space. Since all cells produce the same number of molecules per unit time, only $(1-p)$- and p-times the number of molecules per unit time are added to the extracellular spaces at the respective system boundaries. Therefore, if their volume is as large as that of the extracellular spaces in the bulk, the increase in concentration due to the production by the neighbouring cells is only $(1-p)$- and p-times as large as in the bulk. Combined with the same degradation rate at the boundaries as in the bulk, this appears as an effective sink leading to a non-zero profile slope at the system boundaries (Fig. B.4).

If, on the other hand, we chose the boundary conditions as $V_0 = (1-p)\,V$, $V_N = p\,V$, we obtain a profile with no slope at the boundaries (Fig. B.4). This is due to the fact that the volumes of the extracellular spaces at the system boundaries are chosen such that the increase in concentration due to the production by the neighbouring cells is equivalent to that of the extracellular spaces in the bulk. Let us consider the example of $p = 1/2$. In this case of symmetric secretion, each cells distributes the molecules produced per unit time equally to its adjacent extracellular spaces on the left and on the right. That is, half its production goes to the left and the other half to the right. The extracellular spaces at the boundaries are half as big as the ones in the bulk. When half the number of molecules per unit time gets to an extracellular space half as big as the ones in the bulk, the resulting increase in concentration is exactly the same as in the bulk. Since the degradation is also the same as in the bulk this leads to a zero slope in the concentration profile at the boundaries (Fig. B.4). We chose these boundary conditions for the further discussion of the problem in this thesis as we would like to analyse the properties of the bulk of the system and not the boundary effects.

Note that the effect of the boundaries becomes more and more pronounced as the length scale of the profile increases (Fig. B.4). As discussed in Chapter 3, the maximum length scale is reached at $\alpha^{\mathrm{in/out}} = \alpha^{\mathrm{crit}}$ (middle panel in Fig. B.4). Since the boundary effects are propagated into the bulk of the system with the length scale of the system, they are most widely visible in this regime.

C. Numerical solution to differential equations: Implicit-explicit Euler method

C.1. Explicit Euler

In order to solve a differential equation numerically, we discretise it. We will use a simple one-dimensional diffusion/degradation equation as an example.

$$\partial_t C = D\partial_x^2 C - kC \ . \tag{C.1}$$

Discretising in space, we obtain:

$$\partial_t C = D\frac{C_{\text{n-1}} - 2\,C_{\text{n}} + C_{\text{n+1}}}{\Delta x^2} - kC_{\text{n}} \ . \tag{C.2}$$

Discretising time in a classical forward Euler scheme, i.e. explicitly, we obtain

$$\frac{C_{\text{n}}^{\text{t}} - C_{\text{n}}^{\text{t-1}}}{\Delta t} = D\frac{C_{\text{n-1}}^{\text{t-1}} - 2\,C_{\text{n}}^{\text{t-1}} + C_{\text{n+1}}^{\text{t-1}}}{\Delta x^2} - kC_{\text{n}}^{\text{t-1}} \ , \tag{C.3}$$

which we can rearrange to get to the known numerical implementation of the forward Euler, i.e.

$$C_{\text{n}}^{\text{t}} = C_{\text{n}}^{\text{t-1}} + \Delta t\left[D\frac{C_{\text{n-1}}^{\text{t-1}} - 2\,C_{\text{n}}^{\text{t-1}} + C_{\text{n+1}}^{\text{t-1}}}{\Delta x^2} - kC_{\text{n}}^{\text{t-1}}\right] \ . \tag{C.4}$$

C.2. Implicit Euler

We can also solve this equation implicitly. Essentially this means, using the current value of C to obtain the current value. This produces a coupling in space, i.e. C_{n} can no longer be solved independently, but is coupled to all other C_{n}. In order to see this, we spell out this way of solving the equation. In particular, when discretising the time, we now use t on both the left and the right hand-side of the equation:

$$\frac{C_{\mathrm{n}}^{\mathrm{t}} - C_{\mathrm{n}}^{\mathrm{t\text{-}1}}}{\Delta t} = D\frac{C_{\mathrm{n\text{-}1}}^{\mathrm{t}} - 2\,C_{\mathrm{n}}^{\mathrm{t}} + C_{\mathrm{n+1}}^{\mathrm{t}}}{\Delta x^2} - kC_{\mathrm{n}}^{\mathrm{t}}\ . \tag{C.5}$$

Rearranging, we obtain

$$C_{\mathrm{n}}^{\mathrm{t\text{-}1}} = C_{\mathrm{n}}^{\mathrm{t}} - \Delta t\left[D\frac{C_{\mathrm{n\text{-}1}}^{\mathrm{t}} - 2\,C_{\mathrm{n}}^{\mathrm{t}} + C_{\mathrm{n+1}}^{\mathrm{t}}}{\Delta x^2} - kC_{\mathrm{n}}^{\mathrm{t}}\right]\ . \tag{C.6}$$

If we impose no-flux boundary conditions, the equations at the boundaries read:

$$C_{0}^{\mathrm{t\text{-}1}} = C_{0}^{\mathrm{t}} - \Delta t\left[D\frac{-C_{0}^{\mathrm{t}} + C_{1}^{\mathrm{t}}}{\Delta x^2} - kC_{0}^{\mathrm{t}}\right]\ , \tag{C.7}$$

$$C_{\mathrm{N}}^{\mathrm{t\text{-}1}} = C_{\mathrm{N}}^{\mathrm{t}} - \Delta t\left[D\frac{C_{\mathrm{N\text{-}1}}^{\mathrm{t}} - C_{\mathrm{N}}^{\mathrm{t}}}{\Delta x^2} - kC_{\mathrm{N}}^{\mathrm{t}}\right]\ . \tag{C.8}$$

Expressing this system of equations in matrix notation, we find:

$$\mathbf{C}^{\mathrm{t\text{-}1}} = (\mathbb{1} - \Delta t\,\mathbf{M})\cdot\mathbf{C}^{\mathrm{t}}\ . \tag{C.9}$$

with

$$\mathbf{M} = \begin{bmatrix} -\frac{D}{\Delta x^2} - k & \frac{D}{\Delta x^2} & 0 & \dots & 0 & \\ \frac{D}{\Delta x^2} & \frac{-2\,D}{\Delta x^2} - k & \frac{D}{\Delta x^2} & 0 & 0 & \\ \dots & \dots & \dots & \dots & \dots & \dots \\ 0 & \frac{D}{\Delta x^2} & \frac{-2\,D}{\Delta x^2} - k & \frac{D}{\Delta x^2} & 0 & \\ 0 & \dots & 0 & \frac{D}{\Delta x^2} & 1 - \frac{D}{\Delta x^2} - k & \end{bmatrix}.$$

Thus, we can obtain C^{t} by inverting the matrix:

$$\mathbf{C}^{\mathrm{t}} = [\mathbb{1} - \Delta t\,\mathbf{M}]^{-1}\cdot\mathbf{C}^{\mathrm{t\text{-}1}}\ . \tag{C.10}$$

For a constant time step width Δt the matrix that is being inverted $(([\mathbb{1} - \Delta t\,\mathbf{M}])$ is independent of time. Thus, it only needs to be inverted once and the inverse can be used for all time steps: The next time step can always be obtained multiplying with the inverted matrix. Moreover, an implicit solver is numerically stable for an arbitrarily large choice of Δt [83].

Using the same approach, we can solve a diffusion/degradation problem with a local source s,

$$\mathbf{s} = \begin{bmatrix} s \\ \dots \\ s \\ 0 \\ \dots \\ 0 \end{bmatrix}$$

and obtain

$$\mathbf{C}^{\mathrm{t}} = [\mathbb{1} - \Delta t\, \mathbf{M}]^{-1} \cdot \left[\mathbf{C}^{\mathrm{t\text{-}1}} + \Delta t\, \mathbf{s}\right] \ . \tag{C.11}$$

C.3. Implicit-explicit Euler

The implicit method is very powerful to solve linear differential equations. However, it is not easily applicable to non-linear problems. One can, nonetheless, combine the implicit and the explicit approach in an implicit-explicit method. To this end, we divide the equation up in one part that we want to solve explicitly and one part that we want to solve implicitly [5]. In our case, those will be the non-linear and linear parts, respectively.

Consider the system we solved above plus a non-linear term $\mathbf{f}(\mathbf{C})$:

$$\frac{C_{\mathrm{n}}^{\mathrm{t}} - C_{\mathrm{n}}^{\mathrm{t\text{-}1}}}{\Delta t} = D \frac{C_{\mathrm{n\text{-}1}}^{\mathrm{t}} - 2\, C_{\mathrm{n}}^{\mathrm{t}} + C_{\mathrm{n+1}}^{\mathrm{t}}}{\Delta x^2} - k C_{\mathrm{n}}^{\mathrm{t}} + s + f(C_{\mathrm{n\text{-}1}}^{\mathrm{t\text{-}1}}, C_{\mathrm{n}}^{\mathrm{t\text{-}1}}, C_{\mathrm{n+1}}^{\mathrm{t\text{-}1}}) \ . \tag{C.12}$$

In matrix notation, the equation reads:

$$\frac{\mathbf{C}^{\mathrm{t}} - \mathbf{C}^{\mathrm{t\text{-}1}}}{\Delta t} = \mathbf{M} \cdot \mathbf{C}^{\mathrm{t}} + \mathbf{s} + \mathbf{f}(\mathbf{C}^{\mathrm{t\text{-}1}}) \ . \tag{C.13}$$

Using boundary conditions equivalent to Eqs. C.7 and C.8, $\mathbf{M}$ is given by Eq. C.10.

Solving for $\mathbf{C}^{\mathrm{t}}$, we obtain:

$$\Leftrightarrow \mathbf{C}^{\mathrm{t}} = (\mathbb{1} - \Delta t\,\mathbf{M})^{-1} \cdot \left[\mathbf{C}^{\text{t-1}} + \Delta t\left(\mathbf{s} + \mathbf{f}(\mathbf{C}^{\text{t-1}})\right)\right] \ . \tag{C.14}$$

That is, the linear part of the equation, specified by $\mathbf{M}$, is solved implicitly, while the non-linear part $(\mathbf{s} + \mathbf{f}(\mathbf{C}^{\text{t-1}}))$ is solved explicitly.

C.4. Steady-state solution

We can appreciate that the implicit-explicit solver gives the same steady-state solution as the explicit one when plugging in the respective solutions. At steady state, $\mathbf{C}$ does not change in time, thus $\mathbf{C}^{\text{t-1}} = \mathbf{C}^{\mathrm{t}} = \mathbf{C}^{\mathrm{t+1}} = \mathbf{C}^{*}$, where the star denotes the steady-state solution. Consider Eq. C.14 and its corresponding explicit form

$$\frac{\mathbf{C}^{\mathrm{t}} - \mathbf{C}^{\text{t-1}}}{\Delta t} = \mathbf{M} \cdot \mathbf{C}^{\text{t-1}} + \mathbf{s} + \mathbf{f}(\mathbf{C}^{\text{t-1}}) \tag{C.15}$$

$$\Leftrightarrow \mathbf{C}^{\mathrm{t}} = \mathbf{C}^{\text{t-1}} + \Delta t\left[\mathbf{M} \cdot \mathbf{C}^{\text{t-1}} + \mathbf{s} + \mathbf{f}(\mathbf{C}^{\text{t-1}})\right] \ . \tag{C.16}$$

In order to find the steady-state solution to either of these two equations, we would keep computing the next time-step as specified by the respective equations until $\mathbf{C}$ would no longer change in time. At this point, $\mathbf{C}^{\text{t-1}} = \mathbf{C}^{\mathrm{t}} = \mathbf{C}^{\mathrm{t+1}} = \mathbf{C}^{*}$. Plugging this numerically obtained steady-state solution $\mathbf{C}^{*}$ into Eq. C.16, we get

$$\mathbf{C}^{*} = \mathbf{C}^{*} + \Delta t\left[\mathbf{M} \cdot \mathbf{C}^{*} + \mathbf{s} + \mathbf{f}(\mathbf{C}^{*})\right] \tag{C.17}$$

$$\Leftrightarrow 0 = \Delta t\left[\mathbf{M} \cdot \mathbf{C}^{*} + \mathbf{s} + \mathbf{f}(\mathbf{C}^{*})\right] \ , \tag{C.18}$$

which is the definition of the steady state.

Equivalently, for the implicit-explicit scheme, we find

$$\mathbf{C}^{*} = (\mathbb{1} - \Delta t\,\mathbf{M})^{-1} \cdot \left[\mathbf{C}^{*} + \Delta t\left(\mathbf{s} + \mathbf{f}(\mathbf{C}^{*})\right)\right] \tag{C.19}$$

$$\Leftrightarrow 0 = \left[\mathbb{1} - (\mathbb{1} - \Delta t\mathbf{M})\right] \cdot \mathbf{C}^{*} + \Delta t\left[\mathbf{s} + \mathbf{f}(\mathbf{C}^{*})\right] \tag{C.20}$$

$$= \Delta t\left[\mathbf{M} \cdot \mathbf{C}^{*} + \mathbf{s} + \mathbf{f}(\mathbf{C}^{*})\right] \ , \tag{C.21}$$

which also is the definition of the steady state, showing that both schemes give the same steady-state solution. Since Δt can be chosen larger for the implicit-explicit solver without causing numerical instabilities [83], the steady state can be reached faster with this solver compared to the explicit Euler method. However, numerical stability is not the same as accuracy, i.e. the solver may reach the correct steady-state solution very efficiently, but the dynamics in between may be inaccurate if the time-steps are chosen too large.

We can test if the solver has reached steady state by inserting the result of the last time point of the solver into the steady-state equation and verifying that it solves the equation to a reasonable precision. In general, 'reasonable' in this context is close to machine precision. The machine precision in Python is 10^{-15} for floats. We consider the solution a veritable steady-state solution if the steady-state equation evaluates to $\leq \mathcal{O}(10^{-10})$ where the exact solution would evaluate to 0 (i.e. $\mathcal{O}(10^{-15})$ when using floats).

D. Numerical solution to the model

We can obtain the dynamic solution to our system numerically by starting from an initial condition and computing the time evolution. In order to obtain the concentration profile of the signalling molecules and effectors at time t , $\mathbf{a}^{\mathrm{t}}$, and $\mathbf{b}^{\mathrm{t}}$, respectively:

$$\mathbf{a}^{\mathrm{t}} = \begin{bmatrix} a_0^{\mathrm{t}} \\ \vdots \\ a_N^{\mathrm{t}} \end{bmatrix}, \mathbf{b}^{\mathrm{t}} = \begin{bmatrix} b_0^{\mathrm{t}} \\ \vdots \\ b_{N-1}^{\mathrm{t}} \end{bmatrix} , \tag{D.1}$$

where the upper index refers to the time step and bold fond indicates vector notation, we need both of their concentration profiles at time $t-1$, $\mathbf{a}^{\text{t-1}}$, and $\mathbf{b}^{\text{t-1}}$. We use a forward (explicit) Euler method (see [83] and Appendix C) to compute the (non-linear) dynamics of the concentration profile of the effector molecule. Specifically, we add the change in concentration during one time-step of length Δt to the current concentration profile $\mathbf{b}^{\text{t-1}}$:

$$\mathbf{b}^{\mathrm{t}} = \mathbf{b}^{\text{t-1}} + \Delta t \, \mathbf{G}(\mathbf{a}^{\text{t-1}}, \mathbf{b}^{\text{t-1}}) , \tag{D.2}$$

where the differential equation for the effector dynamic $\mathbf{G}(\mathbf{a}^{\text{t-1}}, \mathbf{b}^{\text{t-1}})$ is defined equivalently to Eq. 2.9:

$$[\mathbf{G}(\mathbf{a}^{\text{t-1}}, \mathbf{b}^{\text{t-1}})]_{\mathrm{n}} = \mathbf{s}_{\mathrm{B}} - k_{\mathrm{B}} \frac{1}{1 + \frac{a_n^{\text{t-1}} + a_{n+1}^{\text{t-1}}}{c_{\mathrm{A}}}} b_n^{\text{t-1}} . \tag{D.3}$$

To compute the dynamics of the signalling molecule, we use an implicit-explicit Euler method ([5], see C). In particular, we evaluate the linear parts (diffusion and degradation, described by the matrix $\mathbf{M}$) implicitly and the non-linear parts (feedback and constant source) explicitly (see [5] and appendix C for details on the method). This results in the following dynamics:

$$\mathbf{a}^{\text{t}} = (\mathbb{1} - \Delta t \mathbf{M})^{-1} \cdot \left[\mathbf{a}^{\text{t-1}} + \Delta t \; \mathbf{F}(\mathbf{b}^{\text{t-1}})\right] \; . \tag{D.4}$$

The non-linear part of the dynamics of the signalling molecule, $\mathbf{F}(\mathbf{b}^{\text{t-1}})$, is given by the constant production in the local source with rate s_{A} and the positive feedback according to Eq. 2.2. This results in:

$$[\mathbf{F}(\mathbf{b}^{\text{t-1}})]_{n \in [1,\dots,w-1]} = s_{\text{A}} + p\,\alpha^{\text{in}} \frac{b_{n-1}^{\text{t-1}}}{c_{\text{B}} + b_{n-1}^{\text{t-1}}} + (1-p)\,\alpha^{\text{in}} \frac{b_{n}^{\text{t-1}}}{c_{\text{B}} + b_{n}^{\text{t-1}}} \tag{D.5}$$

$$[\mathbf{F}(\mathbf{b}^{\text{t-1}})]_{w} = p\,s_{\text{A}} + p\,\alpha^{\text{in}} \frac{b_{n-1}^{\text{t-1}}}{c_{\text{B}} + b_{n-1}^{\text{t-1}}} + (1-p)\,\alpha^{\text{out}} \frac{b_{n}^{\text{t-1}}}{c_{\text{B}} + b_{n}^{\text{t-1}}} \tag{D.6}$$

$$[\mathbf{F}(\mathbf{b}^{\text{t-1}})]_{n \in [w+1,\dots,N-1]} = p\,\alpha^{\text{out}} \frac{b_{n-1}^{\text{t-1}}}{c_{\text{B}} + b_{n-1}^{\text{t-1}}} + (1-p)\,\alpha^{\text{out}} \frac{b_{n}^{\text{t-1}}}{c_{\text{B}} + b_{n}^{\text{t-1}}} \; . \tag{D.7}$$

The boundary conditions are specified equivalently to Eqs. 2.10, 2.11. This way, we can compute the dynamic solution to our model and in particular, for long times, the steady-state solution (Fig. 2.6).

E. Analytical approximate steady-state solution to the model

E.1. Linearisation of the steady-state equations for signalling molecule concentration

As described in Section 3.2, we linearise the steady-state equations for a_n^* (Eqs. 2.6 - 2.8, 3.1, 3.2, using Eq. 3.3) around the piece-wise constant steady-state solution given by a_c^in (Eq. 3.4) and $a_\mathrm{c}^\mathrm{out}$ (Eq. 3.5). To this end, we first express a_n^* as a small deviation from the respective constant steady-state solution (Eq. 3.6, Eq. 3.7). We then linearise the equations for small deviations from a_c^in and $a_\mathrm{c}^\mathrm{out}$, respectively, i.e. for small δa_n^*. Note that, when expanding around a_c^in or $a_\mathrm{c}^\mathrm{out}$, we are not linearising around a single point in space, but around every point in space at once. In this sense our computation is the discrete version of a functional derivative. As the Taylor expansion is linear, we can expand all terms individually and add the expansions in order to obtain the linearised version of the equation. In this case, only the positive feedback term is non-linear. Linearising this term, we obtain the linearised version of the system of steady-state equations:

$$\partial_t a_0^* = 0 = \frac{D}{(1-p)} \frac{-\delta a_0^* + \delta a_1^*}{\delta^2} - k_\mathrm{A} \delta a_0^* + \alpha^\mathrm{in} \frac{(\delta a_0^* + \delta a_1^*) \frac{c_\mathrm{A}\, c_\mathrm{B}\, k_\mathrm{B}}{s_\mathrm{B}}}{[c_\mathrm{A} + \frac{c_\mathrm{A}\, c_\mathrm{B}\, k_\mathrm{B}}{s_\mathrm{B}} + 2a_\mathrm{c}^\mathrm{in}]^2} \tag{E.1}$$

for $n \in [1, ..., (w-1)]$:

$$\begin{aligned} \partial_t a_n^* = 0 = {} & D \frac{\delta a_{n-1}^* - 2\delta a_n^* + \delta a_{n+1}^*}{\delta^2} - k_\mathrm{A} \delta a_n^* \\ & + p\, \alpha^\mathrm{in} \frac{(\delta a_{n-1}^* + \delta a_n^*) \frac{c_\mathrm{A}\, c_\mathrm{B}\, k_\mathrm{B}}{s_\mathrm{B}}}{[c_\mathrm{A} + \frac{c_\mathrm{A}\, c_\mathrm{B}\, k_\mathrm{B}}{s_\mathrm{B}} + 2a_\mathrm{c}^\mathrm{in}]^2} + (1-p)\, \alpha^\mathrm{in} \frac{(\delta a_n^* + \delta a_{n+1}^*) \frac{c_\mathrm{A}\, c_\mathrm{B}\, k_\mathrm{B}}{s_\mathrm{B}}}{[c_\mathrm{A} + \frac{c_\mathrm{A}\, c_\mathrm{B}\, k_\mathrm{B}}{s_\mathrm{B}} + 2a_\mathrm{c}^\mathrm{in}]^2} \end{aligned} \tag{E.2}$$

$$
\begin{aligned}
\partial_t a^*_w = 0 = {} & D\frac{-a_\mathrm{c}^\mathrm{in} + a_\mathrm{c}^\mathrm{out}}{\delta^2} - k_\mathrm{A}\, a_\mathrm{c}^\mathrm{in} + p\, s_\mathrm{A} \\
& + p\,\alpha^\mathrm{in}\frac{c_\mathrm{A} + 2a_\mathrm{c}^\mathrm{in}}{c_\mathrm{A} + \frac{c_\mathrm{A}\, c_\mathrm{B}\, k_\mathrm{B}}{s_\mathrm{B}} + 2a_\mathrm{c}^\mathrm{in}} + (1-p)\,\alpha^\mathrm{out}\frac{c_\mathrm{A} + a_\mathrm{c}^\mathrm{in} + a_\mathrm{c}^\mathrm{out}}{c_\mathrm{A} + \frac{c_\mathrm{A}\, c_\mathrm{B}\, k_\mathrm{B}}{s_\mathrm{B}} + a_\mathrm{c}^\mathrm{in} + a_\mathrm{c}^\mathrm{out}} \\
& + D\frac{\delta a^*_{w-1} - 2\delta a^*_w + \delta a^*_{w+1}}{\delta^2} - k_\mathrm{A}\delta a^*_w + p\,\alpha^\mathrm{in}\frac{(\delta a^*_{w-1} + \delta a^*_w)\frac{c_\mathrm{A}\, c_\mathrm{B}\, k_\mathrm{B}}{s_\mathrm{B}}}{[c_\mathrm{A} + \frac{c_\mathrm{A} + c_\mathrm{A}\, c_\mathrm{B}\, k_\mathrm{B}}{s_\mathrm{B}} + 2\, a_\mathrm{c}^\mathrm{in}]^2} \\
& + (1-p)\,\alpha^\mathrm{out}\frac{(\delta a^*_w + \delta a^*_{w+1})\frac{c_\mathrm{A}\, c_\mathrm{B}\, k_\mathrm{B}}{s_\mathrm{B}}}{[c_\mathrm{A} + \frac{c_\mathrm{A}\, c_\mathrm{B}\, k_\mathrm{B}}{s_\mathrm{B}} + a_\mathrm{c}^\mathrm{in} + a_\mathrm{c}^\mathrm{out}]^2}
\end{aligned}
\tag{E.3}
$$

$$
\begin{aligned}
\partial_t a^*_{w+1} = 0 = {} & D\frac{a_\mathrm{c}^\mathrm{in} - a_\mathrm{c}^\mathrm{out}}{\delta^2} - k_\mathrm{A} a_\mathrm{c}^\mathrm{out} + p\,\alpha^\mathrm{out}\frac{c_\mathrm{A} + a_\mathrm{c}^\mathrm{in} + a_\mathrm{c}^\mathrm{out}}{c_\mathrm{A} + \frac{c_\mathrm{A}\, c_\mathrm{B}\, k_\mathrm{B}}{s_\mathrm{B}} + a_\mathrm{c}^\mathrm{in} + a_\mathrm{c}^\mathrm{out}} \\
& + (1-p)\,\alpha^\mathrm{out}\,\frac{c_\mathrm{A} + 2a_\mathrm{c}^\mathrm{out}}{c_\mathrm{A} + \frac{c_\mathrm{A}\, c_\mathrm{B}\, k_\mathrm{B}}{s_\mathrm{B}} + 2a_\mathrm{c}^\mathrm{out}} \\
& + D\frac{\delta a^*_w - 2\delta a^*_{w+1} + \delta a^*_{w+2}}{\delta^2} - k_\mathrm{A}\delta a^*_{w+1} \\
& + p\,\alpha^\mathrm{out}\frac{(\delta a^*_w + \delta a^*_{w+1})\frac{c_\mathrm{A}\, c_\mathrm{B}\, k_\mathrm{B}}{s_\mathrm{B}}}{[c_\mathrm{A} + \frac{c_\mathrm{A}\, c_\mathrm{B}\, k_\mathrm{B}}{s_\mathrm{B}} + a_\mathrm{c}^\mathrm{in} + a_\mathrm{c}^\mathrm{out}]^2} + (1-p)\,\alpha^\mathrm{out}\,\frac{(\delta a^*_{w+1} + \delta a^*_{w+2})\frac{c_\mathrm{A}\, c_\mathrm{B}\, k_\mathrm{B}}{s_\mathrm{B}}}{[c_\mathrm{A} + \frac{c_\mathrm{A}\, c_\mathrm{B}\, k_\mathrm{B}}{s_\mathrm{B}} + 2a_\mathrm{c}^\mathrm{out}]^2}
\end{aligned}
\tag{E.4}
$$

for $n \in [(w+2), ..., (N-1)]$:

$$
\begin{aligned}
\partial_t a^*_n = 0 = {} & +D\frac{\delta a^*_{n-1} - 2\delta a^*_n + \delta a^*_{n+1}}{\delta^2} - k_\mathrm{A}\delta a^*_n \\
& + p\,\alpha^\mathrm{out}\frac{(\delta a^*_{n-1} + \delta a^*_n)\frac{c_\mathrm{A}\, c_\mathrm{B}\, k_\mathrm{B}}{s_\mathrm{B}}}{[c_\mathrm{A} + \frac{c_\mathrm{A}\, c_\mathrm{B}\, k_\mathrm{B}}{s_\mathrm{B}} + 2a_\mathrm{c}^\mathrm{out}]^2} + (1-p)\,\alpha^\mathrm{out}\frac{(\delta a^*_n + \delta a^*_{n+1})\frac{c_\mathrm{A}\, c_\mathrm{B}\, k_\mathrm{B}}{s_\mathrm{B}}}{[c_\mathrm{A} + \frac{c_\mathrm{A}\, c_\mathrm{B}\, k_\mathrm{B}}{s_\mathrm{B}} + 2a_\mathrm{c}^\mathrm{out}]^2}
\end{aligned}
\tag{E.5}
$$

$$
\partial_t a^*_N = 0 = \frac{D}{p}\,\frac{\delta a^*_{N-1} - \delta a^*_N}{b^2} - k_\mathrm{A}\,\delta a^*_N + \alpha^\mathrm{out}\frac{(\delta a^*_{N-1} + \delta a^*_N)\frac{c_\mathrm{A}\, c_\mathrm{B}\, k_\mathrm{B}}{s_\mathrm{B}}}{[c_\mathrm{A} + \frac{c_\mathrm{A}\, c_\mathrm{B}\, k_\mathrm{B}}{s_\mathrm{B}} + 2a_\mathrm{c}^\mathrm{out}]^2}\ . \tag{E.6}
$$

The term for the production of signalling molecules based on the positive feedback for cell w at steady-state is given by $\frac{b^*_w}{c_\mathrm{B} + b^*_w}$. When re-writing this using Eq. 3.3, it contains a^*_w and a^*_{w+1}. Therefore, it needs to be linearised around the sum of a_c^in and $a_\mathrm{c}^\mathrm{out}$. Thus, for a^*_w and a^*_{w+1}, the constant term does not vanish (see Eqs. E.3 and E.4) as it contains both a_c^in and $a_\mathrm{c}^\mathrm{out}$.

E.2. Solution to the linearised steady-state equations

The presented set of linearised steady-state equations (Eqs. E.1 - E.6), can be solved using an exponential Ansatz (Eqs. 3.8 and 3.9), repeated here for convenience:

$$\delta a_n^* = C_1^{\mathrm{in}} e^{n/\bar{\lambda}_1^{\mathrm{in}}} + C_2^{\mathrm{in}} e^{-n/\bar{\lambda}_2^{\mathrm{in}}} \quad \text{for } n \in [0, \dots, w] \tag{E.7}$$

$$\delta a_n^* = C_1^{\mathrm{out}} e^{n/\bar{\lambda}_1^{\mathrm{out}}} + C_2^{\mathrm{out}} e^{-n/\bar{\lambda}_2^{\mathrm{out}}} \quad \text{for } n \in [w+1, \dots, N]\ . \tag{E.8}$$

The length scales of the steady-state solution inside the source region ($\bar{\lambda}_{1,2}^{\mathrm{in}}$) are defined by Eqs. 3.8 and E.2. Re-writing Eq. E.2, we obtain:

$$\begin{aligned}
&\text{for } n \in [1, ..., (w-1)] : \\
0 = {}& \delta a_{n-1}^* \left[\frac{D}{\delta^2} + p\, \alpha^{\mathrm{in}} \frac{c_{\mathrm{A}}\, c_{\mathrm{B}}\, k_{\mathrm{B}}}{s_{\mathrm{B}}\, [c_{\mathrm{A}} + \frac{c_{\mathrm{A}}\, c_{\mathrm{B}}\, k_{\mathrm{B}}}{s_{\mathrm{B}}} + 2a_{\mathrm{c}}^{\mathrm{in}}]^2} \right] \\
&+ \delta a_{n+1}^* \left[\frac{D}{\delta^2} + (1-p)\, \alpha^{\mathrm{in}} \frac{c_{\mathrm{A}}\, c_{\mathrm{B}}\, k_{\mathrm{B}}}{s_{\mathrm{B}}\, [c_{\mathrm{A}} + \frac{c_{\mathrm{A}}\, c_{\mathrm{B}}\, k_{\mathrm{B}}}{s_{\mathrm{B}}} + 2a_{\mathrm{c}}^{\mathrm{in}}]^2} \right] \\
&+ \delta a_n^* \left[-\frac{2D}{\delta^2} - k_{\mathrm{A}} + \alpha^{\mathrm{in}} \frac{c_{\mathrm{A}}\, c_{\mathrm{B}}\, k_{\mathrm{B}}}{s_{\mathrm{B}}\, [c_{\mathrm{A}} + \frac{c_{\mathrm{A}}\, c_{\mathrm{B}}\, k_{\mathrm{B}}}{s_{\mathrm{B}}} + 2a_{\mathrm{c}}^{\mathrm{in}}]^2} \right]\ .
\end{aligned}$$

Defining

$$z^{\mathrm{in}} = \frac{c_{\mathrm{A}}\, c_{\mathrm{B}}\, k_{\mathrm{B}}}{s_{\mathrm{B}}\, [c_{\mathrm{A}} + \frac{c_{\mathrm{A}}\, c_{\mathrm{B}}\, k_{\mathrm{B}}}{s_{\mathrm{B}}} + 2a_{\mathrm{c}}^{\mathrm{in}}]^2}\ , \tag{E.9}$$

and plugging in a simplified version of the exponential ansatz ($\delta a_n^* = C^{\mathrm{in}} e^{n/\bar{\lambda}^{\mathrm{in}}}$), we obtain:

$$\begin{aligned}
0 = {}& \cosh\left(1/\bar{\lambda}^{\mathrm{in}}\right) \left[\frac{2\,D}{\delta^2} + \alpha^{\mathrm{in}}\, z^{\mathrm{in}} \right] + \sinh\left(1/\bar{\lambda}^{\mathrm{in}}\right) \left(-2\, p\, \alpha^{\mathrm{in}}\, z^{\mathrm{in}} + \alpha^{\mathrm{in}}\, z^{\mathrm{in}} \right) \\
&+ \left[-\frac{2D}{\delta^2} - k_{\mathrm{A}} + \alpha^{\mathrm{in}} z^{\mathrm{in}} \right]\ .
\end{aligned} \tag{E.10}$$

We aim to understand length scales much larger than the width of one cell, $1/\bar{\lambda} \ll 1$. Therefore, we can express cosh and sinh by the first terms of their

Taylor series expansions according to:

$$\cosh(x) = 1 + \frac{x^2}{2} + \mathcal{O}(x^4)\ ,$$
$$\sinh(x) = x + \mathcal{O}(x^3)\ .$$

Using these approximations, Eq. E.10 simplifies to:

$$0 = \frac{1}{(\bar{\lambda}^{\mathrm{in}})^2}\left[\frac{D}{\delta^2} + \alpha^{\mathrm{in}}\,\frac{z^{\mathrm{in}}}{2}\right] + \left(1/\bar{\lambda}^{\mathrm{in}}\right)\left[(1-2\,p)\,\alpha^{\mathrm{in}}\,z^{\mathrm{in}}\right] + \left[-k_{\mathrm{A}} + 2\,\alpha^{\mathrm{in}} z^{\mathrm{in}}\right]$$

$$\Rightarrow \frac{1}{\bar{\lambda}^{\mathrm{in}}_{1,2}} = \frac{-\left[(1-2\,p)\,\alpha^{\mathrm{in}}\,z^{\mathrm{in}}\right] \pm \sqrt{\left[(1-2\,p)\,\alpha^{\mathrm{in}}\,z^{\mathrm{in}}\right]^2 - 4\left[\frac{D}{\delta^2} + \alpha^{\mathrm{in}}\,\frac{z^{\mathrm{in}}}{2}\right]\left[-k_{\mathrm{A}} + 2\,\alpha^{\mathrm{in}} z^{\mathrm{in}}\right]}}{2\left[\frac{D}{\delta^2} + \alpha^{\mathrm{in}}\,\frac{z^{\mathrm{in}}}{2}\right]}$$

$$\Rightarrow \bar{\lambda}^{\mathrm{in}}_{1,2} = \frac{\frac{2\,D}{\delta^2} + \alpha^{\mathrm{in}}\,z^{\mathrm{in}}}{\left[(2\,p-1)\,\alpha^{\mathrm{in}}\,z^{\mathrm{in}}\right] \pm \sqrt{\left[(2\,p-1)\,\alpha^{\mathrm{in}}\,z^{\mathrm{in}}\right]^2 - 2\left[\frac{2\,D}{\delta^2} + \alpha^{\mathrm{in}}\,z^{\mathrm{in}}\right]\left[-k_{\mathrm{A}} + 2\,\alpha^{\mathrm{in}} z^{\mathrm{in}}\right]}}\ .$$

We chose to write the exponential ansatz as presented in Eq. 3.8, i.e. using $e^{-n/\bar{\lambda}^{\mathrm{in}}_2}$, in order to make it more obvious that this part of the solution is the decreasing exponential function. In accordance, we re-define $\bar{\lambda}^{\mathrm{in}}_2$ obtained using the simplified exponential ansatz ($\delta a^*_n = C^{\mathrm{in}} e^{n/\bar{\lambda}^{\mathrm{in}}}$) to:

$$\bar{\lambda}^{\mathrm{in}}_2 := -\frac{\frac{2\,D}{\delta^2} + \alpha^{\mathrm{in}}\,z^{\mathrm{in}}}{\left[(2\,p-1)\,\alpha^{\mathrm{in}}\,z^{\mathrm{in}}\right] - \sqrt{\left[(2\,p-1)\,\alpha^{\mathrm{in}}\,z^{\mathrm{in}}\right]^2 - 2\left[\frac{2\,D}{\delta^2} + \alpha^{\mathrm{in}}\,z^{\mathrm{in}}\right]\left[-k_{\mathrm{A}} + 2\,\alpha^{\mathrm{in}} z^{\mathrm{in}}\right]}}\ . \tag{E.11}$$

We determine $\bar{\lambda}^{\mathrm{out}}_{1,2}$ from Eq. E.5 in an equivalent way. The solution for $\bar{\lambda}^{\mathrm{out}}_2$ is given in the main text (Eq. 3.11). We define $\bar{\lambda}^{\mathrm{out}}_2$ as the length scale of the analytical approximate steady-state solution, as it describes the exponentially decreasing part of the profile outside of the source region and thus the one we are most interested in, see Section 3.2.

The constants in Eq. 3.8 and Eq. 3.9 are defined by the boundary conditions at $n = 0$ and $n = N$, as well as by the source/non-source interface at $n = w$ and $n = w + 1$ (Eqs. E.1, E.3, E.4, and E.6). Plugging the exponential ansatz

(Eqs. 3.8 and 3.9) into Eqs. E.1, E.3, E.4, and E.6, we obtain:

$$\begin{pmatrix} \partial_t a_0^* \\ \partial_t a_w^* \\ \partial_t a_{w+1}^* \\ \partial_t a_N^* \end{pmatrix} = 0 = \begin{pmatrix} M_{11} & M_{12} & 0 & 0 \\ M_{21} & M_{22} & M_{23} & M_{24} \\ M_{31} & M_{32} & M_{33} & M_{34} \\ 0 & 0 & M_{43} & M_{44} \end{pmatrix} \cdot \begin{pmatrix} C_1^{\mathrm{in}} \\ C_2^{\mathrm{in}} \\ C_1^{\mathrm{out}} \\ C_2^{\mathrm{out}} \end{pmatrix} + \begin{pmatrix} s_1 \\ s_2 \\ s_3 \\ s_4 \end{pmatrix} \tag{E.12}$$

$$= \mathbf{M} \cdot \mathbf{c} + \mathbf{s} \; . \tag{E.13}$$

Thus, the constants in $\mathbf{c}$ are given as:

$$\Leftrightarrow \mathbf{c} = \mathbf{M^{-1}} \cdot (-\mathbf{s}) \; . \tag{E.14}$$

The explicit values of $\mathbf{M}$, $\mathbf{c}$, and $\mathbf{s}$ read:

$$s_1 = 0$$

$$s_2 = D \frac{-a_{\mathrm{c}}^{\mathrm{in}} + a_{\mathrm{c}}^{\mathrm{out}}}{\delta^2} - k_{\mathrm{A}} a_{\mathrm{c}}^{\mathrm{in}} + p\, s_{\mathrm{A}} + p\, \alpha^{\mathrm{in}} \frac{c_{\mathrm{A}} + 2a_{\mathrm{c}}^{\mathrm{in}}}{c_{\mathrm{A}} + \frac{c_{\mathrm{A}}\, c_{\mathrm{B}}\, k_{\mathrm{B}}}{s_{\mathrm{B}}} + 2a_{\mathrm{c}}^{\mathrm{in}}}$$

$$+ (1-p)\, \alpha^{\mathrm{out}} \frac{c_{\mathrm{A}} + a_{\mathrm{c}}^{\mathrm{in}} + a_{\mathrm{c}}^{\mathrm{out}}}{c_{\mathrm{A}} + \frac{c_{\mathrm{A}}\, c_{\mathrm{B}}\, k_{\mathrm{B}}}{s_{\mathrm{B}}} + a_{\mathrm{c}}^{\mathrm{in}} + a_{\mathrm{c}}^{\mathrm{out}}}$$

$$s_3 = D \frac{a_{\mathrm{c}}^{\mathrm{in}} - a_{\mathrm{c}}^{\mathrm{out}}}{\delta^2} - k_{\mathrm{A}} a_{\mathrm{c}}^{\mathrm{out}} + p\, \alpha^{\mathrm{out}} \frac{c_{\mathrm{A}} + a_{\mathrm{c}}^{\mathrm{in}} + a_{\mathrm{c}}^{\mathrm{out}}}{c_{\mathrm{A}} + \frac{c_{\mathrm{A}}\, c_{\mathrm{B}}\, k_{\mathrm{B}}}{s_{\mathrm{B}}} + a_{\mathrm{c}}^{\mathrm{in}} + a_{\mathrm{c}}^{\mathrm{out}}}$$

$$+ (1-p)\, \frac{c_{\mathrm{A}} + 2a_{\mathrm{c}}^{\mathrm{out}}}{c_{\mathrm{A}} + \frac{c_{\mathrm{A}}\, c_{\mathrm{B}}\, k_{\mathrm{B}}}{s_{\mathrm{B}}} + 2a_{\mathrm{c}}^{\mathrm{out}}}$$

$$s_4 = 0$$

$$M_{11} = \left(-\frac{D}{(1-p)\,\delta^2} - k_{\mathrm{A}} + \alpha^{\mathrm{in}} \frac{\frac{c_{\mathrm{A}}\, c_{\mathrm{B}}\, k_{\mathrm{B}}}{s_{\mathrm{B}}}}{[c_{\mathrm{A}} + \frac{c_{\mathrm{A}}\, c_{\mathrm{B}}\, k_{\mathrm{B}}}{s_{\mathrm{B}}} + 2a_{\mathrm{c}}^{\mathrm{in}}]^2} \right) e^{0/\bar{\lambda}_1^{\mathrm{in}}}$$

$$+ \left(\frac{D}{(1-p)\,\delta^2} + \alpha^{\mathrm{in}} \frac{\frac{c_{\mathrm{A}}\, c_{\mathrm{B}}\, k_{\mathrm{B}}}{s_{\mathrm{B}}}}{[c_{\mathrm{A}} + \frac{c_{\mathrm{A}}\, c_{\mathrm{B}}\, k_{\mathrm{B}}}{s_{\mathrm{B}}} + 2a_{\mathrm{c}}^{\mathrm{in}}]^2} \right) e^{1/\bar{\lambda}_1^{\mathrm{in}}}$$

$$M_{12} = \left(-\frac{D}{(1-p)\,\delta^2} - k_{\mathrm{A}} + \alpha^{\mathrm{in}} \frac{\frac{c_{\mathrm{A}}\, c_{\mathrm{B}}\, k_{\mathrm{B}}}{s_{\mathrm{B}}}}{[c_{\mathrm{A}} + \frac{c_{\mathrm{A}}\, c_{\mathrm{B}}\, k_{\mathrm{B}}}{s_{\mathrm{B}}} + 2a_{\mathrm{c}}^{\mathrm{in}}]^2} \right) e^{-0/\bar{\lambda}_2^{\mathrm{in}}}$$

$$+ \left(\frac{D}{(1-p)\,\delta^2} + \alpha^{\mathrm{in}} \frac{\frac{c_{\mathrm{A}}\, c_{\mathrm{B}}\, k_{\mathrm{B}}}{s_{\mathrm{B}}}}{[c_{\mathrm{A}} + \frac{c_{\mathrm{A}}\, c_{\mathrm{B}}\, k_{\mathrm{B}}}{s_{\mathrm{B}}} + 2a_{\mathrm{c}}^{\mathrm{in}}]^2} \right) e^{-1/\bar{\lambda}_2^{\mathrm{in}}}$$

$$M_{21} = \left(\frac{D}{\delta^2} + p\, \alpha^{\mathrm{in}} \frac{\frac{c_{\mathrm{A}}\, c_{\mathrm{B}}\, k_{\mathrm{B}}}{s_{\mathrm{B}}}}{[c_{\mathrm{A}} + \frac{c_{\mathrm{A}}\, c_{\mathrm{B}}\, k_{\mathrm{B}}}{s_{\mathrm{B}}} + 2a_{\mathrm{c}}^{\mathrm{in}}]^2} \right) e^{(w-1)/\bar{\lambda}_1^{\mathrm{in}}}$$

$$
\begin{aligned}
&+\Bigg(-\frac{2D}{\delta^2}-k_{\mathrm{A}}+p\,\alpha^{\mathrm{in}}\frac{\frac{c_{\mathrm{A}}\,c_{\mathrm{B}}\,k_{\mathrm{B}}}{s_{\mathrm{B}}}}{[c_{\mathrm{A}}+\frac{c_{\mathrm{A}}\,c_{\mathrm{B}}\,k_{\mathrm{B}}}{s_{\mathrm{B}}}+2a_{\mathrm{c}}^{\mathrm{in}}]^2}\\
&+(1-p)\,\alpha^{\mathrm{out}}\frac{\frac{c_{\mathrm{A}}\,c_{\mathrm{B}}\,k_{\mathrm{B}}}{s_{\mathrm{B}}}}{[c_{\mathrm{A}}+\frac{c_{\mathrm{A}}\,c_{\mathrm{B}}\,k_{\mathrm{B}}}{s_{\mathrm{B}}}+a_{\mathrm{c}}^{\mathrm{in}}+a_{\mathrm{c}}^{\mathrm{out}}]^2}\Bigg)\,e^{w/\bar{\lambda}_1^{\mathrm{in}}}
\end{aligned}
$$

$$
\begin{aligned}
M_{22}={}&\Bigg(\frac{D}{\delta^2}+p\,\alpha^{\mathrm{in}}\frac{\frac{c_{\mathrm{A}}\,c_{\mathrm{B}}\,k_{\mathrm{B}}}{s_{\mathrm{B}}}}{[c_{\mathrm{A}}+\frac{c_{\mathrm{A}}\,c_{\mathrm{B}}\,k_{\mathrm{B}}}{s_{\mathrm{B}}}+2a_{\mathrm{c}}^{\mathrm{in}}]^2}\Bigg)\,e^{-(w-1)/\bar{\lambda}_2^{\mathrm{in}}}\\
&+\Bigg(-\frac{2D}{\delta^2}-k_{\mathrm{A}}+p\,\alpha^{\mathrm{in}}\frac{\frac{c_{\mathrm{A}}\,c_{\mathrm{B}}\,k_{\mathrm{B}}}{s_{\mathrm{B}}}}{[c_{\mathrm{A}}+\frac{c_{\mathrm{A}}\,c_{\mathrm{B}}\,k_{\mathrm{B}}}{s_{\mathrm{B}}}+2a_{\mathrm{c}}^{\mathrm{in}}]^2}\\
&+(1-p)\,\alpha^{\mathrm{out}}\frac{\frac{c_{\mathrm{A}}\,c_{\mathrm{B}}\,k_{\mathrm{B}}}{s_{\mathrm{B}}}}{[c_{\mathrm{A}}+\frac{c_{\mathrm{A}}\,c_{\mathrm{B}}\,k_{\mathrm{B}}}{s_{\mathrm{B}}}+a_{\mathrm{c}}^{\mathrm{in}}+a_{\mathrm{c}}^{\mathrm{out}}]^2}\Bigg)\,e^{-w/\bar{\lambda}_2^{\mathrm{in}}}\\
M_{23}={}&\Bigg(\frac{D}{\delta^2}+(1-p)\,\alpha^{\mathrm{out}}\frac{\frac{c_{\mathrm{A}}\,c_{\mathrm{B}}\,k_{\mathrm{B}}}{s_{\mathrm{B}}}}{[c_{\mathrm{A}}+\frac{c_{\mathrm{A}}\,c_{\mathrm{B}}\,k_{\mathrm{B}}}{s_{\mathrm{B}}}+a_{\mathrm{c}}^{\mathrm{in}}+a_{\mathrm{c}}^{\mathrm{out}}]^2}\Bigg)\,e^{(w+1)/\bar{\lambda}_1^{\mathrm{out}}}\\
M_{24}={}&\Bigg(\frac{D}{\delta^2}+(1-p)\,\alpha^{\mathrm{out}}\frac{\frac{c_{\mathrm{A}}\,c_{\mathrm{B}}\,k_{\mathrm{B}}}{s_{\mathrm{B}}}}{[c_{\mathrm{A}}+\frac{c_{\mathrm{A}}\,c_{\mathrm{B}}\,k_{\mathrm{B}}}{s_{\mathrm{B}}}+a_{\mathrm{c}}^{\mathrm{in}}+a_{\mathrm{c}}^{\mathrm{out}}]^2}\Bigg)\,e^{-(w+1)/\bar{\lambda}_2^{\mathrm{out}}}\\
M_{31}={}&\Bigg(\frac{D}{\delta^2}+p\,\alpha^{\mathrm{out}}\frac{\frac{c_{\mathrm{A}}\,c_{\mathrm{B}}\,k_{\mathrm{B}}}{s_{\mathrm{B}}}}{[c_{\mathrm{A}}+\frac{c_{\mathrm{A}}\,c_{\mathrm{B}}\,k_{\mathrm{B}}}{s_{\mathrm{B}}}+a_{\mathrm{c}}^{\mathrm{in}}+a_{\mathrm{c}}^{\mathrm{out}}]^2}\Bigg)\,e^{w/\bar{\lambda}_1^{\mathrm{in}}}\\
M_{32}={}&\Bigg(\frac{D}{\delta^2}+p\,\alpha^{\mathrm{out}}\frac{\frac{c_{\mathrm{A}}\,c_{\mathrm{B}}\,k_{\mathrm{B}}}{s_{\mathrm{B}}}}{[c_{\mathrm{A}}+\frac{c_{\mathrm{A}}\,c_{\mathrm{B}}\,k_{\mathrm{B}}}{s_{\mathrm{B}}}+a_{\mathrm{c}}^{\mathrm{in}}+a_{\mathrm{c}}^{\mathrm{out}}]^2}\Bigg)\,e^{-w/\bar{\lambda}_2^{\mathrm{in}}}\\
M_{33}={}&\Bigg(-\frac{2D}{\delta^2}-k_{\mathrm{A}}+p\,\alpha^{\mathrm{out}}\frac{\frac{c_{\mathrm{A}}\,c_{\mathrm{B}}\,k_{\mathrm{B}}}{s_{\mathrm{B}}}}{[c_{\mathrm{A}}+\frac{c_{\mathrm{A}}\,c_{\mathrm{B}}\,k_{\mathrm{B}}}{s_{\mathrm{B}}}+a_{\mathrm{c}}^{\mathrm{in}}+a_{\mathrm{c}}^{\mathrm{out}}]^2}\\
&+(1-p)\,\alpha^{\mathrm{out}}\frac{\frac{c_{\mathrm{A}}\,c_{\mathrm{B}}\,k_{\mathrm{B}}}{s_{\mathrm{B}}}}{[c_{\mathrm{A}}+\frac{c_{\mathrm{A}}\,c_{\mathrm{B}}\,k_{\mathrm{B}}}{s_{\mathrm{B}}}+2a_{\mathrm{c}}^{\mathrm{out}}]^2}\Bigg)\,e^{(w+1)/\bar{\lambda}_1^{\mathrm{out}}}\\
&+\Bigg(\frac{D}{\delta^2}+(1-p)\,\alpha^{\mathrm{out}}\frac{\frac{c_{\mathrm{A}}\,c_{\mathrm{B}}\,k_{\mathrm{B}}}{s_{\mathrm{B}}}}{[c_{\mathrm{A}}+\frac{c_{\mathrm{A}}\,c_{\mathrm{B}}\,k_{\mathrm{B}}}{s_{\mathrm{B}}}+2a_{\mathrm{c}}^{\mathrm{out}}]^2}\Bigg)\,e^{(w+2)/\bar{\lambda}_1^{\mathrm{out}}}\\
M_{34}={}&\Bigg(-\frac{2D}{\delta^2}-k_{\mathrm{A}}+p\,\alpha^{\mathrm{out}}\frac{\frac{c_{\mathrm{A}}\,c_{\mathrm{B}}\,k_{\mathrm{B}}}{s_{\mathrm{B}}}}{[c_{\mathrm{A}}+\frac{c_{\mathrm{A}}\,c_{\mathrm{B}}\,k_{\mathrm{B}}}{s_{\mathrm{B}}}+a_{\mathrm{c}}^{\mathrm{in}}+a_{\mathrm{c}}^{\mathrm{out}}]^2}\\
&+(1-p)\,\alpha^{\mathrm{out}}\frac{\frac{c_{\mathrm{A}}\,c_{\mathrm{B}}\,k_{\mathrm{B}}}{s_{\mathrm{B}}}}{[c_{\mathrm{A}}+\frac{c_{\mathrm{A}}\,c_{\mathrm{B}}\,k_{\mathrm{B}}}{s_{\mathrm{B}}}+2a_{\mathrm{c}}^{\mathrm{out}}]^2}\Bigg)\,e^{-(w+1)/\bar{\lambda}_2^{\mathrm{out}}}\\
&+\Bigg(\frac{D}{\delta^2}+(1-p)\,\alpha^{\mathrm{out}}\frac{\frac{c_{\mathrm{A}}\,c_{\mathrm{B}}\,k_{\mathrm{B}}}{s_{\mathrm{B}}}}{[c_{\mathrm{A}}+\frac{c_{\mathrm{A}}\,c_{\mathrm{B}}\,k_{\mathrm{B}}}{s_{\mathrm{B}}}+2a_{\mathrm{c}}^{\mathrm{out}}]^2}\Bigg)\,e^{-(w+2)/\bar{\lambda}_2^{\mathrm{out}}}\\
M_{43}={}&\Bigg(\frac{D}{p\,\delta^2}+\alpha^{\mathrm{out}}\frac{\frac{c_{\mathrm{A}}\,c_{\mathrm{B}}\,k_{\mathrm{B}}}{s_{\mathrm{B}}}}{[c_{\mathrm{A}}+\frac{c_{\mathrm{A}}\,c_{\mathrm{B}}\,k_{\mathrm{B}}}{s_{\mathrm{B}}}+2a_{\mathrm{c}}^{\mathrm{out}}]^2}\Bigg)\,e^{(N-1)/\bar{\lambda}_1^{\mathrm{out}}}
\end{aligned}
$$

$$+\left(-\frac{D}{p\,\delta^2}-k_\mathrm{A}+\alpha^\mathrm{out}\frac{\frac{c_\mathrm{A}\,c_\mathrm{B}\,k_\mathrm{B}}{s_\mathrm{B}}}{[c_\mathrm{A}+\frac{c_\mathrm{A}\,c_\mathrm{B}\,k_\mathrm{B}}{s_\mathrm{B}}+2a_\mathrm{c}^\mathrm{out}]^2}\right)e^{N/\bar{\lambda}_1^\mathrm{out}}$$

$$M_{44}=\left(\frac{D}{p\,\delta^2}+\alpha^\mathrm{out}\frac{\frac{c_\mathrm{A}\,c_\mathrm{B}\,k_\mathrm{B}}{s_\mathrm{B}}}{[c_\mathrm{A}+\frac{c_\mathrm{A}\,c_\mathrm{B}\,k_\mathrm{B}}{s_\mathrm{B}}+2a_\mathrm{c}^\mathrm{out}]^2}\right)e^{-(N-1)/\bar{\lambda}_2^\mathrm{out}}$$

$$+\left(-\frac{D}{p\,\delta^2}-k_\mathrm{A}+\alpha^\mathrm{out}\frac{\frac{c_\mathrm{A}\,c_\mathrm{B}\,k_\mathrm{B}}{s_\mathrm{B}}}{[c_\mathrm{A}+\frac{c_\mathrm{A}\,c_\mathrm{B}\,k_\mathrm{B}}{s_\mathrm{B}}+2a_\mathrm{c}^\mathrm{out}]^2}\right)e^{-N/\bar{\lambda}_2^\mathrm{out}}\;.$$

E.3. Steady-state length scale in the limit of an infinitely high feedback response

The length scale of the signalling gradient at steady-state (Eq. 3.11) approaches that of a diffusion/degradation system in the limit of an infinitely high feedback response. In this section, we show this by formally taking this limit. To this end, we take the limit of the individual terms. z^in depends on a_c^in, z^out depends on $a_\mathrm{c}^\mathrm{out}$. Starting with this piece-wise constant solution in the limit of an infinitely high feedback response, we find:

$$\lim_{\alpha^\mathrm{in}\to\infty}a_\mathrm{c}^\mathrm{in}=\frac{1}{2}\frac{\alpha^\mathrm{in}}{k_\mathrm{A}}+\sqrt{\frac{1}{4}\left[\frac{\alpha^\mathrm{in}}{k_\mathrm{A}}\right]^2+\frac{c_\mathrm{A}}{2k_\mathrm{A}}\alpha^\mathrm{in}} \tag{E.15}$$

$$\Rightarrow\lim_{\alpha^\mathrm{in}\to\infty}a_\mathrm{c}^\mathrm{in}\to\infty\;, \tag{E.16}$$

and similarly based on Eq. 3.5:

$$\lim_{\alpha^\mathrm{out}\to\infty}a_\mathrm{c}^\mathrm{out}\to\infty\;. \tag{E.17}$$

We thus use l'Hospital's rule to compute $\alpha^\mathrm{in}z^\mathrm{in}$ in the limit $\alpha^\mathrm{in}\to\infty$. Using Eq. E.9, we obtain:

$$\lim_{\alpha^\mathrm{in}\to\infty}\alpha^\mathrm{in}z^\mathrm{in}=\lim_{\alpha^\mathrm{in}\to\infty}\frac{c_\mathrm{A}\,c_\mathrm{B}\,k_\mathrm{B}}{s_\mathrm{B}}\frac{\partial_{\alpha^\mathrm{in}}\alpha^\mathrm{in}}{\partial_{\alpha^\mathrm{in}}[c_\mathrm{A}+\frac{c_\mathrm{A}\,c_\mathrm{B}\,k_\mathrm{B}}{s_\mathrm{B}}+2a_\mathrm{c}^\mathrm{in}]^2} \tag{E.18}$$

$$=\lim_{\alpha^\mathrm{in}\to\infty}\frac{c_\mathrm{A}\,c_\mathrm{B}\,k_\mathrm{B}}{s_\mathrm{B}}\frac{1}{2\,[c_\mathrm{A}+\frac{c_\mathrm{A}\,c_\mathrm{B}\,k_\mathrm{B}}{s_\mathrm{B}}+2a_\mathrm{c}^\mathrm{in}]\,2\,\partial_{\alpha^\mathrm{in}}a_\mathrm{c}^\mathrm{in}} \tag{E.19}$$

$$=\lim_{\alpha^\mathrm{in}\to\infty}\frac{c_\mathrm{A}\,c_\mathrm{B}\,k_\mathrm{B}}{s_\mathrm{B}}\frac{1}{6\,a_\mathrm{c}^\mathrm{in}\,\partial_{\alpha^\mathrm{in}}a_\mathrm{c}^\mathrm{in}}\;. \tag{E.20}$$

Based on Eq. 3.4, we find that:

$$\lim_{\alpha^{\text{in}} \to \infty} \partial_{\alpha^{\text{in}}} a_{\text{c}}^{\text{in}} = \frac{1}{2\, k_{\text{A}}} \ .$$

Thus, taken together:

$$\lim_{\alpha^{\text{in}} \to \infty} \alpha^{\text{in}} z^{\text{in}} = 0 \ .$$

Performing the same steps for $\alpha^{\text{out}} z^{\text{out}}$, we find:

$$\lim_{\alpha^{\text{out}} \to \infty} \alpha^{\text{out}} z^{\text{out}} = 0 \ .$$

Using this result, we can take the respective limits for all length scales in Eqs. 3.8 and 3.9:

$$\lim_{\alpha^{\text{in}} \to \infty} \bar{\lambda}_{1,2}^{\text{in}} = \sqrt{\frac{D/\delta^2}{k_{\text{A}}}} = \bar{\lambda}_{\text{Diff/Degr}} \ ,$$

as well as

$$\lim_{\alpha^{\text{in}} \to \infty} \bar{\lambda}_{1,2}^{\text{out}} = \sqrt{\frac{D/\delta^2}{k_{\text{A}}}} = \bar{\lambda}_{\text{Diff/Degr}} \ .$$

Thus, $\bar{\lambda}$ (Eq. 3.11) indeed collapses to the length scale of the diffusion/degradation mechanism in the limit of an infinity high feedback response.

E.4. Steady-state length scale in the limit of feedback saturation

The feedback response saturate when $b_n \gg c_{\text{B}}$. We can thus analyse the effect of saturation formally by taking the limit $c_{\text{B}} \to 0$. Starting with the piece-wise constant solution as above, based on Eq. 3.4, we find:

$$\lim_{cB \to 0} a_{\text{c}}^{\text{in}} = \frac{s_{\text{A}} + \alpha^{\text{in}}}{k_{\text{A}}} \ , \tag{E.21}$$

and analogously for $a_{\mathrm{c}}^{\mathrm{out}}$ based on Eq. 3.5:

$$\lim_{cB \to 0} a_{\mathrm{c}}^{\mathrm{out}} = \frac{\alpha^{\mathrm{out}}}{k_{\mathrm{A}}} \ . \tag{E.22}$$

Thus, based on Eq. E.9 and Eq. E.21, we find that

$$\lim_{cB \to 0} z^{\mathrm{in}} = 0 \ . \tag{E.23}$$

Similarly, based on Eq. 3.12 and Eq. E.22, we find that:

$$\lim_{cB \to 0} z^{\mathrm{out}} = 0 \ . \tag{E.24}$$

Thus, for finite feedback strengths $\alpha^{\mathrm{in/out}}$, based on Eq. 3.11, and the corresponding equations for the other length scales defined in 3.8 and 3.9 we find:

$$\lim_{cB \to 0} \bar{\lambda}_{1,2}^{\mathrm{in}} = \sqrt{\frac{D/\delta^2}{k_{\mathrm{A}}}} = \bar{\lambda}_{\mathrm{Diff/Degr}} \ , \tag{E.25}$$

$$\lim_{cB \to 0} \bar{\lambda}_{1,2}^{\mathrm{out}} = \sqrt{\frac{D/\delta^2}{k_{\mathrm{A}}}} = \bar{\lambda}_{\mathrm{Diff/Degr}} \ . \tag{E.26}$$

We thus see that in the limit of feedback saturation, the length scale approaches that of a diffusion/degradation mechanism.

E.5. Limit of a linear feedback response

In Section 3.3, we calculated the steady-state solution to the model in the limit of $b_n \ll c_{\mathrm{B}}$ (Eqs. 3.17 - 3.19). Formally, these equations are derived from Eqs. 2.6 - 2.8 by taking the limit $b_n/c_{\mathrm{B}} \ll 1$ of the Hill activator function (Eq. 3.16). This corresponds to analysing the initial linear increase of the Hill function far away from saturation. Hence, Eqs. 2.6 - 2.8 should be exactly represented by Eqs. 3.17 - 3.19 in the limit of $b_n/c_{\mathrm{B}} \to 0$. Here, we show that this is true for the steady-state solutions we obtained based on the respective sets of equations.

Both, the steady-state solution to the model in the limit of a linear feedback response (Eqs. 3.17 - 3.19), as well as the approximate steady-state solution to the non-linear model (Eqs. 3.8 - 3.9) are defined in a piecewise manner inside and outside of the source region. Inside the source region, the solution to the latter is defined by the constants a_c^in, $\bar{\lambda}_1^\mathrm{in}$, and $\bar{\lambda}_2^\mathrm{in}$; outside of the source region, it is defined by $a_\mathrm{c}^\mathrm{out}$, $\bar{\lambda}_1^\mathrm{out}$, and $\bar{\lambda}_2^\mathrm{out}$. In order to show that the model in the limit of a linear feedback response becomes an exact representation of the approximate steady-state solution to the non-linear model in the limit of $b_n/c_\mathrm{B} \to 0$, we thus need to show that the respective constants are equal in both models in this limit. In the following, we go through each of the constants defining the approximate steady-state solution to the non-linear model and show that they indeed collapse to those defining the steady-state solution to the model in the linear feedback response, when taking the limit $b_n/c_\mathrm{B} \to 0$.

In the limit $b_n/c_\mathrm{B} \to 0$, the Hill activator term $\frac{\alpha^\mathrm{in/out}}{c_\mathrm{B}}\, b_n\, \frac{1}{1+b_n/c_\mathrm{B}}$ goes to zero for finite values of b_n. In order to be able to study the approximate steady-state solution to the non-linear model in this limit, we choose $\alpha^\mathrm{in/out}$ such that $\frac{\alpha^\mathrm{in/out}}{c_\mathrm{B}} = \alpha_0^\mathrm{in/out} = \mathrm{const}$. That is, we express $\alpha^\mathrm{in/out}$ as a multiple of c_B.

In the following, we will first re-write the constants defining the approximate the steady-state solution to the non-linear model using $\alpha^\mathrm{in/out} = \alpha_0^\mathrm{in/out}\, c_\mathrm{B}$, then take the limit $b_n/c_\mathrm{B} \to 0$, and then show that they reduce to the constants defining the steady-state solution to the model in the limit of a linear feedback response.

Plugging $\frac{\alpha^\mathrm{in}}{c_\mathrm{B}} = \alpha_0^\mathrm{in}$ into Eq. 3.4, and rearranging, we obtain:

$$
\begin{aligned}
a_\mathrm{c}^\mathrm{in} = {} & \frac{1}{2}\Big(\frac{s_\mathrm{A}}{k_\mathrm{A}} - \frac{c_\mathrm{A}}{2}\Big) + \frac{1}{2} c_\mathrm{B} \Big[\frac{\alpha_0^\mathrm{in}}{k_\mathrm{A}} - \frac{c_\mathrm{A} k_\mathrm{B}}{2\, s_\mathrm{B}}\Big] \\
& + \frac{c_\mathrm{B}}{2}\Big\{\frac{1}{c_\mathrm{B}^2}\Big[\Big(\frac{s_\mathrm{A}}{k_\mathrm{A}} - \frac{c_\mathrm{A}}{2}\Big)^2 + \frac{2\, c_\mathrm{A}\, s_\mathrm{A}}{k_\mathrm{A}}\Big] \\
& + \frac{1}{c_\mathrm{B}}\Big[2\,\Big(\frac{s_\mathrm{A}}{k_\mathrm{A}} - \frac{c_\mathrm{A}}{2}\Big)\Big(\frac{\alpha_0^\mathrm{in}}{k_\mathrm{A}} - \frac{c_\mathrm{A}\, k_\mathrm{B}}{2\, s_\mathrm{B}}\Big) + \frac{2\, c_\mathrm{A}}{k_\mathrm{A}}\Big(\frac{s_\mathrm{A}\, k_\mathrm{B}}{s_\mathrm{B}} + \alpha_0^\mathrm{in}\Big)\Big] \\
& + \Big(\frac{\alpha_0^\mathrm{in}}{k_\mathrm{A}} - \frac{c_\mathrm{A}\, k_\mathrm{B}}{2\, s_\mathrm{B}}\Big)^2\Big\}^{1/2} .
\end{aligned}
$$

Simplify individual the individual terms:

$$
\Big(\frac{s_\mathrm{A}}{k_\mathrm{A}} - \frac{c_\mathrm{A}}{2}\Big)^2 + \frac{2\, c_\mathrm{A}\, s_\mathrm{A}}{k_\mathrm{A}} = \Big(\frac{s_\mathrm{A}}{k_\mathrm{A}} + \frac{c_\mathrm{A}}{2}\Big)^2 ,
$$

and

$$
\begin{aligned}
&2\,\Big(\frac{s_{\mathrm{A}}}{k_{\mathrm{A}}}-\frac{c_{\mathrm{A}}}{2}\Big)\Big(\frac{\alpha_0^{\mathrm{in}}}{k_{\mathrm{A}}}-\frac{c_{\mathrm{A}}\,k_{\mathrm{B}}}{2\,s_{\mathrm{B}}}\Big)+\frac{2\,c_{\mathrm{A}}}{k_{\mathrm{A}}}\Big(\frac{s_{\mathrm{A}}\,k_{\mathrm{B}}}{s_{\mathrm{B}}}+\alpha_0^{\mathrm{in}}\Big)\\
&=\frac{2\,s_{\mathrm{A}}\,\alpha_0^{\mathrm{in}}}{k_{\mathrm{A}}^2}+\frac{s_{\mathrm{A}}\,c_{\mathrm{A}}\,k_{\mathrm{B}}}{s_{\mathrm{B}}\,k_{\mathrm{A}}}+\frac{c_{\mathrm{A}}\,\alpha_0^{\mathrm{in}}}{k_{\mathrm{A}}}+\frac{c_{\mathrm{A}}^2\,k_{\mathrm{B}}}{2\,s_{\mathrm{B}}}\ ,
\end{aligned}
$$

we obtain:

$$
\begin{aligned}
a_{\mathrm{c}}^{\mathrm{in}}&=\frac{1}{2}\Big(\frac{s_{\mathrm{A}}}{k_{\mathrm{A}}}-\frac{c_{\mathrm{A}}}{2}\Big)+\frac{1}{2}c_{\mathrm{B}}\Big[\frac{\alpha_0^{\mathrm{in}}}{k_{\mathrm{A}}}-\frac{c_{\mathrm{A}}\,k_{\mathrm{B}}}{2\,s_{\mathrm{B}}}\Big]\\
&+\frac{c_{\mathrm{B}}}{2}\Big\{\frac{1}{c_{\mathrm{B}}^2}\Big(\frac{s_{\mathrm{A}}}{k_{\mathrm{A}}}+\frac{c_{\mathrm{A}}}{2}\Big)^2+\frac{1}{c_{\mathrm{B}}}\Big[2\frac{s_{\mathrm{A}}}{k_{\mathrm{A}}}\frac{\alpha_0^{\mathrm{in}}}{k_{\mathrm{A}}}+c_{\mathrm{A}}\Big(\frac{\alpha_0^{\mathrm{in}}}{k_{\mathrm{A}}}+\frac{s_{\mathrm{A}}}{k_{\mathrm{A}}}\frac{k_{\mathrm{B}}}{s_{\mathrm{B}}}\Big)+\frac{c_{\mathrm{A}}^2\,k_{\mathrm{B}}}{2s_{\mathrm{B}}}\Big]\\
&+\Big(\frac{\alpha_0^{\mathrm{in}}}{k_{\mathrm{A}}}-\frac{c_{\mathrm{A}}\,k_{\mathrm{B}}}{2\,s_{\mathrm{B}}}\Big)^2\Big\}^{1/2}\ .
\end{aligned}
$$

Taylor expanding the square root around $\frac{1}{c_{\mathrm{B}}}\to 0$ according to:

$$
\begin{aligned}
f(x)&=(ax^2+bx+c)^{1/2}\\
&\approx\sqrt{c}+\frac{1}{2}\frac{b}{\sqrt{c}}x\ ,
\end{aligned}
$$

where

$$
\begin{aligned}
x&=\frac{1}{c_{\mathrm{B}}}\\
a&=\Big(\frac{s_{\mathrm{A}}}{k_{\mathrm{A}}}+\frac{c_{\mathrm{A}}}{2}\Big)^2\\
b&=\Big[2\frac{s_{\mathrm{A}}}{k_{\mathrm{A}}}\frac{\alpha_0^{\mathrm{in}}}{k_{\mathrm{A}}}+c_{\mathrm{A}}\Big(\frac{\alpha_0^{\mathrm{in}}}{k_{\mathrm{A}}}+\frac{s_{\mathrm{A}}}{k_{\mathrm{A}}}\frac{k_{\mathrm{B}}}{s_{\mathrm{B}}}\Big)+\frac{c_{\mathrm{A}}^2\,k_{\mathrm{B}}}{2s_{\mathrm{B}}}\Big]\\
c&=\Big(\frac{\alpha_0^{\mathrm{in}}}{k_{\mathrm{A}}}-\frac{c_{\mathrm{A}}\,k_{\mathrm{B}}}{2\,s_{\mathrm{B}}}\Big)^2\ ,
\end{aligned}
$$

we find that

$$
a_{\mathrm{c}}^{\mathrm{in}}\approx\Big|\frac{\alpha_0^{\mathrm{in}}}{k_{\mathrm{A}}}-\frac{c_{\mathrm{A}}\,k_{\mathrm{B}}}{2\,s_{\mathrm{B}}}\Big|+\frac{1}{2}\frac{\Big[2\frac{s_{\mathrm{A}}}{k_{\mathrm{A}}}\frac{\alpha_0^{\mathrm{in}}}{k_{\mathrm{A}}}+c_{\mathrm{A}}\Big(\frac{\alpha_0^{\mathrm{in}}}{k_{\mathrm{A}}}+\frac{s_{\mathrm{A}}}{k_{\mathrm{A}}}\frac{k_{\mathrm{B}}}{s_{\mathrm{B}}}\Big)+\frac{c_{\mathrm{A}}^2\,k_{\mathrm{B}}}{2s_{\mathrm{B}}}\Big]}{\Big|\frac{\alpha_0^{\mathrm{in}}}{k_{\mathrm{A}}}-\frac{c_{\mathrm{A}}\,k_{\mathrm{B}}}{2\,s_{\mathrm{B}}}\Big|}\frac{1}{c_{\mathrm{B}}}\ . \tag{E.27}
$$

In order to evaluate the absolute values, we need to determine sign of $\left(\frac{\alpha_0^{\mathrm{in}}}{k_{\mathrm{A}}}-\frac{c_{\mathrm{A}}\,k_{\mathrm{B}}}{2\,s_{\mathrm{B}}}\right)$. As we will see in Chapter 5, the model in the limit of a linear feedback response only reaches a steady state if $\alpha^{\mathrm{in/out}}<\alpha^{\mathrm{crit}}$ (Eqs. 5.11, 5.12). Rewriting α^{crit} in terms of $\alpha_0^{\text{in/out}}$, we obtain:

$$\alpha_0^{\text{in}} < \frac{c_{\text{A}}\, k_{\text{A}}\, k_{\text{B}}}{2\, s_{\text{B}}} \ .$$

From here, we see:

$$\frac{\alpha_0^{\text{in}}}{k_{\text{A}}} - \frac{c_{\text{A}}\, k_{\text{B}}}{2\, s_{\text{B}}} < 0 \ ,$$

and thus:

$$|\frac{\alpha_0^{\text{in}}}{k_{\text{A}}} - \frac{c_{\text{A}}\, k_{\text{B}}}{2\, s_{\text{B}}}| = -\left(\frac{\alpha_0^{\text{in}}}{k_{\text{A}}} - \frac{c_{\text{A}}\, k_{\text{B}}}{2\, s_{\text{B}}}\right) \ .$$

Plugging this result into Eq. E.27 and rearranging, we obtain:

$$\Rightarrow a_{\text{c}}^{\text{in}} = \frac{s_{\text{A}} + \frac{\alpha_0^{\text{in}}\, s_{\text{B}}}{k_{\text{B}}}}{k_{\text{A}} - \frac{2\, \alpha_0^{\text{in}}\, s_{\text{B}}}{c_{\text{A}}\, k_{\text{B}}}} \ ,$$

which is equal to $a_{\text{c, lin}}^{\text{in}}$ (Eq. 3.22) using $\alpha^{\text{in}}/c_{\text{B}} = \alpha_0^{\text{in}}$. Thus, we confirmed that

$$\lim_{b_n/c_{\text{B}} \to 0} a_{\text{c}}^{\text{in}} = a_{\text{c, lin}}^{\text{in}} \ . \tag{E.28}$$

Taking the limit $\lim_{b_n/c_{\text{B}} \to 0} a_{\text{c}}^{\text{out}}$ ($a_{\text{c}}^{\text{out}}$ defined in Eq. 3.5), following the same steps as shown for a_{c}^{in} above, and using $\frac{\alpha^{\text{out}}}{c_{\text{B}}} = \alpha_0^{\text{out}}$, we obtain

$$\lim_{b_n/c_{\text{B}} \to 0} a_{\text{c}}^{\text{out}} = a_{\text{c}}^{\text{out}} \ . \tag{E.29}$$

Comparing the expressions for the length scale in the approximate stead-state solution (Eq. 3.11) to the one for the model in the limit of a linear feedback response (Eq. 3.24), we identify that the two expressions are equal if

$$\alpha^{\text{in}} z^{\text{in}} = \alpha^{\text{in}} \frac{s_{\text{B}}}{c_{\text{A}}\, c_{\text{B}}\, k_{\text{B}}} = \alpha_0^{\text{in}} \frac{s_{\text{B}}}{c_{\text{A}}\, k_{\text{B}}} \ ,$$

where z^{in} is given by Eq. E.9.

Using the result obtained for a_{c}^{in} in the limit $b_n/c_{\text{B}} \to 0$ (Eq. E.28), rearranging, and Taylor-expanding, we find:

$$\begin{aligned}\alpha^{\text{in}} z^{\text{in}} &\approx \frac{\alpha_0^{\text{in}}\, s_{\text{B}}}{c_{\text{A}}\, k_{\text{B}}}\Big[1 - 2\,\frac{s_{\text{B}}}{c_{\text{A}} k_{\text{B}}}\,\frac{1}{c_{\text{B}}}\big(c_{\text{A}} + 2 a^{\text{in}}_{\text{c, lin}} + O(\frac{1}{c_{\text{B}}})\big)\Big] \\ \Rightarrow \lim_{b_n/c_{\text{B}}\to 0} \alpha^{\text{in}} z^{\text{in}} &= \alpha_0^{\text{in}}\,\frac{s_{\text{B}}}{c_{\text{A}}\, k_{\text{B}}}\ ,\end{aligned}$$

and thus,

$$\lim_{b_n/c_{\text{B}}\to 0} \bar{\lambda}^{\text{in}}_{1,2} = \bar{\lambda}^{\text{in}}_{\text{lin }1,2}\ .$$

Performing the same steps as for $\bar{\lambda}^{\text{in}}$, we find

$$\lim_{b_n/c_{\text{B}}\to 0} \bar{\lambda}^{\text{out}}_{1,2} = \bar{\lambda}^{\text{out}}_{\text{lin }1,2}\ .$$

We have thus shown, that the approximate steady-state solution to the non-linear model collapses to the steady-state solution to the model in the limit of a linear feedback response, when taking the limit $\lim b_n/c_{\text{B}} \to 0$.

E.6. Shape of the signalling gradient at steady state

In order to analyse how the shape of the profile depends on the strength of the signalling-independent production in the source region with rate s_{A}, we analyse the threshold for gradient-shape change $\alpha^{\text{out}}_{\text{T}}$ (Eq. 3.32) in the limit of infinite and zero signalling-independent production in the source region.

In the limit $s_{\text{A}} \to 0$, we find:

$$\lim_{s_{\text{A}}\to 0} \alpha^{\text{out}}_{\text{T}} = \frac{1}{2\, c_{\text{A}}\, k_{\text{A}}\, s_{\text{B}}}\left[2\, c_{\text{A}}\, k_{\text{A}}\, s_{\text{B}}\, \alpha^{\text{in}}\right] \tag{E.30}$$

$$= \alpha^{\text{in}}\ . \tag{E.31}$$

Thus, in the absence of signalling-independent production in the source region, the feedback strength outside of the source region must be smaller than inside of the source region ($\alpha^{\text{out}} < \alpha^{\text{in}}$) in order to obtain decreasing steady-state concentration profiles.

In the limit $s_\mathrm{A} \to \infty$ we find:

$$
\begin{aligned}
\lim_{s_\mathrm{A}\to\infty} \alpha_\mathrm{T}^\mathrm{out} = \lim_{s_\mathrm{A}\to\infty} \frac{1}{2 s_\mathrm{B}\, 2 s_\mathrm{A}} & \Bigg[c_\mathrm{A} k_\mathrm{A} (c_\mathrm{B} k_\mathrm{B} s_\mathrm{A} + s_\mathrm{B} s_\mathrm{A}) \\
& + s_\mathrm{A}\, s_\mathrm{B} \left(2 s_\mathrm{A} + k_\mathrm{A} \sqrt{\frac{c_\mathrm{A}^2 (c_\mathrm{B}\, k_\mathrm{B} + s_\mathrm{B})^2}{s_\mathrm{B}^2} + \frac{4 c_\mathrm{A} (c_\mathrm{B} k_\mathrm{B} s_\mathrm{A} + s_\mathrm{B} s_\mathrm{A})}{k_\mathrm{A} s_\mathrm{B}} + \frac{(2\, s_\mathrm{A})^2}{k_\mathrm{A}^2}} \right) \Bigg] \\
& = \lim_{s_\mathrm{A}\to\infty} \frac{1}{4\, s_\mathrm{B}} \Bigg[c_\mathrm{A} k_\mathrm{A} (c_\mathrm{B} k_\mathrm{B} + s_\mathrm{B}) \\
& + s_\mathrm{B} \left(2 s_\mathrm{A} + k_\mathrm{A} \sqrt{\left(\frac{c_\mathrm{A} (c_\mathrm{B}\, k_\mathrm{B} + s_\mathrm{B})}{s_\mathrm{B}} + \frac{(2\, s_\mathrm{A})}{k_\mathrm{A}} \right)^2} \right) \Bigg] \\
& = \lim_{s_\mathrm{A}\to\infty} \frac{1}{4\, s_\mathrm{B}} s_\mathrm{B} \Bigg[2 s_\mathrm{A} + 2\, s_\mathrm{A} \Bigg] \\
& = \lim_{s_\mathrm{A}\to\infty} s_\mathrm{A} \to \infty\ .
\end{aligned}
\tag{E.32}
$$

Thus, in the limit of infinitely strong signalling-independent production in the source region ($s_\mathrm{A} \to \infty$), the threshold for profile shape change diverges. In this case, the profiles always decrease, irrespective of how large α^out is compared to α^in, i.e. irrespective of the respective signalling-dependent production rates inside and outside of the source region. In particular, that means that for a large production rates s_A the feedback strength outside of the source region α^out can be larger than that inside of the source region α^in and yet a decreasing steady-state concentration profile can be obtained.

F. Definition of length scale based on the numerical steady-state solution

In order to verify the finding that the length scale of the steady-state profile reaches a maximum at the critical feedback strength for a given set of parameters, we compute the length scale of the steady-state solution obtained numerically. To this end, we need to define a profile length scale based on the numerical steady-state solution. We compute the length scale based on the second derivative of the profile. As discussed in Section 3.2, the steady-state profile outside of the source region is well described by a decreasing exponential. Thus, in order to obtain the length scale from the numerical steady-state solution, consider an exponentially decaying steady-state concentration profile C^* with amplitude C_0 and length scale λ:

$$C^* = C_0 \, e^{-x/\lambda} \; .$$

Its length scale can be obtained numerically based on its second spatial derivative:

$$\partial_{x^2} C^* = \frac{1}{\lambda^2} \, C_0 \, e^{-x/\lambda} \; ,$$

and thus

$$\lambda = \sqrt{\frac{C^*}{\partial_{x^2} C^*}} \; . \tag{F.1}$$

However, the steady-state profile of our system outside of the source region is not just a simple exponentially decaying profile: It has a constant offset, i.e. it does not decay to zero (see Fig. 3.3). Therefore, we need to subtract the offset, given by a_N, before we can use Eq. F.1 to estimate the length scale of the numerically obtained steady-state profile. Note that this offset is related to $a_{\mathrm{c}}^{\mathrm{out}}$ in Eq. 3.7. In particular, $a_N = a_{\mathrm{c}}^{\mathrm{out}}$ if $N \gg \bar{\lambda}$.

After subtracting the offset a_N, we compute the length scale of the profile according to Eq. F.1. This way, we define $\bar{\lambda}_{\mathrm{num}}$. This allows comparing the values of $\bar{\lambda}$ defined by the analytical approximate steady-state solution (Eq. 3.11) to a quantity based on the numerical steady-state solution. We find a good qualitative and partially quantitative agreement between the length scales computed based on the numerical steady-state solution and the analytical approximate steady-state solution (Fig. 3.7). In particular, the length scale obtained from the analytical approximate steady-state solution quantitatively agrees well with the length scale computed based on the numerical steady-state solution for non-critical feedback strengths. Using the numerical approach, we confirm the finding that the system reaches a maximal feedback strength for given set of parameters at the critical feedback strength (Fig. 3.7). However, we see that the profile length scale is overestimated by the analytical approximate steady-state solution at this point (Fig. 3.7).

G. Dynamic solution in the limit of a linear feedback response

G.1. Approximate dynamic solution to the model in the limit of a linear feedback response

In order to solve the dynamic equations of the system in the limit of a linear feedback response (Eqs. 5.1, 5.2), we need to solve the dynamic equations for δa_n and δb_n, gathered in Eq. 5.4, that we repeat here for convenience:

$$\partial_t \boldsymbol{\delta x} = \boldsymbol{M} \ \cdot \ \boldsymbol{\delta x} \ , \quad \text{where } \boldsymbol{\delta x} = \begin{bmatrix} \delta a_0 \\ \delta b_0 \\ \vdots \\ \delta a_{N-1} \\ \delta b_{N-1} \\ \delta a_N \end{bmatrix} . \tag{G.1}$$

The matrix $\boldsymbol{M}$ in Eq. 5.4 is defined by the dynamics equations for δa_n and δb_n. The dynamic equations for δa_n are given by Eqs. 3.17 - 3.19. Using Eqs. 5.1 and 5.2, they read:

$$\partial_t \delta a_0 = \frac{D}{(1-p)} \frac{(-\delta a_0 + \delta a_1)}{\delta^2} - k_\mathrm{A} \delta a_0 + \frac{\alpha^{\mathrm{in}}}{c_\mathrm{B}} \delta b_0 \tag{G.2}$$

for $n \in [1, ..., (w-1)]$:

$$\begin{aligned} \partial_t \delta a_n &= D \, \frac{(\delta a_{n-1} - 2\, \delta a_n + \delta a_{n+1})}{\delta^2} - k_\mathrm{A} \delta a_n \\ &\quad + p \, \frac{\alpha^{\mathrm{in}}}{c_\mathrm{B}} \, \delta b_{n-1} + (1-p) \, \frac{\alpha^{\mathrm{in}}}{c_\mathrm{B}} \, \delta b_n \end{aligned} \tag{G.3}$$

$$\partial_t \delta a_w = D \, \frac{(\delta a_{w-1} - 2\, \delta a_w + \delta a_{w+1})}{\delta^2} - k_\mathrm{A} \delta a_w$$

$$+\,p\,\frac{\alpha^{\mathrm{in}}}{c_{\mathrm{B}}}\,\delta b_{w-1} + (1-p)\,\frac{\alpha^{\mathrm{out}}}{c_{\mathrm{B}}}\,\delta b_{w} \tag{G.4}$$

for $n \in [(w+1), ..., (N-1)]$:

$$\partial_t \delta a_n = D\,\frac{(\delta a_{n-1} - 2\,\delta a_n + \delta a_{n+1})}{\delta^2} - k_{\mathrm{A}}\delta a_n +$$

$$+\,p\,\frac{\alpha^{\mathrm{out}}}{c_{\mathrm{B}}}\,\delta b_{n-1} + (1-p)\,\frac{\alpha^{\mathrm{out}}}{c_{\mathrm{B}}}\,\delta b_{n} \tag{G.5}$$

$$\partial_t \delta a_N = \frac{D}{p}\,\frac{(\delta a_{N-1} - \,\delta a_N)}{\delta^2} - k_{\mathrm{A}}\delta a_N \,+ \frac{\alpha^{\mathrm{out}}}{c_{\mathrm{B}}}\,\delta b_{N-1}\ . \tag{G.6}$$

In order to obtain the dynamic equation for δb_n, we linearise the dynamic equation for b_n (Eq. 2.9) around the steady-state solution. We obtain:

$$\partial_t \delta b_n = \frac{c_{\mathrm{A}}}{c_{\mathrm{A}} + a^*_n + a^*_{n+1}} \left(\frac{s_{\mathrm{B}}}{c_{\mathrm{A}}}(\delta a_n + \delta a_{n+1}) - k_{\mathrm{B}}\delta b_n \right)\ . \tag{G.7}$$

In order to solve Eq. 5.4, we diagonalise $\boldsymbol{M}$. To this end, we solve the eigenvalue problem:

$$\boldsymbol{v}^{\mathrm{l}}_{\boldsymbol{i}} \cdot\ \boldsymbol{M} = -\frac{1}{\tau_i}\boldsymbol{v}^{\mathrm{l}}_{\boldsymbol{i}}\ ,$$

$$\boldsymbol{M} \cdot\ \boldsymbol{v}^{\mathrm{r}}_{\boldsymbol{i}} = -\frac{1}{\tau_i}\boldsymbol{v}^{\mathrm{r}}_{\boldsymbol{i}}\ ,$$

where $\boldsymbol{M}$ is given by Eq. 5.4 and $\boldsymbol{v}^{\mathrm{l}}_{\boldsymbol{i}}$ and $\boldsymbol{v}^{\mathrm{r}}_{\boldsymbol{i}}$ denote the left and right eigenvector to the eigenvalue $-\frac{1}{\tau_i}$, respectively. We need to distinguish between the left and the right eigenvectors, since M is not symmetric (see Section G.2) and hence the right eigenvalues are not necessarily orthogonal to their transpose

$$\boldsymbol{v}^{\mathrm{l}}_{\boldsymbol{i}} \neq (\boldsymbol{v}^{\mathrm{r}}_{\boldsymbol{i}})^T\ .$$

For any matrix including $\boldsymbol{M}$, the left and right eigenvector to the same eigenvalue are orthogonal to each other, that is:

$$\boldsymbol{v}^{\mathrm{l}}_{\boldsymbol{m}} \cdot\ \boldsymbol{v}^{\mathrm{r}}_{\boldsymbol{i}} = \begin{cases} 0 & \text{for } m \neq n \\ r \in \mathbb{R} & \text{for } m = n\ . \end{cases} \tag{G.8}$$

The coefficients K_i are determined by the initial conditions $\mathbf{a}(0)$ and $\mathbf{b}(0)$ for the signalling molecule and effector concentration, respectively. Gathering these initial conditions, as well as the steady-state solution in respective vectors similar to what we did for δx:

$$\boldsymbol{x}(0) = \begin{bmatrix} a_0(0) \\ b_0(0) \\ \vdots \\ a_{N-1}(0) \\ b_{N-1}(0) \\ a_N(0) \end{bmatrix} , \ \boldsymbol{x}^* = \begin{bmatrix} a_0^* \\ b_0^* \\ \vdots \\ a_{N-1}^* \\ b_{N-1}^* \\ a_N^* \end{bmatrix} , \tag{G.9}$$

we obtain the K_i according to:

$$K_i = \frac{1}{r} \left[\boldsymbol{v}_{\boldsymbol{i}}^{\mathrm{l}} \cdot (\boldsymbol{x}(0) - \boldsymbol{x}^*) \right] .$$

That is, we compute the K_i by projecting the initial condition onto the corresponding elements of the left eigenvector and normalising to $\boldsymbol{v}_{\boldsymbol{i}}^{\mathrm{l}} \cdot \boldsymbol{v}_{\boldsymbol{i}}^{\mathrm{r}} = r$ (see Eq. G.8). Note that we use the *left* eigenvectors to compute the K_i as we used the *right* ones to obtain the Eigenmodes.

G.2. Symmetry considerations

Note that $\boldsymbol{M}$ (Eq. 5.4) is not symmetric. This is due to the fact that the effect of δa_n on δb_n is different from the effect of δb_n on δa_n. Thus, $\mathbf{M}_{\mathrm{i,\,j}} \neq \mathbf{M}_{\mathrm{j,\,i}}$ and hence, $\mathbf{M}$ is not symmetric. In other words, the contribution from the neighbour-dependent production/degradation is not symmetric, while the contribution of the diffusion is.

If we re-order the matrix in such a way that we first write all the equations for $\partial_t \delta a_n$ followed by all the equations for δb_n, we observe the same phenomenon: The contributions of the diffusion for the equations for $\partial_t \delta a_n$ are now located on the diagonal and upper/lower off-diagonal of the upper half of the matrix and are symmetric corresponding to δa_n. Additionally, we find the effect of δb_n on δa_n in upper right quadrant of the matrix and the effect of δa_n on δb_n in the mirrored lower left quadrant of the matrix. Albeit the fact that the mutual effect of δb_n and δa_n on each other lie on mirror symmetric locations in the matrix, the entries are not the same as the effect of δb_n on δa_n is different from the effect of δa_n on δb_n. Thus, the matrix is not symmetric when re-ordered in this way, either. This makes sense, as the re-ordering was obtained by first swapping lines and then swapping columns, two operations that do not change the properties of the matrix.

Note further, that this is independent of the choice of discretisation. The descretisation we chose gives rise to the phenomenon that reaction terms directly lead to fluxes. The fact that the matrix is asymmetric, though, is simply due to the effect of δb_n on δa_n being different from the effect of δa_n on δb_n. That is, also a two component classic reaction-diffusion system gives rise to an asymmetric matrix as soon as the effect of δb_n on δa_n is different from the effect of δa_n on δb_n as this leads to the corresponding matrix elements having different values.

G.3. Analytical approximation to slowest relaxation time in the limit of no feedback

In the absence of positive feedback, we recover the relaxation time known for a diffusion/degradation mechanism (k_A^{-1}) and an additional relaxation time that depends on the dynamics of the effector b_n. We obtain these based on $\tau_{1,2}^\mathrm{in}$ by setting $\alpha^\mathrm{in} = 0$ and from $\tau_{1,2}^\mathrm{out}$ by setting $\alpha^\mathrm{out} = 0$.

$$(\tau_1^\mathrm{in})^{-1} = k_\mathrm{A} \tag{G.10}$$

$$\begin{aligned}(\tau_2^\mathrm{in})^{-1} &= \frac{k_\mathrm{B}\, c_\mathrm{A}}{c_\mathrm{A} + 2\, a_\mathrm{c}^\mathrm{in}} \\ &= \frac{k_\mathrm{B}\, c_\mathrm{A}}{c_\mathrm{A} + 2\, \frac{s_\mathrm{A}}{k_\mathrm{A}}}\ , \text{as } a_\mathrm{c}^\mathrm{in} = \frac{s_\mathrm{A}}{k_\mathrm{A}} \text{ for } \alpha^\mathrm{in} = 0 (\tau_1^\mathrm{out})^{-1} \qquad = k_\mathrm{A}\end{aligned} \tag{G.11}$$

$$\begin{aligned}(\tau_2^\mathrm{out})^{-1} &= \frac{k_\mathrm{B}\, c_\mathrm{A}}{c_\mathrm{A} + 2\, a_\mathrm{c}^\mathrm{out}} \\ &= k_\mathrm{B}\ , \text{ as } a_\mathrm{c}^\mathrm{out} = 0 \text{ for } \alpha = 0\ .\end{aligned} \tag{G.12}$$

List of Figures

1.1. Bilaterians have three body axes 3
1.2. The Spemann organiser 5
1.3. Turing patterns 6
1.4. The French flag model 7
1.5. Crick's model for gradient formation 8
1.6. The first observation of a morphogen gradient 9
1.7. Experimental evidence for concentration-dependent gene expression 10
1.8. The Dpp gradient in the *Drosophila* wing imaginal disk 11
1.9. The canonical Wnt signalling pathway 14
1.10. Regeneration and dynamic growth of the flatworm *Schmidtea mediterranea* 19
1.11. Planarian anatomy 20
1.12. Cell renewal in planarians 22
1.13. Patterning challenges posed by planarians 23
1.14. *Wnt* expression in planarians 24
1.15. Wnt signalling in planarians during homeostasis 26
1.16. Wnt signalling during planarian regeneration 30
1.17. A steady-state concentration profile generated by diffusion and degradation 33
1.18. A steady-state concentration profile generated by diffusion, degradation and drift 36
1.19. Scaling of morphogen gradients 38
1.20. An expander mechanism for gradient scaling 40

2.1. A cell-to-cell relay for signal propagation 44
2.2. A discrete model of signalling gradient formation 45
2.3. Model dynamics 46
2.4. Hill functions 47
2.5. The cell-to-cell relay mechanism 51

2.6. Numerical steady-state solution of our model 56

3.1. Steady-state solution for varying feedback strength 60
3.2. The piece-wise constant solution is reached far away from the boundaries 65
3.3. Analytical approximate steady-state solution 66
3.4. For $b_n \ll c_{\mathrm{B}}$, the Hill activator function can be approximated by a linear function 68
3.5. For large threshold concentrations c_{B}, the linear response limit is a good approximation 71
3.6. In the limit of a linear feedback response, the length scale diverges for a critical feedback strengths α^{crit} 72
3.7. The length scale reaches a maximum at the critical feedback strength α^{crit} 75
3.8. Possible steady-state profile shapes 77
3.9. Gradient shape varies qualitatively dependent on the ratio $a_{\mathrm{c}}^{\text{in}}/a_{\mathrm{c}}^{\text{out}}$ 79
3.10. The strength of the local source influences gradient shape 80
3.11. Piece-wise constant steady-state solution increases for increasing neighbour-dependent production rate 81

4.1. The length scale of the steady-state profiles scales with system size 86
4.2. The steady-state profiles scale with system size 89
4.3. Offset-corrected profiles exhibit close-to-perfect shape scaling . . . 91

5.1. Dynamic solution to the linearised model 99
5.2. Scaling of the slowest relaxation time with feedback strength . . . 104
5.3. Trade-off between length scale and time scale 106
5.4. Scaling of the relaxation time with length scale for $\delta\alpha^{\text{in}} = r\ (\delta\alpha^{\text{out}})^{\nu}$ 108

6.1. Secretion polarity influences profile length scale 113
6.2. Secretion polarity influences steady-state concentrations 114
6.3. The effect of secretion polarity is strongest close to the critical feedback strength 115
6.4. Effect of secretion polarity on trade-off between length scale and time scale 117

A.1. Symmetric continuous one-dimensional diffusion/degradation system125

B.1. Polarised secretion 131
B.2. Definition of the diffusive molecule flux 134
B.3. Illustration of the diffusive flux 134
B.4. Boundary effects 138

Bibliography

[1] K. Agata, Y. Soejima, K. Kato, C. Kobayashi, Y. Umesono, and K. Watanabe. Structure of the Planarian Central Nervous System (CNS) Revealed by Neuronal Cell Markers. *Zoological Science*, 15(3):433–440, 1998.

[2] D. Aguilar-Hidalgo, Z. Hadjivasilou, M. Romanova-Michaelides, M. González-Gaitán, and F. Jülicher. Dynamic modes of morphogen transport. *arXiv*, 2019.

[3] B. Alberts, A. Johnson, J. Lewis, D. Morgan, M. Raff, K. Roberts, and P. Walter. *Molecular biology of the cell.* Garland Science, New York, NY, 6 edition, 2015.

[4] C. Alexandre, A. Baena-Lopez, and J.-P. Vincent. Patterning and growth control by membrane-tethered Wingless. *Nature*, 505(7482):180–185, 2014.

[5] U. M. Ascher, S. J. Ruuth, and R. J. Spiteri. Implicit-explicit Runge-Kutta methods for time-dependent partial differential equations. *Applied Numerical Mathematics*, 25:151–167, 1997.

[6] J. Bagunia and R. Romero. Quantitative analysis of cell types during growth, degrowth and regeneration in the planarians Dugesia mediterranea and Dugesia tigrina. *Hydrobiologia*, 84:181–194, 1981.

[7] N. Barkai and D. Ben-Zvi. 'Big frog, small frog'- maintaining proportions in embryonic development: Delivered on 2 July 2008 at the 33rd FEBS Congress in Athens, Greece. *FEBS Journal*, 276(5):1196–1207, 2009.

[8] K. Bartscherer and M. Boutros. Regulation of Wnt protein secretion and its role in gradient formation. *EMBO Reports*, 9(10):977–982, 2008.

[9] C. Basquin, D. Ershov, N. Gaudin, H. T. K. Vu, B. Louis, J. F. Papon, A. M. Orfila, S. Mansour, J. C. Rink, and J. Azimzadeh. Emergence of a Bilaterally Symmetric Pattern from Chiral Components in the Planarian Epidermis. *Developmental Cell*, 51(4):516–525.e5, 2019.

[10] J. V. Beira and R. Paro. The legacy of Drosophila imaginal discs. *Chromosoma*, 125(4):573–592, 2016.

[11] D. Ben-Zvi and N. Barkai. Scaling of morphogen gradients by an expansion-repression integral feedback control. *Proceedings of the National Academy of Sciences of the United States of America*, 107(15):6924–6929, 2010.

[12] D. Ben-Zvi, G. Pyrowolakis, N. Barkai, and B. Z. Shilo. Expansion-repression mechanism for scaling the Dpp activation gradient in drosophila wing imaginal discs. *Current Biology*, 21(16):1391–1396, 2011.

[13] S. Bergmann, O. Sandler, H. Sberro, S. Shnider, E. Schejter, B. Z. Shilo, and N. Barkai. Pre-steady-state decoding of the bicoid morphogen gradient. *PLoS Biology*, 5(2):0232–0242, 2007.

[14] T. Berleth, M. Burri, G. Thoma, D. Bopp, S. Richstein, G. Frigerio, M. Noll, and C. Nüsslein-Volhard. The role of localization of bicoid RNA in organizing the anterior pattern of the Drosophila embryo. *The EMBO Journal*, 7(6):1749–1756, 1988.

[15] E. Bier and E. M. De Robertis. BMP gradients: A paradigm for morphogen-mediated developmental patterning. *Science*, 348(6242):1444–1455, 2015.

[16] B. W. Bisgrove and H. J. Yost. Classification of left-right patterning defects in zebrafish, mice, and humans. *American Journal of Medical Genetics*, 101(4):315–323, 2001.

[17] T. Bollenbach, K. Kruse, P. Pantazis, M. González-Gaitán, and F. Jülicher. Morphogen transport in epithelia. *Physical Review E - Statistical, Nonlinear, and Soft Matter Physics*, 75(1):1–16, 2007.

[18] J. P. Campanale, T. Y. Sun, and D. J. Montell. Development and dynamics of cell polarity at a glance. *Journal of Cell Science*, 130(7):1201–1207, 2017.

[19] F. Cebrià, T. Guo, J. Jopek, and P. A. Newmark. Regeneration and maintenance of the planarian midline is regulated by a slit orthologue. *Developmental Biology*, 307(2):394–406, 2007.

[20] F. Cebrià, M. Vispo, P. Newmark, D. Bueno, and R. Romero. Myocyte differentiation and body wall muscle regeneration in the planarian Girardia tigrina. *Development Genes and Evolution*, 207(5):306–316, 1997.

[21] G. Chai, C. Ma, K. Bao, L. Zheng, X. Wang, Z. Sun, E. Salò, T. Adell, and W. Wu. Complete functional segregation of planarian β-catenin-1 and -2 in mediating Wnt signaling and cell adhesion. *Journal of Biological Chemistry*, 285(31):24120–24130, 2010.

[22] S. M. Cohen and G. Jürgens. Mediation of Drosophila head development by gap-like segmentation genes. *Nature*, 346(6283):482–485, 1990.

[23] F. Crick. Diffusion in embryogenesis. *Nature*, 225(5233):671, 1970.

[24] W. Driever and C. Nüsslein-Volhard. A gradient of bicoid protein in Drosophila embryos. *Cell*, 54(1):83–93, 1988.

[25] W. Driever and C. Nüsslein-Volhard. The bicoid protein determines position in the Drosophila embryo in a concentration-dependent manner. *Cell*, 54(1):95–104, 1988.

[26] W. Driever and C. Nüsslein-Volhard. The bicoid protein is a positive regulator of hunchback transcription in the early Drosophila embryo. *Nature*, 337(6203):138–143, 1989.

[27] J. O. Dubuis, G. Tkacik, E. F. Wieschaus, T. Gregor, and W. Bialek. Positional information, in bits. *Proceedings of the National Academy of Sciences of the United States of America*, 110(41):16301–16308, 2013.

[28] C. T. Fincher, O. Wurtzel, T. de Hoog, K. M. Kravarik, and P. W. Reddien. Cell type transcriptome atlas for the planarian Schmidtea mediterranea. *Science*, 360(6391):1–12, 2018.

[29] R. Finkelstein and N. Perrimon. The orthodenticle gene is regulated by bicoid and torso and specifies Drosophila head development. *Nature*, 346(6283):485–488, 1990.

[30] P. Fried and D. Iber. Dynamic scaling of morphogen gradients on growing domains. *Nature Communications*, 5(5077):1–12, 2014.

[31] G. Frigerio, M. Burri, D. Bopp, S. Baumgartner, and M. Noll. Structure of the segmentation gene paired and the Drosophila PRD gene set as part of a gene network. *Cell*, 47(5):735–746, 1986.

[32] H. G. Frohnhöfer and C. Nüsslein-Volhard. Organization of anterior pattern in the Drosophila embryo by the maternal gene bicoid. *Nature*, 324(6093):120–125, 1986.

[33] M. A. Gaviño and P. W. Reddien. A Bmp/Admp regulatory circuit controls maintenance and regeneration of dorsal-ventral polarity in planarians. *Current Biology*, 21(4):294–299, 2011.

[34] A. Gierer, S. Berking, H. Bode, C. N. David, K. Flick, G. Hansmann, H. Schaller, and E. Trenkner. Regeneration of hydra from reaggregated cells. *Nature New Biology*, 239(91):98–101, 1972.

[35] S. F. Gilbert and M. J. Barresi. *Developmental biology*. Sinauer Associates, Inc., New York, NY, 11 edition, 2018.

[36] S. Grainger and K. Willert. Mechanisms of Wnt signaling and control. *Wiley Interdisciplinary Reviews: Systems Biology and Medicine*, 10(5):1–22, 2018.

[37] V. Greco, M. Hannus, and S. Eaton. Argosomes: A potential vehicle for the spread of morphogens through epithelia. *Cell*, 106(5):633–645, 2001.

[38] J. B. A. Green and J. C. Smith. Graded changes in dose of a Xenopus activin A homologue elicit stepwise transitions in embryonic cell fate. *Nature*, 34:391–394, 1990.

[39] T. Gregor, E. F. Wieschaus, A. P. Mcgregor, W. Bialek, and D. W. Tank. Stability and Nuclear Dynamics of the Bicoid Morphogen Gradient. *Cell*, 130:141–152, 2007.

[40] D. T. Grimes and R. D. Burdine. Left–Right Patterning: Breaking Symmetry to Asymmetric Morphogenesis. *Trends in Genetics*, 33(9):616–628, 2017.

[41] U. Grossniklaus, K. M. Cadigan, and W. J. Gehring. Three maternal coordinate systems cooperate in the patterning of the Drosophila head. *Development*, 120(11):3155–3171, 1994.

[42] J. B. Gurdon, P. Harger, A. Mitchell, and P. Lemaire. Activin signalling and response to a morphogen gradient. *Nature*, 371(6497):487–492, 1994.

[43] K. A. Gurley, S. A. Elliott, O. Simakov, H. A. Schmidt, T. W. Holstein, and A. S. Alvarado. Expression of secreted Wnt pathway components reveals unexpected complexity of the planarian amputation response. *Developmental Biology*, 347(1):24–39, 2010.

[44] K. A. Gurley, J. C. Rink, and A. Sanchez Alvarado. b-Catenin Defines Head Versus Tail Identity During Planarian Regeneration and Homeostasis. *Science*, 319(5861):323–327, 2008.

[45] H. Hamada. Breakthroughs and future challenges in left-right patterning. *Development Growth and Differentiation*, 50:71–78, 2008.

[46] B. Hobmayer, F. Rentzsch, K. Kuhn, C. M. Happel, C. C. Von Laue, P. Snyder, U. Rothbächer, and T. W. Holstein. WNT signalling molecules act in axis formation in the diploblastic metazoan Hydra. *Nature*, 407(6801):186–189, 2000.

[47] J. Howard. *Mechanics of Motor Proteins and the Cytoskeleton*. Sinauer Associates, Inc., Sunderland, 1 edition, 2001.

[48] J. Howard, S. W. Grill, and J. S. Bois. Turing's next steps: The mechanochemical basis of morphogenesis. *Nature Reviews Molecular Cell Biology*, 12(6):400–406, 2011.

[49] M. Iglesias, J. L. Gomez-Skarmeta, E. Salo, and T. Adell. Silencing of Smed-catenin1 generates radial-like hypercephalized planarians. *Development*, 135(7):1215–1221, 2008.

[50] M. Ivankovic, R. Haneckova, A. Thommen, M. A. Grohme, M. Vila-Farré, S. Werner, and J. C. Rink. Model systems for regeneration: Planarians. *Development*, 146:1–12, 2019.

[51] M. M. Jenkins. Bipolar planarians in a stock culture. *Science*, 142(3596):1187, 1963.

[52] K. Kato, H. Orii, K. Watanabe, and K. Agata. Dorsal and ventral positional cues required for the onset of planarian regeneration may reside in differentiated cells. *Developmental Biology*, 233(1):109–121, 2001.

[53] Y. Kato. The multiple roles of Notch signaling during left-right patterning. *Cellular and Molecular Life Sciences*, 68(15):2555–2567, 2011.

[54] A. Kicheva, P. Pantazis, T. Bollenbach, Y. Kalaidzidis, T. Bittig, F. Julicher, and M. Gonzalez-Gaitan. Kinetics of morphogen gradient formation. *Science*, 315(5811):521–525, 2007.

[55] R. Lander and C. Petersen. Wnt, Ptk7, and FGFRL expression gradients control trunk positional identity in planarian regeneration. *eLife*, 5(9):1689–1699, 2016.

[56] P. A. Lawrence and J. Casal. Planar cell polarity: Two genetic systems use one mechanism to read gradients. *Development*, 145(23):1–10, 2018.

[57] E. Lee, A. Salic, R. Krüger, R. Heinrich, and M. W. Kirschner. The roles of APC and axin derived from experimental and theoretical analysis of the Wnt pathway. *PLoS Biology*, 1(1):116–132, 2003.

[58] M. Levin. Left-right asymmetry in embryonic development: A comprehensive review. *Mechanisms of Development*, 122(1):3–25, 2005.

[59] S.-Y. Liu, C. Selck, B. Friedrich, R. Lutz, M. Vila-Farré, A. Dahl, H. Brandl, N. Lakshmanaperumal, I. Henry, and J. C. Rink. Reactivating head regrowth in a regeneration-deficient planarian species. *Nature*, 500(7460):81–84, 2013.

[60] M. Lucila Scimone, L. E. Cote, and P. W. Reddien. Orthogonal muscle fibres have different instructive roles in planarian regeneration. *Nature*, 551(7682):623–628, 2017.

[61] T. Malinauskas and E. Y. Jones. Extracellular modulators of Wnt signalling. *Current Opinion in Structural Biology*, 29:77–84, 2014.

[62] H. Meinhardt. Different strategies for midline formation in bilaterians. *Nature Reviews Neuroscience*, 5(6):502–510, 2004.

[63] Y. Mii and M. Taira. Secreted Frizzled-related proteins enhance the diffusion of Wnt ligands and expand their signalling range. *Development*, 136(24):4083–4088, 2009.

[64] R. Milo and R. Phillips. *Cell biology by the numbers*. Garland Science, New York, NY, 2016.

[65] M. D. Molina, A. Neto, I. Maeso, J. L. Gómez-Skarmeta, E. Saló, and F. Cebrià. Noggin and noggin-like genes control dorsoventral axis regeneration in planarians. *Current Biology*, 21(4):300–305, 2011.

[66] M. D. Molina, E. Saló, and F. Cebrià. The BMP pathway is essential for re-specification and maintenance of the dorsoventral axis in regenerating and intact planarians. *Developmental Biology*, 311(1):79–94, 2007.

[67] A. M. Molinaro and B. J. Pearson. In silico lineage tracing through single cell transcriptomics identifies a neural stem cell population in planarians. *Genome Biology*, 17(1):1–17, 2016.

[68] T. H. Morgan. Experimental studies of the regeneration of Planaria maculata. *Archiv für Entwickelungsmechanik der Organismen*, 7(2-3):364–397, 1898.

[69] T. H. Morgan. *Regeneration*. Macmillan, New York, NY, 1901.

[70] T. H. Morgan. Regenration and liability to injury. *Science*, 14(346):235–248, 1901.

[71] P. Müller, K. W. Rogers, B. M. Jordan, J. S. Lee, D. Robson, S. Ramanathan, and A. F. Schier. Differential Diffusivity of Nodal and Lefty Underlies a Reaction-Diffusion Patterning System. *Science*, 336:721–724, 2012.

[72] C. Nüsslein-Volhard and E. Wieschaus. Mutations affecting segment number and polarity in Drosophila. *Nature*, 287:795–801, 1980.

[73] D. Panáková, H. Sprong, E. Marois, C. Thiele, and S. Eaton. Lipoprotein particles are required for Hedgehog and Wingless signalling. *Nature*, 435(7038):58–65, 2005.

[74] A. M. Pani and B. Goldstein. Direct visualization of a native wnt in vivo reveals that a long-range Wnt gradient forms by extracellular dispersal. *eLife*, 7:1–22, 2018.

[75] R. B. Pepinsky, C. Zeng, D. Went, P. Rayhorn, D. P. Baker, K. P. Williams, S. A. Bixler, C. M. Ambrose, E. A. Garber, K. Miatkowski, F. R. Taylor, E. A. Wang, and A. Galdes. Identification of a palmitic acid-modified form of human Sonic hedgehog. *Journal of Biological Chemistry*, 273(22):14037–14045, 1998.

[76] N. Perrimon, J. Q. Ni, and L. Perkins. In vivo RNAi: today and tomorrow. *Cold Spring Harbor perspectives in biology*, 2(8), 2010.

[77] C. P. Petersen and P. W. Reddien. Smed-b-Catenin-1 is required for anteroposterior blastema polarity in planarian regeneration. *Science*, 319(5861):327–330, 2008.

[78] C. P. Petersen and P. W. Reddien. A wound-induced Wnt expression program controls planarian regeneration polarity. *PNAS*, 106(40):17061–17066, 2009.

[79] C. P. Petersen and P. W. Reddien. Wnt Signaling and the Polarity of the Primary Body Axis. *Cell*, 139(6):1056–1068, 2009.

[80] C. P. Petersen and P. W. Reddien. Polarized notum activation at wounds inhibits Wnt function to promote planarian head regeneration. *Science*, 332:852–855, 2011.

[81] M. Plass, J. Solana, F. Alexander Wolf, S. Ayoub, A. Misios, P. Glažar, B. Obermayer, F. J. Theis, C. Kocks, and N. Rajewsky. Cell type atlas and lineage tree of a whole complex animal by single-cell transcriptomics. *Science*, 360(6391), 2018.

[82] J. A. Porter, K. E. Young, and P. A. Beachy. Cholesterol modification of hedgehog signaling proteins in animal development. *Science*, 274(5285):255–259, 1996.

[83] W. H. Press, S. A. . Teukolsky, W. T. Vetterling, and B. P. Flannery. *Numerical recipes the art of scientific computing.* Cambridge University Press, New York, NY, 3 edition, 2007.

[84] P. W. Reddien. The Cellular and Molecular Basis for Planarian Regeneration. *Cell*, 175(2):327–345, 2018.

[85] P. W. Reddien, A. L. Bermange, A. M. Kicza, and A. Sánchez Alvarado. BMP signaling regulates the dorsal planarian midline and is needed for asymmetric regeneration. *Development*, 134(22):4043–4051, 2007.

[86] S. Restrepo, J. J. Zartman, and K. Basler. Coordination of patterning and growth by the morphogen DPP. *Current Biology*, 24(6):R245–R255, 2014.

[87] H. Reuter, M. März, M. C. Vogg, D. Eccles, L. Grífol-Boldú, D. Wehner, S. Owlarn, T. Adell, G. Weidinger, and K. Bartscherer. β-Catenin-Dependent Control Of Positional Information Along The AP body axis in planarians involves a teashirt family member. *Cell Reports*, 10(2):253–265, 2015.

[88] D. Ribatti. The chemical nature of the factor responsible for embryonic induction: An historical overview. *Organogenesis*, 10(1):38–43, 2014.

[89] E. Saló and J. Baguna. Proximal and distal transformation during intercalary regeneration in the planarian Dugesia(S)mediterranea. *Roux's Archives of Developmental Biology*, 194:364–368, 1985.

[90] M. L. Scimone, L. E. Cote, T. Rogers, and P. W. Reddien. Two FGFRL-Wnt circuits organize the planarian anteroposterior axis. *eLife*, 5:1–19, 2016.

[91] R. L. Setten, J. J. Rossi, and S. ping Han. The current state and future directions of RNAi-based therapeutics. *Nature Reviews Drug Discovery*, 18(6):421–446, 2019.

[92] J. Sharpe. Wolpert's French flag: What's the problem? *Development*, 146(24):1–5, 2019.

[93] H. Spemann and H. Mangold. über Induktion von Embryonalanlagen durch Implantation artfremder Organisatoren. *Archiv für Mikroskopische Anatomie und Entwicklungsmechanik*, 100(3-4):599–638, 1924.

[94] A. Spirov, K. Fahmy, M. Schneider, E. Frei, M. Noll, and S. Baumgartner. Formation of the bicoid morphogen gradient: an mRNA gradient dictates the protein gradient. *Development*, 136(4):605–614, 2009.

[95] E. Stanganello, A. I. Hagemann, B. Mattes, C. Sinner, D. Meyen, S. Weber, A. Schug, E. Raz, and S. Scholpp. Filopodia-based Wnt transport during vertebrate tissue patterning. *Nature Communications*, 6(5846):1–14, 2015.

[96] C. E. Stringer. The Means of Locomotion in Planarians. *Proceedings of the National Academy of Sciences of the United States of America*, 3(12):691–692, 1917.

[97] G. Struhl, K. Struhl, and P. M. Macdonald. The gradient morphogen bicoid is a concentration-dependent transcriptional activator. *Cell*, 57(7):1259–1273, 1989.

[98] T. Stückemann, J. P. Cleland, S. Werner, H. T.-K. Vu, S. Y. Liu, B. M. Friedrich, F. Jülicher, and J. C. Rink. Antagonistic self-organizing patterning systems control maintenance and regeneration of the anteroposterior axis in planarians. *Developmental Cell*, 40:248–263, 2017.

[99] M. Sureda-Gómez, J. M. Martín-Durán, and T. Adell. Localization of planarian β-CATENIN-1 reveals multiple roles during anterior-posterior regeneration and organogenesis. *Development*, 143(22):4149–4160, 2016.

[100] M. Sureda-Gómez, E. Pascual-Carreras, and T. Adell. Posterior wnts have distinct roles in specification and patterning of the planarian posterior region. *International Journal of Molecular Sciences*, 16(11):26543–26554, 2015.

[101] H. Thi-Kim Vu, J. C. Rink, S. A. McKinney, M. McClain, N. Lakshmanaperumal, R. Alexander, and A. S. Alvarado. Stem cells and fluid flow drive cyst formation in an invertebrate excretory organ. *eLife*, 4:1–28, 2015.

[102] A. Thommen, S. Werner, O. Frank, J. Philipp, O. Knittelfelder, Y. Quek, K. Fahmy, A. Shevchenko, B. M. Friedrich, F. Jülicher, and J. C. Rink. Body size-dependent energy storage causes Kleiber's law scaling of the metabolic rate in planarians. *eLife*, 8:1–29, 2019.

[103] G. Tkačik, C. G. Callan, and W. Bialek. Information flow and optimization in transcriptional regulation. *Proceedings of the National Academy of Sciences of the United States of America*, 105(34):12265–12270, 2008.

[104] A. M. Turing. The Chemical Basis of Morphogenesis. *Philosophical transactions of the Royal Society of London. Series B, Biological sciences*, 237(641):37–72, 1952.

[105] J. C. van Wolfswinkel, D. E. Wagner, and P. W. Reddien. Single-cell analysis reveals functionally distinct classes within the planarian stem cell compartment. *Cell Stem Cell*, 15(3):326–339, 2014.

[106] M. Vila-Farre and J. C. Rink. The ecology of freshwater planarians. In *Methods Mol. Biol. 1774*, pages 173–205. Springer Science+Business Media, LLC, part of Springer Nature 2018, New York, NY, 1 edition, 2018.

[107] H. T. K. Vu, S. Mansour, M. Kücken, C. Blasse, C. Basquin, J. Azimzadeh, E. W. Myers, L. Brusch, and J. C. Rink. Dynamic Polarization of the Multiciliated Planarian Epidermis between Body Plan Landmarks. *Developmental Cell*, 51(4):526–542.e6, 2019.

[108] D. E. Wagner, I. E. Wang, and P. W. Reddien. Clonogenic neoblasts are pluripotent adult stem cells that underlie planarian regeneration. *Science*, 332(6031):811–816, 2011.

[109] O. Wartlick, A. Kicheva, and M. González-Gaitán. Morphogen gradient formation. *Cold Spring Harbor perspectives in biology*, 1(a001255):1–22, 2009.

[110] O. Wartlick, P. Mumcu, F. Jülicher, and M. Gonzalez-Gaitan. Understanding morphogenetic growth control-lessons from flies. *Nature Reviews Molecular Cell Biology*, 12(9):594–604, 2011.

[111] O. Wartlick, P. Mumcu, A. Kicheva, T. Bittig, C. Seum, F. Jülicher, and M. González-Gaitán. Dynamics of Dpp signaling and proliferation control. *Science*, 331(6021):1154–1159, 2011.

[112] S. Werner. *Growth and Scaling during Development and Regeneration.* PhD thesis, TU Dresden, 2016.

[113] S. Werner, T. Stückemann, M. Beirán Amigo, J. C. Rink, F. Jülicher, and B. M. Friedrich. Scaling and regeneration of self-organized patterns. *Physical Review Letters*, 114(13):1–5, 2015.

[114] K. E. Wiese, R. Nusse, and R. van Amerongen. Wnt signalling: Conquering complexity. *Development*, 145(165902):1–9, 2018.

[115] K. Willert, J. D. Brown, E. Danenberg, A. W. Duncan, I. L. Weissman, T. Reya, J. R. Yates, and R. Nusse. Wnt proteins are lipid-modified and can act as stem cell growth factors. *Nature*, 423(6938):448–452, 2003.

[116] J. N. Witchley, M. Mayer, D. E. Wagner, J. H. Owen, and P. W. Reddien. Muscle cells provide instructions for planarian regeneration. *Cell Reports*, 4(4):633–641, 2013.

[117] L. Wolpert. The French flag problem: A contribution to the discussion on pattern development and regeneration, Vol.1. In C. H. Waddington, editor, *Towards a theoretical biology*. Aldine Publishing Company, 1968.

[118] L. Wolpert. Positional information and the spatial pattern of cellular differentiation. *Journal of Theoretical Biology*, 25(1):1–47, 1969.

[119] Y. Yang and M. Mlodzik. Wnt-Frizzled/Planar Cell Polarity Signaling: Cellular Orientation by Facing the Wind (Wnt). *Annual Review of Cell and Developmental Biology*, 31(1):623–646, 2015.

[120] A. Zeng, H. Li, L. Guo, X. Gao, S. McKinney, Y. Wang, Z. Yu, J. Park, C. Semerad, E. Ross, L. C. Cheng, E. Davies, K. Lei, W. Wang, A. Perera, K. Hall, A. Peak, A. Box, and A. Sánchez Alvarado. Prospectively Isolated Tetraspanin + Neoblasts Are Adult Pluripotent Stem Cells Underlying Planaria Regeneration. *Cell*, 173:1593–1608, 2018.

[121] S. Zhou, W. C. Lo, J. L. Suhalim, M. A. Digman, E. Gratton, Q. Nie, and A. D. Lander. Free extracellular diffusion creates the Dpp morphogen gradient of the Drosophila wing disc. *Current Biology*, 22(8):668–675, 2012.

Versicherung

Hiermit versichere ich, dass ich die vorliegende Arbeit ohne unzulässige Hilfe Dritter und ohne Benutzung anderer als der angegebenen Hilfsmittel angefertigt habe; die aus fremden Quellen direkt oder indirekt übernommenen Gedanken sind als solche kenntlich gemacht. Die Arbeit wurde bisher weder im Inland noch im Ausland in gleicher oder ähnlicher Form einer anderen Prüfungsbehörde vorgelegt.

Die vorgelegte Arbeit wurde im Zeitraum von August 2016 bis September 2020 unter Betreuung durch Prof. Dr. Frank Jülicher und Dr. Jochen Rink am Max-Planck-Institut für Physik komplexer Systeme und am Max-Planck-Institut für molekulare Zellbiologie und Genetik in Dresden durchgeführt.

Ich versichere, dass ich bisher keine erfolglosen Promotionsverfahren unternommen habe. Ich erkenne die Promotionsordnung der Fakultät der Mathematik und Naturwissenschaften der Technischen Universität Dresden an.

Dresden, den 04.09.2020